Search for supersymmetric particles in final states with multi-leptons with the ATLAS detector

Huan Ren

CPPM-T-2017-03

Aix-Marseille University
Institute of High Energy Physics
ECOLE DOCTORALE 352
Centre de Physique des Particules de Marseille

Thèse présentée pour obtenir le grade universitaire de docteur

Discipline : PHYSIQUE ET SCIENCES DE LA MATIERE
Spécialité : PHYSIQUE DES PARTICULES ET ASTROPARTICULES

Huan REN

Recherche de particules supersymétriques dans des états finaux multileptoniques avec le détecteur ATLAS
Search for Supersymmetric Particles in Final States with Multi-Leptons with the ATLAS Detector

Soutenue le 18/10/2017 devant le jury :

Monica D'ONOFRIO	University of Liverpool	Rapporteur
Huaqiao ZHANG	Particle Astrophysics Division, CAS	Rapporteur
Eric KAJFASZ	CPPM	Examinateur
Yanwen LIU	USTC	Examinateur
Tianjun LI	Institute of Theoretical Physics, CAS	Examinateur
Emmanuel MONNIER	CPPM	Directeur de thèse
Xuai ZHUANG	IHEP	Co-Directeur de thèse
Jin SHAN	IHEP	Co-Directeur de thèse

Abstract

Since a long time, humans have been eager to explore and understand the foundations and basic elements of the universe. The Standard Model (SM) was built up, since the second half of the 20th century, to give answers on elementary physics by introducing all the elementary particles including quarks, leptons, gauge bosons and the Higgs boson.

The Large Hadron Collider (LHC) is the largest collider located at CERN (European Organization for Nuclear Research), Geneva. Massive collision dataset was produced and collected since 2009 at a collision center of mass energy of up to 8 TeV before 2012 (Run1) and 13 TeV in 2015 and 2016 (Run2). The ATLAS detector, located at one of the LHC interaction points revealed in 2012 the last member of the SM elementary particles, the Higgs boson. Meanwhile, more thoughts and questions were raised-up, such as the hierarchy problem, the dark matter, the origin of gravity and gauge unification at higher scale. Supersymmetry(SUSY) models are an appealing extension of the SM to answer some of these questions.

SUSY theory models link each boson (of integer spin) to a certain fermion (of half-integer spin) as super-partner. New elementary particles like squarks, sleptons, gauginos and higgsinos are introduced. The simplest form of spontaneously-broken supersymmetry is called Minimal Supersymmetric Standard Model (MSSM), a very good candidate for beyond Standard Model physics.

In this thesis, a brief presentation of the Standard Model and of the main supersymmetry models is given first. Then the LHC complex and the ATLAS detector are described followed by a performance study on tau isolation. The main part of the document finally describes in details two searches for SUSY particles with the ATLAS detector and the obtained results.

The first one is a search for direct stau production with final state of two opposite-sign taus and multi-jets in proton-proton collision at an 8 TeV center of mass energy and a 20.1 fb^{-1} integrated luminosity. The low cross-section for signals in the Electro-Weak sector has pushed to use multivariable analysis techniques to improve the sensitivity. No significant excess over the Standard Model expectation was observed. Upper-limit was set on the cross-section of the signal models. For "direct stau" search, we excluded the signal point with $m(LSP) = 0$ GeV and $m(\tilde{\tau}) = 100$ GeV.

The second one is a search for squarks and gluinos strong production in final states with jets and two same-sign leptons or three leptons at 13 TeV proton-proton collision and a 13.2 fb^{-1} integrated luminosity. No significant excess over the Standard Model expectation was observed. Upper-limit was set on the cross-section of all the models involved. Generally, region with $\tilde{g}$ mass up to 1.7 TeV have been excluded.

Keywords: ATLAS Detector, Supersymmetry, Multivariate Analysis, Matrix Method

Résumé

Depuis longtemps, l'homme est profondément intéressé à explorer et tenter de comprendre les fondements de notre univers. Le Modèle Standard (SM) des particules a été construit au cours de la deuxième moitié du 20ème siècle pour répondre aux questionnements en physique corpusculaire en introduisant toutes les particules élémentaires que sont les quarks, les leptons, les bosons de jauge et le boson de Higgs.

Le grand collisionneur de Hadron (LHC) est le plus grand et plus puissant accélérateur au monde, situé au CERN (Organisation Européenne pour la recherche Nucléaire) à Genève. Une énorme quantité de données de collision a été produite et collectée depuis 2009 à une énergie de collision atteignant 8 TEV dans le centre de masse en 2012 (Run1) et 13 TeV en 2015 et 2016 (Run2). Le détecteur ATLAS, situé sur une de point de collision du LHC, a permis de découvrir en 2012 le boson de Higgs, dernier des constituants du SM non encore découvert. Mais d'autre questions et réflexions ont surgi, comme le problème de la hiérarchie, la matière noire, l'origine de la gravité ou encore l'unification de jauge à grande échelle. Les modèles supersymétriques ou SUSY sont une élégante extension du modèle standard apportant une réponse à certaines de ces questions.

Les modèles théoriques SUSY relient chaque boson (de spin entier) à un fermion spécifique (de spin demi entier) comme super partenaire. De nouvelles particules élémentaires telles que les squarks, sleptons, sgauginos ou higgsinos sont ainsi introduites. La forme la plus simple de brisure spontanée de supersymétrie est appelée le Modèle Standard Super-symétrique Minimal (MSSM), un très bon candidat de physique au-delà du modèle standard.

Dans cette thèse, une brève description du Modèle Standard et des principaux modèles supersymétriques est d'abord donnée. Le LHC et le détecteur ATLAS sont ensuite présentés suivi d'une étude de performance sur l'isolation des taus. La partie principale du mémoire décrit enfin en détails deux recherches de particule SUSY avec le détecteur ATLAS et les résultats obtenus.

La première recherche décrite est celle de production directe de stau avec un état final à deux tau de signes opposés et plusieurs jets dans des collisions proton proton a 8 TeV d'énergie dans le centre de masse et une luminosité totale intégrée de 20.1 fb^{-1}. La faible section efficace pour des signaux dans le secteur électrofaible a nécessité l'utilisation de techniques d'analyse multi variables (MVA) pour améliorer la sensibilité de la recherche. Aucun excés significatif par rapport au Modèle Standard n'a été observé. Des limites supérieures ont été extraite sur la section efficace des modèles de signal. Pour la recherche direct de "stau", le signal est exclu pour $m(LSP) = 0GeV, m(stau) =$ 100 GeV.

La deuxième recherche présentée est celle de la production forte de squarks et de gluions avec des états finaux, à deux leptons de mêmes signes ou à trois leptons, associées à des jets dans des collisions proton-proton à $\sqrt{s} = 13$ TeV et une luminosité intégrée de 13.2 fb^{-1}. Aucun excès significatif par rapport au Modèle Standard n'a été observé. Une limite supérieure a été extraite sur la section efficace de tous les modèles impliqués. La région avec une masse de gluino inférieure à 1.7 TeV a été exclue.

Mots-clés: ATLAS Détecteur, Super-Symétriques, Analyse Multi Variables, Méthode Matrice

Contents

Acknowledgements

I would like to express my gratitude to all those who helped me during the writing of this thesis.

First of all, I am deeply indebted to my supervisor, Emmanuel Monnier, for his instructive advice and useful suggestions on my thesis. Dr. Emmanuel Monnier has been helping me a lot since 4 years ago, when I first arrive CPPM. Realistic, dutiful and dependable are the first impressions he has left on me. During my co-PhD time in Marseille, he has indicated the direction of my scientific research, and was always providing the best resource for my studies. With his help, I was able to join the SS2l analysis group, to get adapted to the local life of France, and to have better understanding of my responsibilities. His unique personality has deep influence on me, and I can always benifit from each of the conversations between us. Grateful acknowledgement is made to him for all his important comments and encouragement to me during the thesis writing.

High tribute shall be paid to my co-supervisor, Professor Shan Jin. I've been always looking up to him for being knowledgeable, precise and industrious. Mr. Jin has a sharp intuition of physics, good professionalism, as well as attainment in math and statistics. It has been 6 years since Prof. Jin started to supervising me, with good introductions to the ATLAS experiment. He is then providing a lot of opportunities for me during my PhD time, in all the analyses I've been involved. He has always been analytical and expressive in all the discussions between us. His talent and accomplishment have profound impacts on my life. So here, I would also give my gratitude and blessing to him.

Special thanks should go to Professor Xuai Zhuang, my co-supervisor. She is always responsible, punctual, and earnest. She has been helping me a lot since the very beginning of my PhD time, from the set-up of ATLAS framework, step-by-step TROOT instructions, to an overview of SUSY theory and experiments. She has provded directly guidance for most of the analyses that I participated. With the accurate judgment and description from her, I was able to finish several physics analyses, covering many SUSY searches with quite different final states. Also, I received much help form her during the thesis writing and reviewing. She has put considerable time and effort into her comments on my manuscripts. Her profound knowledge of physics has always been an instruction for my researches.

Also, I would like to thank all the people in the SUSY 2τ group. Mz. Da Xu has always been temperate and cooperative. I've benift quite a lot for her continuous support for the analysis framework and comments for my thesis. Mr. Yu Bai has also sent much help when I first come to the subject of SUSY search, with very detailed explaination and clear physical thoughts. Many thanks would go to other guys in the group: Huajie Cheng, Yang Liu, Peng Zhang and Chenzheng Zhu. As well, I gratefully acknowledge the help of the SUSY SS2l group, especially from Julien Maurer, Ximo Poveda Torres and Otilia Ducu, for the opportunity to join the nice team, and for the support for the analysis framework.

I'll also say "thank you" to all the people in CPPM and IHEP who helps me, especially for Pascal Pralavorio, who has provided lots of ideas and helpful suggestions for the SUSY searches that I envolved. The others are: Esthere Garnier, Jian Liu, Anqing Wang, Chao Wang and Ruiqi Zhang; Tianjue Min, Jiesheng Yu, Liwen Yao, Zhenghao Zhang, Huijun Zhang, Liqing Qin, Cong Peng, Jingjing Xu, Qin Qin and Weifeng Qiu. Meanwhile, I would like to thank all the guys in the Chinese Students' Federation of Marseilles, who

make my life more colorful in France.

Last but not the least, my gratitude also extends to both universities and institutes: Aix-Marseille University with CPPM, Chinese Academy of Sciency with IHEP. Thank you both for the co-PhD opportunity and support for the funding.

Résumé détaillé

Le Modèle Standard (SM) est une théorie générale décrivant les principes de base de la matière, les particules élémentaires et leurs interactions. Il est devenu une des théories les plus réussie, dans laquelle toutes les particules prédites ont été observées : les quarks, et les leptons avec, pour chaque famille, leurs six différentes saveurs, mais aussi les vecteurs des interactions, le photon, les gluons, les bosons $W^{\pm}$ et Z^0 et finalement le boson de Higgs, découvert avec succès en 2012 par les expériences ATLAS et CMS. La SuperSymétrie (SUSY), une élégante théorie pour décrire la physique au-delà du Modèle Standard, prédit une liste de nouvelles particules, dites particules super-symétriques. Ces particules sont nommées "sparticules", et sont les super partenaires de chaque particule SM. Le Modèle Super-Symétrique Minimal, dit MSSM, est le plus simple de ces modèles SUSY et permet de compléter le SM pour résoudre les problèmes suivant qui y sont non résolus : le problème de hiérarchie, la matière noire, l'origine de la gravité, l'absence d'unification de jauge à grande échelle...

Le grand collisionneur de hadron (LHC) est le plus grand et plus puissant accélérateur au monde. Situé au CERN (Organisation Européenne pour la recherche Nucléaire) à Genève, il a été construit pour obtenir des mesures précises du Modèle Standard et permettre une recherche dédiée de phénomènes physiques au-delà du SM. Une énorme quantité de collision a été produite et collectée depuis 2009. Le détecteur ATLAS, un des deux détecteurs généralistes, est situé sur une de point de collision du LHC et a commencé à les enregistrer dès cette période. Les deux périodes principales de prise de données sont les campagnes dites "Run1" (2010-2013), avec une énergie de collision dans le centre de masse atteignant 8 TeV en 2012, et "Run2" (depuis 2015) avec 13 TeV. La luminosité totale intégrée pour le Run1 a été de 20.1 fb^{-1}. Elle a permis de découvrir avec succès en 2012 le boson de Higgs, dernier des constituants du SM non encore découvert. Pour le Run2, cette luminosité totale intégrée a été de 36.5 fb^{-1}. Beaucoup de recherches de nouvelles particules ont été faites avec ces campagnes de prise de données faites par ATLAS et en particulier les deux recherches auxquelles j'ai contribué significativement après avoir d'abord effectué une estimation des performances d'isolation des τ également cadre de ma qualification comme auteur ATLAS.

La première recherche présentée dans cette thèse concerne la production directe de stau, dans des états finaux avec au moins deux taus de signes opposés et de l'énergie manquante. Elle a été effectuée dans les collisions proton proton à 8TeV dans le centre de masse du Run1 avec une luminosité intégrée de 20.1 fb^{-1}. La deuxième recherche a été effectuée dans les premières collisions proton proton à 13TeV du Run2 avec une luminosité intégrée de 13.2 fb^{-1} obtenue jusqu'en juin 2016. Elle concerne la production forte de squarks et de gluinos dans des états finaux avec deux leptons ou trois leptons, dont deux de mêmes signes, associés à des jets.

Par ailleurs, l'étude de performance d'isolation des leptons τest effectuée par une estimation sur l'erreur de comptage de traces associées. Pour cela, des évènements $Z \rightarrow \mu\mu$ sont sélectionnés dans les données réelles et dans les données simulées par Monte Carlo (MC) et sont ensuite utilisés dans une méthode de sonde et d'étiquetage. Après l'étiquetage d'un des muons, le comportement du muon sonde est ensuite étudié dans les données réelles et simulées. La stratégie de comptage de trace est utilisée comme un sous algorithme

de l'algorithme de collection de jets dit "Anti-K_T". Il compte le nombre de traces dans l'environnement d'un objet physique, pions, muons... Cela est très important pour la reconstruction jet / τ dans l'expérience ATLAS. Ainsi, la précision du comptage des traces est essentielle dans de nombreuses analyses incluant les leptons τ et plusieurs jets dans l'état final. Pour toute analyse qui utilise le comptage des traces, l'incertitude des algorithmes doit être prise en compte. La différence entre la réponse des données et de la simulation MC est assignée comme systématique du comptage des traces. Le rapport données / MC en fonction de η et p_T sur le comptage des traces internes est montrée dans le tableau 1. En général, l'incertitude obtenue est inférieure à 10%.

Table 1: Rapport entre le nombre moyen de traces dans les données et la simulation MC. L'incertitude du comptage des traces internes peut être obtenue en retranchant 1.0 à chacune des valeurs données dans la table.

	$\|\eta\| < 1.05$	$1.05 < \|\eta\| < 1.30$	$1.30 < \|\eta\| < 2.00$	$\|\eta\| > 2.00$
		ratio		
baseline	1.026 ±0.010 ±0.006	1.093 ±0.023 ±0.008	1.062 ±0.014 ±0.006	1.105 ±0.022 ±0.008
$p_T > 0.5GeV$	0.999 ±0.006 ±0.003	1.019 ±0.014 ±0.004	1.030 ±0.009 ±0.003	1.072 ±0.014 ±0.003
$p_T > 0.9GeV$	1.017 ±0.009 ±0.005	1.077 ±0.021 ±0.007	1.057 ±0.013 ±0.006	1.101 ±0.020 ±0.007
$p_T > 1.1GeV$	1.027 ±0.010 ±0.007	1.093 ±0.025 ±0.009	1.071 ±0.015 ±0.007	1.104 ±0.023 ±0.009
1 pixel hit	1.032 ±0.009 ±0.006	1.100 ±0.023 ±0.008	1.068 ±0.014 ±0.007	1.105 ±0.021 ±0.009
$SCT + pixel \geq 8$	1.126 ±0.006 ±0.004	1.137 ±0.014 ±0.004	1.095 ±0.008 ±0.002	1.082 ±0.013 ±0.003
inverted $\|z_0 sin\theta\|$	1.025 ±0.009 ±0.006	1.086 ±0.023 ±0.007	1.060 ±0.014 ±0.006	1.109 ±0.022 ±0.009

La production directe de slepton de troisième génération ($\tilde{\tau}$) est étudiée car elle fournit une structure claire de désintégration fortement corrélée au lepton tau dans l'état final et avec un bruit de fond assez bas. Une analyse traditionnelle en coupure et comptage a été publiée utilisant ce scénario. La distribution de meff obtenue dans les régions de signal sélectionnées par les coupures est illustrée dans la Figure 1. Les résultats des données observées et du bruit de fond attendu sont donnés dans le tableau 2.

On voit clairement dans les figures et les tables ci-dessus que la sensibilité de l'analyse en coupure et comptage donne un résultat assez faible principalement à cause de la très petite section efficace du processus. Une analyse multi variables présentée dans cette thèse a donc été développée pour améliorer nettement la sensibilité à la production directe de stau. Cela est réalisé en utilisant un ensemble de variables discriminantes appropriées pour atteindre une séparation maximale. L'outillage logiciel pour l'analyse multivarié, appelé TMVA, utilise une phase d'entrainement s'appuyant sur ces variables choisies avec des lots d'événements respectivement de signal et de bruit de fond. La procédure d'entra?nement se traduit par une fonction d'évaluation avec une valeur de sortie montrant le degré de certains événements à être plutôt de type signal ou plutôt de type bruit de fond. Le mélange de bruit de fond et de signal est alors appliqué avec la fonction obtenue pour donner plus de sensibilité à l'étude. La procédure d'arbre de décision renforcée, dite BDT, a été adoptée après comparaison avec d'autres méthodes fournies par TMVA, car elle fournit la plus grande sensibilité et des algorithmes d'entrainement plus intuitifs. La réponse de l'algorithme BDT est ensuite utilisée dans la définition de la Région de Signal (SR).

Avec la détermination de SR, les bruits de fond sont principalement des événements provenant des processus suivants: W + jets, Z + jets, multi-jets et de processus avec des

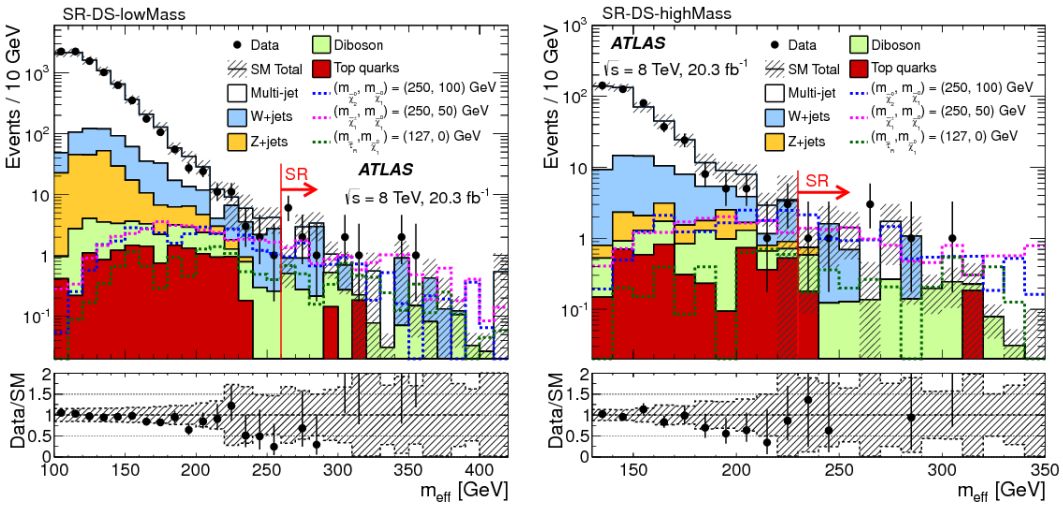

Figure 1: Distribution de m_{eff} ($p_{T,\tau 1}$ + $p_{T,\tau 2}$ + MET) dans et hors des régions SR-DSlowMass (gauche) et SR-DShighMass (droite). Les incertitudes statistiques et systématiques sont montrées.

Table 2: Nombre d'événements observés et attendus dans les régions de signal sélectionnées par coupure pour une luminosité intégrée de 20.3 fb^{-1}. Les incertitudes données sont combinées statistiques et systématiques.

SM process	SR-DS-highMass	SR-DS-lowMass
Top	0.9 ± 0.4	1.3 ± 0.6
Z+jets	0.6 ± 0.4	0.40 ± 0.27
W+jets	2.7 ± 0.9	4.1 ± 1.2
Diboson	2.5 ± 1.0	2.9 ± 1.0
Multi-jet	0.9 ± 1.2	2.8 ± 2.3
SM total	7.5 ± 1.9	11.5 ± 2.9
Observed	7	15
Ref. point 1	10.2 ± 2.6	7.5 ± 2.0
Ref. point 2	12.4 ± 2.8	12.8 ± 2.7
Ref. point 3	3.8 ± 1.0	5.2 ± 1.3
p_0	0.50	0.21
Expected σ_{vis}^{95} (fb)	$< 0.37^{+0.17}_{-0.10}$	$< 0.51^{+0.18}_{-0.15}$
Observed σ_{vis}^{95} (fb)	< 0.37	< 0.66

quarks top. Les bruits de fonds ont été estimés (et validés) en utilisant différentes méthodes (et différentes régions de validation) présentée et étudiées de façon approfondie dans cette thèse. La méthode dite "ABCD" est utilisée pour l'estimation du bruit de fond multi-jet. La réponse du BDT et les distributions cinématiques dans et hors de la région du signal MVA sont illustrés dans la Figure 2. Le résultat final de cette étude complète ne montre aucun excès significatif pour le processus "direct-stau". Cependant, la région de l'espace

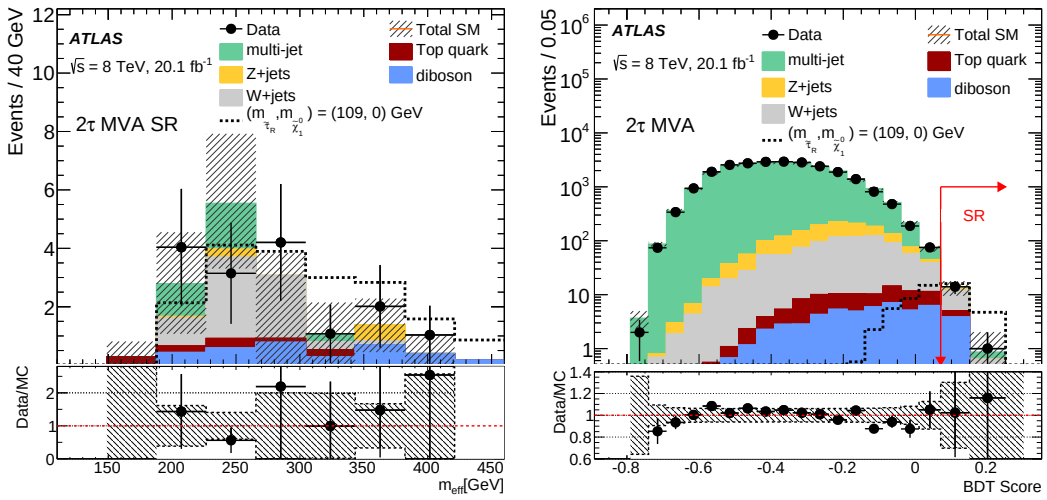

Figure 2: Distribution de Meff (gauche) et de la réponse BDT (droite) pour la region de signal de recherche de production directe de stau.

de phase où $m(LSP) = 0$ GeV et $m(\tilde{\tau}) = 100$ GeV est exclu, comme le montre la Figure 3.

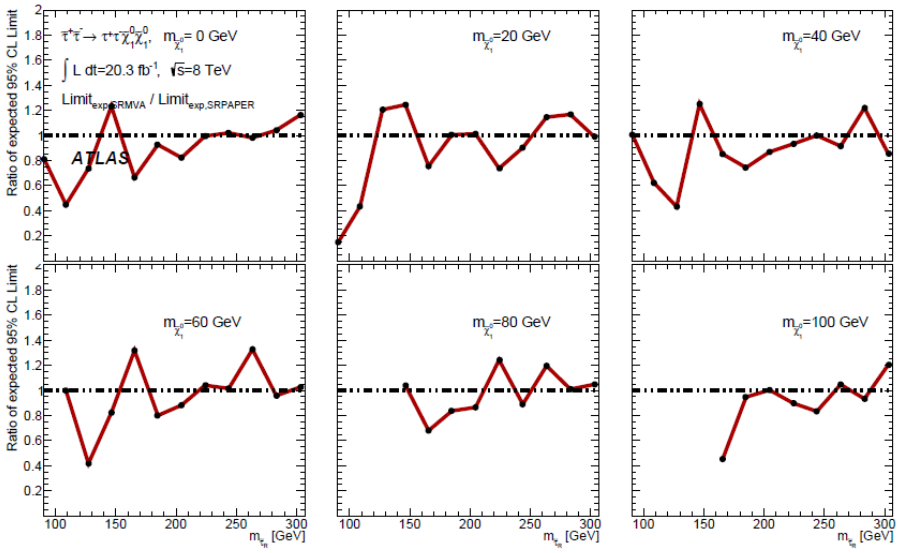

Figure 3: Comparaison de la limite supérieure attendue sur la force du signal avec la région de signal MVA et de la limite supérieure attendue sur la force du signal avec la région de signal combinée utilisant la méthode de coupure.

La recherche de production forte de squarks et de gluinos avec deux ou trois leptons légers dont deux de même signe a été étudiée en utilisant les données 2015-2016 du Run2. Les canaux utilisé dans cette recherche sont très intéressants en raison du très faible bruit de fond SM. Les scénarios intéressants comprennent la production de paires de gluino avec désintégration de stop, la production de paires de gluino avec désintégration en deux étapes via des neutralinos et sleptons (ou de gauginos et de bosons W et Z), désintégration directe

Table 3: Rendements des bruits de fond attendus dans les régions de signal SR3L1, SR3L2, SR0b1, SR0b2 et SR1b. Les rendements de l'événement sont donnés pour 13.2 fb^{-1}. Les incertitudes affichées comprennent à la fois des sources systématiques et statistiques.

	SR3L1	SR3L2	SR0b1	SR0b2	SR1b	SR3b
Observed	6	2	5	0	12	2
SM total	6.05 ± 2.15	1.18 ± 0.49	8.81 ± 2.87	1.57 ± 0.77	11.40 ± 2.76	1.60 ± 0.61
ttZ	0.69 ± 0.25	0.10 ± 0.04	0.45 ± 0.18	0.10 ± 0.04	1.58 ± 0.55	0.19 ± 0.07
ttW	0.09 ± 0.04	0.02 ± 0.01	0.45 ± 0.17	0.13 ± 0.06	1.97 ± 0.68	0.17 ± 0.06
Diboson	4.18 ± 1.96	0.70 ± 0.43	3.72 ± 1.86	0.71 ± 0.52	0.47 ± 0.41	0.00 ± 0.00
Rare	0.80 ± 0.44	0.21 ± 0.13	0.76 ± 0.44	0.18 ± 0.12	2.69 ± 0.90	0.89 ± 0.31
Fakes	0.29 ± 0.29	0.15 ± 0.15	2.92 ± 1.97	0.37 ± 0.53	3.25 ± 2.08	0.20 ± 0.49
MisCharge	0.00 ± 0.00	0.00 ± 0.00	0.50 ± 0.09	0.08 ± 0.03	1.43 ± 0.19	0.14 ± 0.03

de sbottom. Des régions de signal spécifiques ont alors été définies pour cibler tous les processus.

Le bruit de fond de l'analyse 2 leptons de même signe (SS) peut être principalement classé en trois catégories:

- Les processus de leptons SS "prompt";
- Les processus d'électrons de charges inversée dit "Charge Flip";
- Les processus de faux-lepton.

Le bruit de fond "Prompt lepton" est prédit en s'appuyant sur la simulation de Monte Carlo des processus pertinents. Le bruit de fond "Charge-Flip" est estimé en utilisant le taux de d'inversion de charge calculé par une estimation basée sur les données. Le bruit de fond de "faux-lepton" est estimé en utilisant une autre méthode basée sur les données, connue sous le nom de méthode de la matrice ou "Matrix-Method". Cette méthode utilise des efficacités de faux-lepton (également appelé "taux de faux" ou "Fake Rate") et de leptons vrais comme entrée. Les efficacités de faux et de vrais sont attribuées dans des régions de contrôle dédiées. Les distributions de m_{eff} pour les données et pour le bruit de fond SM attendu dans les régions de signal sont présentées à la figure 4. Les rendements des données observées et des bruits de fond attendus dans les régions de signal sont présentés dans le tableau 3.

Les tableaux et figures obtenus ci-dessus pour cette étude ne montrent aucun excès significatif pour tous les processus corrélés. Cependant, la limite dans l'espace de phase est largement étendue, comme le montre la figure 5:

- pour la production de paires de gluinos via des neutralinos et des W/Z, la région exclue est étendue jusqu'à 1.55 TeV le long de l'axe de masse des gluinos et 850 GeV le long de celui des neutralino;
- pour la production de paires de gluinos via des sleptons, la région exclue est étendue jusqu'à 1.7 GeV le long de l'axe de masse des gluino et 1.1 GeV le long de celui des neutralino;
- pour la production de paires sbottom, la région exclue s'étend jusqu'à 700 GeV le long de l'axe de masse des sbottom et 250 GeV le long de celui des neutralino;
- pour le processus Gtt, la région exclue est étendue jusqu'à 1.5 TeV le long de l'axe de masse des gluinos et jusqu'à 900 GeV le long de l'axe de masse des neutralino.

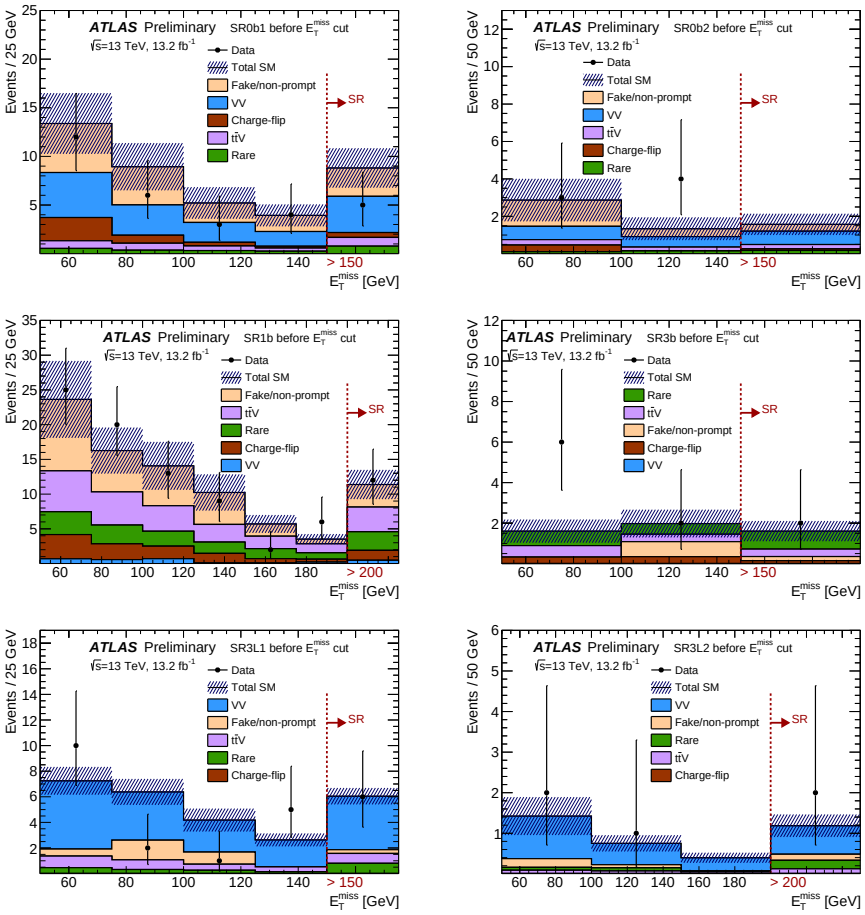

Figure 4: Comparaisons entre les données observées (2015 + 2016, 13.2 fb^{-1}) et les bruits de fond SM + détecteur attendues pour six régions de signal. Les incertitudes comprennent des sources statistiques et systématiques combinées pour les bruits de fond basés sur les données.

De plus, depuis lors, des résultats nouvellement mis à jour de cette analyse ont été récemment publiés en utilisant la totalité des données de 2015 et 2016. Plus d'espace dans l'espace de phase sont maintenant exclu:

- pour la production de paires de gluino via des neutralino et des W / Z, la région exclue est élargie de 50 GeV le long de l'axe de masse gluino et de 50 GeV le long de celui des neutralino;
- pour la production de paires de gluinos via des sleptons, la région exclue est agrandie de 200 GeV le long de l'axe de masse des gluino et de 100 GeV le long de l'axe de masse des neutralino;
- pour la production de paires de sbottom, la région exclue est étendue de 50 GeV le long de l'axe de masse des sbottom et de 50 GeV le long de l'axe de masse des neutralino;
- pour le processus Gtt, la région exclue est agrandie de 200 GeV le long de l'axe des masses de gluinos.

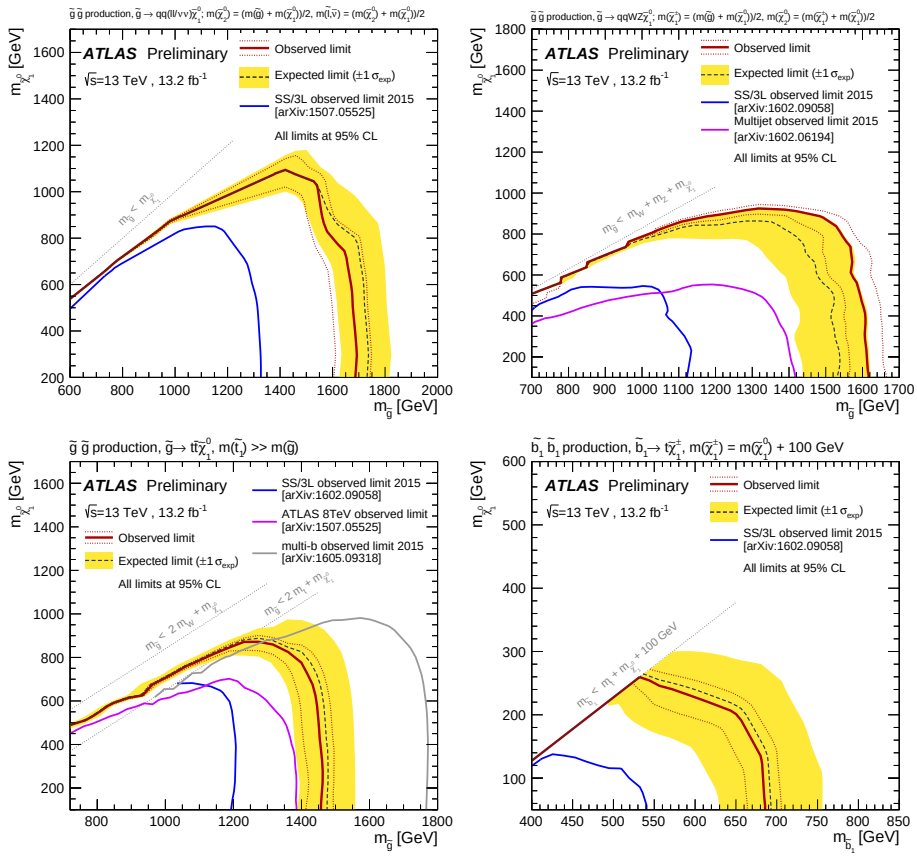

Figure 5: Limites d'exclusion sur les masses des super partenaires dans différents scénarii SUSY de conservation de la parité R, pour 9.5 fb^{-1}. Les régions de signal utilisées pour contenir chaque scénario sont spécifiées dans les légendes.

Chapter 1

The Standard Model and Beyond

1.1 The Standard Model

The Standard Model(SM) is a general theory describing the basic units of matter, the elementary particles and their interactions. It has become one of the most successful theory, in which all the predicted particles are observed experimentally, including quarks and leptons with 6 different flavors respectively (as well as their anti-particle), photon, gluon, $W^{\pm}$ and Z^0 gauge boson, and finally the Higgs boson, successfully discovred in 2012 [1, 2, 3, 4, 5, 6]. All the interactions between those particles can be described by a $SU(3)_c \otimes SU(2)_l \otimes U(1)_y$ gauge theory, which also coincides with experimental observations [7] .

1.1.1 Gauge invariance and interactions

Starting with a "toy" model to review the relationship between gauge theory and the interactions, for an 1-D scalar field $\phi(x)$ with mass m, its free field can be described using Lagrangian:

$$\mathcal{L} = \partial^{\mu}\phi^{*}(x)\partial_{\mu}\phi(x) - m^2\phi^{*}(x)\phi(x).$$

The lagrangian has global U(1) symmetry that remains unchanged under any U(1) transform ($\phi(x) \rightarrow e^{i\alpha}\phi(x)$). However, the symmetry of L will be broken if the α is a function of coordinate, which is called gauge U(1) symmetry. Appropriate Modifications can be applied to the lagrangian to keep its gauge U(1) symmetry. An extra vector field A^{μ} is introduced to L where:

$$A_{\mu}(x) \rightarrow A^{'}_{\mu}(x) = A_{\mu}(x) + \frac{1}{g}\partial_{\mu}\alpha(x).$$

Replacement of ∂_{μ} to

$$D_{\mu} \equiv [\partial_{\mu} - igA_x]$$

forms the new lagrangian:

$$\mathcal{L} = [D^{\mu}\phi(x)]^{*}D_{\mu}\phi(x) - m^2\phi^{*}(x)\phi(x),$$

which also has gauge U(1) symmetry. A term

$$-ig\partial^{\mu}\phi^{*}(x)A_{\mu}(x)\phi(x) + hc$$

is presented in the final expression [8] [9].

In this case, the filed $\phi(x)$ acts as a representation of a U(1) group, while the introduction of the vector field A^{μ} is necessary to construct a theory with U(1) gauge symmetry. The introduced vector field will have interaction with the ϕ field - A^{μ} is called gauge field while the interaction is called gauge interaction.

Similarly, the Standard Model is a $SU(3)_c \otimes SU(2)_l \otimes U(1)_y$ gauge theory, which has 3 different gauge interactions respectively.

1.1.2 Quantum Chromodynamics

As discribed by the the colored quark model, each quark carry one of the three colors: red, green and blue. Thus, the Quantum Chromodynamics part of the Standard Model can be described by $SU(3)_c$ gauge theory. The theory involves quarks and gluons, but makes no distinction among the quark/gluon flavor or chirality. The gluons are described by the Gell-Mann matrices, which have eight generators.

The lagrangian of Quantum Chromodynamics is:

$$\mathcal{L}_C = \sum_i \overline{q}_i(i\not{D}_c - m_i)q_i - \frac{1}{4}G^{\alpha}_{\mu\nu}G^{\alpha,\mu\nu},$$

where i stands for all possible quarks with different flavors and chiral,

$$\not{D}_0 \equiv \gamma_{\mu}D^{\mu}_C$$

is the covariant derivative, where

$$D^{\mu}_C = \partial^{\mu} - ig_S T^{\alpha}G^{\alpha,\mu}.$$

G^{α}_{μ} stands for the gluon field strength tensor:

$$G^{\alpha}_{\mu\nu} \equiv \partial^{\mu}G^{\alpha}_{\nu} - \partial^{\nu}G^{\alpha}_{\mu} + g_S f^{abc}G^{b}_{\mu}G^{c}_{\nu}.$$

The $SU(3)_c$ group generator T^a is related to the Gell Mann matrix:

$$T^a = \frac{\lambda^a}{2},$$

satisfying:

$$[T^a, T^b] = if^{abc}T^c.$$

Within the gauge transformation, the property of quark/gluon field would be:

$$q(x) \rightarrow q^{'}(x) = exp[i\alpha^a(x)T^a]q(x),$$

$$G^a_{\mu}(x) \rightarrow G^{'a}_{\mu}(x) = G^a_{\mu}(x) + \frac{1}{g_S}\partial^{\mu}\alpha^a(x) + f^{abc}G^b_{\mu}(x)\alpha^c(x).$$

In this case, the lagrangian remains invariant. Here in $\mathcal{L}$, the mass term of gluon field G^a_μ, which is $m^2 G^a_\mu G^{a,\mu}$, cannot be introduced. Otherwise, the $SU(3)_c$ symmetry of L_C would be broken. In this case, we need the gluon mass to be 0 theoretically, which is in accordance with the experiment observation. The final global and local Lagrangian can be then written as:

$$\mathcal{L}_C = \overline{q}q + G^2 + g_s\overline{q}qG + g_sG^3 + g_s^2G^4,$$

where $\overline{q}q$ and G^2 are the kinematic terms of quarks and gluons, $g_s\overline{q}qG$ is the color interaction term between quarks and gluons.

The QCD introduces a property called color-charge: quarks are carrying defferent color and gluons are the force carrier of strong interaction. Color-charged particles such as quarks and gluons cannot be isolated and exist only within hadrons or high-temperature plasmas. This is because a constant force between two color charges as they are separated. In order to increase the separation between two quarks within a hadron, ever-increasing amounts of energy are required. Eventually this energy produces of a quark-antiquark pair, turning the initial hadron into a pair of hadrons instead of producing an isolated color charge. This is called "Color confinement".

1.1.3 Higgs physics and Symmetry breaking

Similar to the Quantum Chromodynamics, the Electroweak part is described by $SU(2)_l \otimes U(1)_y$ gauge group theory, with the lagrangian:

$$\mathcal{L}_{I,Y} = \sum_f \overline{f} i \not{D}_{L,Y} f - \frac{1}{4} W^i_{\mu\nu} W^{i,\mu\nu},$$

where f stands for all possible fermion with different flavors and chiral, and

$$W^i_{\mu\nu} \equiv \partial_\mu W^i_\nu - \partial_\nu W^i_\mu + g\epsilon^{ijk} W^j_\mu W^k_\nu$$

are 2 gauge field strength tensor,

$$D^\mu_{L,Y} = \partial^\mu - igY_f B^\mu - ig\frac{\sigma^i}{2} W^{i,\mu}$$

is the covariant derivative(Y_f is the corresponding $U(1)_y$ hypercharge of f), where

$$B_{\mu\nu} \equiv \partial_\mu B_\mu - \partial_\nu B_\mu.$$

The lagrangian should have a gauge invariance under both $SU(2)_l$ and $U(1)_y$ transformations. This requires the mass of B and W to be 0, which does not agree with experiments.

The Higgs mechanism allow to deal with this, making $SU(2)_l * U(1)_y$ symmetry spontaneously break into U(1)EM and grant masses to the gauge bosons meanwhile. A complex scalar field ψ was introduced, which is both $SU(3)_c$ singlet and $SU(2)_l$ doublet with 1/2 charge for $U(1)_y$. With this scalar field, the lagrangian can be written as:

$$\mathcal{L}_H = [D_\mu \Phi]^+ D^\mu \Phi - V(\Phi),$$

where the higgs potential V(ψ) are chosen as:

$$V(\Phi) = -\mu^2\Phi^+\Phi + \lambda(\Phi^+\Phi)^2.$$

Here Φ can be transformed into the following formula:

$$\Phi = \frac{1}{\sqrt{2}}\begin{pmatrix} -i\phi^+(x) \\ v + H(x) + i\phi(x) \end{pmatrix},$$

or on the other way:

$$< \Phi >= \frac{1}{\sqrt{2}}(0, v)^T.$$

This form of potential makes the vacuum expectation value of Φ to be $v/\sqrt{2}$ instead of 0.

Apparently, ψ breaks $SU(2)_l$ and $U(1)_y$ symmetry. But in this case, the remaining symmetry would be

$$< \Phi > \rightarrow < \Phi >' = e^{i\theta} diag[1, 0] < \Phi >=< \Phi >,$$

which is known as the U(1)EM symmetry. Also, the mass term

$$-\frac{g^2v^2}{2}W^+_\mu W^{-,\mu} - \frac{g^2v^2}{4cos^2\theta_W}Z_\mu Z^\mu$$

can be observed from the quadratic term of $\mathcal{L}_H$, where the mass field Z^μ can be defined by the following mixing:

$$\begin{pmatrix} Z_\mu \\ A_\mu \end{pmatrix} = \begin{pmatrix} cos\theta_W & -sin\theta_W \\ sin\theta_W & cos\theta_W \end{pmatrix}\begin{pmatrix} W_\mu \\ B_\mu \end{pmatrix},$$

with mixing angle

$$\theta_W = arctan\frac{g'}{g}$$

. Here, W and Z boson gain mass from the mixing, while A_μ maintained massless to correspond to the remainning U(1)EM symmetry. Vector boson W and Z will have 3 degrees of freedom instead of 2 previously(transverse polarization) after gaining mass - the one more degree of freedom comes from the complex scalar field ϕ by excluding the Higgs field [10] [11] [12].

1.1.4 Fermions and Glashow-Weinberg-Salam (GWS) theory

In the Standard Model theory, the fermion fields are classified into quarks and leptons, by different properties in $SU(3)_c$ group transform. Quark is $SU(3)_L$ triplet and lepton is singlet. Also, the fermions can be either left-handed or right-handed field, and they are $SU(2)_L$ doublet and singlet respectively. Different $U(1)_Y$ charge can be observed for different fermions[13] [14]. Here are all the fermion fields and corresponding gauge transformation properties:

$$Q_L = [\begin{pmatrix} u \\ d \end{pmatrix}_L, \begin{pmatrix} c \\ s \end{pmatrix}_L, \begin{pmatrix} t \\ b \end{pmatrix}_L]^T, (3, 2, \frac{1}{6})$$

$$U_R = [u_R, c_R, t_R]^T, (3, 1, \frac{2}{3})$$

$$D_R = [d_R, s_R, b_R]^T, (3, 1, -\frac{1}{3})$$

$$L_L = [\begin{pmatrix} \nu_e \\ e \end{pmatrix}_L, \begin{pmatrix} \nu_\mu \\ \mu \end{pmatrix}_L, \begin{pmatrix} \nu_\tau \\ \tau \end{pmatrix}_L]^T, (1, 2, -\frac{1}{2})$$

$$l_R = [e_R, \mu_R, \tau_R]^T, (1, 1, -1)$$

$$\nu_R = [\nu_{eR}, \nu_{\mu R}, \nu_{\tau R}]^T, (1, 1, 0)$$

The SM does not include right-handed neutrino ν_R, not be in conflict with experimental observations. The right-handed neutrino will not have direct gauge interaction. Meanwhile, by considering it, neutrinos may gain mass and will have a Yukawa coupling with the higgs boson.

The $SU(2)_L$ doublets are all left-handed while singlets are all right-handed, which makes the presentation of the fermion mass term to break $SU(2)$ symmetry. On the other hand, by coupling with scalar fields, the fermion fields can be gauge invariant - they are called Yukawa coupling:

$$\mathcal{L}_Y \ -\overline{Q}_L \Phi Y^d d_R - \overline{Q}_L \widetilde{\Phi} Y^u u_R - \overline{L}_L \Phi Y^e e_R - \overline{L}_L \widetilde{\Phi} Y^\nu \nu_R + h.c..$$

The mass term of the fermions can be expressed through the lagrangian.

1.1.5 Elementary particles

The elementary particles in Standard Model contains 12 flavors of elementary fermions, plus their corresponding antiparticles, as well as elementary bosons that mediate the interaction and the Higgs boson. As discussed above, the 12 flavors of elementary fermions are including 6 quarks (each flavour of quark has 3 colors) and 6 leptons, dividing into 3 generations. The bosons stands for the interactions. The vector ($spin = -1$) bosons are including gluons, photons, and the W/Z bosons: gluons mediate the strong interaction, photon mediate the electromagnetic interaction, while the weak gauge bosons(W and Z) mediate the weak interaction. Whereas the Higgs boson ($spin = 0$) is responsible for the intrinsic mass of particles. All the elementary particles are shown in Fig. 1.1.

1.2 Beyond Standard Model (BSM)

1.2.1 Introduction

Since the discovery of the Higgs boson at LHC, the most essential part of the Standard Model(SM) was confirmed. However, we still have some remaining issues after this: hierachy problem, dark matter, origin of gravity and no gauge unification at higher scale [15] [16]. Supersymmetry (SUSY) has become a very appealing extension of the SM to answer these questions.

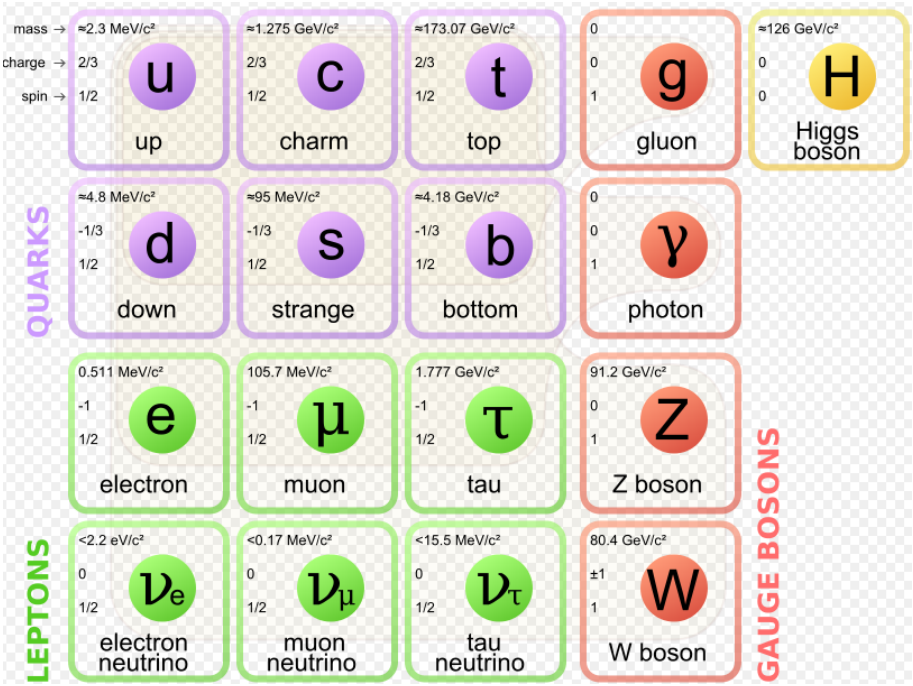

Figure 1.1: The elementary particles of the Standard Model.

The basic idea of supersymmetry is proposed by H. Miyazawa in 1966, when he was trying to connect the mesons and baryons with a SU(6,21) super group. Later in 1974, Julius Wess and Bruno Zumino reformulated the theory into a form of four-dimentional quantum field, making it an important theory in modern physics.

1.2.2 Minimal Supersymmetric Standard Model (MSSM)

SUSY can be realized in many different ways. The LHC can probe extensively the low-energy (or weakscale) realization of N=1 SUSY, called the Minimal Supersymmetric Standard Model (MSSM)[17].

1.2.2.1 Superspace and superfield

Generally, an SU(2) supersymmetry transformation can be written as $\phi \rightarrow \phi + \xi\psi$, where ϕ is boson filed, ψ is fermion field and ξ is a minimum parameter. This transformation changes a boson into a fermion, vice versa:

$$Q_\alpha|j>=|j\pm 1/2> .$$

Here, Q_α is the super charge operator, and α is the subscript of the rotation fraction.

The SUSY theory is built in a four-dimentional Minkowski space with spin direction, which is called superspace. An scala SUSY field with N=1 can be written as:

$$\begin{aligned} S(x^\mu,\theta_\alpha,\overline{\theta}_{\dot{\alpha}}) = f(x)+\theta^\alpha\phi_\alpha(x)+\overline{\theta}^{\dot{\alpha}}\overline{\chi}_{\dot{\alpha}}(x)+\theta^\alpha\theta_\alpha m(x)+\theta^{\dot{\alpha}}\theta_{\dot{\alpha}}n(x) \\ +\overline{\theta}^{\dot{\alpha}}(\sigma^\mu\theta)_{\dot{\alpha}}v_\mu(x)+\theta^\alpha\theta_\alpha\overline{\theta}^{\dot{\alpha}}\overline{\lambda}_{\dot{\alpha}}(x)+\overline{\theta}^{\dot{\alpha}}\overline{\theta}_{\dot{\alpha}}\theta^\alpha\psi_\alpha(x)+\theta^\alpha\theta_\alpha\overline{\theta}^{\dot{\alpha}}\overline{\theta}_{\dot{\alpha}}d(x) \end{aligned} .$$

Here, θ_α and $\overline{\theta}^{\dot{\alpha}}$ are Gelman 2D rotation; f, m, n and d are complex scalar field; $v_\mu(x)$ is complex vector field; ϕ,χ,λ and ψ are fermion fields. Therefore, the super charge operator can be discribed as:

$$Q_\alpha = -i\frac{\partial}{\partial\theta^\alpha} - (\sigma^\mu_\alpha\overline{\theta})^{\dot{\alpha}}\partial_\mu.$$

1.2.2.2 MSSM-Lagrangian and super potential

The Lagrangian of MSSM consists of a chiral superfield and a vector superfield. The chiral superfield corresponds to fermions and the vector one corresponds to $SU(3)_c$, $SU(2)_w$ and $U(1_)Y$ bosons. It can be written as:

$$\mathcal{L} = (\Phi_i^* e^{2gq_iV}\Phi^i)_D + 1/2M_{ij}[(\Phi^i\Phi^j)_F + cc] + 1/6y^{ijk}(\Phi_i\Phi_j\Phi_k)_F + 1/4[(W^\alpha W_\alpha)_F + cc],$$

with

$$(W^\alpha W_\alpha)_F = D^2 + 2i\lambda\sigma^\mu\partial_\mu\lambda^\dagger.$$

According to the Lagrangian, the super potential can be discribed as :

$$W = u_R Y_u(u_L H_u^0 - d_L H_u^+) - d_R Y_d(u_L H_d^- - d_L H_d^0) - l_R Y_l(\nu H_d^- - l_L H_d^0) + \mu(H_u^+ H_d^- - H_u^0 H_d^0).$$

Here Y_u, Y_d, Y_l are the Yukawa coupling terms; μ stands for higgino mass; and the conbinition of H_u and H_d gives mass to top/bottom quarks and leptons.

1.2.2.3 R-Parity and violation

The super potential can be re-written as:

$$W = 1/2\lambda_{ijk}(\nu^i e_L^j - e_L^i\nu^j)e_R^k + \lambda'_{ijk}(\nu^i e_L^j - e_L^i\nu^j)e_R^k + \mu'(\nu H_u^0 - e_L H_u^+) + 1/2\lambda''_{ijk}u_R^i d_R^j d_R^k.$$

This is invariant with a gauge transformation, but the sum of baryon number and lepton number is not. Therefore, a new quantum number, R-parity, is introduced: $R = (-1)^{2s+3B+L}$. Here s is the spin, B is the baryon number and L is the lepton number. The R-parity is a conserved quantitiy within the MSSM framework. The value of the R-parity is +1 for a SM particle, while being −1 for a supersymmetry particle. Therefore, the sparticles have the same quantum numbers as their SM partners, except for the R-parity, and the spin with 1/2 difference.

In assumption of R-parity conservation, the superpartners are always in pair production. Also, the lightest superpartners is stable, leading to missing transverse energy in the detector. But in the case R-parity is not conserved, these constraints nomore exists.

In the definition of R-parity, the additive quantum numbers - baryon number B and lepton number L - are defined with all known fermions (quarks and leptons). In the transition from an R-even particle to an R-odd particle, like photon into “photino” or quark into squark, we must give a different interpretation for B and L for the super-partners since squark are bosons. In other words, B and L are now carried not only by fundamental fermions, but also by fundamental bosons. In this case, R-parity may be viewed as having a very fundamental origin, in relation with the reflection symmetry ($\theta \to -\theta$), or with the existence of extra dimensions which may be responsible for supersymmetry breaking

by dimensional reduction [18]. Therefore, R-parity violations are allowed, but sufficiently well hidden and not too large.

In these scenarios, if only one of B or L is violated, the limit of the proton decay can be reached, as well as non-zero neutrino masses and neutrino oscillations. The RPV superpotential can be described as:

$$W_{RPV} = \frac{1}{2}\lambda_{ijk}L_iL_j\bar{(E)}_k + \lambda'_{ijk}L_iQ_j\bar{(D)}_k + \lambda''_{ijk}\overline{U}_i\overline{D}_j\bar{(D)}_k,$$

where i, j, k are generation indices, L and Q are the SU(2)_L doublet superfields of the leptons and quarks, and, $\bar{(E)}, \bar{(D)}, \bar{(U)}$ are the SU(2)_L singlet superfields of the leptons, the up-quarks and the down-quarks. LSP in RPV models may be charged or colored.

Specially, the quark RPV interactions described by λ''_{ijk} can be searched through multi-jets final states. In the same-sign two leptons or three leptons analysis mentioned in Chapter. 6, a search for RPV SUSY particles is also included parallelly. The involved scenario is predicted by some RPV models like the Minimal Flavor Violation.

1.2.3 Super particles

MSSM predicts new particles, called sparticles, that are superpartners of each SM particle in the chiral multiplets, showing in Fig. 1.2. [19, 20, 21, 22, 23] The spectrum is char-

Names	Spin	P_R	Gauge Eigenstates	Mass Eigenstates
Higgs bosons	0	+1	$H_u^0\ H_d^0\ H_u^+\ H_d^-$	$h^0\ H^0\ A^0\ H^\pm$
squarks	0	−1	$\widetilde{u}_L\ \widetilde{u}_R\ \widetilde{d}_L\ \widetilde{d}_R$ $\widetilde{s}_L\ \widetilde{s}_R\ \widetilde{c}_L\ \widetilde{c}_R$ $\widetilde{t}_L\ \widetilde{t}_R\ \widetilde{b}_L\ \widetilde{b}_R$	(same) (same) $\widetilde{t}_1\ \widetilde{t}_2\ \widetilde{b}_1\ \widetilde{b}_2$
sleptons	0	−1	$\widetilde{e}_L\ \widetilde{e}_R\ \widetilde{\nu}_e$ $\widetilde{\mu}_L\ \widetilde{\mu}_R\ \widetilde{\nu}_\mu$ $\widetilde{\tau}_L\ \widetilde{\tau}_R\ \widetilde{\nu}_\tau$	(same) (same) $\widetilde{\tau}_1\ \widetilde{\tau}_2\ \widetilde{\nu}_\tau$
neutralinos	1/2	−1	$\widetilde{B}^0\ \widetilde{W}^0\ \widetilde{H}_u^0\ \widetilde{H}_d^0$	$\widetilde{N}_1\ \widetilde{N}_2\ \widetilde{N}_3\ \widetilde{N}_4$
charginos	1/2	−1	$\widetilde{W}^\pm\ \widetilde{H}_u^+\ \widetilde{H}_d^-$	$\widetilde{C}_1^\pm\ \widetilde{C}_2^\pm$
gluino	1/2	−1	$\widetilde{g}$	(same)
goldstino (gravitino)	1/2 (3/2)	−1	$\widetilde{G}$	(same)

Figure 1.2: SUSY particles in MSSM.

acterized by 25 elementary scalars and 10 elementary fermions without counting the SM particles [24] [25].

Sleptons are the superpartners of the Standard Model leptons. Direct production of sleptons is expected to be observed only if their masses are small. There will be left-right mixing for the staus because of the high mass of them:

$$\tilde{\tau}_1 = e^{+i\phi}\cos\theta\tilde{\tau_L} + \sin\theta\tilde{\tau_R},$$

$$\tilde{\tau}_2 = e^{-i\phi}\cos\theta\tilde{\tau_L} - \sin\theta\tilde{\tau_R},$$

where the $\tilde{\tau}_1$ and $\tilde{\tau}_2$are mass eigenstates. Typically, the charginos and neutralinos can decay into final states with sleptons.

Squarks are the superpartners of the Standard Model quarks. The lighter two generations of the squarks have nearly the same mass. While the same as the sleptons, the mass eigenstates for superpartners of the third generation quarks, called stop and sbottom, will be linear mixing of the left and right handed stops or sbottoms:

$$\tilde{t}_1 = e^{+i\phi}\cos\theta\tilde{t_L} + \sin\theta\tilde{t_R},$$

$$\tilde{t}_2 = e^{-i\phi}\cos\theta\tilde{t_L} - \sin\theta\tilde{t_R}.$$

While for sbottom:

$$\tilde{b}_1 = e^{+i\phi}\cos\theta\tilde{b_L} + \sin\theta\tilde{b_R},$$

$$\tilde{b}_2 = e^{-i\phi}\cos\theta\tilde{b_L} - \sin\theta\tilde{b_R},$$

where the parameter θ and ϕ are for sbottom only. The production of squarks may be the strong interactions of the hadron collider.

Neutralinos are mixture of the superpartners for the photons, gauge bosons and Higgs. Theoretically, there are four neutralinos (electrically neutral) that are fermions, labelled as $\tilde{\chi}_1^0, \tilde{\chi}_2^0, \tilde{\chi}_3^0$ and $\tilde{\chi}_4^0$, of which the lightest ($\tilde{\chi}_1^0$) is stable. These neutralinos are linear mixture of Bino, the neutral Wino and the neutral Higgsino, Bino is the superpartners of the B boson (mixture of the photon and Z), and Wino is the superpartners of $W^{\pm}$ and W^3. The neutralino can decay to a lower mass neutralino or sleptons:

$$\tilde{\chi}_x^0 \rightarrow W\tilde{\chi}_{x-1}^0,$$

where x=2,3,4;

$$\tilde{\chi}_2^0 \rightarrow l^{\pm}\tilde{l}^{\mp}.$$

The neutralinos are Majorana particles, meaning that they are identical to their antiparticle. Thus in R-parity conserving models, the lightest neutralino$\tilde{\chi}_1^0$ is stable and all supersymmetric cascades decays end up in final state with visible SM particles and $\tilde{\chi}_1^0$, which cannot be seen by the detector, leaving missing energy or unbalanced momentum.

Gluinos are Majorana fermions and interact via the strong force. In the case R-parity conserves, They decay via the strong interaction to a squark and a quark. The squark then decays to another quark and the LSP. This makes a typical signal for a gluino at LHC being multi-jets with missing transverse energy.

Charginos are mixture of the superpartners of $W^{\pm}$ and charged Higgs. There are four Charginos labeled as $\tilde{\chi}_1^{\pm}$ and $\tilde{\chi}_2^{\pm}$. The typically decay products of charginos are a lepton-slepton pair or neutralino and a $W^{\pm}$ boson:

$$\tilde{\chi}_1^{\pm} \rightarrow \tilde{\tau}\nu_{\tau},$$

$$\tilde{\chi}_1^{\pm} \rightarrow W^{\pm}\tilde{\chi}_1^0.$$

Higgs doublets are assumed in the MSSM for self-consistent. Each of the SU(2)L complex doublet has a vacuum expectation value (vev) labelled v_u and v_d, constrained by the SM higgs vev:

$$v = \sqrt{v_u^2 + v_d^2}.$$

The ratio $\tan\beta = \frac{v_u}{v_d}$ is usually used as an important parameter for certain models. Taking into account the superpartner of the higgs complex doublets, there are 8 degrees of freedom, leading to eight mass eigenstates after electroweak symmetry breaking:

- 3 neutral higgs boson h^0, H^0 and A^0;
- 2 charged higgs boson $H^{\pm}$;
- 3 "GoldStone" bosons which give masses to Z and $W^{\pm}$ [26].

The **higginos** are the superpartners of the 5 higgs bosons. By mixing the higginos, Winos and Binos, we obtain 9 eigenstates (Neutralinos and Charginos).

In the MSSM framework, three main theoretical unknowns influence the search direction: the LSP nature, the compression (or not) of the SUSY spectra and the status of R-parity. For the first one, experimental constraints restrict the LSP to be the lightest neutralino or the almost massless gravitino. In the later case, final states are increased compared to the former. The reason is that the Next-to-Lightest SUSY Particle (NLSP) which can be any of the SUSY particles (squark, gluino, slepton, chargino or neutralino) will decay to the gravitino and the SM partner of the NLSP. The second MSSM theory unknown is the diffence of the mass of the highest sparticle produced at the LHC (MSUSY) and the LSP (MLSP), resulting in compressed or open spectra. The third MSSM theory unknown is the status of R-parity. In a plain MSSM scenario R-parity is conserved (RPC), otherwise we call it an R-parity Violating model (RPV).

1.2.3.1 ElectroWeakino particles and sleptons

The superpartner of electroweak gauge bosons are called electroweakinos. Many weakly interacting particles are expected to be close to the electroweak scale. Many searches are done for neutral and charged Higgses with positive R-parity, super partners of the Higgses and electroweakinos, as well as sleptons [27].

The LHC SUSY search are concentrating on processes involving the two lightest neutralinos and the lightest chargino[28]. Assuming that the EWKinos are the lightest sparticles, the main production would be decays via the s-channel exchange of a virtual gauge boson. EWKinos then naturally decay as $\tilde{\chi}_2^0 \rightarrow Zh^{0(*)}\tilde{\chi}_1^0$ and $\tilde{\chi}_1^{\pm} \rightarrow W^*\tilde{\chi}_1^0$. Generally the EWK process have small cross sections compared to the SM backgrounds. Therefore, current searches are mainly for leptonic decays of Z and W, giving 1-4 leptons+E_T^{miss} in the final states.

Sleptons are governed by 5 parameters:

- masses of the left-handed and right-handed e/mu, which are assumed to be mass degenerate in the MSSM;
- masses of the left-handed and right-handed taus;
- the stau mixing angle.

ν masses can be related to the charged slepton parameters. From naturalness arguments slepton masses are expected to be around 1TeV, with very low slepton production cross-section.

1.2.3.2 Gluino and first/second generation of squarks

In the MSSM, TeV-scale squarks and gluinos produced in pp collisions will decay promptly in long decay chains containing mainly quark and gluon jets and the LSP. SUSY events are therefore characterized by multiple energetic jets as well as transverse missing energy (E_T^{miss}). Depending on the sparticle present (or not) in between the squarks/gluinos and the LSP, charged lepton(s) and/or photons could also appear in the cascade.

To probe other regions of the parameter space, including compressed mass spectra, requiring at least one isolated light leptons as well as multi-jets and E_T^{miss} cuts helps a lot. The required light lepton are typically from W leptonic decay, top quark or slepton decay.

For compressed scenarios, experimental signature would be lowering cuts on E_T^{miss} and HT (scalar sum of leptons p_T, jets p_T and E_T^{miss}) and very soft leptons (6-25 GeV) [29]. Many other variables exists in the searches like the transverse mass m_T, which elementary efficiently reduces $t\bar{t}$ and W+jets backgrounds by requiring $mT > mW$.

As for leptons, identifying b-tagged jets in the multi-jet final states together with leptons can be a precious help. Taken the Gtt process as an example:

$$pp \rightarrow \tilde{g}\tilde{g} \rightarrow tt\tilde{\chi}_1^0 tt\tilde{\chi}_1^0.$$

it will provide 4 tops+E_T^{miss} final states. Reducing the dominant $tt- > WWbb$ background is possible when considering the following two situations:

(i) a single isolated lepton and at least five jets, two or three of which are identified as b-jets.

(ii) two same-sign leptons with one, two or three b-tagged jets.

1.2.3.3 Third generation of squarks

Many searches have been done in LHC for light third-generations squarks decay. As discussed above, the gauge eigenstates and the mass eigenstates of the third-generations squarks satisfy the following equation:

$$\tilde{b}_1 = e^{+i\phi}\cos\theta\tilde{b_L} + \sin\theta\tilde{b_R},$$

$$\tilde{b}_2 = e^{-i\phi}\cos\theta\tilde{b_L} - \sin\theta\tilde{b_R}.$$

The off-diagonal elements of the mass matrix θ are proportional to the mass of the SM partner particle, the Higgs-related parameters μ and $\tan\beta$. Therefore, the $\tilde{b}_1$ mass is expected to be light for large $\tan\beta$. While for small $\tan\beta$, the $\tilde{b}_1$ mass is still expected to be small, since the effects of the large top Yukawa coupling as it is part of the doublet containing $\tilde{t}_L$.

Here we only consider the third-generation squarks to be lighter than gluinos. In case the gluino masses are too heavy to be produced at the LHC energy, searches for direct

third-generation squark pair production might be the only way to observe them. For top squarks, the possible decays would be:

$$\tilde{t} \rightarrow t\tilde{\chi}_1^0,$$

$$\tilde{t} \rightarrow b\tilde{\chi}_1^{\pm} \rightarrow bW^{\pm}\tilde{\chi}_1^0.$$

One of the most interesting searches for bottom squarks are via the decay:

$$\tilde{b} \rightarrow b\tilde{\chi}_1^0,$$

in which the final states are including zero-lepton, as well as two b-tagged jets (no prompt leptons are expected from b decays). Another decay is only possible in assumption that $m_{\tilde{b}} > m_t + m_{\tilde{\chi}_1^0}$. Therefore, sbottom can decay into a top quark and $\tilde{\chi}_1^-$:

$$\tilde{b} \rightarrow t\tilde{\chi}_1^-,$$

where $\tilde{\chi}_1^- \rightarrow W^-\tilde{\chi}_1^0$. In this case, searches with lepton signatures are advisable. A same-sign dilepton search is well suited due to the low SM background in this channel.

1.2.4 Cross-sections and phase space of SUSY models

The cross-sections of different SUSY models are shown on Fig. 1.3. The EWK sector provides a promising approach for new physics among all SUSY searches. Generally, the hadronic activity is quite low in many EWK processes despite the low production cross-section. For most of the EWK models, we have 1-4 leptons in the final state, as well as large missing transverse energy(Etmiss) and 0-2 jets(or b-jets). While for SUSY strong productions, the cross-sections are much larger than the EWK sector. Currently, limits on most of the SUSY models probe masses up to $900GeV$(squarks) and $1.4TeV$(gluinos) [30] [31].

In this document, I mainly present two analyses. The first one is about the super-symmetric particle searches in the EWK sector, to be more specific, direct decay of third generation lepton pair. This is an important channel with no area in the phase space being excluded by other analysis. The second one is about the strong productions, such as decays of gluino pair into four top quarks and neutralinos.

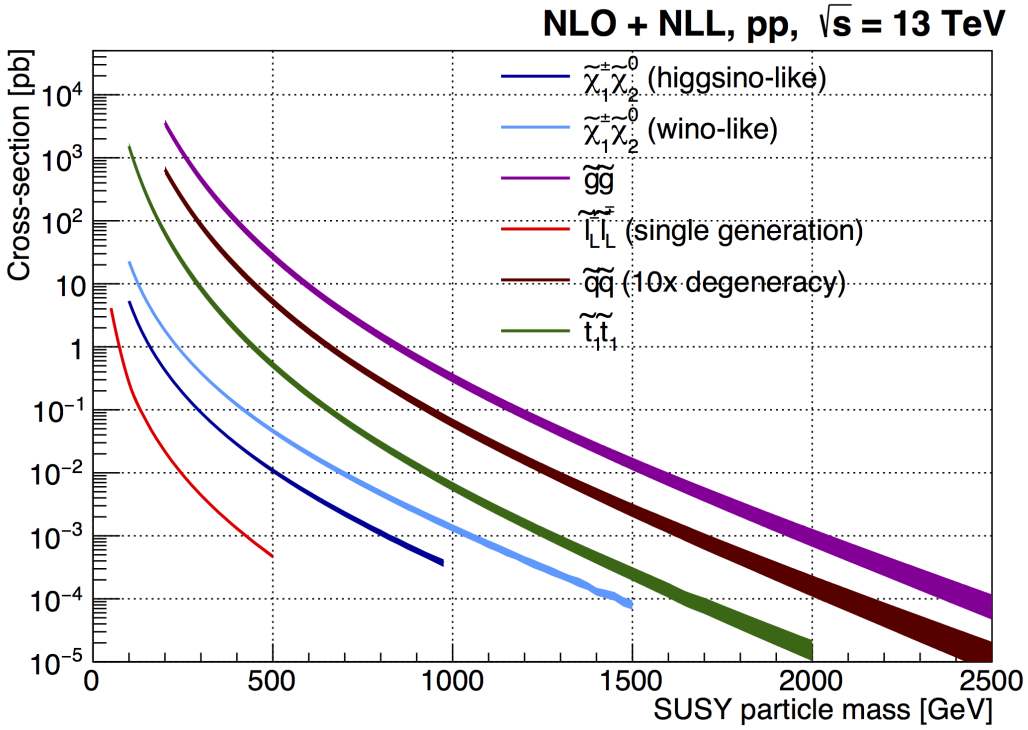

Figure 1.3: Cross sections of several SUSY production channels.

Chapter 2

The Large Hadron Collider and the ATLAS detector

2.1 Introduction

The **Large Hadron Collider (LHC)** is the world's largest hadron accelerator and collider. The construction of the LHC can be traced back to the late 1990s, when the previous Large Electron-Positron (LEP) collider was dismantled. It is installed in the existing tunnel ever built between the year 1984 and 1989 in which LEP machine has located, which is 26.7km long. CERN is established in 1954 and located in the northwest of Geneva on the Franch-Swiss border. It has now more than 10,000 fellow, associates and visiting scientists from more than 100 countries and hundreds of universities.

The aim of the LHC is to search for new particles predicted by different theories, including the Higgs boson in the Standard Model, and possible supersymmetric or exotic particles predicted by Beyond Standard Model theories. The first high energy proton proton collision physics run at the LHC took place in 2010, with an initial center-of-mass energy of 7 Tera electron Volts (TeV) - 3.5 TeV per beam. Then the collision energy increase to 8TeV in 2012. On February 13th, 2013, the first data taking campaign of the LHC called run 1 (RUN1) ended officially, and after that the LHC entered in a 2-years-long shut down period for maintenance and upgrade. The data-taking restarted early 2015 at a new unprecedent center of mass energy of 13 TeV and continued in 2016 at this energy. A total integrated luminosity of 36.5 fb^{-1} was recorded during those two years campaign so-called run 2 (RUN2) [32] [33].

Unlike the particle-antiparticle collider with 2 beams sharing the same ring, the LHC used two rings for counter-rotating beams since it is a particle-particle collider. There are seven main detectors and corresponding experiments around the rings:

- **ATLAS** - A Toroidal LHC ApparatuS. It is one of the two general purpose detectors, aiming at the validation of the Standard Model, the hunt for the Higgs boson and the search for clues on new physics phenomena.
- **CMS** - Compact Muon Solenoid. It is the other general purpose detector with a similar scientific program as ATLAS.[34]
- **ALICE** - Large Ion Collider Experiment. ALICE is a heavy-ion detector, aiming at

searching and studying for a new matter state called quark-gluon plasma that may probably gives evidence for the origin of matter.

- **LHCb** - Large Hadron Collider beauty. It is a specialized b-physics experiment, aiming at measuring the parameters of CP violation correlated to b-hadrons.
- **TOTEM** - Total, elastic and diffractive cross-section measurement. TOTEM experiment is designed to investigate phenomena relating to protons emerging from collisions at small angles, which is also called 'forward' direction protons.
- **MoEDAL** - Monopole and Exotics Detector at the LHC. MoEDAL is aiming at looking for a hypothetical particle with magnetic charge - the magnetic monopole.
- **LHCf** - Large Hadron Collider forward. LHCf is a special-purpose experiment for cosmic ray physics.

The beam and detectors in the LHC are shown on Fig 2.1.

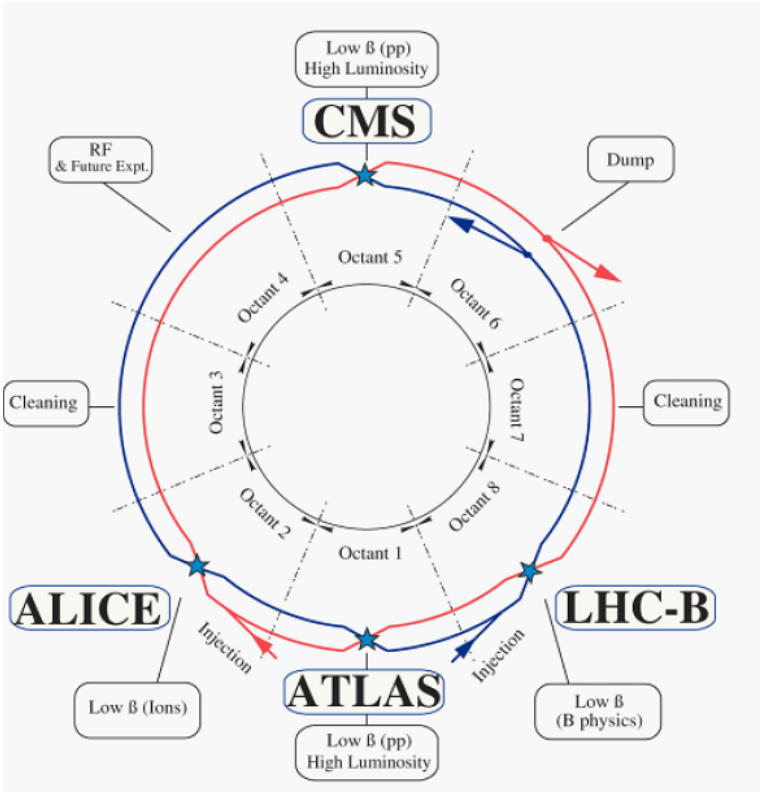

Figure 2.1: The beam turnel and detectors of the LHC. Only four main detectors and corresponding experiments are shown.

2.2 The LHC and Beam

The two proton beams are initially accelerated to 450GeV in a series of consecutive accelerator, and then injected to the circular accelerator in the tunnel in opposite directions within two different pipes, as shown on Fig. 2.2.

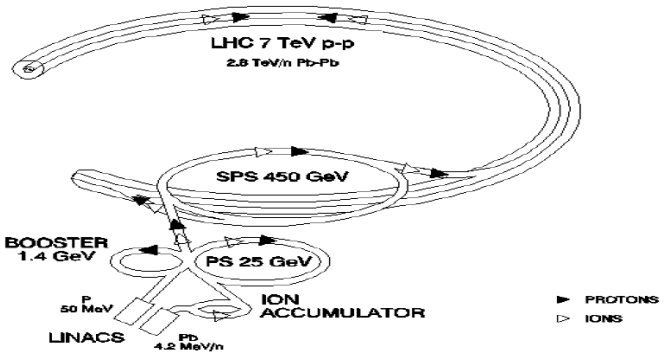

Figure 2.2: Beam system of the LHC.

First, from a bottle of hydrogen gas, a linear accelerator, the Linac 2, accelerates protons stripped of their electron to 50 MeV. Then the beam is injected into the Proton Synchrotron Booster (PSB) to gain energy up to 1.4GeV. After that, the protons are accelerated to 26GeV in Proton Synchrotron (PS), and finally reached 450GeV int the Super Proton Synchrotron (SPS). The proton grouped in isolated bunches are then transfered in the LHC beam pipes and accelerated to their final energy, which went over the years from 7 TeV, 8 TeV then 13 TeV and will reach the designed energy of 14 TeV in 2018. The bunch structures in the LHC is such that there is roughly a 40MHz collision rate. More specifically, in each beam there are up to 2808 bunches and each bunch, separated from nearest bunch by 25ns, contains an average of 10^{11} protons.

Aiming at revealing the physics beyond the Standard Model, the centre of mass energies have reached 13 TeV in 2015 and will go to its design value of 14 TeV in 2018. The number of events for a certain process generated in the LHC collisions can be written as:

$$N_{event} = L\sigma_{event},$$

where L is the machine(integral) luminosity for events per second(for whole run), σ is the cross-section of the process. The machine luminosity can be written with the beam parameter assuming a Gaussian distribution as:

$$L = \frac{N_b^2 n_b f_{rev} \gamma_r}{4\pi\epsilon_n \beta^*} F,$$

where N_b is the number of protons per bunch(10^{11}), n_b the number of bunches per beam (up to 2808), f_{rev} the revolution frequency, γ_r the relativistic gamma factor, ϵ_n the normalized transverse beam emittance, β^* the beta function at the collision point, and, F the geometric luminosity reduction factor. ATLAS and CMS are two high luminosity experiments designed cope with $O(10^{34} cm^{-2} s^{-1})$ peak luminosity while TOTEM and LHCb are low luminosity experiments designed cope with $O(10^{32} cm^{-2} s^{-1})$ peak luminosity.

To hold the protons and to drive them along the beam pipes, the LHC needs a very high magnetic field. Superconducting magnets are used to meet the requirement of such high intensities. The LHC magnet system use the NbTi cables, cool down to 2K with liquid helium, and can provid magnetic field up to 8 T.

The LHC has three vacuum systems:

- the insulation vacuum for cryomagnets,
- the insulation vacuum for helium distribution,
- the beam vacuum.

For different part of the accelerator, we have different criteria in vacuum degree. 10^{-1} mbar is enough for the insulation vacua before cool-down, while for the case at cryogenic temperatures, the pressure will be 10^{-6} mbar. The beam lifetime is required to be 100 hours, thus the hydrogen gas densities should remain $10^{15} H_2 m^{-3}$, while the density should be $10^{13} H_2 m^{-3}$ around the interaction regions. Generally, this beam vacuum criteria makes the pressure to be around 10^{-10} to 10^{-11} mbar.

The pileup number μ (mean number of interaction per crossing) of the beam is shown in Figure. 2.3. The μ value increase with higher luminosity and larger center-of-mass energy.

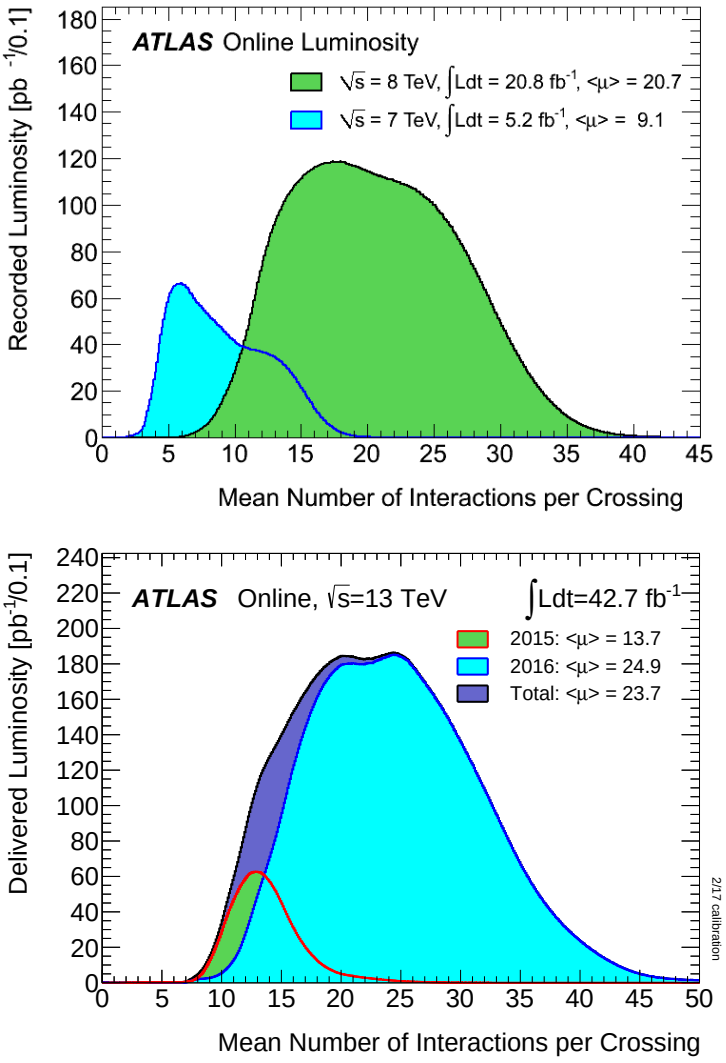

Figure 2.3: The mean number of interaction per crossing of the LHC beam for 2011-2012 data (upper) and for 2015-2016 data (lower)[35] [36].

2.3 ATLAS Structure and Physics Requirements

2.3.1 Introduction

Inside the LHC, bunches of 10^{11} protons collide 40 million times per second to provide 14 TeV proton-proton collisions at a design luminosity of $10^{34} cm^{-2} s^{-1}$ [37]. To meet the requirements of high precision measurement under high interaction rate, radiation dose, particle multiplicity and energy, the particle detectors have to be designed with series of stringent standard. The ATLAS detector has been built for p-p collisions as one of the two general purpose detectors. Physicists from more than 175 institutions in 38 countries are involved in the experiment. ATLAS is 46 metres long, 25 metres in diameter, and weighs about 7,000 tonnes, with 3000 km of cable inside. The structure of ATLAS is shown on Fig.2.4. The detector are composed by the following parts from the inside to the outside:

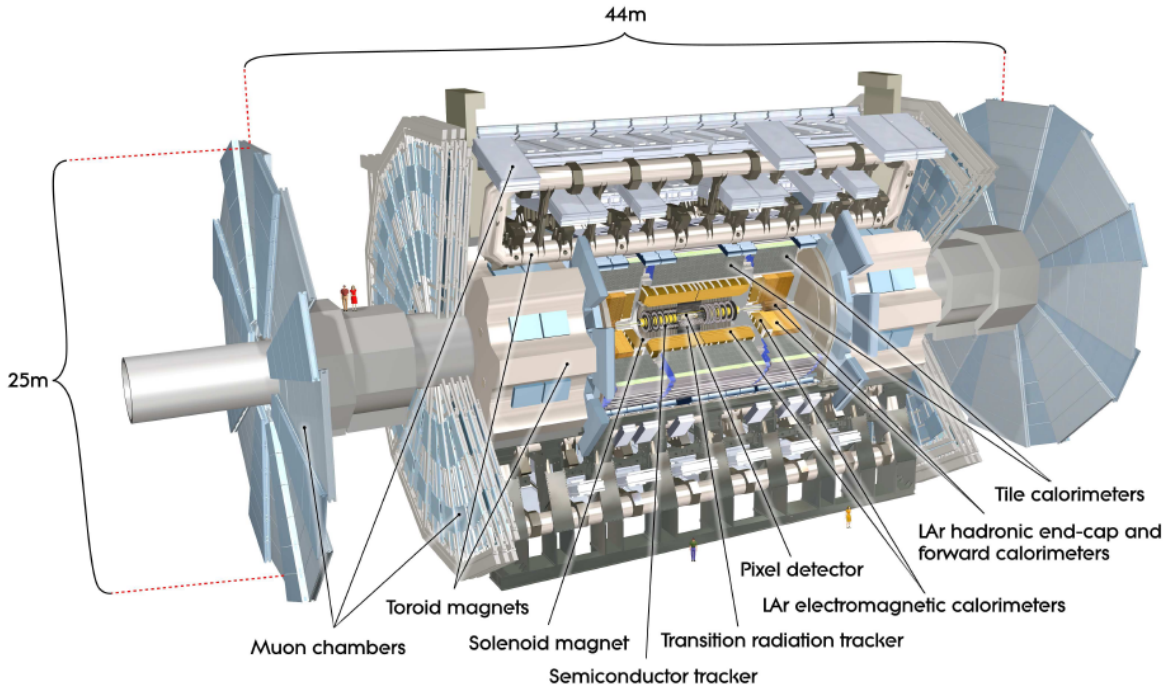

Figure 2.4: Structure of ATLAS.

- Inner detector,
- Calorimeter,
- Muon spectrometer,
- Magnet system,
- Forward detectors.

The ATLAS detector was designed using requirement linked to several typical physics processes covering most of the expected new physics objects at the TeV scale. The high collision energy and luminosity of the LHC boost the cross-sections of major process, including multi-jets, electroweak interactions and heavy flavour physics . The production of

top quark at LHC is at a rate of a few tens Hz, which is high enough for the couplings and spin study. Also, one of the most important goals of ATLAS is the search for the missing piece of SM, the Higgs boson. And this search has become a benchmark for the performance of the ATLAS subsystems. At the time of the design, the Higgs boson had a wide mass range up to 1 TeV depending of its production and decay mechanism. At low Higgs masses, less than 2 Z boson mass, the natural width would only be a few MeV, therefore the resolution would be quite important for the observed width. For high Higgs masses around 600GeV, the channel diboson decaying to forward jets would be promising. So, the tagging of forward jets would be quite important. Also, for beyond Standard Model Higgs search, good understanding of b-tagging and τ lepton performance are required. On July 2012, ATLAS has reported the discovery of a higgs-like boson at 125GeV, together with CMS [1, 2, 3, 4, 5, 6]. Specifically, for supersymmetric search, the decay of squarks and gluinos would always end up with a lightest stable supersymmetric particle(LSP). This LSP would have little interaction with the detector, which forms missing transverse energy (E_T^{miss}). The rest of the decay products are including multi-jets and multi-leptons. Therefore, the detector should have good performance for E_T^{miss}, as well as jets and leptons. Further more, for SUSY searches with τ leptons, the hadronic dacaying modes of τ are contaminated with QCD background. In this case, high resolution of the EM calorimeter would be helpful for the discriminating of τ leptons and jets.

Generally speaking, the physics goals of ATLAS are requiring the detectors to have the following properties:

- fast, radiation-hard electronics and sensor elements, as well as high detector granularity, which is essential to handle the particle fluxes and reduce the overlapping events impact.
- Large acceptance in pseudorapidity (η) with almost full azimuthal angle coverage.
- Good charged-particle momentum resolution, as well as reconstruction efficiency in the inner tracker.
- Very good electromagnetic (EM) calorimetry for electron and photon identification and measurement, full-coverage hadronic calorimetry for accurate jet and E_T^{miss} measurements.
- Good muon identification and momentum resolution over a wide range of momenta and the ability to determine unambiguously the charge of high p_T muons.
- Highly efficient triggering on low transverse-momentum objects with sufficient background rejection.

The details of all the subsystem of the ATLAS is introduced in the following sections.

A brief summary of the **ATLAS Coordinate System** are introduced here since they are repeatedly used in the following chapters. The ATLAS Coordinate System is a right-handed system with the x-axis pointing to the centre of the LHC ring, the y-axis pointing upwards, and the z-axis following the beam line. The side-A of the detector is defined as that with positive z and side-C is that with negative z. The azimuthal angle ϕ is measured in the xy-plane from the positive x-axis, increasing towards positive y-axis. The polar angle θ is the angle from the beam axis. However, the polar angle is usually specified as

pseudorapidity η, which is defined as:

$$\eta = -ln[tan(\frac{\theta}{2})].$$

In the case of massive objects such as jets, the rapidity

$$y = \frac{1}{2} ln(\frac{E + p_z}{E - p_z})$$

is used, where E is the energy of the particle and p_z is the momentum along the z-axis. The transverse momentum p_T, the transverse energy E_T, and the missing transverse energy E_T^{miss} are defined in the x-y plane unless stated otherwise. The distance ΔR in the pseudorapidity-azimuthal angle space is defined as:

$$\Delta R = \sqrt{\Delta^2\eta + \Delta^2\phi}.$$

The impact parameter d_0 is the closest distance from the track to the interaction point in the transverse plane, while z_0 is the closest distance from the track to the interaction point in the longitudinal plane.

2.3.2 Inner detector

The layout of the inner detector of ATLAS is shown on Fig. 2.5 and Fig. 2.6. Its first part is located a few centimeters away from the proton beam axis, and extends to a radius of 1.2 metres. The length of the inner detector is 6.2 m along the beam pipe. The inner detector consists of 4 sub-detectors:

- Silicon pixel layers,
- Semi-Conductor Tracker (SCT),
- Transition Radiation Tracker (TRT).
- Insertable BLayer (IBL).

In average, a track of a charged particle going through the inner detector would have 36 hits among all the 3 sub-detectors, which is enough to provide continuous tracking. The pattern recognition is thus enhanced and the momentum resolution within $|\eta| < 2.0$ is much improved.

Pixel detector As the innermost part of the ATLAS detector, the Pixel detector is situated at $5 - 10$cm distance of the interaction point, The Pixel detector is mainly used to measure the momentum and impact parameter of charged particles, as well as providing information for vertices position and identification [38]. It provides a high resolution of 3D space point measurements. It has 1,744 modules made of silicon in all the three concentric layers each with 3 disks on either of the 2 end-caps. Each of the modules contains 16 readout chips, and the basic unit of a chip is a pixel which is around 100 micrometres. The proximity to the interaction point makes the pixel detector exposed to a high radiation rate, therefore its radiation hardness is an important characteristic for the materials that compose the detector.

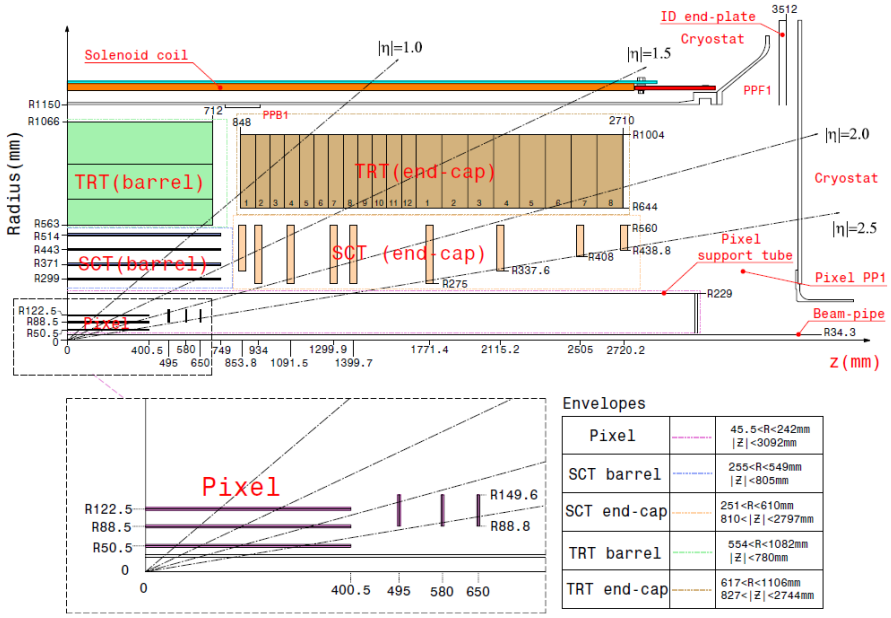

Figure 2.5: Plan view for the structure of the Inner Detector of ATLAS.

The average noise for each active module is shown in Fig. 2.7(left). The pixel occupancy for the active modules in one of the end-cap disks is shown in Fig. 2.7(right). The occupancy is around 10^{-7} - 10^{-8} for Bunch-Crossing IDentification (BCID) value 4, 5 or 6, and 10^{-9} - 10^{-10} for other BCID values.

SCT

The Semi-Conductor Tracker (SCT) locates in the middle level of the inner detector. In the barrel region, the SCT has 4 cylindrical layers, while in the end cap, it has 9 disk layers each side. The basic working principle and function of the SCT is similar to the Pixel detector, which can be seen from Fig. 2.6. However, the SCT is using strips instead of pixels, which allow to cover a larger area. Moreover, the SCT is covering more area in the radial direction than the Pixel detector, making it a critical sub-detector of the Inner Detector. The SCT is thus providing more information for tracking.

The SCT consists of 4088 modules, covering a surface of $63m^2$ of silicon, of which 2112 modules are in the barrel region [39]. These barrel region modules 80 mm pitch micro-strip sensors, connected to signal readout chips. The spatial resolution of a single SCT modules is around 16 mm in $R-\phi$.

TRT

The TRT is the short term of Transition Radiation Tracker, which is the outermost level of the inner detector. It contains 72 layers of straws interleaved with fibres in the barrel, and, 160 straw planes interleaved with foils in the end-cap. The foil composed by polypropylene allow to produce transition radiation induced by relativistic particles going through it. Each straw is filled with gas, mixture of Xe (70%), CO_2 (27%) and O_2 (3%), which will be ionized when a charged particle passes through.

In the TRT, all charged tracks with $p_T > 0.5GeV$ and $|\eta| < 2.0$ will at least pass through 36 straws, except those with $0.8 < |\eta| < 1.0$ (at least 22 crossed straws). In this

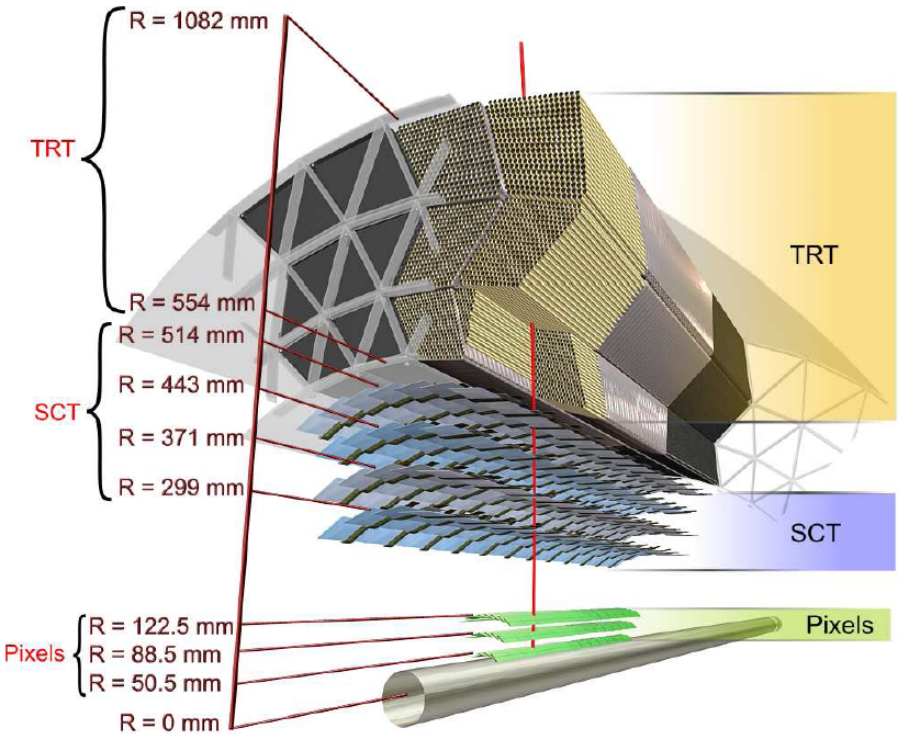

Figure 2.6: The inner detector of ATLAS.

way, the TRT provides important transition radiation information for electron identification. Moreover, relativistic light particles (such as electrons) would have a higher speed than heavier ones (such as pions) at a given energy, therefore they would produce a higher amount of transition radiation allowing their separation. For electrons with $E > 2$ GeV, $7 - 10$ high-threshold hits from transition radiation are expected.

The track position resolution of TRT is larger than the SCT and Pixel detector (200 mm). At the end of Run-1, the number of nonoperational TRT channels was about 2.5%. These channels were due to mechanical problems or electrical problems.

IBL The update during the first long shutdown of LHC machine in 2013-2014 consists in the construction of a new innermost Pixel Detector layer, also called **Insertable BLaye** (IBL). The IBL is installed together with a new beam pipe to maintain an excellent vertex detector performance and compensate possible inefficiencies of the current Pixel Detector.

Being the fourth layer added to the present Pixel Detector, the IBL contains 14 tilted ($\phi = 14°$) staves which is 64 cm long and 2 cm wide. It locates between a new beam pipe and the current inner Pixel Detector layer (B-layer). The front-end chip foreseen for the IBL is called FE-I4[40]. The FE-I4 chip was designed in 130 nm CMOS technology and consists of 26880 pixel cells. These cells are organized in a matrix of 80 columns by 336 rows[41]. The FE-I4 keeps tracks of the firing time of each discriminator as the time over threshold (ToT) with 4-bit resolution. The basic unit of the IBL is a module that consists of two or one front-end chips bump bonded to one sensor. For single-chip (two-chip) assemblies the nominal active coverage for particles normal to the beam is 98.8% (97.4%).

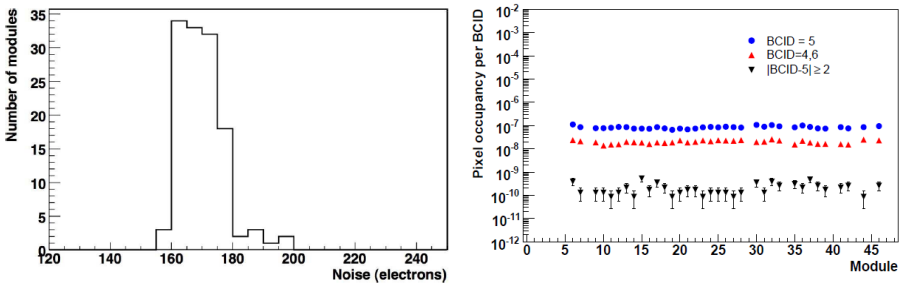

Figure 2.7: The average noise in electrons for each active module (left) and the pixel occupancy for active modules in one end-cap disk (right) in the pixel end-cap cosmic ray test. The BCID is calibrated so that particles originating together at the interaction point and travelling at the speed of light would have the same value of BCID assigned to them in all detector elements.

2.3.3 Calorimeter

The calorimeters are placed outside the inner detector. The ATLAS experiment uses both electromagnetic (EM) calorimeter and hadronic calorimeter. Both of the 2 calorimeters are sampling calorimeters, since they consist of interlaced metal (to absorb energy) and sampling material (like scintillator to periodically sample the shower shape). The energy deposited by an absorbed particle is measured after calibration, the shape of the deposited energy is used to further identify the particle. The calorimeter system of ATLAS covers the range $|\eta| < 4.9$ [42].

The EM calorimeter is mainly aiming at fully contain electrons and photons and measure their energy. By using the fact whether there is a track measured in the ID matches the energy shower measured in the calorimeter, electrons and photons can be separated. The Hadronic parts of the calorimeter system is not as accurate as the EM barrel one, but they are able to fully contain the hadronic particles and provide accurate information for jets and E_T^{miss} measurement. The overall structure of the calorimeter system is shown in Fig. 2.8. Note that the calorimeter system is also part of the trigger system, especially the first level.

EM Calorimeter

The electromagnetic calorimeter is divided into 2 parts: the barrel part with $0 < |\eta| < 1.475$ and the end-cap part with $1.375 < |\eta| < 3.2$ (EMEC). The former one is splitted into 2 half-barrels by a plane vertical to the Z-axis (beam line) and passing the collision point. Each of the half-barrels has a length of 3.2m and radii in range $2.8 - 4$m, weighting 57 tonnes. The latter one is made up of 2 coaxial wheels: an outer wheel covering $1.375 < |\eta| < 2.5$ and an inner wheel covering $2.5 < |\eta| < 3.2$. The active medium of the calorimeter is Liquid Argen (LAr), therefore it is called LAr electromagnetic calorimeter [43]. The absorbing material is lead (Pb) with a thickness of $1.1 - 2.2$ mm, which is optimised as a function of η by reviewing the EM calorimeter energy resolution. Kapton electrodes is used in LAr calorimeter. This geometry allows a multi-active-layer structure for the calorimeter. The calorimeter have 3 layers in the precision-measurement region ($0 < |\eta| < 2.5$) and 2 layers in: high-η region ($2.5 < |\eta| < 3.2$) and overlap region. The structure of a module is shown in Fig. 2.9. For the region $0 < |\eta| < 1.8$, an additional instrumented argon

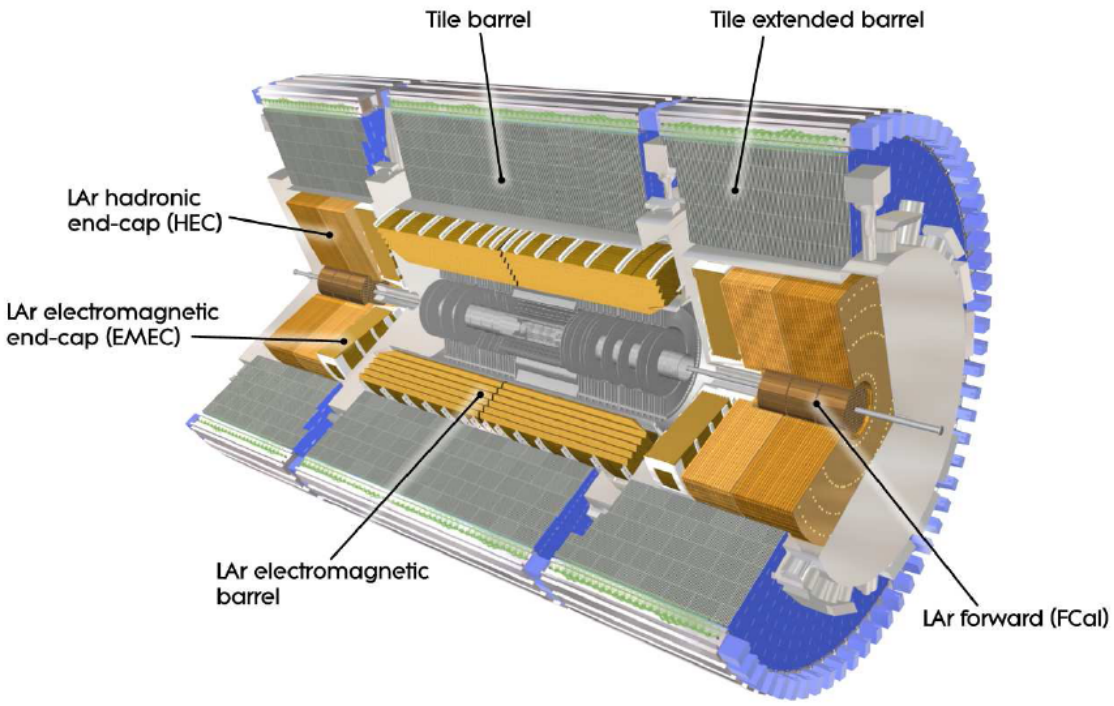

Figure 2.8: The ATLAS calorimeter system.

layer, called the "presampler", are situated to measure the energy loss in front of the EM calorimeter. For photons passing through the EM calorimeter, the η value is determined by the cluster in the first and the second layers.

Hadronic Calorimeter

The function of the hadronic calorimeter is to measure the energy of jets and the position of the particles. Compared to the electromagnetic calorimeter, the hadronic ones are less precise. The hadronic calorimeters of ATLAS are including:

- The tile calorimeter,
- the liquid-argon hadronic end-cap calorimeter (HEC),
- the liquid-argon forward calorimeter (FCal).

The **tile calorimeter** is localed in the region $|\eta| < 1.7$, which is behind the LAr barrel calorimeter. It consists of a central barrel and two extended barrels. The central barrel is 5.8 m in length with $|\eta| < 1.0$, while each of the extended ones is 2.6 m with $1.0 < |\eta| < 1.7$. They all uses steel as the absorber and scintillator the active medium. The whole calorimeter locates between 2.28m to 4.25m from the beam, formed by 64 modules and divided in three layers.

Designed as a self-supporting and segmented structure, the tile calorimeter consists of 64 modules with each covers 5.625 sr. Each module has a steel girder used to establish module-to-module gaps. In the gap locates the readout electronics. The absorbers of the tile calorimeter are 5mm thick master plates, separated by 4mm thick spacer plates which is used to hold the scintillator tiles. The function of master plate is mainly enhancing the

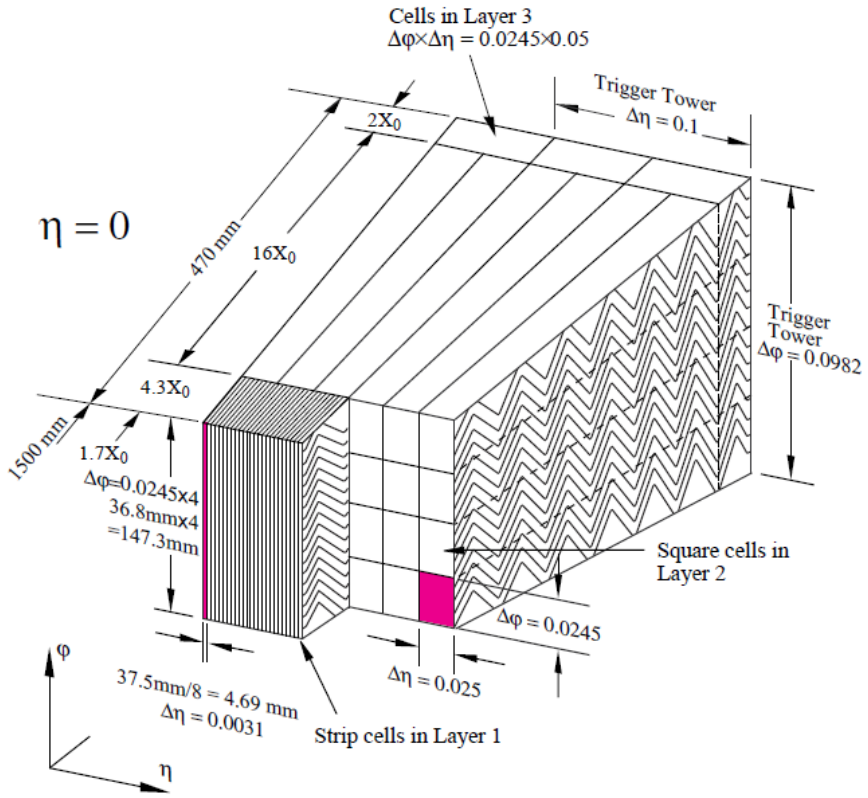

Figure 2.9: Sketch of a barrel module.

dimensional tolerances for the gaps. While, the spacer plates are aligned into the readout fibres slots. The total 1480 tiles are 3 mm thick and 200-400 mm long.

The **HEC** is a copper/liquid-argon sampling calorimeter located in the end-cap region with $1.5 < |\eta| < 3.2$. It consists of 2 wheels in each end-cap: a front wheel (HEC1) and a rear wheel (HEC2), each with an outer radius of 2030 mm.. The 4 wheels contains 32 identical wedge-shaped modules each. The modules of the front wheels consists of 24 copper plates with 25mm thick and a 12.5mm thick front plate. While, each of the modules in the rear wheels has 16 copper plates 50mm with thick and a 25mm thick front plate. Therefore the rear wheels are having less accuracy. The sampling fractions for HEC1 and for HEC2 are 4.4% and 2.2% respectively. 7 stainless-steel tie-rods will maintain the structural strength of the modules, with 12mm (16mm) in diameter for the front (rear) modules.

The **FCal**s are located in the end-cap region with the coverage $3.1 < |\eta| < 4.9$. They are situated at very high η region at a distance from the interaction point around 4.7m, and are exposed to high particle fluxes. To cope with this, the FCal is designed with very small liquid-argon gaps centred in tubes parallel to the beam. The liquid-argon gaps are smaller than the usual 2mm gap. This helps to avoid ion build-up problems and to provide higher possible density. Each FCal is split into three 45cm deep modules: one electromagnetic module (FCal1) and two hadronic modules (FCal2 and FCal3). For FCal1, copper is used as the absorber, while for FCal2 and FCal3, tungsten is used, which can minimise the

lateral spread of hadronic showers. Also, a shielding plug made of a copper alloy has been designed and located behind FCal3 to reduce backgrounds in the end-cap muon system.

In some hard scaterring, quark and anti-quark are producted and then interact with the detector material. Each of them forms a cluster of particles and then absobed by the calorimeter - this is called a jet. Specially, if the original quark is a bottom quark, then the corresponding jet is named b-jet.

2.3.4 Muon detector

The muon detector is designed to trigger on high momentum muons, to measure their tracks bent by a toroidal magnet surrounding this detector, and to extract their momentum [44]. The η coverage of this muon spectrometer is $|\eta| < 2.7$, however for triggering purposes only $|\eta| < 2.4$ region is used. The measurement of the muon detector is quite precise with a designed resolution around 10% for 1 TeV tracks. And, it can cover a momentum range for muons from 3 GeV to 3 TeV. The inner tracker with the solenoid can give a precise measurement of the momentum of low energy muons. While for high energy muons, the stand-alone measurements of the spectrometer should be combined with the Inner Detector track, to provide high resolution and excellent charge identification.

The structure of the muon detector is shown in Fig. 2.10. The detector comprises a magnetic system and tracking chambers. The magnetic system consists of one barrel toroid ($|\eta| < 1.1$) and two end-caps toroids ($1.1 < |\eta| < 2.7$). The length of the toroid in the barrel region is 25.3m, with the inner (outer) radius of 9.4m (20.1m). It is made up of eight coils which is placed in annular stainless-steel vacuum containers. The end-cap toroid is located inside the barrel toroid with a length of 5m and the inner (outer) radius of 1.65m (10.7m). The cool temperature is 4.8K using helium. The barrel tracking chambers are situated between the eight coils, while the end-cap chambers locates between the two end-cap toroid magnets. The total magnetic system is operated under a current of 20.5 kA, with the generated magnetic field up to 0.5T.

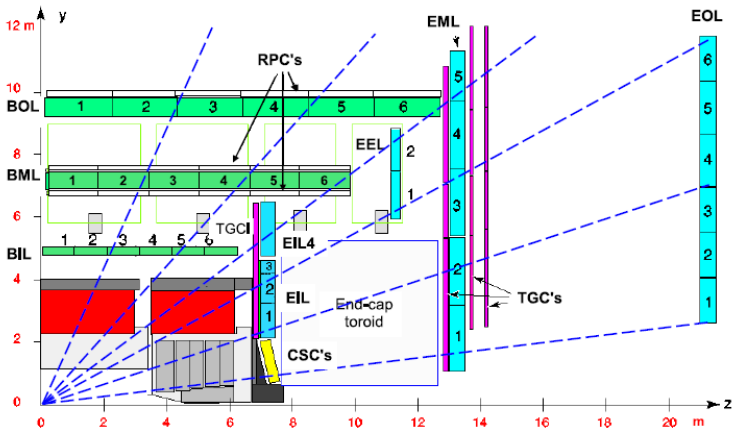

Figure 2.10: Structure of the muon system.

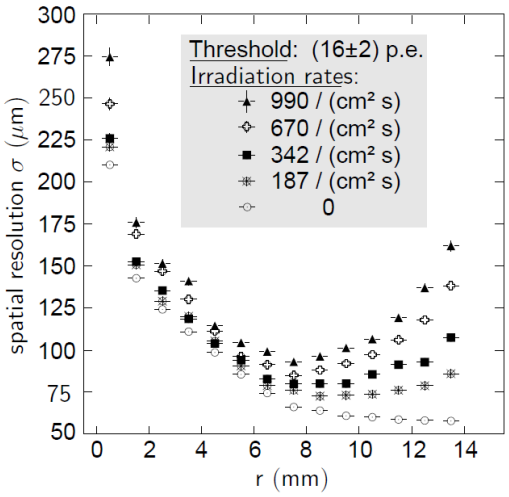

Figure 2.11: Muon Detector resolution as a function of the impact parameter of the track with respect to the tube wire at various levels of hit rates induced by γ-irradiation.

The **MDT** (Monitored Drift Tube) chambers are providing precision momentum measurement, by combining high measurement accuracy, the ability for mechanical deformation prediction, as well as simplicity of construction. Most of these chambers are covering the region $|\eta| < 2.7$. While chambers in the innermost end-cap layer have a limited coverage $|\eta| < 2.0$. Each of the chambers is made up of 3-8 layers of drift tubes, providing a resolution of about 80mm per tube with a working pressure of 3 bar. The case of 2 muons with 4GeV and 20GeV momentum respectively passing the muon spectrometer is shown in Fig. 2.12. The layer dimensions and the chamber sizes of the MDT are increasing in

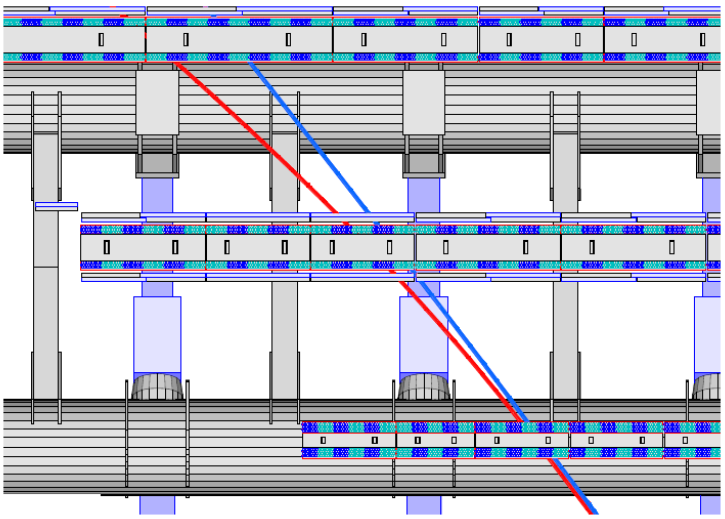

Figure 2.12: Path of muons with 4 GeV and 20 GeV momenta in the barrel muon spectrometer. Typically, the track crosses 2×4 inner, 2×3 middle and 2×3 outer layers of MDT tubes.

proportion of the distance from the interaction point.

The cathode-strip chambers, **CSC**, is designed to measure the charged particles momentum in the deepest layer of the end-cap region - $2.0 < |\eta| < 2.7$. The CSCs are segmented in the η plane consisting of 16 sub-chambers, of which 8 are large (small) with width 1.5 mm (1.6mm). Locating 7 m from the interaction point, the drift time of CSC is only 3.6 ns. Compared to the MDT layer, the CSC one could have a better resolution of 60 mm per plane. Moreover, the CSCs are having the following property so that they work better for regions with high particle densities:

- Good two-track resolution;
- In the case if more than one track is present, the chamber will provide pairing of the measurements to resolve the ambiguities.
- Electron drift times of less than 40 ns resulting in a timing resolution of about 7 ns per plane.
- The chamber gas is a mixture of Ar/CO_2, the absence of hydrogen leads to low neutron sensitivity.

The **alignment** of the MDT and CSC is quite important for particle position and momentum measurement. The position for a chambers of the MDT or CSC is known with a precision of 5 mm and 2 mrad. While experimentally, the muon track position is required to be within 30 μm in precision, which is two orders of magnitude tighter than the positioning accuracy. In order to reach the experimental requirement, an alignment system was built to relate the position of each chamber to its neighbours.

The **trigger chambers** are providing fast information on muon tracks, allowing the L1 trigger logic to recognise their multiplicity and approximate energy range. The trigger chambers will provide acceptance for muons in range $|\eta| < 2.4$ with full ϕ-range. It will reconstruct the muon tracks pointing to the interaction point. In the trigger system, **resistive plate chambers** are used in the central region ($|\eta| < 1.05$). While in the end-cup region, **thin gap chambers** are designed.

The resistive plate chambers consists of three concentric cylindrical layers (called "station") around the beam axis. Each station includes two parallel plastic resistive plates with copper based bands as the electrode. The electric field between the two plates is 49000 V/mm in the 2mm space. A 5ns signal is generated if a charged particle pass through and interacts with the detector. For particles with $6GeV < p_T < 35GeV$ passing through all the three stations, a track associated with 6 hits in the $|\phi|$ plane would be observed.

The thin gap chambers are multi-wire chambers. It provides very high resolution for most of the muon tracks, locating in the innermost layer and in the middle layers of the end-cup region. Also, the thin gap chambers have good time resolution which helps to tag the beam-crossing with high 99% granularity, providing a sufficiently sharp cut-off in the momentum of the triggering muon.

In some events like the τ leptonic decay, neutrinos are producted and run through the detector material with little interaction. These products (like neutrinos or SUSY particles) cannot be detected directly by ATLAS. However, this causes a missing part in the transverse momentum of the total event, which is taken as "missing transverse energy" (E_T^{miss}).

2.3.5 Magnetic system

The ATLAS detector uses four large superconducting magnets to measure the momenta of charged particles with Lorentz force. This magnetic system is 22 m in diameter and 26 m in length, with a stored energy of 1.6 GJ. It consists of a solenoid, a barrel toroid and two end-cap toroid magnets. The solenoid is aligned on the beam axis, providing 2 T axial magnetic field for the inner detector. Note that it minimises the radiative thickness which is located in front of the barrel EM calorimeter. The two end-cap toroids also produce a toroidal field of 1T for the end-cap muon detectors. Even for charged particles with quite large energy, the high magnetic field can bend the trajectory to curve enough for the momentum determination. The barrel toroid provides a toroidal 0.5 T magnetic field for the barrel muon detectors. [45]

2.3.6 Forward detector

Three smaller sets of detectors are built to complement the good coverage of ATLAS in the very forward region [46], including:

- the **LUCID** - LUminosity measurement using Cerenkov Integrating Detector;
- the **ZDC** - Zero-Degree Calorimeter;
- the **ALFA** - Absolute Luminosity For ATLAS.

These detectors are located in the LHC tunnel far away from the interaction point. Their main function is to measure elastic scattering at very small angles, which is important for the luminosity measurement of the ATLAS detector.

The LUCID is the main relative luminosity monitor in ATLAS, which is located ±17m from the interaction point. The main purpose if LUCID is to measure the integrated luminosity, as well as to provide online monitoring of the instantaneous luminosity and beam conditions.

The ZDC is located ±140m from the interaction point, where the LHC beam-pipe is divided into two separate pipes. The purpose of ZDC is to detect forward neutrons ($|\eta| > 8.3$) and heavy-ion collisions.

The ALFA is made up of scintillating fibre trackers, locating at a distance of ±240m from the interaction point. The detected elastic scattering at small angles by ALFA are used to measure the absolute luminosity of hadron colliders.

2.4 Trigger system

Given the very high bunch crossing rate, of 20 MHz during the 2010 - 2012 data taking and 40 MHz in 2015-2016, it is not possible to record all the produced events. Therefore, a dedicated trigger system is designed to record events at a rate of 400 Hz and up to 1000 Hz in 2015/16, which is based on the physics objects identification. It has three levels: L1, L2 and event filter (EV) - the latter two are called the High Level Trigger (HLT). The Level one trigger is selecting events at a rate of 75 kHz (and 100 Hz in 2015/16) using the information from the calorimeters (L1Calo) and muon spectrometers. The L1Calo is formed by 7000 analogue trigger towers with a granularity of $0.1 * 01$ in η and ϕ plane, and

identifies electrons, photons, jets or hadronic taus with a transverse momentum higher than a given value. It has a compact architecture, assuring a very fast response. The L1 muon trigger is relaying on the RPC and TGC detectors, characterized by a line granularity. A total of 256 distinct L1 trigger items, with several selection criteria on the p_T , lepton and jet or isolation, are defining the L1 trigger system. All the selected events are transmitted to the central trigger processor in less than 2.5 s. Beside the first event selection, the L1 triggers are also identifying regions of interest (RoI), used by the HLT system. These zones, defined in the plane of the ATLAS calorimeters and spectrometers, can be regarded as regions with interesting features from where the event was selected.

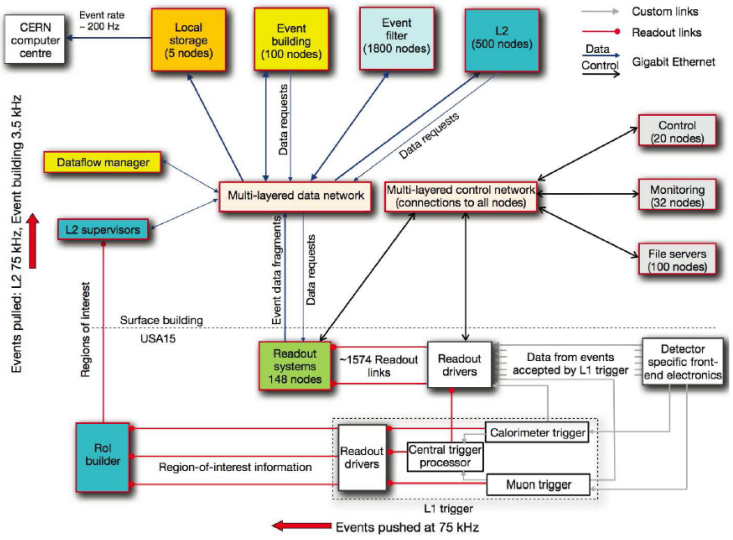

Figure 2.13: The ATLAS trigger and data acquisition systems.

If L1 is a Hardware system based on dedicated electronic boards, the HLT is a software based trigger system using a huge local farm of computers. The L2 trigger selection is performed using all (and only) the data from the RoI, and all the detector sub-systems information (i.e. the inner detector is included). This reduces the time needed to perform the interesting events selection. Looking with precision at the entire detector granularity, L1 selected events are sorted out in less than 40ms. This reduction is possible due to a set of complex reconstruction algorithms. If the events is retained, the data information is to the event filter. Here the event is build using the standard (on-line) ATLAS reconstruction algorithm (called "Athena"). It has the same selection principle as L2, at an average filtering rate of 400 Hz and up to 1kHz, and an event processing time around 4 seconds.

The total integral luminosity of the data acquired by the ATLAS detector is shown in Figure. 2.14.

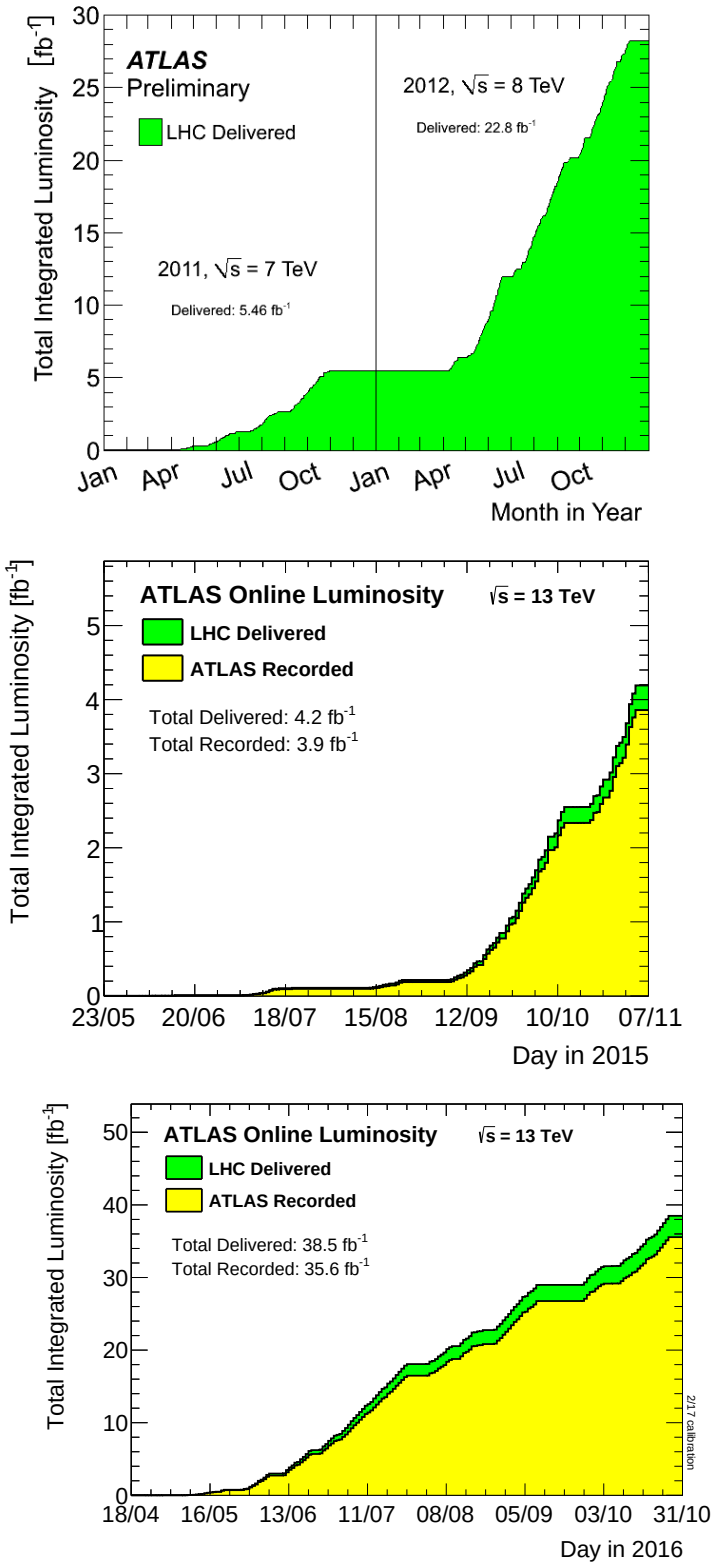

Figure 2.14: Cumulative luminosity versus time delivered and recorded by ATLAS during stable beams for pp collisions at 7-8 TeV centre-of-mass energy in 2011-2012 (upper) at 13 TeV centre-of-mass energy in 2015 (middle), and in 2016 (lower).

Chapter 3

Object Reconstruction

This chapter presents the object reconstruction and identification in the ATLAS experiment. The involved objects are electrons in Section 3.1, muons in Section 3.2, τ-leptons in Section 3.3, E_T^{miss} in Section 3.5 . In this section, MC samples are used to access the performance of the reconstructed objets. The most commonly used generator is Pythia [47] [48].

3.1 Reconstruction of Electrons

Most of the physics studies at the LHC requires excellent particle identification capability[49]. For some new physics decay modes, small cross-sections compared to large (usually multi-jets) backgrounds have been expected. Therefore efficient electron identification is needed to observe such signals. In many analyses, the ratio between the isolated electrons and the QCD jets in collected data with p_T in the range 20-50 GeV is 10^{-5} at the LHC. Thus a jet-rejection factor of 10^5 is needed to extract a relatively pure signal from prompt electrons above the jets faking ones. Physics channels of prime interest at the LHC are expected to produce electrons with p_T between a few GeV and 5 TeV. Good electron identification is therefore needed over a broad energy range.[50]

The required rejection factor decreases sharply with increasing p_T to 10^3 for jets in the TeV region. In the ATLAS detector, the reconstruction software has evolved significantly, leading to several validated steps of the energy reconstruction. At present, two electron reconstruction algorithms have been implemented in the ATLAS offline software, [51] both integrated into one single package and a common event data model.

- The standard one, which is seeded from the electromagnetic (EM) calorimeters, starts from clusters reconstructed in the calorimeters and then builds the identification variables based on information from the inner detector and the EM calorimeters.
- A second algorithm, which is seeded from the inner detector tracks, is optimized for electrons with energies as low as a few GeV, and selects good-quality tracks matching a relatively isolated deposition of energy in the EM calorimeters. The identification variables are then calculated in the same way as for the standard algorithm.

3.1.1 Calorimeter-seeded reconstruction and identification

In the standard reconstruction of electrons, a seed electromagnetic tower with transverse energy above 3 GeV is taken from the EM calorimeter and a matching track is searched for among all reconstructed tracks (not belonging to a photon-conversion pair) reconstructed in the inner detector. After extrapolation to the EM calorimeter, the track is required to match the cluster within a $\Delta\eta\times\Delta\phi$ window of 0.05×0.10. The ratio E/p, which is the energy of the cluster to the momentum of the track, is required to be lower than 10. Approximately 93% of true isolated electrons are selected as electron candidates, with $E_T > 20$ GeV and $|\eta| < 2.5$. The inefficiency is mainly due to the large amount of material in the inner detector. Various identification techniques can be applied to the reconstructed electron candidates, combining calorimeter and track quantities and the TRT information to discriminate jets and background electrons from the signal electrons [52].

3.1.1.1 Cut-based method

A simple cut-based procedure is used for the electron identification. The method is based on a set of cuts on the electron candidates[53]. The electron candidates are classified, based on the type of the Monte Carlo particle associated to the reconstructed track, as well as that of its non-electron parent particle, shown in Table 3.1.

Table 3.1: Classification of simulated electron candidates.

Category	Type of particle	Type of parent particle
Isolated	Electron	Z, W, t, τ or μ
Non-isolated	Electron	J/ψ, b-hadron or c-hadron decays
Background electron	Electron	Photon (conversions), pi^0/η Dalitz decays, u/d/s-hadron decays
Non-electron	Charged hadrons, μ	

Two samples are used to study the fraction of the 4 categories of the electrons. The first one is a sample with filtered di-jets, which contains all hard-scattering QCD processes with $E_T > 15GeV$, including heavy-flavour production, as well as other physics processes of interest, such as prompt-photon production and single W/Z production[54]. The second one, referred to as minimum bias, contains the same processes without any explicit hard-scattering cut-off[55]. The fraction of the 4 categories of the electrons in the 2 samples are shown in Table 3.2.

Table 3.2: Contribution and origin of isolated, non-isolated, and background electron candidates in the two di-jet samples before the identification criteria are applied[56].

$E_T > 17$GeV			$E_T > 8$GeV	
Isolated	Non-isolated	Background	Non-isolated	Background
W 75.0%	b-hadrons 38.7%	γ-conv. 97.8%	b-hadrons 39.3%	γ-conv. 98.4%
Z 20.9%	c-hadrons 60.6%	Dalitz decays 1.8%	c-hadrons 59.7%	Dalitz decays 1.3%
t < 0.1%	J/ψ 0.7%	u/d/s hadrons 0.4%	J/ψ 1.0%	u/d/s hadrons 0.3%
τ 4.1%				

Standard identification of electrons is based on many independent cuts, which have been optimised in up to 7 bins in η and up to 6 bins in p_T. Three reference sets of cuts have been defined as loose, medium and tight.

The **Loose** cuts performs a simple electron identification based only on limited information from the calorimeters. Cuts are applied on the hadronic leakage and shower-shape variables, derived from only the middle layer of the EM calorimeter. This set of cuts is loose so that it provides excellent identification efficiency, but low background rejection.

The **Medium** cuts improves the quality by adding cuts on the strips in the first layer of the EM calorimeter. It also considers the following tracking variables:

- Strip-based cuts are effective to reject $\pi^0 \rightarrow \gamma\gamma$ decays. The energy deposit pattern of π^0 has two maxima due to the $\gamma\gamma$ decay. Thus the variable $\Delta E_s = E_{max2} - E_{min}$ will show different values for electrons and pions. Here E_{max2} stands for the second maxima of energy deposit, and E_{min} is the minimum energy deposit in the region $\Delta\eta \times \Delta\phi = 0.125 \times 0.20$
- The tracking variables include the number of hits in the pixels, the number of silicon hits (pixels plus SCT) and the transverse impact parameter.

The medium cut increases the jet rejection by a factor of 3-4 compared to the loose one, while, it reduces the efficiency by 10%. [57]

The **Tight** cuts use all the identification tools currently available for electrons. In addition to the cuts used in the medium set, more cuts are applied:

- the number of vertexing layer hits. This helps reject electrons from conversions.
- the number of hits in the TRT.
- the ratio of high-threshold hits to the number of hits in the TRT. This helps reject the dominant background from charged hadrons.
- the difference between the cluster and the extrapolated track positions in η and ϕ.
- the ratio of cluster energy to track momentum.

Two additional cuts are applied: tight(isol) and tight(TRT). Typically, the tight(isol) provides the highest isolated electron identification and the highest rejection against jets. The tight(TRT) cuts helps remove the background from charged hadrons.

3.1.1.2 Multivariate techniques

In addition to the standard cut-based electron identification, several multivariate techniques have been developed, including a likelihood discriminant (H-matrix), a boosted decision tree, and a neural network.

The comparison of between the cut-based method and the likelihood discriminant method are shown in Figure. 3.1. The likelihood works better than the cut-based one: a gain in rejection of about 20-40% for the same efficiency of 61-64%, and a gain in efficiency of 5-10% for the same rejection.

3.1.1.3 Expected performance

The results of the performance studies of the isolation likelihood are shown in Figure. 3.2. The best results are achieved for high-p_T electrons in the barrel region of the EM calorime-

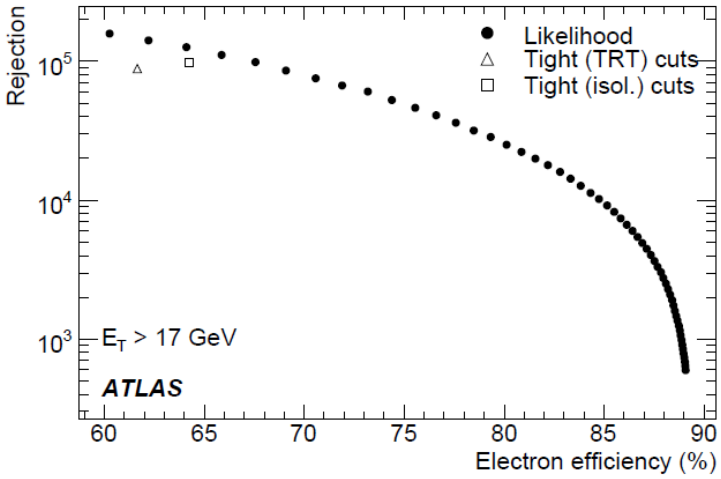

Figure 3.1: Jet rejection versus isolated electron efficiency obtained with a likelihood method compared to the results from the two sets of tight cuts.

ter.

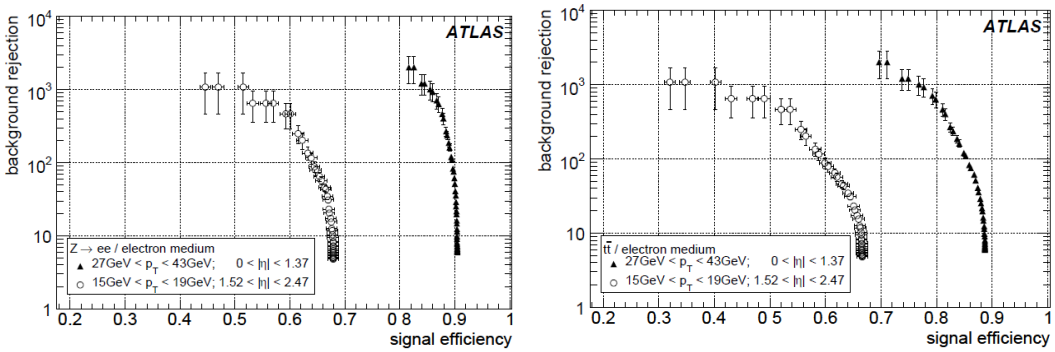

Figure 3.2: Background rejections versus signal efficiencies for electrons in $Z \rightarrow ee$ decays (upper) and in $t\bar{t}$ decays (lower).

As seen from the upper plot which shows electrons from $Z \rightarrow ee$ decay, for electrons with only low hadronic activity, the isolation likelihood provides a background rejection of 10^3, as well providing signal efficiencies around 80% in the barrel region and 50% in the end-cap. Also, as seen in the lower plot which shows electrons from $t\bar{t}$ decay, the additional hadronic activity in the final states decreases the signal efficiencies for 10% at the same background rejection value.

Specially, if one considers the identification requirements to simulated electrons from SUSY process, the signal efficiency with respect to E_T is hown in Figure. 3.3. Single electrons shows higher efficiencies than those in SUSY events because of large hadronic activity.

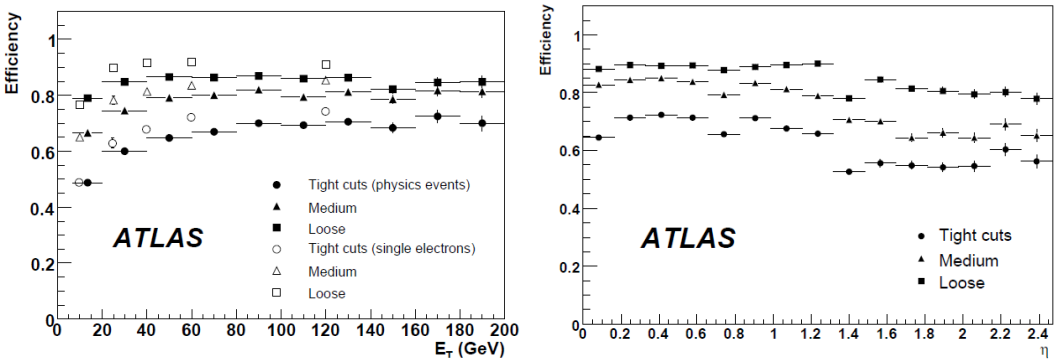

Figure 3.3: Electron identification efficiency as a function of E_T (left) and η (right). The efficiencies as a function of η are shown only for electrons with $E_T > 17$ GeV.

3.1.2 Electron identification within large η region

The identification for the electrons in the forward region ($|\eta| > 2.5$) is also important in many analyses including SUSY search. Different as the central ones, forward electron reconstruction can only use calorimeters information since the inner detector only covers the region $|\eta| < 2.5$.

A topological clustering algorithm is used for the identification. The algorithm is using the following discriminating variables:

- the fraction of the total cluster energy deposited in the cell with maximum energy;
- the relative lateral moment;
- the first moment of the energy density;
- the relative longitudinal moment;
- the second moments of the distances of each cell to the shower barycentre and to the shower axis;
- the distance of the cluster barycentre from the front face of the calorimeter.

The relative lateral moment is defined as $lat_2/(lat_2 + lat_{max})$, where the lateral moments lat_2 and lat_{max} differ in the treatment of the two most energetic cells. An likelihood identification method is also applied, by using the same variables as the cut-based method.

The performance of the identification algorithm is studied by selecting electrons from $Z \rightarrow ee$ and a QCD di-jet sample. Both method can provide fake rate of less than 1% under the requirement of 80% electron identification efficiency. The Receiver-Operating-Characteristic curve (ROC curve) for both method in different $|\eta|$ region are shown in Figure. 3.4.

3.2 Reconstruction of Muons

Muons, especially those with high transverse momentum and isolated, will be much more common in these interesting events than in the background, thus being meaningful to be accurately identified. The ATLAS detector can precisely measure the kinematics of muons up

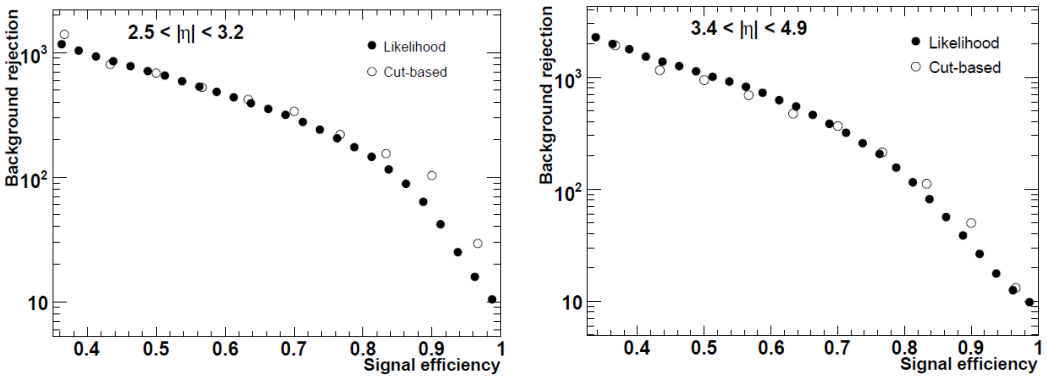

Figure 3.4: The ROC curve for signal electrons from $Z \rightarrow ee$ decay against QCD jets. Both the cut-based and likelihood methods are shown in the inner wheel of the electromagnetic endcap(left) and in the FCal (right).

to 1 TeV. The software to reconstruct muons has also been developed, including identification and position/direction/momentum measuring. The reconstruction algorithm is studied in terms of efficiency, fake rate and precision/accuracy of measurement [58].

3.2.1 Categories of reconstructed muons

Varies ideas have been developed to reconstruct a muon at the ATLAS detector. Thus, several category of muons are defined according to different reconstruction procedure.

- **Standalone** muons are reconstructed by finding a tracks in the muon spectrometer and then extrapolating to the beam line.
- **Combined** muons are reconstructed by matching standalone muons to nearby inner detector tracks and then combining the measurements from the two systems.
- Oppositely, **tagged** muons are found by extrapolating inner detector tracks to the spectrometer detectors and searching for nearby hits.

Two different families of algorithms are used for the reconstruction of each strategy above. The algorithms result into 2 standard muon collections: **Staco** and **Muid**. The Staco collection is used as default for the ATLAS physics analysis.

The **standalone** algorithms will firstly reconstruct track segments in three muon stations respectively and then combine them to form a complete track. The Staco-family algorithm finds the spectrometer tracks and extrapolates them to the beam line. (called "Muonboy") While for the Muid algorithm, it uses "Moore" to perform the inward extrapolation. Both multiple scattering and energy loss in the calorimeter are considered in the extrapolation procedure. "Muonboy" assigns energy loss based on the material crossed in the calorimeter. Muid additionally accounts for the calorimeter energy measurements if they are significantly larger than the most likely value and the muon appears to be isolated.

Standalone algorithms have a slightly larger $|\eta|$ coverage (2.7) than the inner detector (2.5). However, there are holes in the coverage in the region $|\eta| < 1.2$. It is difficult to reconstruct muons with low momentum around a few GeV since they will not penetrate through the out-most stations. Some of the mesons (e.g. π and K) may decay in the calorimeter and

produce muons. These muons are likely to be found in the standalone reconstruction and are assigned as "fake" muons for many analyses.

For the reconstruction of category **combined** muons, both Staco and Muid will match muon-spectrometer tracks with inner detector tracks. The match chi-square is used in the procedure, as an evaluation of the matching quality, which is defined as the difference between outer and inner track vectors weighted by their combined covariance matrix:

$$\chi^2 = (T_{MS} - T_{ID})^T (C_{ID} + C_{MS})^{-1} (T_{MS} - T_{ID}).$$

Here T is a vector of 5 track parameters expressing the closest point to the beam line and C is the covariance matrix. The subscript ID refers to the inner detector and MS to the muon spectrometer. Staco algorithms does a statistical combination of the inner and outer track vectors to obtain the combined track vector:

$$T = (C_{ID}^{-1} + C_{MS}^{-1})^{-1} (C_{ID}^{-1} T_{ID} + C_{MS}^{-1} T_{MS}).$$

Muid does a partial refit, which starts from the inner track vector and covariance matrix and adds the measurements from the outer track.

For **tagging** muons, 2 algorithms - "MuTag" and "MuGirl" - are used. They propagate all inner detector tracks out to the first station of the muon spectrometer and then search for nearby segments. "MuTag" defines a tag chi-square using the difference between any nearby segment and its prediction from the extrapolated track. "MuGirl" uses an artificial neural network to define a discriminant. In both case, if a segment is sufficiently close to the predicted track position, then the inner detector track is tagged as corresponding to a muon.

3.2.2 Standalone muon performance

The efficiency, fake-rate and resolution of the reconstruction algorithms for standalone muons are shown in Figure. 3.5. The performance plots are obtained using $t\bar{t}$ sample. Most of the efficiency loss for standalone muons reconstruction are in regions where the detector holes locates (like $|\eta| < 1.2$). Otherwise, the muon efficiency is almost 100% for Muonboy and 99% for Moore. At high luminosity, the fake rates of the Staco is less than 3% even for low p_T muons. But the fake rate of the Moore goes rather high at for low p_T muons. For both algorithms, the resolution is degraded at intermediate pseudorapidity ($1.2 < |\eta| < 1.7$), because of the reduced number of measurements and the material in the endcap toroid. However, the average resolution is similar for both.

3.2.3 Combined muon performance

The performance of the algorithms for combined muons reconstruction are compared to that for the standalone ones. $t\bar{t}$ samples are also used for this comparison. Staco shows a small drop in efficiency with little reduction of the fake rate except for the lowest p_T. Muid efficiency is significantly worse than that of Staco. The combined resolution is significantly better. As well, mis-reconstruction and charge misidentification rates are around 0.01% for

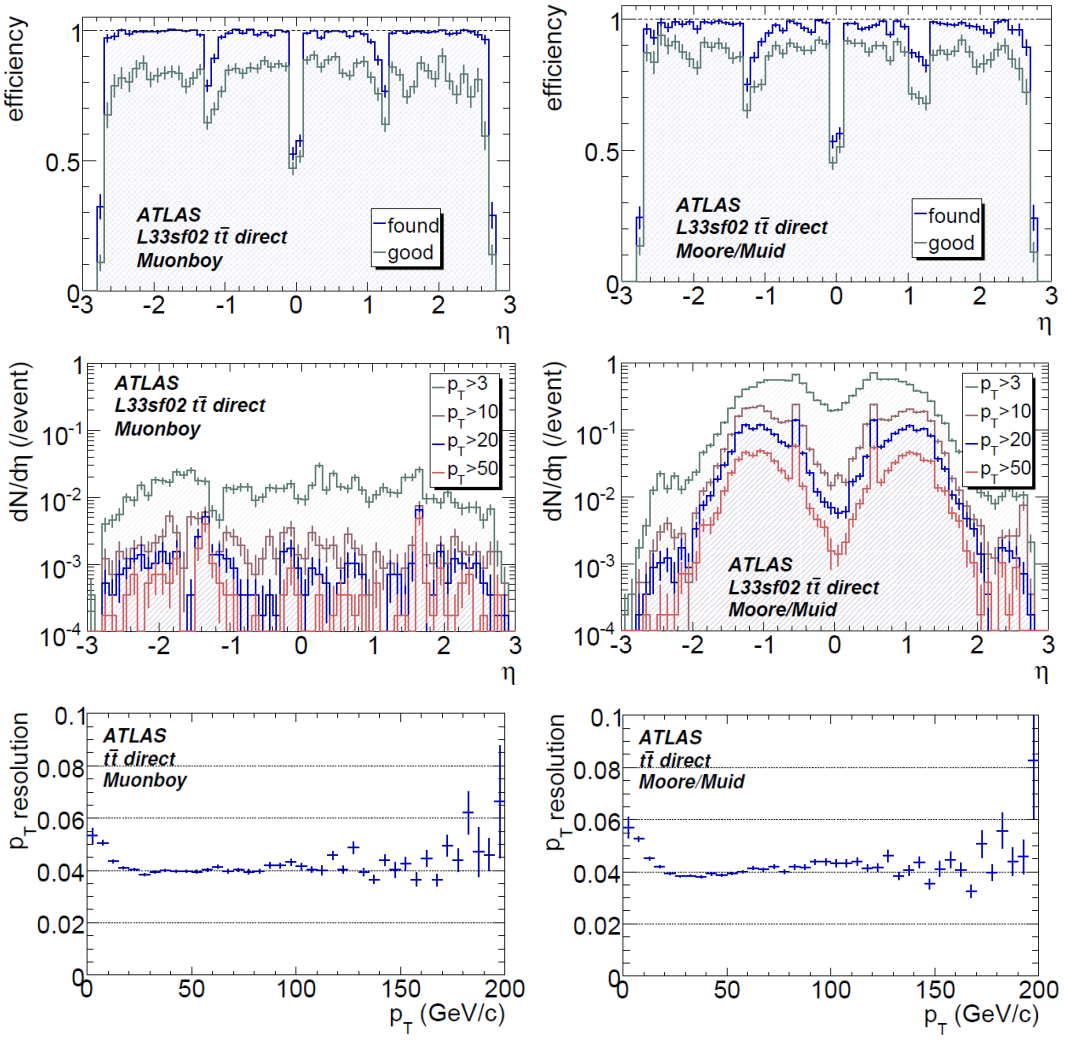

Figure 3.5: Performance plots for reconstruction algorithms of standalone muons.

the combined muons instead of 0.1% for the standalone. The performance study are shown in Figure. 3.6 [59] [60].

As discussed above, when matching inner detector and muon spectrometer tracks, both Staco and Muid calculate χ^2_{match} which serves as a discriminant for separating real and fake muons. Figure. 3.7 shows the χ^2_{match} distributions for both direct found muons and fakes. It can be observed that with a cut $\chi^2_{match} < 100$, many of the Staco high-p_T fakes can be suppressed with only a modest loss in efficiency.

3.2.4 Tagging muon performance

The MuGirl has lower efficiency and a higher fake rate than the combined muon results. For the resolution, MuGirl does not refit the tracks so that the inner detector resolution dominants. Comparing with the standalone and combined muon results, it is clear that higher precision is obtained by combining inner measurements with the standalone one, as

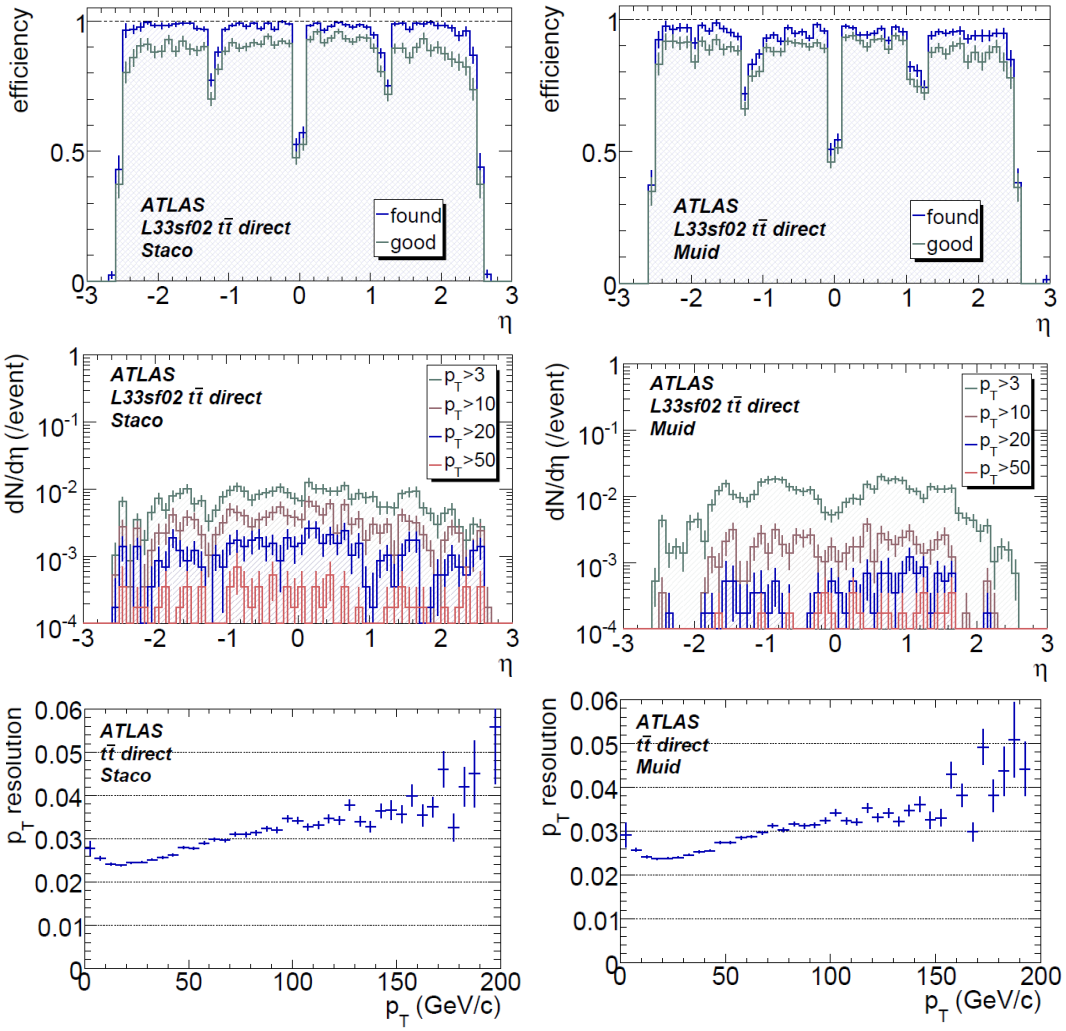

Figure 3.6: Performance plots for reconstruction algorithms of combined muons.

shown in Figure. 3.8 [61].

Generally, at low luminosity, Muid $t\bar{t}$ shows a small decrease in both efficiency and fake rate. But when background is added, the fakes for Muid is not changing too much, while Moore has a dramatic increase. The matching suppresses most of the fakes, and the Muid high-p_T fake rates are lower than those of Staco. However, the high-luminosity $t\bar{t}$ Muid efficiency is significantly worse than that of Staco.

3.3 Reconstruction of Taus

Being very similar to an electron or a muon, but with a mass of 1776.82 ± 0.16 MeV, the τ lepton is the only lepton heavy enough to decay into hadrons as well as into leptons. The lifetime of τ is $2.9 \times 10^{-13} s$, with a proper decay length $87.11 \mu m$, making it decay inside the LHC beam pipe.

τ leptons, especially hadronic decay ones, are playing an important role at the LHC,

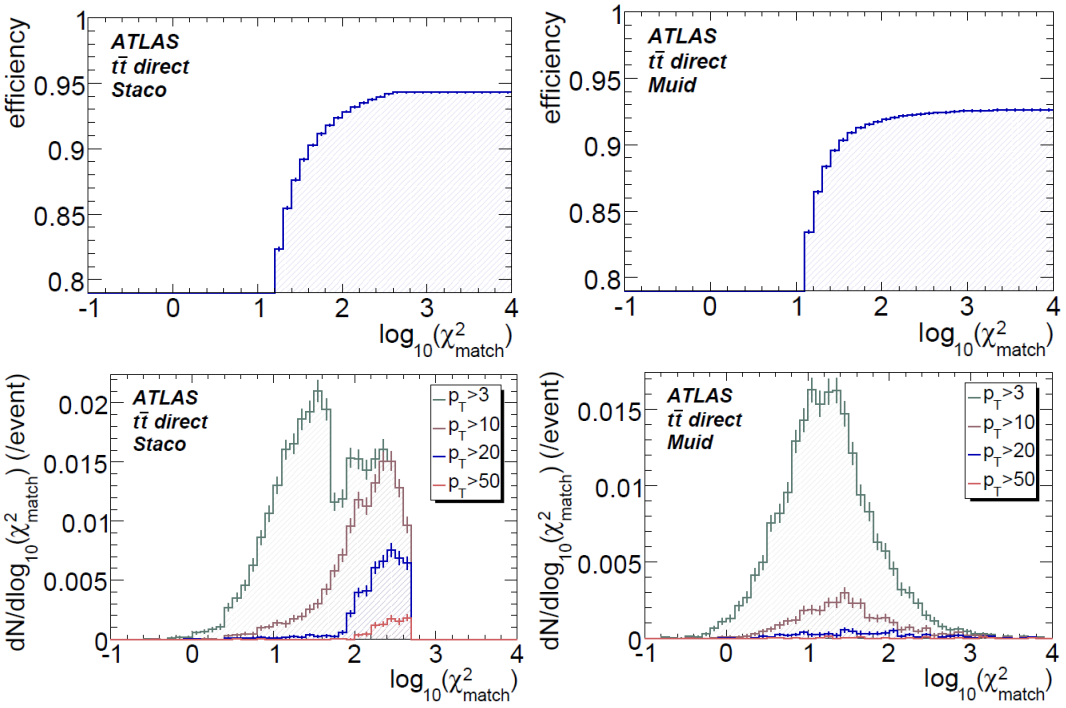

Figure 3.7: Performance plots for reconstruction algorithms of combined muons.

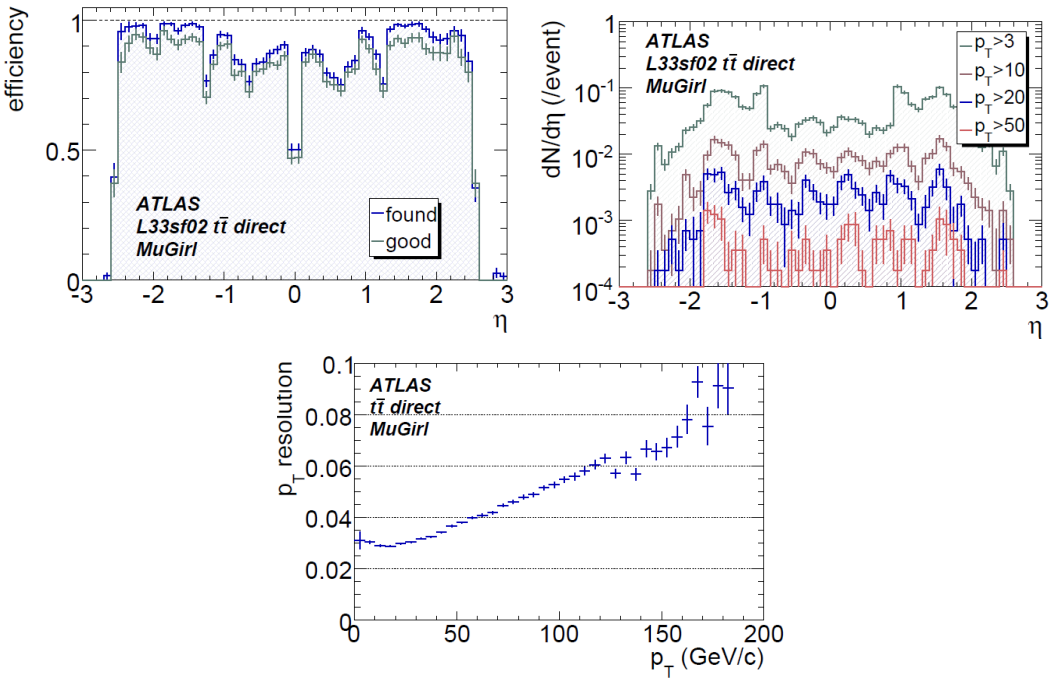

Figure 3.8: Performance plots for reconstruction algorithms of tagging muons.

particularly for SUSY search. They are massive particles having electroweak interactions within a measurable lifetime. Also, the production and the decay of τ are well separated in

time and space (Γ_{tau}/m_{τ} 10^{-11}). This provides possibility for unbiased measurements f the polarisation, spin correlations, and the parity of the resonances decaying into τ. Typically, the transverse momentum of interested τs are in a wide range from below 10GeV to more than 500 GeV at the LHC. The low energy τs reconstruction should be optimized because of corresponding W/Z/Higgs analyses and SUSY particle decays. While the high energy τs is important to heavy Higgs searches in MSSM [62] [63].

The reconstruction of τ leptons usually considers only the hadronic decay modes, since leptonic decaying modes are difficult to be distinguished from primary electrons and muons[64]. The difficulty exists when distinguishing interesting events with τ lepton from background processes with QCD multi-jet production[65]. Another related challenge is to provide efficient triggering for interested events while keeping proper trigger rates. The idea to distinguish hadronically decaying τs from QCD jets is that τ has low track multiplicities contained in a narrow cone, forms different response in the track system and the shapes of the calorimetric showers. Therefore, isolation from the rest of the event is required, both in the inner detector and the calorimeter. A traditional cut-based selection and multi-variate discrimination techniques are applied.

The inner detector provides information for the charged hadronic tracks from the rest of the event. These tracks should not match track segments in the muon spectrometer, nor reveal features characteristic of an electron track. The charge of the τ lepton can be directly determined from the charge(s) of its decay product(s). Calorimetry provides information on the energy deposit from the visible decay products. Hadronically decaying τ leptons are well collimated leading to a relatively narrow shower in the EM calorimeter. For single-prong (1 charged-pion or 3 charged pions among the decay products) decays with one or few π^0, about 55% of the energy is carried by these π^0.

The algorithms for the reconstruction of hadronically decaying τs are higher level reconstruction as they use components provided by algorithms specific to different sub-detectors[66]. Two complementary algorithms have been implemented into the ATLAS offline reconstruction software:

- The calorimetry-based algorithm. It starts from clusters reconstructed in the hadronic and EM calorimeters and then builds the identification variables based on information from both the tracker and the calorimeter.
- The track-based algorithm. This algorithm starts from seeds built from few high quality tracks collimated around the leading one. The energy is calculated with an energy-flow algorithm based only on tracks and the energy in the EM calorimeter. All identification variables are built using information from the tracker and the calorimeter.

3.3.1 Tracking and vertexing

The efficiency for track reconstruction in τ decays is defined as the probability for a given charged π from a τ decay to be reconstructed as a track. Good quality tracks reconstructed with p_T as low as 1 GeV are required by the track-based algorithm, while the calorimeter-based algorithm accepts any track with $p_T > 2$ GeV. Good quality tracks are required to satisfy $\chi^2/n.d.f < 1.7$, to have a number of pixel and SCT hits ≥ 8 and transverse impact parameters $|d0| < 1$ mm. For the leading track, the selection would be even more strict. The

low threshold of TRT hits has to be larger than 10, as well satisfying $|\eta| < 1.9$. A dedicated veto against electron tracks being used as leading tracks is not applied at the reconstruction level. The reconstruction efficiency for tau tracks is show in Figure. 3.9. It can be observed that the overall efficiency is more than 83%. Also, the efficiency of single prong decays is slightly larger than three-prong case.

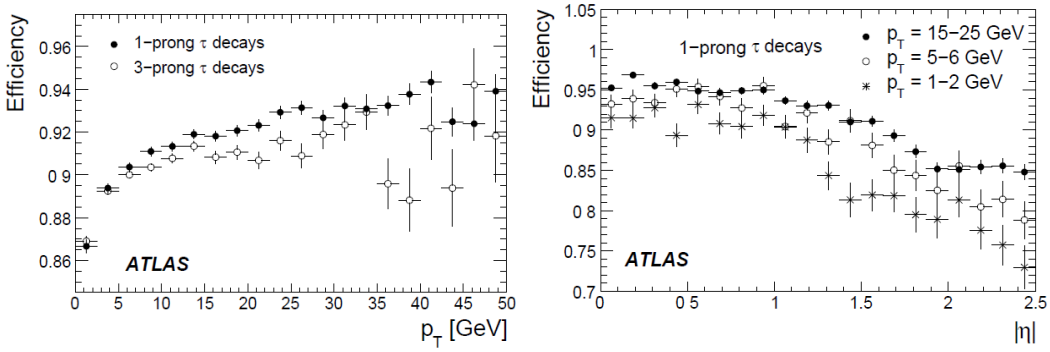

Figure 3.9: Reconstruction efficiency for tracks from charged πs for 1 and 3 prong hadronic τ decays, as a function of the transverse momentum of the track (left) and of the pseudorapidity for three different ranges of track p_T (right). [67]

The lifetime of the τ lepton is $87.11\mu m/c$. This allows the reconstruction of three-prong decays vertex. Various algorithms have been applied in the ATLAS experiment for the reconstruction. Among them the adaptive vertex fitter is optimal, which is an iterative reweighted fit with tracks down-weighted according to their weighted distance to the vertex. The performance of the adaptive vertex fitter is assigned with τ_{had} selected from $Z \rightarrow \tau\tau$ and $W \rightarrow \tau\nu$ events. The resolution and mean of the distribution for residuals of the secondary vertex position of the τ_{had} candidate obtained from the adaptive vertex fitter are shown in Table.3.3.

Table 3.3: The resolution and mean of the distribution for residuals of the secondary vertex position of the τ_{had} candidate obtained from the adaptive vertex fitter.

	Resolution	Mean
Parallel		
Fully matched 3-prong	0.593 ± 0.008 mm	0.006 ± 0.006 mm
Partially matched	0.703 ± 0.030 mm	0.035 ± 0.020 mm
Combined	0.613 ± 0.008 mm	0.004 ± 0.006 mm
Transverse		
Fully matched 3-prong	10.1 ± 0.2 μm	0.2 ± 0.1 μm
Partially matched	11.3 ± 0.5 μm	-0.1 ± 0.2 μm
Combined	10.5 ± 0.2 μm	0.1 ± 0.1 μm

3.3.2 Calorimeter-based algorithm for offline reconstruction

The calorimeter-based algorithm for offline τ_{had} reconstruction is a sliding window clustering algorithm. It is applied to calorimeter towers - all cells of all calorimeter layers on a

grid of size $\Delta\eta\times\Delta\phi = 0.1\times 2\pi/64$. The energy and position are calculated from the clusters with $E_T > 15$ GeV. The probability for a true τ to be reconstructed as a cluster increases from 20% to 68% over the E_T range from 15 to 20 GeV, and will reach up to 98% for E_T higher than 30 GeV. More specifically, all cells within $\Delta R < 0.4$ around the center of the cluster are then calibrated with an H1-style calibration [68]. An optimized weight for each cell is applied as a function of energy density, η and the calorimeter region [69].

To discriminate hadronic τ decay from fake QCD jets, we introduce several variables evaluating the properties for the reconstructed τ, and then combine them into a vector to obtain a likelihood function. These variables are:

- The electromagnetic radius R_{em}:

$$R_{em} = \frac{\sum_{i=1}^{n} E_{T,i}\sqrt{(\eta_i - \eta_{cluster})^2 + (\phi_i - \phi_{cluster})^2}}{\sum_{i=1}^{n} E_{T,i}}.$$

  Here, i runs over all cells in the EM calorimeter in a cluster with $\Delta R < 0.4$. η,ϕ and E are position and energy of the cell. This variable shows good discrimination power at low E_T.

- Isolation in the calorimeter:

$$\Delta E_T^{12} = \frac{\sum_i E_{T,i}}{\sum_j E_{T,j}}.$$

  Here i and j runs over all cells in the cone around the cluster with $0.1 < \Delta R < 0.2$ and $\Delta R < 0.4$ respectively. The same as R_{em}, the isolation variable works better at lower E_T.

- Charge of the τ candidate.
- Number of associated tracks ($p_T > 2$GeV) within the cone $\Delta R < 0.3$ to a cluster.
- Number of hits in the η strip layer within the cone $\Delta R < 0.4$ to a cluster.
- Transverse energy width in the η strip layer:

$$\Delta\eta = \sqrt{\frac{\sum_{i=1}^{n} E_{T,i}^{strip}(\eta_i - \eta_{cluster})^2}{\sum_{i=1}^{n} E_{T,i}^{strip}}}.$$

  The runs over region for i is $\Delta R < 0.4$. This variable is also less efficient at higher E_T.

- Lifetime signed pseudo impact parameter significance:

$$sig_{d_0} = d_0/\sigma_{d_0}^2.$$

  Here σ is the resolution of d_0.

- E_T over p_T of the leading track: E_T/p_{T1}. p_{T1} is the transverse momentum of leading track. The distribution of this variable against p_T is more uniform for τ_{had} decay than QCD jets.

The τ identification is based on a one-dimensional likelihood ratio formed by the variables above. The distribution of the likelihood for τs and jets are shown in Figure. 3.10, as well as the rejection for jets.

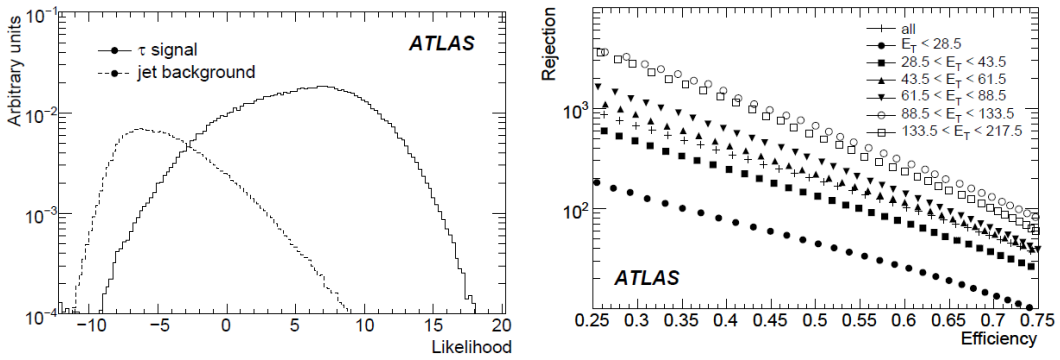

Figure 3.10: The log likelihood (LLH) distribution for τ_{had} (solid) and QCD jets (dashed). (left) Efficiency for τ leptons with respect to rejection against jets for different ET ranges. (right)

3.4 Reconstruction of Jets

Jets are playing very important role in many new physics searches in ATLAS. The reconstruction of jets are combining the 3D topological clusters built in the calorimeters and the charged tracks in the inner detector. The algorithm used in jet reconstruction is called "anti-kt". Also, the performance of jet reconstruction is shown in this section.

3.4.1 Jet reconstruction procedure

The jet reconstruction starts with the finding of the calorimeter jets and the track jets.

The input to calorimeter jets can be topological calorimeter clusters or calorimeter towers. Only those inputs with positive energy are considered as input to jet finding. The topological clusters are groups of calorimeter cells which will follow the shower development. The topocluster formation algorithm starts from a seed cell, with a signal-to-noise ratio above 4. Cells neighbouring the seed that have a signal-to-noise ratio of at least S/N = 2 are included iteratively. Finally, all calorimeter cells neighbouring the formed topocluster are added. The topo-cluster algorithm efficiently suppresses the calorimeter noise.

The input of track jets includes charged tracks originating from the primary hard scattering vertex. Tracks with $p_T > 0.5$ GeV and $|\eta| < 2.5$ are selected, which also have at least one (six) hit(s) in the Pixel(SCT) detector. The transverse (d0) and longitudinal (z0) impact parameters of the tracks measured with respect to the primary vertex are also required to be $|d_0| < 1.5$ mm and $|z_0 sin\theta < 1.5$ mm. The track jets must have at least two constituent tracks and a total transverse momentum of 3 GeV.

Besides, Monte Carlo simulation truth jets are also built from stable particles defined to have proper lifetimes longer than 10 ps excluding muons and neutrinos[70]. For certain studies, jets in the Monte Carlo simulation are additionally identified as jets initiated by light or heavy quarks or by gluons based on the generator event record. The highest energy parton that points to the truth jet determines the flavour.

3.4.2 Anti-kT algorithm

The anti-kt algorithm [71] is used to reconstruct jets in the ATLAS detector, with the distance paremeter set to 0.4 or 0.6. It is a simple and soft-resilient jet reconstruction algorithm.

The algorithm uses two distances:

- $d_{ij} = min(k_{ti}^{2p}, k_{kj}^{2p})\frac{\Delta_{ij}^2}{R^2}$, this stands for the distance between particles or pseudo-jets, with subscript i and j.
- $d_{iB} = k_{ti}^{2p}$, this stands for the distance between particles i and the beam.

Here, $\Delta_{ij}^2 = (y_i - y_j)^2 + (\phi_i - \phi_j)^2$; k_{ti}, y and ϕ are the transverse momentum, rapidity and azimuth; R is the radius parameter; p is an index used to master the power of the energy versus geometrical scales. For $p = 1$, one recovers the inclusive k_t algorithm. While for $p = -1$, it corresponds to the "anti-kt" jet-clustering algorithm.

This algorithm loops all particles for the smallest value of the two distances. If the smallest value corresponds to d_{ij}, the i and j entities are grouped; otherwise if it corresponds to d_{iB}, the i entity is called a jet. This procedure will continues until no entities are left.

3.4.3 Jet cleaning and Calibration

Background jets are aminly coming from proton collisions with the gas from the beam pipe, cosmic muons and calorimeter noise. Four sets of jets are defined to separate real jets from the background ones: looser, loose, medium and tight. The looser category has the highest real jet efficiency but lowest background rejection. Variables like the reconstructed energy, deposited jet energy and the number of associated tracks matched to the jets are used to define these jet containers.

Also, several corrections are considered for the reconstructed calorimeter jets:

- Pile-up corrections, an calibration to account for energy offset due to in-time and out-of-time pile-up.
- Origin corrections are applied to the jet direction, to point back to the primary vertex instead of the nominal center of ATLAS.
- Jet calibration based on MC simulations. This calibration is applied to reconstructed jet energy and assigned by corresponding variables as a function of p_T and η.

3.4.4 Performance of jet reconstruction

The jet reconstruction efficiency is measured in Monte Carlo simulation by counting in how many cases a calorimeter jet can be matched to a truth jet. Reconstructed jets are matched to truth jets, if their jet axes are within $dR < 0.4$. The reconstruction efficiency as a function of jet p_T are shown in Fig. 3.11.

See from the top two plots, the efficiency of truth jet and track jets reconstruction reaches its maximum value for a truth jet transverse momentum of 20 GeV. The jet reconstruction efficiency is well described by the Monte Carlo simulation and is within the systematic uncertainty. A systematic uncertainty of 2% for jets with $p_T < 30$ GeV is assigned and negligible for higher p_T jets.

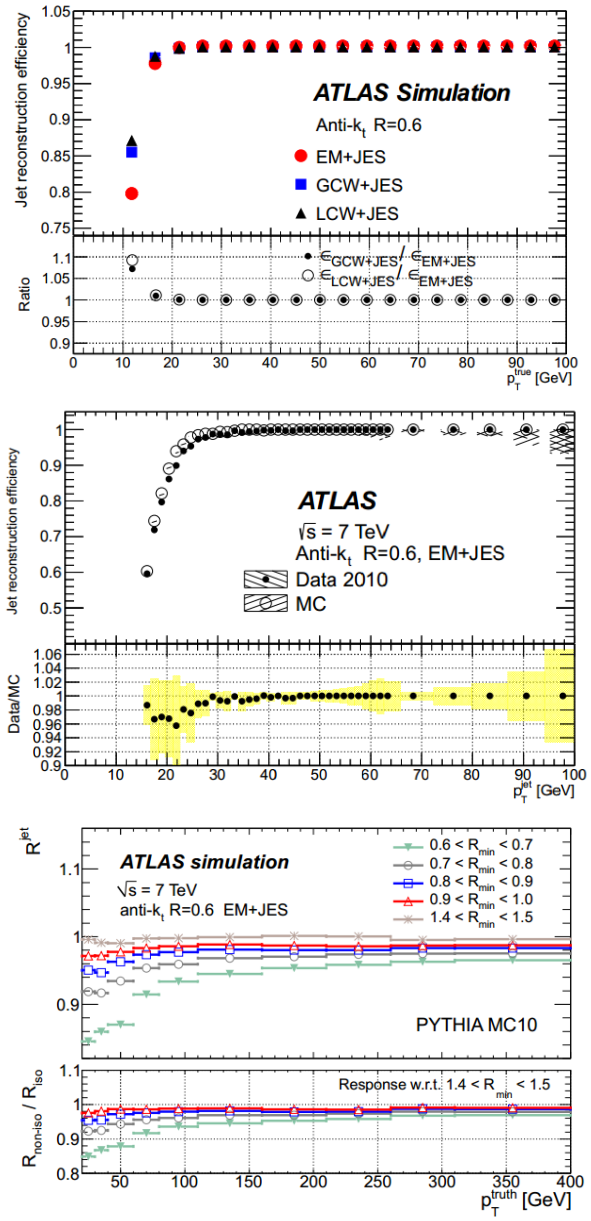

Figure 3.11: Calorimeter jet reconstruction efficiency with respect to truth jets (top) and track jets (medium) as a function of the jet p_T. Average ratio of calorimeter jet to the matched truth jet p_T as a function of truth jet p_T for anti-kt jets with $R = 0.6$ (lower), for different R_min values.

While for calorimeter jets, the calorimeter jet response are defined for the performance: $R = p_T^{calorimeter\,jet} / p_T^{truth\,jet}$. An uncertainty is assigned accordingly by comparing in data and Monte Carlo simulation the track jet response. They are both examined as function of the distance R_min between the jet and the closest jet in the calorimeter. Further study shows that the close-by jet systematic uncertainty on the jet energy scale is 2.5 – 5.1% and 1.6 – 1.9% for $R = 0.6$ jets with $20 < p_T < 30$ GeV and $p_T > 30$ GeV respectively.

3.5 Reconstruction of Missing Transverse Energy

A very good measurement of the missing transverse energy (E_T^{miss}), is essential for many physics studies in ATLAS. Events with large E_T^{miss} are expected to be the key signature for new physics such as supersymmetry and extra dimensions. Good E_T^{miss} measurement in terms of linearity and resolution is also important for the reconstruction of the top-quark mass from $t\bar{t}$ events with one top quark decaying semileptonically. Furthermore, it is crucial for the efficient and accurate reconstruction of the Higgs boson mass when the Higgs boson decays to a pair of τ-leptons [72].

An important requirement on the measurement of E_T^{miss} is to minimize the impact of limited detector coverage, finite detector resolution, presence of dead regions and different sources of noise that produce fake-E_T^{miss}. The ATLAS calorimeter coverage extends to large pseudorapidity angles to minimize the impact of high energy particles escaping in the very forward direction. Dead and noisy readout channels in the running detector will also produce Fake-E_T^{miss}. Such Fake-E_T^{miss} sources can significantly enhance the background from QCD multi-jet events in supersymmetry searches.

3.5.1 The algorithms for E_T^{miss} reconstruction

The missing transverse energy in the ATLAS experiment is primarily reconstructed from energy deposits in the calorimeter and reconstructed muon tracks. Apart from the hard scattering process of interest, many other sources such as the underlying event, multiple interactions, pile-up and coherent electronics noise, lead to energy deposits and/or muon tracks. Classifying the energy deposits into various types and calibrating them accordingly is the essential key for an optimal E_T^{miss} measurement. In addition, the loss of energy in dead regions and readout channels make the E_T^{miss} measurement a real challenge. There are two algorithms for E_T^{miss} reconstruction in ATLAS that emphasize different aspects of energy classification and calibration. **The Cell-based algorithm** starts from the energy deposits in calorimeter cells that survive a noise suppression procedure. The cells can be calibrated using global calibration weights depending on their energy density. This procedure will be robust already at initial data taking because it does not rely on other reconstructed objects. In a subsequent step, the cells can be calibrated according to the reconstructed object they are assigned to. Corrections are applied for the muon energy and for the energy lost in the cryostat. **The Object-based algorithm** starts from the reconstructed, calibrated and classified objects in the event. The energy outside these objects is further classified as low p_T deposit from charged and neutral pions and calibrated accordingly.

3.5.1.1 Cell-based E_T^{miss} reconstruction

The Cell-based E_T^{miss} reconstruction includes contributions from transverse energy deposits in the calorimeters, corrections for energy loss in the cryostat and measured muons:

$$E_{x,y}^{final} = E_{x,y}^{Calo} + E_{x,y}^{Cryo} + E_{x,y}^{Muon}.$$

The term $E_{x,y}^{Calo}$ are described as:

$$E_{x,y}^{Calo} = -\sum_{TopoCells} E_{x,y},$$

which are calculated from the transverse energies measured in TopoCells. To classify energy deposits, schemes to calibrate hadronic showers uses the energy density in a cell. Electromagnetic showers tend to have higher energy densities as compared to hadronic showers. The "Local-Hadronic" calibration scheme uses further information related to shape and depth of the calorimetric shower to classify a TopoCluster. The next step in the cell-based E_T^{miss} reconstruction is to globally calibrate all calorimeter cells using the "H1-like" or "Local-Hadronic" calibration schemes.

The term $E_{x,y}^{Muon}$ are described as:

$$E_{x,y}^{Muon} = -\sum_{RecMuon} E_{x,y},$$

which is the opposite number of momenta of muons measured in region $|\eta| < 2.7$. Here, the muon momentum measured by the muon spectrometer is taken. Energy lost in the calorimeter is already included in the calorimeter term.

The thickness of the cryostat between the LAr barrel electromagnetic calorimeter and the tile barrel hadronic calorimeter is about half an interaction length where hadronic showers can lose energy. The E_T^{miss} reconstruction recovers this loss in the cryostat using the correlation of energies between the last layer of the LAr calorimeter and the first layer of the hadronic calorimeter. This correction is called the cryostat term:

$$E_{x,y}^{Cryo} = -\sum_{RecJets} Ejet_{x,y}^{cryo},$$

where $Ejet_{x,y}^{cryo}$ is defined as:

$$E_{x,y}^{Cryo} = w^{cryo}\sqrt{E_{EM3} \times E_{HAD}}.$$

Here w^{cryo} is the calibration weight, EEM3 are the jet energies in the third layer of the EM calorimeter, and EHAD are the energies in the first layer of the hadronic calorimeter.

3.5.1.2 Object-based E_T^{miss} reconstruction

For those case sensitive to low p_T deposits coming mostly from neutral and charged pions, soft jets, the underlying event and pile-up, the object-based E_T^{miss} reconstruction method is more reliable. The method firstly establish a classification between high p_T objects and low p_T ones: the high p_T objects are including $e/\gamma, \mu, \tau$, *jet*, while the low p_T ones includes neutral and charged pions. Then the object-based calibration are applied, and the E_T^{miss} is calculated as:

$$E_{x,y} = -E_{x,y}^{high} - E_{x,y}^{low}.$$

This algorithm uses mostly the calorimeter information to reconstruct E_T^{miss}. Some objects, such as electrons and taus, also use the inner detector tracking. While the muons use both inner detector and muon spectrometer information. Tracking is also used for the low p_T deposits of soft objects.

3.5.1.3 Performance of the E_T^{miss} reconstruction

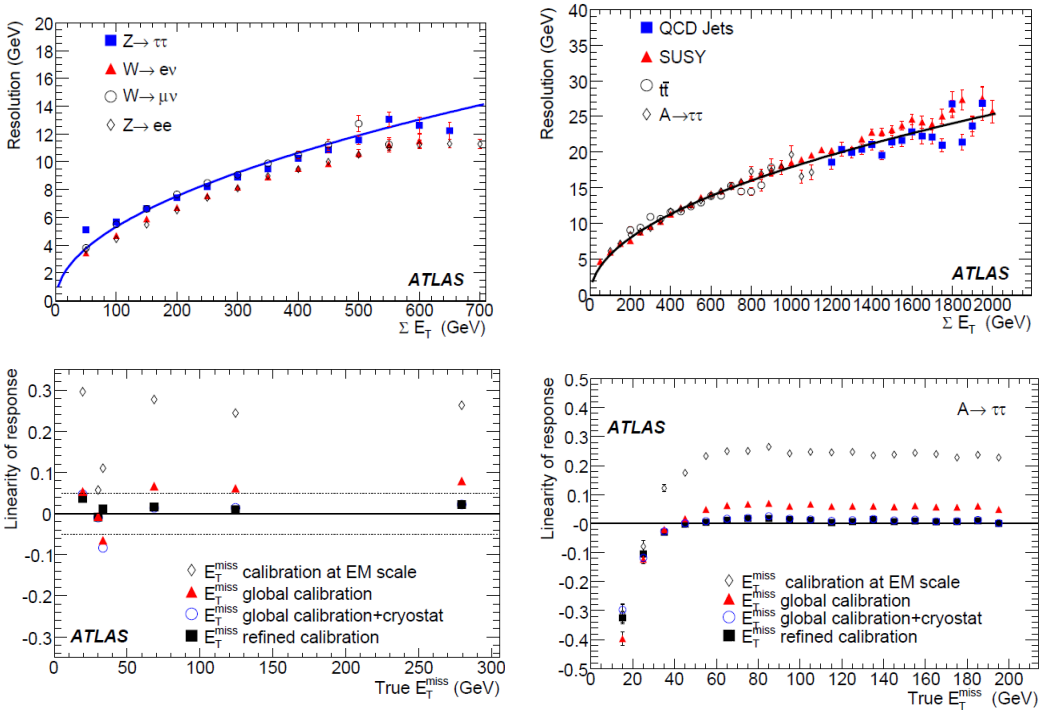

Figure 3.12: Performance of the E_T^{miss} reconstruction. Linearity of response for reconstructed E_T^{miss} as a function of the average true E_T^{miss} for the different steps of E_T^{miss} reconstruction. (Upper-left) Linearity of response for reconstructed E_T^{miss} as a function of the true E_T^{miss} for $A \rightarrow \tau\tau$ events with $m_A = 800$ GeV. (Upper-right) Resolution of the two E_T^{miss} components with refined calibration as a function of the total transverse energy, $\sum E_T$ for low to medium values (lower-left) and for higher values (lower-right). [73]

Figure. 3.12 shows the linearity and resolution for the E_T^{miss} reconstruction. We can obtain the following conclusions:

- The uncalibrated E_T^{miss} corresponds to the use of cell energies at the electromagnetic-scale, also shows a large systematic bias of 30%.
- The reconstructed E_T^{miss} based on globally calibrated cell energies and reconstructed muons gives a linearity to within 5%.
- The reconstructed E_T^{miss} including the cryostat correction shows a linearity to within 1% for almost all processes.
- The refined calibration gives the best resolution when compared with the above steps of calibration.

Also, Figure. 3.13 shows the performance of the direction for the reconstructed E_T^{miss} reconstruction. Large energy fluctuations in the calorimeter or muon mis-measurements can produce large Fake-E_T^{miss}. Generally, for events with prompt E_T^{miss}, the E_T^{miss} angular resolution will depend on the relative fraction of Fake-E_T^{miss} and the event topology. The

measurement of the E_T^{miss} azimuth is more accurate for $W \rightarrow e\nu$ events, which in general contain one high-p_T electron and moderate hadronic activity in addition. For values of truth-E_T^{miss} below 40 GeV, the accuracy of the measurement of the direction degrades rapidly.

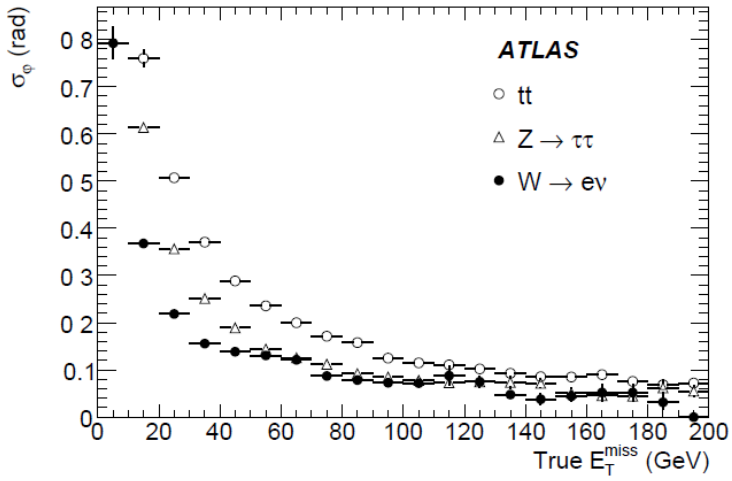

Figure 3.13: Accuracy of the measurement of the azimuth of the E_T^{miss} vector as a function of the true E_T^{miss} for three different physics processes: semi-leptonic $t\bar{t}$ events, $Z \rightarrow \tau\tau$ and $W \rightarrow e\nu$ events.

3.6 Conclusions

This section presents the electron, muon and τ objects reconstruction and identification in ATLAS. As a key varibale in SUSY searches, the missing transverse energy is also shown with its reconstruction and performance. Some of the uncertainties sources associated to these measurements are also presented, which will be further considered in the analyses in the following chapers.

Chapter 4

Track counting uncertainty for hadronic tau decays

4.1 Introduction

The τ leptons provide a useful signature in searches for beyond Standard Model physics in a wide range of theoretical models including SUSY [74] [75] .

The identification algorithms of a τ lepton are developed to reconstruct and identify the visible products (without the neutrino) of the hadronic decay modes since leptonic τ decays are very difficult to be distinguished from prompt electrons or muons.

The $\tau_{had-vis}$ reconstruction algorithm relies on both the inner detector and calorimeter information. The inner detector provides information on the tracks associated to the τ lepton. The number of charged pions in the decay products is called "nprong". Usually, a $\tau_{had-vis}$ can be sorted into 1-prong or 3-prong case. The charge of the decaying τ lepton can be directly determined from the charge(s) of its associated track(s). Particular attention has been given to minimise the amount of charge mis-identification and of migration between the "nprong" categories during the reconstruction. The $\tau_{had-vis}$ reconstruction algorithm is seeded from jets reconstructed using the anti-kt algorithm (described in the following section) [71], with a distance parameter $\Delta R = \sqrt{\Delta\eta^2 + \Delta\phi^2} = 0.4$. Topological clusters made of calorimeter cells calibrated with the Local Hadron Calibration [76] (a scheme to calibrate energy depositions from hadrons based on calorimeter signals only and the observed shower topology) are used as an input for the jet algorithm. All jets with transverse momentum $p_T > 10GeV$ and pseudorapidity $|\eta| < 2.5$ are considered in the $\tau_{had-vis}$ reconstruction algorithm [77] [78].

The probability of incorrectly assigning a pile up vertex as the primary vertex has increased with the larger number of pile up collisions in 2011. This causes tracks to fail the z_0 impact parameter requirement, as observed in simulated $Z \to \mu\mu$ events. Fig. 4.1 demonstrate the $\tau_{had-vis}$ track selection efficiency at different pile up conditions. Here, $\tau_{had-vis}$ track selection efficiency is defined as the probability for a real charged pion from a hadronic decay to be associated with a reconstructed $\tau_{had-vis}$ candidate.

The τ_{had} reconstruction relies much on the classification of nprongs. As shown in the left plot of Fig. 4.2, the distribution of number of charged tracks in $W \to \tau\nu$, $W \to e\nu$

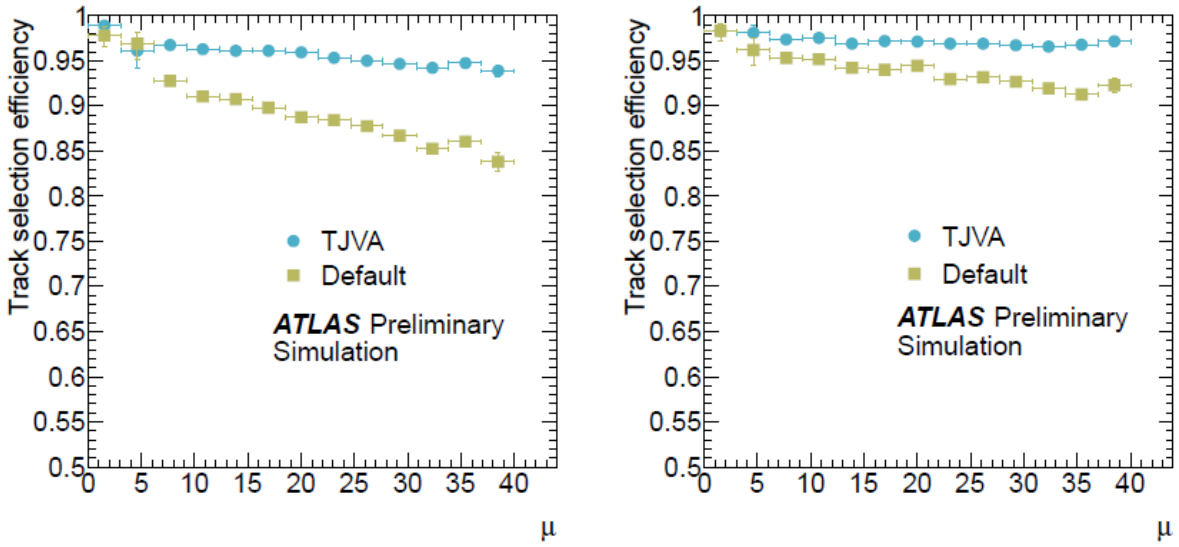

Figure 4.1: The $\tau_{had-vis}$ track selection efficiency with respect to the average number of pile up interactions per bunch crossing (μ) for reconstructed $\tau_{had-vis}$ candidates in $Z \rightarrow \tau\tau$ simulated events. The decay mode of the τ lepton is 1-prong (left) or 3-prong (right).

and jet background are compared. The peaks of the $W \rightarrow \tau\nu$ events are in the bins with 1 or 3 charged tracks. Migration can be observed in the $N_{tracks} = 2$ bin. Moreover, the jet backgrounds contributes a lot in the $N_{tracks} = 1, 3$ bins. To deal with these problems, an "anti-kT" like algorithm is used in counting the charged tracks around a certain π meson, which is called "track-counting" [79, 80, 81, 82, 83]. Acting as a sub-algorithm of the tau identification, this algorithm helps improve the efficiency of the nprong sorting of the τ_{had}. And after the whole tau ID selection, the distributions of number of charged tracks are shown in the right plot of Fig. 4.2. Migration is highly suppressed as well as the jet background.

The "track-counting" algorithm counts tracks in a core cone around a certain π meson or μ. Tracks involved in the algorithm can be classified into core-tracks or isolation-tracks. The core-tracks are typically the charged tracks of the π or μ. The isolation-tracks are required to be a bit far away from the π or μ track, with $d_{kT} < 0.4$ to a core one. Here, d_{kT} is defined as:

$$d_{kT} = \frac{p_T(core)}{p_T(isolation)}\Delta R,$$

where $\Delta R = \sqrt{\Delta\eta^2 + \Delta\phi^2}$.

The goal of the study I made, and presented in this report, is to use selected $Z \rightarrow \mu\mu$ data events to assess the accuracy of the track counting modelling for hadronic tau decays and jet-to-tau fakes in the Monte Carlo (MC) simulation. Contributions to the track counting can come from charged pions from hadronic tau decay or jet-to-tau fake, and also from pileup and underlying event. Events with muons are used to do the performance study since the behaviour of muons are quite similar to pions in track-counting. A "tag-and-probe" method is used to select pure $Z \rightarrow \mu\mu$ sample. The probe muon is expected to contribute with a track in the core cone. Other tracks should only come from pileup and

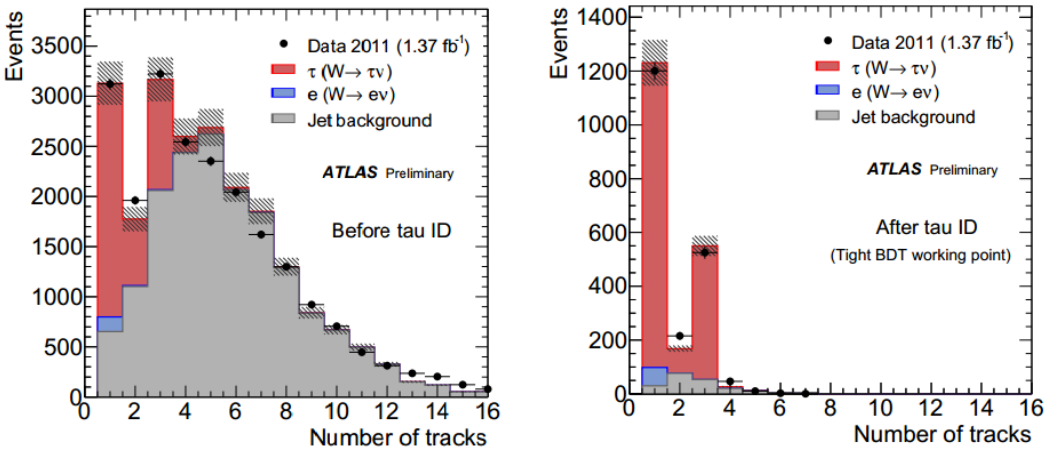

Figure 4.2: Number of charged tracks for tau candidates before (left) and after (right) applying tau identification.

the underlying event.

The original muon selection used in the tag-and probe method in this study is mainly based on the criteria from the Muon Combined Performance (MCP) group, defined as:

- staco loose muon (using algorithm which combines a track reconstructed in the muon spectrometer with its corresponding track in the inner detector);
- trigger: EF_24_tight (at least 1 tau with $p_T > 24$ GeV);
- overlap removal between muon, electron and jets. To be more specific, the muons are required to be isolated from other muons ($\Delta R < 0.1$), electrons ($\Delta R < 0.1$) and jets ($\Delta R < 0.1$).

For Tag Muon, there are a few more requirements:

- $p_{\mathrm{T}} > 25GeV$;
- $|\eta| < 2.4$;
- leading muon (the muon with highest p_T).

For Probe Muon, the following criteria are applied:

- $p_{\mathrm{T}} > 10GeV$;
- $|\eta| < 2.4$;
- opposite charge against the tag muon;
- 66 GeV$< M_{\mu\mu} <$ 116 GeV.

When we count tracks around the probe muon, the following selections are required:

- number of pixel hits ≥ 2,
- number of pixel hits + number of SCT hits ≥ 7,
- $|d_0| < 1.0mm$,
- $|z_0 sin\theta| < 1.5mm$,
- number of B-layer hit ≥ 1 (removed after discrepancy check).

A few additional requirements are applied for core track only:

- $p_{\mathrm{T}} > 1.0GeV$;
- tracks in the region $\Delta R < 1.0$ with regard to the probe muon.

Also for isolation track, additional requirements are:

- $p_{\mathrm{T}} > 0.5GeV$;
- tracks in the region $0.6 < \Delta R < 1.0$ with regard to the probe muon;
- $dkt < 4.0$, correlated to an inner track in the core cone ($\Delta R < 0.2$).

We count the number of core and isolation tracks respectively for each event, making plots for them with regard to p_{T} or η of the probe muon.

4.2 Data/MC samples and comparison

4.2.1 Data/MC samples

Data collected with the ATLAS experiment at $\sqrt(s) = 8TeV$ in 2012 corresponding to a total recorded integrated luminosity of 21.7 fb^{-1} are used in this study. Due to the trigger requirements, data from the muon trigger stream is used. The Monte Carlo samples used in this study are generated by ALPGEN [84]:

- $Z- > \mu\mu$ (AlpgenPythia generator with run-number 11766*);
- $W- > \mu\nu$ (AlpgenPythia generator with run-number 11769*);
- $t\bar{t}$ (McAtNlo_Jimmy generator with run-number 105200).

Fig. 4.4 shows the di-muon invariant mass distribution within Z mass window (66-116 GeV). We can see that the main sources of SM background are $t\bar{t}$ and $Z \rightarrow \mu\mu$ events, estimated from MC prediction. Also, the QCD background is proved to have negligible contribution to our final state. The distributions of the number of track, Ntrack, as a function of p_T, η and ϕ are shown in Fig. 4.5, 4.6. The interval of p_{T} and η are chosen to have enough statistics in each region. Meanwhile, the ϕ separation is made according to modules of the ATLAS detector shown in Fig. 4.3. The agreement between data and MC got reasonable in most of the cases except a close look into the first bin of the core track, which stands for 0 track into the core cone. The first bin problem leads to a discrepancy check including dead module removal and a looser track selection. The B-Layer hits selection are removed in the later study.

4.2.2 Discrepancy check

The first-bin discrepancy has been checked from dead module removal and a looser track selection. Firstly, we checked the number of vertices distribution to make sure the pileup is treated properly, as shown in Fig. 4.7 and Fig. 4.8. There is good agreement between data and MC in each number of track bin, which indicates that the pileup reweighting is reasonable.

Secondly, we counted tracks without the probe muon. The study is performed with removing extra η and ϕ cut of the inner track by using the following selection:

- $p_{\mathrm{T}} > 1.0GeV$

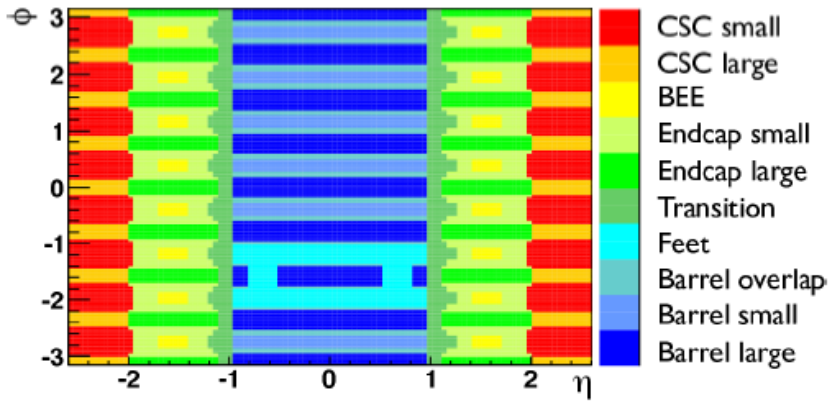

Figure 4.3: Modules of the ATLAS detector. The end points of η bins are set to 1.0 and 2.2 according to the module map.

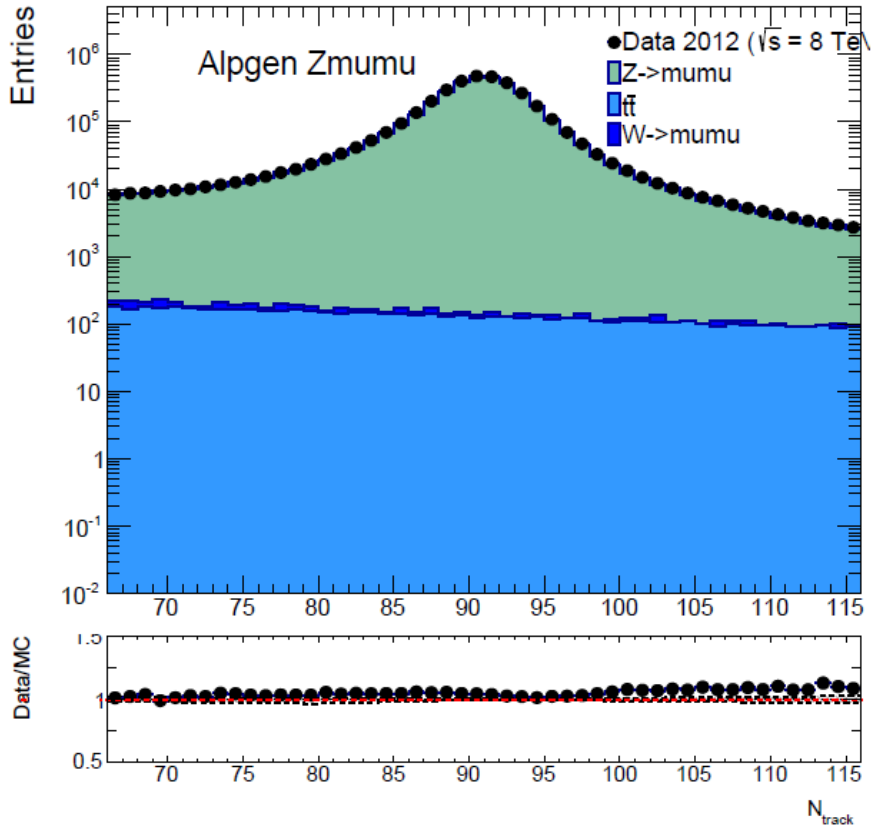

Figure 4.4: Di-muon invariant mass distribution within Z mass window. There is good agreement between data and MC. Further more, the other background except the QCD contribution is quite small.

- tracks in the region $0.05 < \Delta R < 0.2$ with regard to the probe muon (most muon track excluded)

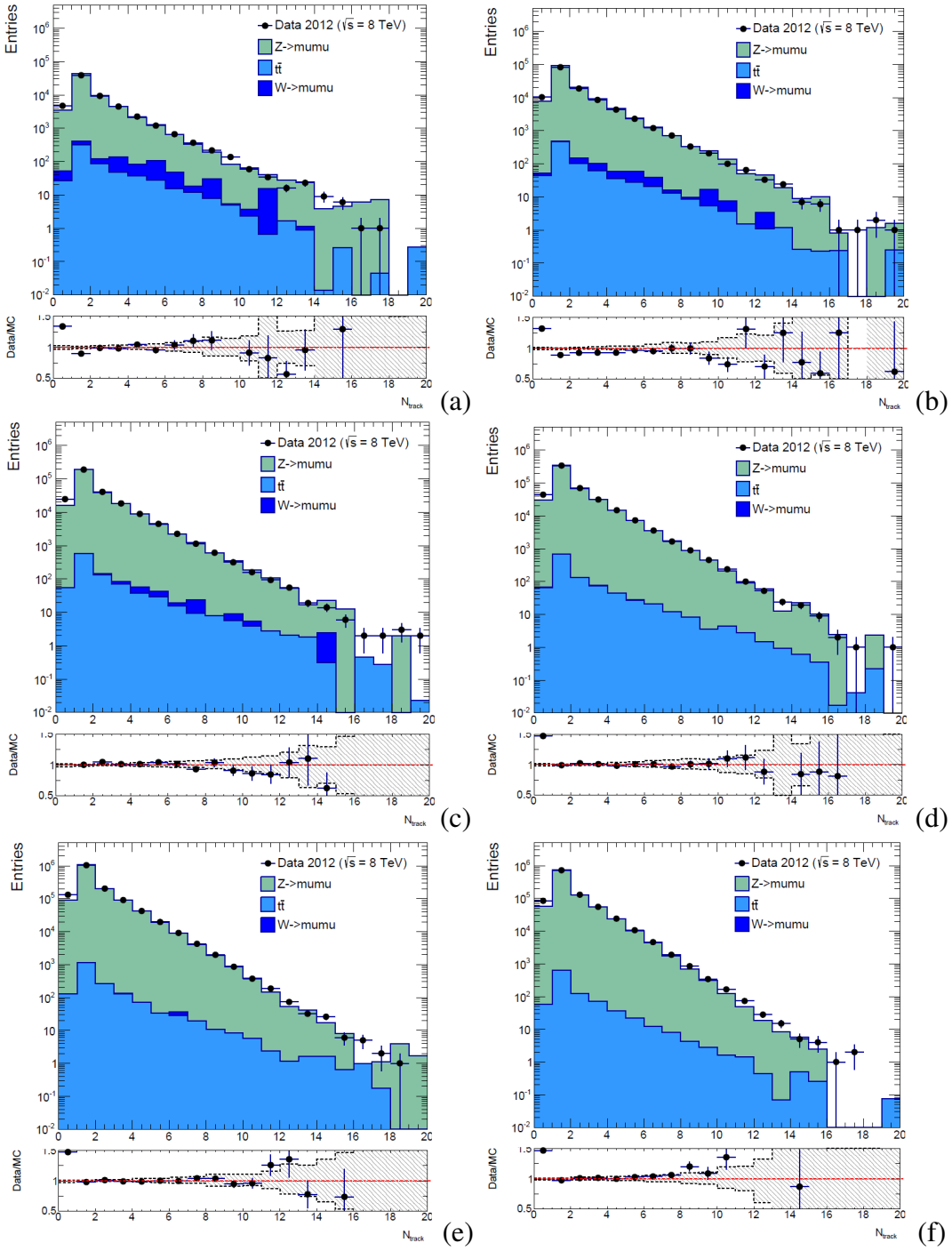

Figure 4.5: Ntrack distribution in different probe muon p_T region: 10 GeV< p_T < 15 GeV (a), 15 GeV< p_T < 20 GeV (b), 20 GeV< p_T < 25 GeV (c), 25 GeV< p_T < 30 GeV (d), 30 GeV< p_T < 40 GeV (e), 40 GeV< p_T < 50 GeV (f), p_T >50 GeV (g). Reasonable agreement between data and MC except for the first bin with no track at current selection.

Figure. 4.5 shows the Ntrack distribution in varied $p_T t$ category with the above selection. Due to the removal of the probe muon in track counting, most events have no track in

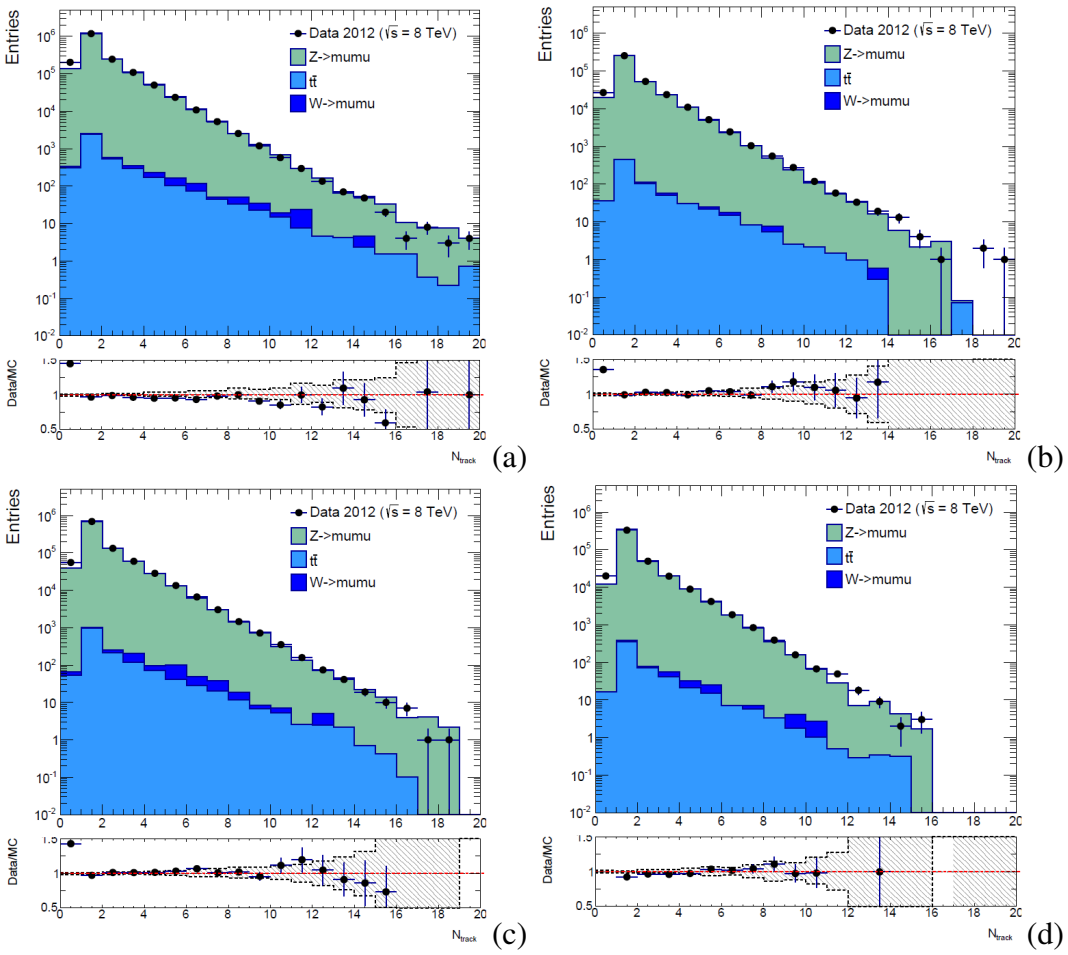

Figure 4.6: Ntrack distribution in different probe muon η region: $|\eta| < 1.05$ (a), $1.05 < |\eta| < 1.30$ (b), $1.30 < |\eta| < 2.00$ (c), $|\eta| > 2.00$ (d). Reasonable agreement between data and MC except for the first bin.

Ntrack distribution. The agreement between data and simulation is quite good if we remove the probe muon, which indicates that this discrepancy is coming from the core track. We may get bad modeling in some eta-phi regions which makes no response to some tracks. This caused some migration from high track number events to low track ones. Distributions are checked after eta-phi cut, according to Figure. 4.6.

With a looser track selection, one should expect a better data vs simulation agreement for Ntrack distributions in different p_T, η, ϕ regions for the first bin, since the bin with 0 track may be due to very tight requirements on the ID hits. So we checked the Ntrack distributions, shown in Figure. 4.9, using a looser track selction.

The old track selection:

- number of pixel hits ≥ 2;
- number of pixel hits + number of SCT hits ≥ 7;
- $|d_0| < 1.0mm$;
- $|z_0 sin\theta| < 1.5mm$;

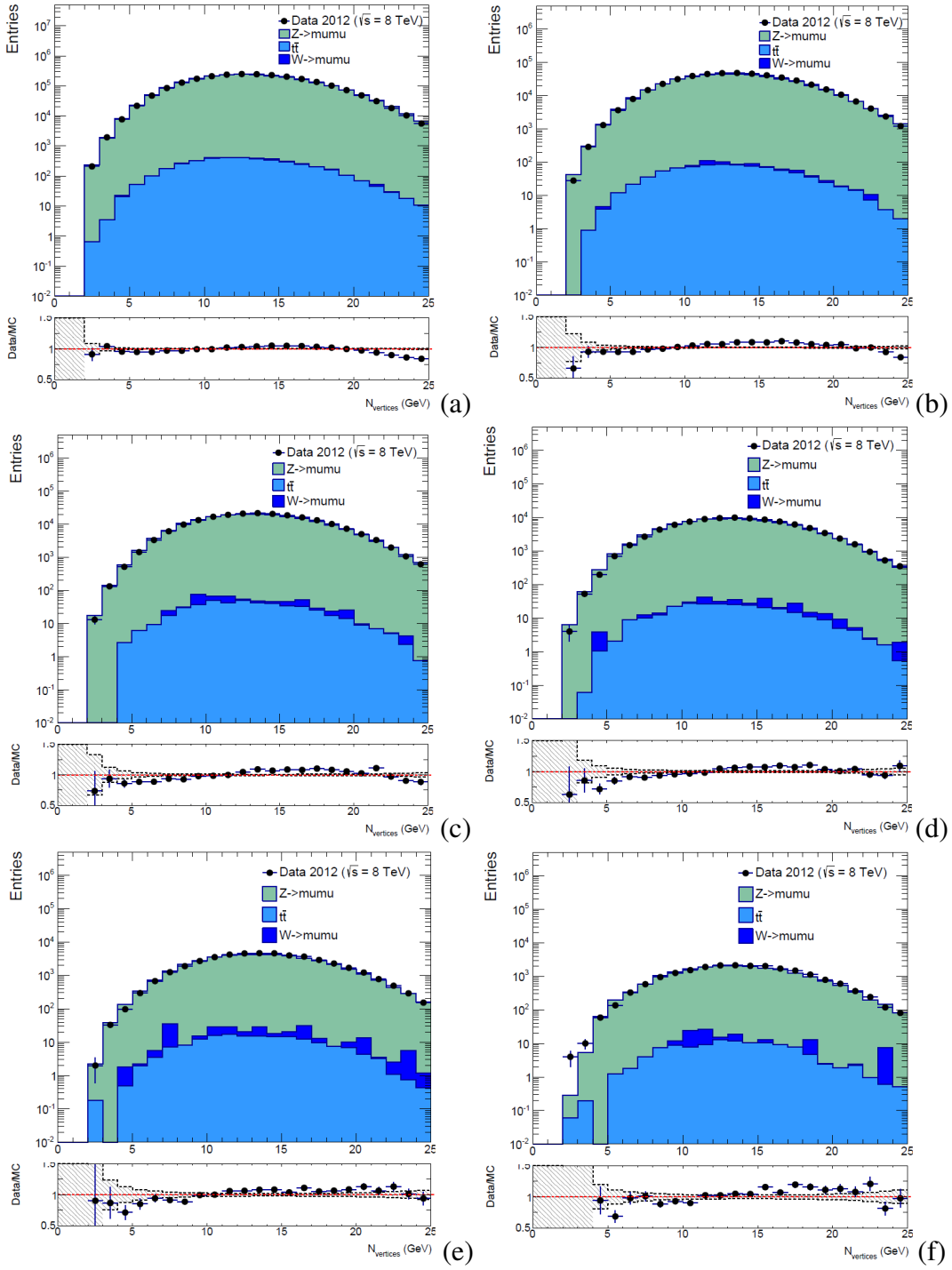

Figure 4.7: Number of vertices distribution with regard to different Ntrack bins: 1 track events (a), 2 tracks events (b), 3 tracks events (c), 4 tracks events (d), 5 tracks events (e), 6 tracks events (f), at least 7 tracks events (g).

- number of B-layer hit ≥ 1 (removed after discrepancy check).

The new track selection:

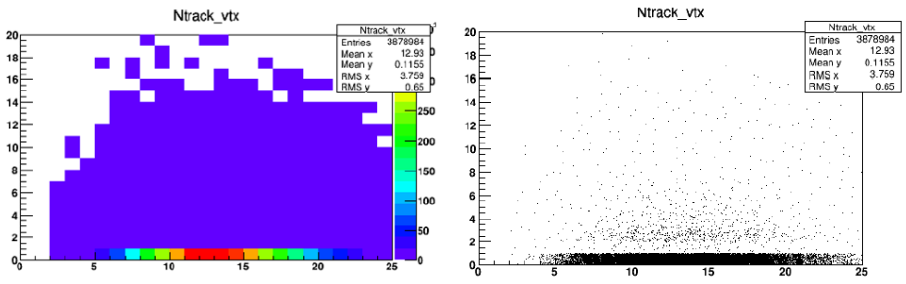

Figure 4.8: Number of events distribution as a function of Number of vertices and Number of tracks without the probe muon, in the form of colored histogram (left) and scattergram (right).

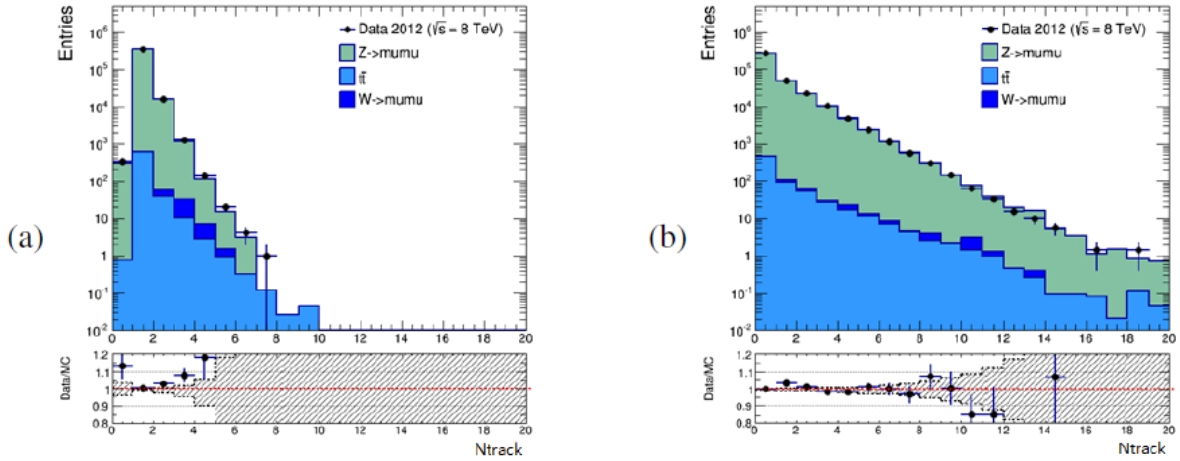

Figure 4.9: Number of core track (a) and isolation track (b) distributions, counting under looser selection.

- number of pixel hits + crossed dead pixel sensors ≥ 0;
- number of SCT hits + crossed dead SCT sensors ≥ 4.

From Figure. 4.9(a), it can be observed that the data to simulation ratio of the number of core tracks in the first bin is reduced to 1.1 with large statistical uncertainty. B-layer hit requirement is removed in further study since it is not recommend.

4.3 Average number of tracks

Since the first bin discrepancy is due to some migration from high Ntrack bins to low ones, it is meaningful to calculate the average number of tracks in a single η/p_T region.

Using the η based region partition, we obtain much more stable Ntrack distribution than the p_{T} based one. The data/MC comparison shows it unnecessary for any scale factors for the MC modelling. It is more reasonable for us to draw some η-based uncertainty for track counting. The uncertainty are presented in terms of 4 track categories listed below:

- Inner track. This refers to the core tracks excluding the probe muon. Tracks are selected using several selection criteria close to the basic selection.
- Middle track. Tracks in a cone $0.2 < \Delta R < 0.4$ (without kt-style track counting) are categorized into this sort.
- Outer track. The same as the isolation track, using varied selection as inner track.
- Muon track. Tracks matched to the probe muon. We apply this category to test the efficiency and reliability of the track selection since the muons are quite well reconstructed in the ATLAS experiment. There should be 0 or 1 muon track in the selection.

Simultaneously, numbers of tracks in the four categories are computed under different track selections to gain knowledge about hadronic tau, jet-to-tau fake, pileup and underlying event. Only one cut was changed each time from the baseline selection:

- $p_{\mathrm{T}} > 1.0$ GeV $\rightarrow$ $p_{\mathrm{T}} > 0.5$ GeV;
- $p_{\mathrm{T}} > 1.0$ GeV $\rightarrow$ $p_{\mathrm{T}} > 0.9$ GeV;
- $p_{\mathrm{T}} > 1.0$ GeV $\rightarrow$ $p_{\mathrm{T}} > 1.1$ GeV;
- number of pixel hits $\geq 2 \rightarrow$ number of pixel hits ≥ 1;
- number of pixel hits + number of SCT hits $\geq 7 \rightarrow$ number of pixel hits + number of SCT hits ≥ 8;
- $|z_0 sin\theta| < 1.5mm \rightarrow |z_0 sin\theta| > 1.5mm$.

Especially, by inverting the $|z_0 sin\theta|$ cut, we can select a sample of pileup or fake tracks. Using the isolation cone instead of k_T-like matching, we can derive the density of these tracks and extrapolate to the core cone, giving us an estimation of the pileup contribution. There are at least four effects we have to consider when computing uncertainty on track counting:

(1) detector modeling;
(2) track losses due to hadronic interactions;
(3) underline event;
(4) pileup events.

Source (2) cannot be checked in this method. So we just considered the other 3 effects using the average number of tracks per event (Na(track)).

4.4 Uncertainty of track counting

The uncertainty of track counting can be estimated using data/MC ratio of average track number in each eta region. The results of the uncertainty of all track categories are shown in Table 4.1, Table 4.2, Table 4.3 and Table 4.4.

For inner track, the Na(track) distribution of date/MC comparison is shown in Fig. 4.14. The data/MC ratio shows an underestimation of pileup in the MC simulation.

4.5 Pileup density

Figure. 4.15 shows the outer track distribution from pileup events by inverting the $|z0 sin\theta|$ cut. The peak of the full spectrum of the $|z0 sin\theta|$ distribution at 0 is due to the tracks

Table 4.1: The Na(track) distribution of data, MC and data/MC ratio for inner track category under 7 different cuts.

	$\|\eta\| < 1.05$	$1.05 < \|\eta\| < 1.30$	$1.30 < \|\eta\| < 2.00$	$\|\eta\| > 2.00$
		data		
baseline	0.052 ± 0.0003	0.053 ± 0.0007	0.053 ± 0.0004	0.056 ± 0.0007
$p_T > 0.5GeV$	0.124 ± 0.0005	0.126 ± 0.0012	0.126 ± 0.0007	0.134 ± 0.0012
$p_T > 0.9GeV$	0.061 ± 0.0003	0.062 ± 0.0008	0.062 ± 0.0005	0.066 ± 0.0008
$p_T > 1.1GeV$	0.044 ± 0.0003	0.045 ± 0.0007	0.045 ± 0.0004	0.048 ± 0.0006
1 pixel hit	0.053 ± 0.0003	0.054 ± 0.0007	0.054 ± 0.0004	0.057 ± 0.0007
$SCT + pixel \geq 8$	0.051 ± 0.0003	0.052 ± 0.0007	0.052 ± 0.0004	0.055 ± 0.0007
inverted $\|z_0 sin\theta\|$	0.219 ± 0.0008	0.211 ± 0.0017	0.191 ± 0.0009	0.169 ± 0.0013
		MC		
baseline	0.050 ± 0.001 ± 0.001	0.048 ±0.001 ±0.001	0.050 ±0.001 ±0.001	0.051 ±0.00 ±0.001
$p_T > 0.5GeV$	0.124 ± 0.001 ± 0.001	0.123 ±0.001 ±0.001	0.123 ±0.001 ±0.001	0.125 ±0.00 ±0.001
$p_T > 0.9GeV$	0.060 ± 0.001 ± 0.001	0.058 ±0.001 ±0.001	0.059 ±0.001 ±0.001	0.060 ±0.00 ±0.001
$p_T > 1.1GeV$	0.043 ± 0.001 ± 0.001	0.041 ±0.001 ±0.001	0.042 ±0.001 ±0.001	0.043 ±0.00 ±0.001
1 pixel hit	0.052 ± 0.001 ± 0.001	0.049 ±0.001 ±0.001	0.050 ±0.001 ±0.001	0.051 ±0.00 ±0.001
$SCT + pixel \geq 8$	0.050 ± 0.001 ± 0.001	0.047 ±0.001 ±0.001	0.049 ±0.001 ±0.001	0.050 ±0.00 ±0.001
inverted $\|z_0 sin\theta\|$	0.195 ± 0.001 ± 0.001	0.185 ±0.001 ±0.001	0.174 ±0.001 ±0.001	0.157 ±0.00 ±0.001
		ratio		
baseline	1.026 ±0.010 ±0.006	1.093 ±0.023 ±0.008	1.062 ±0.014 ±0.006	1.105 ±0.022 ±0.008
$p_T > 0.5GeV$	0.999 ±0.006 ±0.003	1.019 ±0.014 ±0.004	1.030 ±0.009 ±0.003	1.072 ±0.014 ±0.003
$p_T > 0.9GeV$	1.017 ±0.009 ±0.005	1.077 ±0.021 ±0.007	1.057 ±0.013 ±0.006	1.101 ±0.020 ±0.007
$p_T > 1.1GeV$	1.027 ±0.010 ±0.007	1.093 ±0.025 ±0.009	1.071 ±0.015 ±0.007	1.104 ±0.023 ±0.009
1 pixel hit	1.032 ±0.009 ±0.006	1.100 ±0.023 ±0.008	1.068 ±0.014 ±0.007	1.105 ±0.021 ±0.009
$SCT + pixel \geq 8$	1.026 ±0.006 ±0.004	1.137 ±0.014 ±0.004	1.095 ±0.008 ±0.002	1.082 ±0.013 ±0.003
inverted $\|z_0 sin\theta\|$	1.025 ±0.009 ±0.006	1.086 ±0.023 ±0.007	1.060 ±0.014 ±0.006	1.109 ±0.022 ±0.009

from the hard scattering, while the long tail due to pile up degradation at large $|z0sin\theta|$ is correlated to the beam spot size. The plot of $|z0sin\theta|$ is in the range up to 6 mm. (4 bins: 0-1.5, 1.5-3.0, 3.0-4.5, 4.5-6.0 mm should be reasonable) We computed the number of track with the selection $1.5mm < |z0sin\theta| < 6.0mm$ and estimate the number of pile up tracks pouring in the $|z0sin\theta| < 1.5mm$ selection as 1/3 of the number of tracks in the region $1.5mm < |z0sin\theta| < 6.0mm$. Results of the pileup density are shown in table. 4.5 and 4.6.

Tag-and-probe method from $Z \rightarrow \mu\mu$ events has been performed to check how well the track counting is modelled. In the kT-style track counting method, the additional underlying and pileup tracks fitting into the cone is considered since muon track are not affected by track losses due to hadronic interactions, which is the main source of pion inefficiency. There is significant (50%) discrepancy in the zero track bin if too tight track selection is required with b-layer hit, while, the overall effect is small. The systematic uncertainties on the track modeling, pt spectrum and pileup have been studied and shown as a function of pseudorapidity regions. The effect from the hit contents is negligible(< 1%), so the hit distribution is reasonably modeled. There is a good description of the overall amount of tracks in the core and isolation cones.

Table 4.2: The Na(track) distribution of data, MC and data/MC ratio for middle track category under 7 different cuts.

	$\|\eta\| < 1.05$	$1.05 < \|\eta\| < 1.30$	$1.30 < \|\eta\| < 2.00$	$\|\eta\| > 2.00$
		data		
baseline	0.371 ± 0.001	0.373 ± 0.002	0.373 ± 0.001	0.351 ± 0.002
$p_T > 0.5GeV$	0.184 ± 0.001	0.183 ± 0.001	0.182 ± 0.001	0.167 ± 0.001
$p_T > 0.9GeV$	0.134 ± 0.001	0.132 ± 0.001	0.132 ± 0.001	0.119 ± 0.001
$p_T > 1.1GeV$	0.156 ± 0.001	0.155 ± 0.001	0.154 ± 0.001	0.141 ± 0.001
1 pixel hit	0.380 ± 0.001	0.377 ± 0.002	0.376 ± 0.001	0.353 ± 0.002
$SCT + pixel \geq 8$	0.366 ± 0.001	0.365 ± 0.002	0.366 ± 0.001	0.343 ± 0.002
inverted $\|z_0 sin\theta\|$	1.956 ± 0.004	1.896 ± 0.009	1.747 ± 0.006	1.413 ± 0.007
		MC		
baseline	0.382 ± 0.001 ± 0.001	0.375 ± 0.002 ± 0.001	0.374 ± 0.002 ± 0.001	0.332 ± 0.002 ± 0.001
$p_T > 0.5GeV$	0.187 ± 0.000 ± 0.001	0.180 ± 0.001 ± 0.001	0.181 ± 0.001 ± 0.001	0.157 ± 0.001 ± 0.001
$p_T > 0.9GeV$	0.135 ± 0.000 ± 0.001	0.129 ± 0.001 ± 0.001	0.130 ± 0.001 ± 0.001	0.112 ± 0.001 ± 0.001
$p_T > 1.1GeV$	0.158 ± 0.000 ± 0.001	0.152 ± 0.001 ± 0.001	0.153 ± 0.001 ± 0.001	0.133 ± 0.001 ± 0.001
1 pixel hit	0.388 ± 0.001 ± 0.001	0.378 ± 0.002 ± 0.001	0.376 ± 0.001 ± 0.001	0.333 ± 0.002 ± 0.001
$SCT + pixel \geq 8$	0.377 ± 0.001 ± 0.001	0.368 ± 0.002 ± 0.001	0.368 ± 0.001 ± 0.001	0.323 ± 0.002 ± 0.001
inverted $\|z_0 sin\theta\|$	1.891 ± 0.004 ± 0.002	1.830 ± 0.009 ± 0.003	1.706 ± 0.005 ± 0.002	1.377 ± 0.006 ± 0.001
		ratio		
baseline	0.972 ± 0.004 ± 0.002	0.993 ± 0.009 ± 0.003	0.996 ± 0.006 ± 0.002	1.058 ± 0.010 ± 0.002
$p_T > 0.5GeV$	0.983 ± 0.005 ± 0.004	1.012 ± 0.013 ± 0.005	1.002 ± 0.007 ± 0.004	1.059 ± 0.013 ± 0.004
$p_T > 0.9GeV$	0.989 ± 0.006 ± 0.005	1.017 ± 0.014 ± 0.006	1.010 ± 0.009 ± 0.004	1.062 ± 0.015 ± 0.005
$p_T > 1.1GeV$	0.987 ± 0.006 ± 0.004	1.016 ± 0.013 ± 0.006	1.006 ± 0.008 ± 0.004	1.059 ± 0.014 ± 0.004
1 pixel hit	0.978 ± 0.004 ± 0.002	0.996 ± 0.010 ± 0.004	1.000 ± 0.006 ± 0.002	1.060 ± 0.010 ± 0.002
$SCT + pixel \geq 8$	0.972 ± 0.004 ± 0.002	0.991 ± 0.010 ± 0.003	0.995 ± 0.006 ± 0.002	1.061 ± 0.010 ± 0.003
inverted $\|z_0 sin\theta\|$	1.034 ± 0.003 ± 0.001	1.036 ± 0.008 ± 0.002	1.024 ± 0.005 ± 0.001	1.027 ± 0.007 ± 0.001

Table 4.3: The Na(track) distribution of data, MC and data/MC ratio for outer track category under 7 different cuts.

	$\|\eta\| < 1.05$	$1.05 < \|\eta\| < 1.30$	$1.30 < \|\eta\| < 2.00$	$\|\eta\| > 2.00$
		data		
baseline	0.486 ± 0.002	0.487 ± 0.004	0.457 ± 0.002	0.326 ± 0.003
$p_T > 0.5GeV$	0.482 ± 0.002	0.483 ± 0.004	0.454 ± 0.002	0.321 ± 0.003
$p_T > 0.9GeV$	0.485 ± 0.002	0.485 ± 0.004	0.456 ± 0.002	0.324 ± 0.003
$p_T > 1.1GeV$	0.487 ± 0.002	0.488 ± 0.004	0.458 ± 0.002	0.327 ± 0.003
1 pixel hit	0.510 ± 0.002	0.498 ± 0.004	0.465 ± 0.002	0.329 ± 0.003
$SCT + pixel \geq 8$	0.479 ± 0.002	0.477 ± 0.004	0.448 ± 0.002	0.318 ± 0.003
inverted $\|z_0 sin\theta\|$	0.374 ± 0.002	0.346 ± 0.004	0.283 ± 0.002	0.181 ± 0.003
		MC		
baseline	0.506 ± 0.002 ± 0.001	0.494 ± 0.004 ± 0.002	0.468 ± 0.002 ± 0.001	0.327 ± 0.003 ± 0.001
$p_T > 0.5GeV$	0.504 ± 0.002 ± 0.001	0.488 ± 0.004 ± 0.002	0.466 ± 0.002 ± 0.001	0.321 ± 0.003 ± 0.001
$p_T > 0.9GeV$	0.505 ± 0.002 ± 0.001	0.492 ± 0.004 ± 0.002	0.467 ± 0.002 ± 0.001	0.326 ± 0.003 ± 0.001
$p_T > 1.1GeV$	0.507 ± 0.002 ± 0.002	0.495 ± 0.004 ± 0.002	0.469 ± 0.002 ± 0.001	0.329 ± 0.003 ± 0.001
1 pixel hit	0.524 ± 0.002 ± 0.002	0.503 ± 0.004 ± 0.002	0.473 ± 0.002 ± 0.001	0.330 ± 0.003 ± 0.001
$SCT + pixel \geq 8$	0.500 ± 0.002 ± 0.002	0.484 ± 0.004 ± 0.002	0.460 ± 0.002 ± 0.002	0.320 ± 0.003 ± 0.001
inverted $\|z_0 sin\theta\|$	0.328 ± 0.002 ± 0.001	0.303 ± 0.004 ± 0.001	0.258 ± 0.002 ± 0.001	0.178 ± 0.002 ± 0.001
		ratio		
baseline	0.959 ± 0.004 ± 0.003	0.986 ± 0.010 ± 0.004	0.976 ± 0.007 ± 0.003	0.99 ± 0.012 ± 0.003
$p_T > 0.5GeV$	0.956 ± 0.004 ± 0.003	0.990 ± 0.010 ± 0.004	0.975 ± 0.007 ± 0.003	1.00 ± 0.012 ± 0.003
$p_T > 0.9GeV$	0.958 ± 0.004 ± 0.003	0.986 ± 0.010 ± 0.004	0.975 ± 0.007 ± 0.003	0.99 ± 0.012 ± 0.003
$p_T > 1.1GeV$	0.959 ± 0.004 ± 0.003	0.985 ± 0.010 ± 0.004	0.976 ± 0.007 ± 0.003	0.99 ± 0.012 ± 0.003
1 pixel hit	0.972 ± 0.005 ± 0.003	0.990 ± 0.010 ± 0.004	0.984 ± 0.007 ± 0.003	0.99 ± 0.012 ± 0.003
$SCT + pixel \geq 8$	0.958 ± 0.004 ± 0.004	0.985 ± 0.010 ± 0.004	0.973 ± 0.007 ± 0.004	0.99 ± 0.012 ± 0.004
inverted $\|z_0 sin\theta\|$	1.141 ± 0.009 ± 0.005	1.143 ± 0.021 ± 0.005	1.097 ± 0.014 ± 0.003	1.07 ± 0.023 ± 0.004

Table 4.4: The Na(track) distribution of data, MC and data/MC ratio for muon track category under 7 different cuts.

	$\|\eta\| < 1.05$	$1.05 < \|\eta\| < 1.30$	$1.30 < \|\eta\| < 2.00$	$\|\eta\| > 2.00$
		data		
baseline	0.976 ± 0.002	0.988 ± 0.004	0.991 ± 0.003	0.997 ± 0.004
$p_T > 0.5GeV$	0.976 ± 0.002	0.988 ± 0.004	0.991 ± 0.003	0.997 ± 0.004
$p_T > 0.9GeV$	0.976 ± 0.002	0.988 ± 0.004	0.991 ± 0.003	0.997 ± 0.004
$p_T > 1.1GeV$	0.976 ± 0.002	0.988 ± 0.004	0.991 ± 0.003	0.997 ± 0.004
1 pixel hit	1.000 ± 0.002	1.000 ± 0.004	1.000 ± 0.003	1.000 ± 0.004
$SCT + pixel \geq 8$	0.975 ± 0.002	0.986 ± 0.004	0.990 ± 0.003	0.997 ± 0.004
		MC		
baseline	0.983 ± 0.002 ± 0.001	0.992 ± 0.004 ± 0.001	0.996 ± 0.003 ± 0.001	0.997 ± 0.004 ± 0.001
$p_T > 0.5GeV$	0.983 ± 0.002 ± 0.001	0.992 ± 0.004 ± 0.001	0.996 ± 0.003 ± 0.001	0.997 ± 0.004 ± 0.001
$p_T > 0.9GeV$	0.983 ± 0.002 ± 0.001	0.992 ± 0.004 ± 0.001	0.996 ± 0.003 ± 0.001	0.997 ± 0.004 ± 0.001
$p_T > 1.1GeV$	0.983 ± 0.002 ± 0.001	0.992 ± 0.004 ± 0.001	0.996 ± 0.003 ± 0.001	0.997 ± 0.004 ± 0.001
1 pixel hit	1.000 ± 0.002 ± 0.001	1.000 ± 0.004 ± 0.001	1.000 ± 0.003 ± 0.001	1.000 ± 0.004 ± 0.001
$SCT + pixel \geq 8$	0.982 ± 0.002 ± 0.001	0.989 ± 0.004 ± 0.001	0.995 ± 0.003 ± 0.001	0.997 ± 0.004 ± 0.001
		ratio		
baseline	0.993 ± 0.003 ± 0.001	0.996 ± 0.006 ± 0.001	0.995 ± 0.004 ± 0.001	1.000 ± 0.006 ± 0.001
$p_T > 0.5GeV$	0.993 ± 0.003 ± 0.001	0.996 ± 0.006 ± 0.001	0.995 ± 0.004 ± 0.001	1.000 ± 0.006 ± 0.001
$p_T > 0.9GeV$	0.993 ± 0.003 ± 0.001	0.996 ± 0.006 ± 0.001	0.995 ± 0.004 ± 0.001	1.000 ± 0.006 ± 0.001
$p_T > 1.1GeV$	0.993 ± 0.003 ± 0.001	0.996 ± 0.006 ± 0.001	0.995 ± 0.004 ± 0.001	1.000 ± 0.006 ± 0.001
1 pixel hit	1.000 ± 0.003 ± 0.001	1.000 ± 0.006 ± 0.001	1.000 ± 0.004 ± 0.001	1.000 ± 0.006 ± 0.001
$SCT + pixel \geq 8$	0.993 ± 0.003 ± 0.001	0.996 ± 0.006 ± 0.001	0.995 ± 0.004 ± 0.001	1.000 ± 0.006 ± 0.001

Table 4.5: The number of pileup tracks per event pouring into the track selection in 2012 data.

	$\|\eta\| < 1.05$	$1.0 < \|\eta\| < 1.30$	$1.30 < \|\eta\| < 2.00$	$\|\eta\| > 2.00$
inner track / 10^{-3}	7.12 ± 0.12	2.18 ± 0.06	7.95 ± 0.12	5.17 ± 0.10
middle track / 10^{-3}	22.06 ± 0.21	6.45 ± 0.11	23.90 ± 0.22	13.58 ± 0.16
outer track / 10^{-3}	59.74 ± 0.35	17.41 ± 0.18	65.09 ± 0.37	31.41 ± 0.25

Table 4.6: The number of pileup tracks per event pouring into the track selection in MC. Both statistic and systematic uncertainty are shown.

	$\|\eta\| < 1.05$	$1.0 < \|\eta\| < 1.30$	$1.30 < \|\eta\| < 2.00$	$\|\eta\| > 2.00$
inner track / 10^{-3}	5.74 ± 0.07 ± 0.08	1.77 ± 0.03 ± 0.02	6.73 ± 0.08 ± 0.07	4.66 ± 0.06 ± 0.03
middle track / 10^{-3}	17.71 ± 0.13 ± 0.21	5.38 ± 0.07 ± 0.08	20.56 ± 0.14 ± 0.18	12.19 ± 0.10 ± 0.09
outer track / 10^{-3}	48.52 ± 0.21 ± 0.66	14.49 ± 0.11 ± 0.21	55.76 ± 0.23 ± 0.46	28.21 ± 0.15 ± 0.20

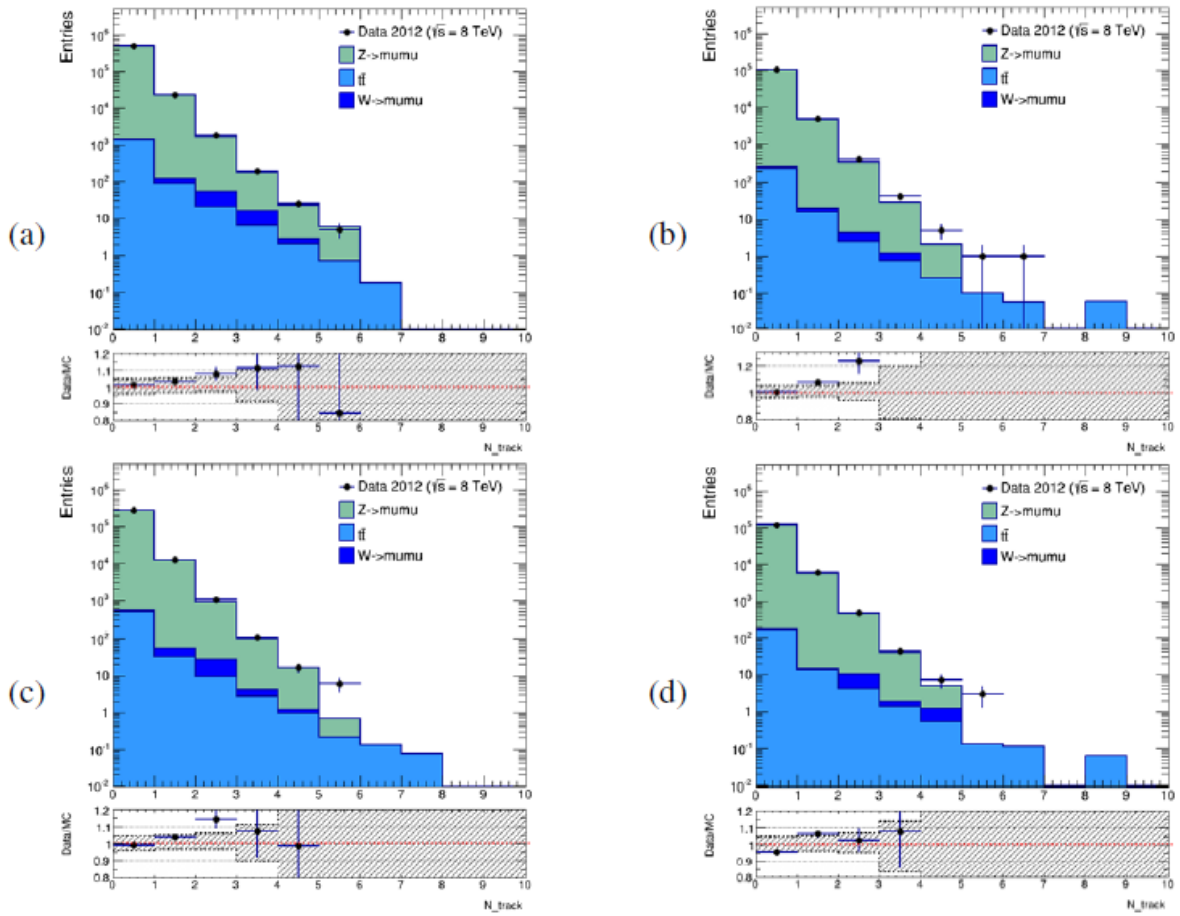

Figure 4.10: Number of inner track distribution, counting under baseline selection and: $|\eta| < 1.05$ (a), $1.05 < |\eta| < 1.30$ (b), $1.30 < |\eta| < 2.00$ (c), $|\eta| > 2.00$ (d).

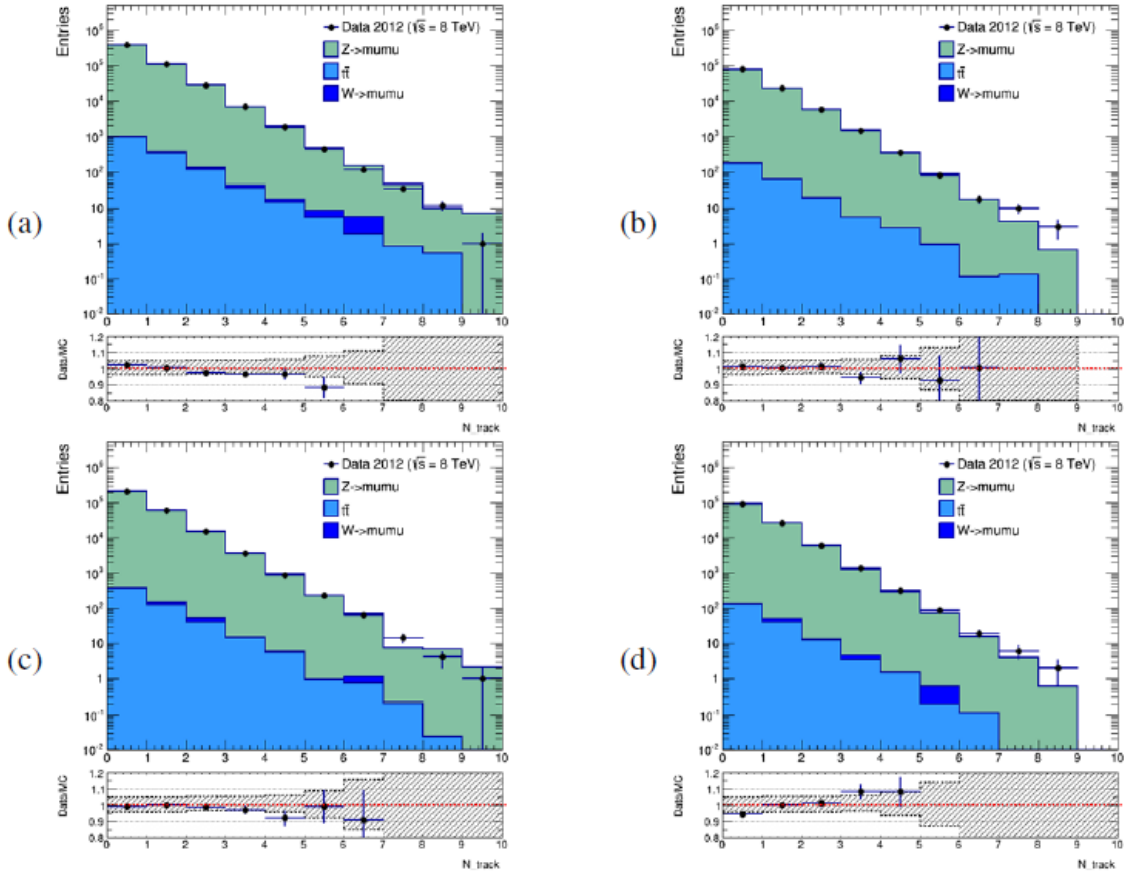

Figure 4.11: Number of middle track distribution, counted under baseline selection and: $|\eta| < 1.05$ (a), $1.05 < |\eta| < 1.30$ (b), $1.30 < |\eta| < 2.00$ (c), $|\eta| > 2.00$ (d). The data/MC ratio is within 1.10.

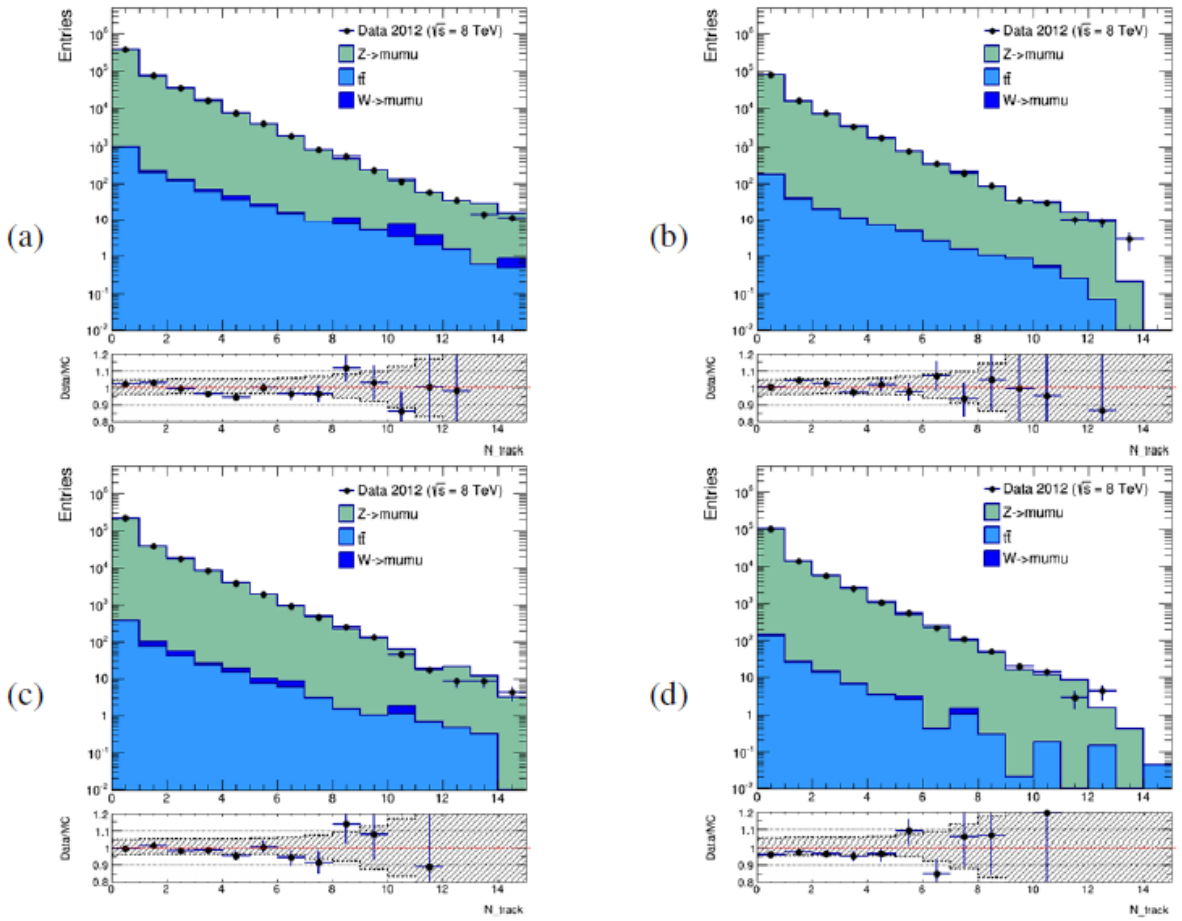

Figure 4.12: Number of outer track distribution, counted under baseline selection and: $|\eta| < 1.05$ (a), $1.05 < |\eta| < 1.30$ (b), $1.30 < |\eta| < 2.00$ (c), $|\eta| > 2.00$ (d).

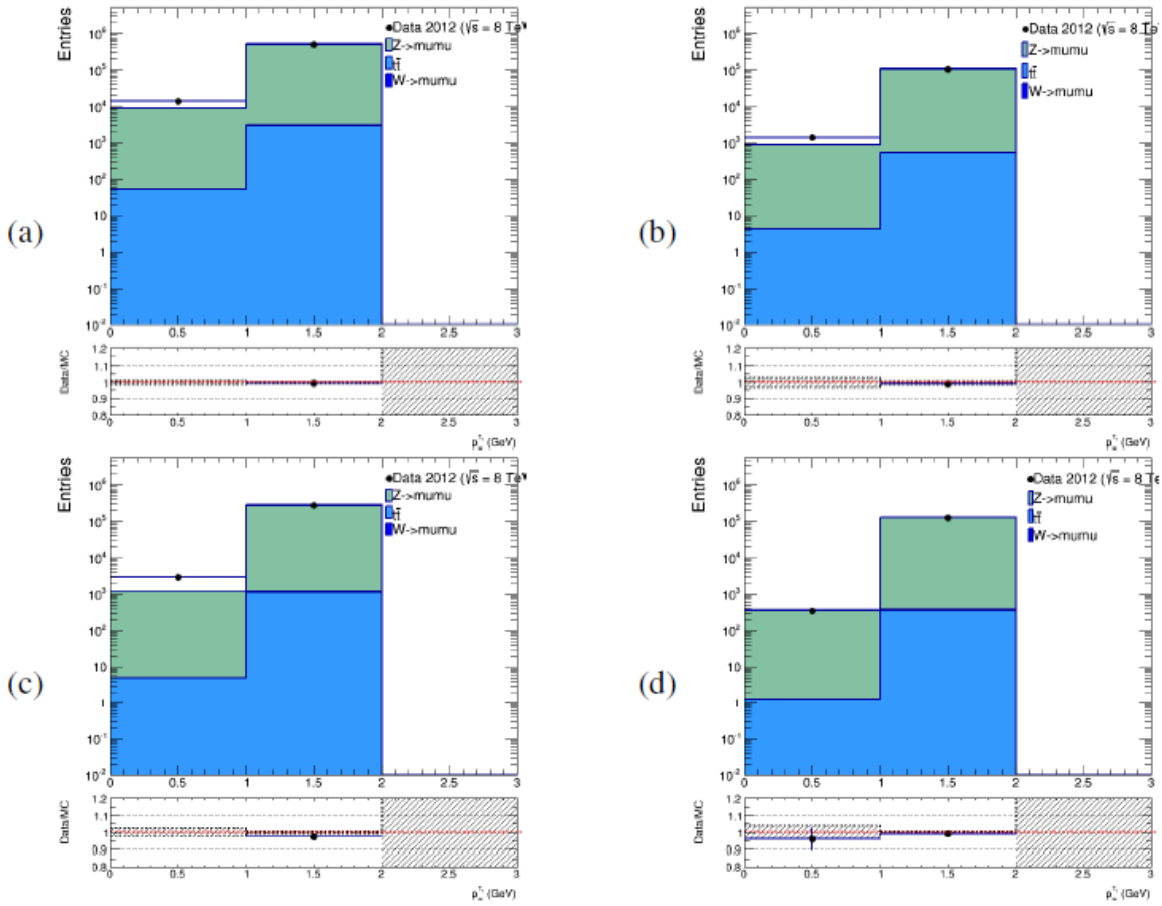

Figure 4.13: Number of muon track distribution, counted under baseline selection and: $|\eta| < 1.05$ (a), $1.05 < |\eta| < 1.30$ (b), $1.30 < |\eta| < 2.00$ (c), $|\eta| > 2.00$ (d).

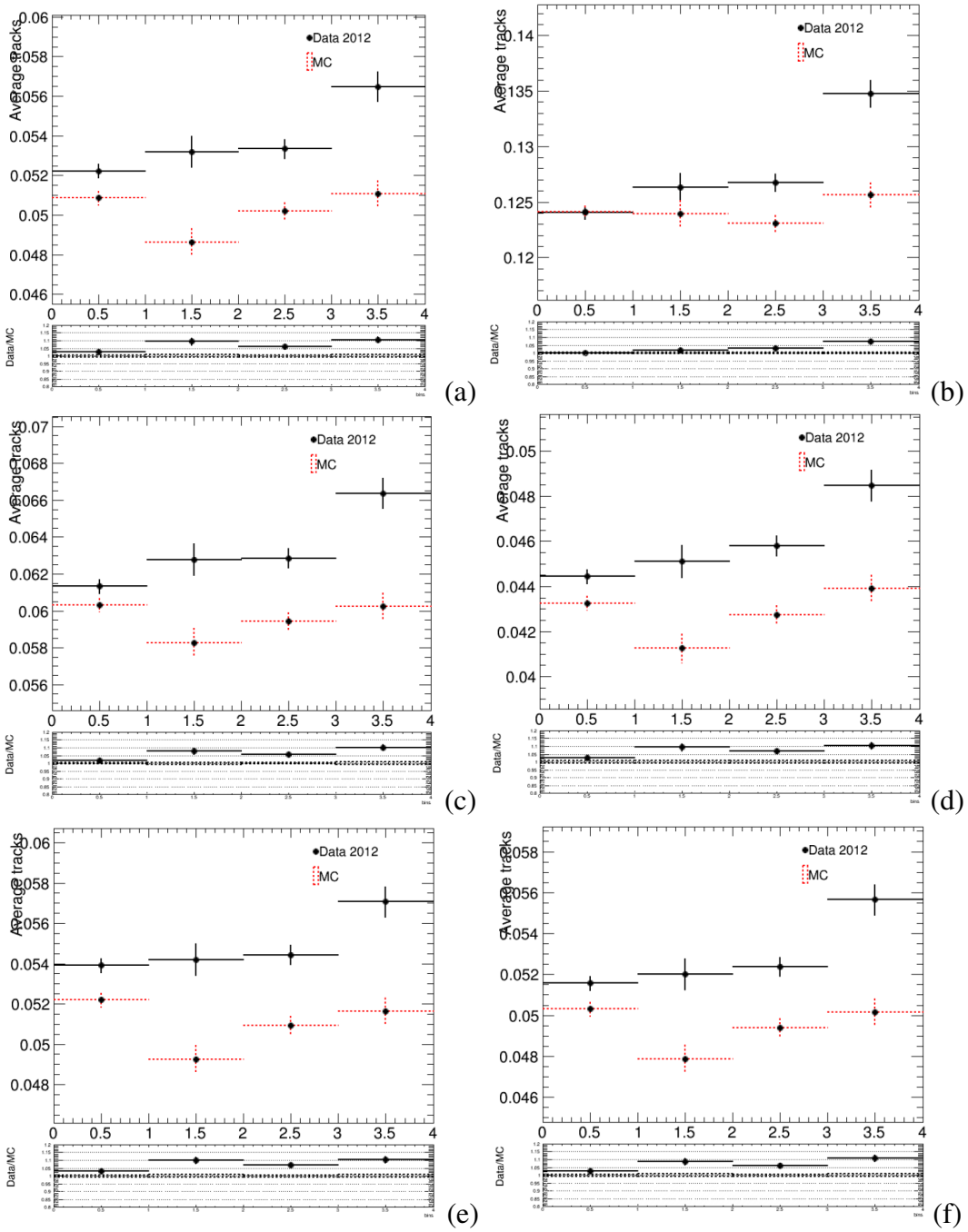

Figure 4.14: Na(track) of inner track, counted under varied selection: baseline cut (a), $p_T cut < 0.5 GeV$ (b), $p_T cut < 0.9 GeV$ (c), $p_T cut < 1.1 GeV$ (d), varied pixel cut (e), varied SCT+pixel hits (f), inverted $|z0 sin\theta$ cut (g).

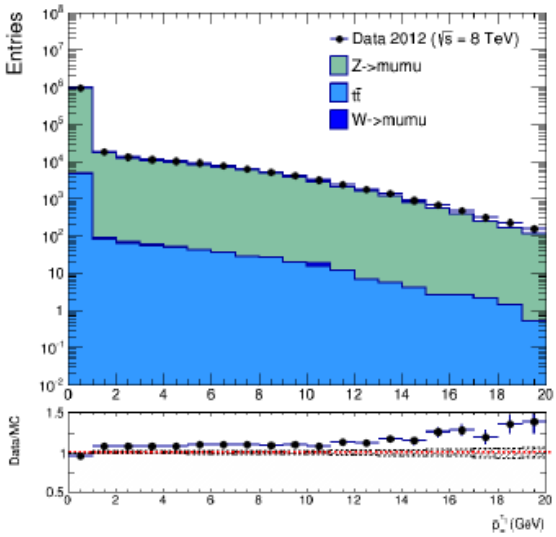

Figure 4.15: Outer track distribution under the inverted $|z0sin\theta|$ cut.

Chapter 5

Search for supersymmetry in final states with two opposite-sign taus

5.1 Introduction

The following section presents the search for electroweak producted SUSY particles with 2 opposite-sign taus in the final state. From a theoretical point of view, if the coloured sparticles (squarks and gluinos) are heavy, and weakinos are light, first sign of SUSY at the LHC can be spotted in events with high lepton multiplicity and low jet activity, such as decays of the electroweakinos (charginos and neutralinos) and the sleptons. This situation can be realized in the framework of the phenomenological Minimal Supersymmetric Standard Model(MSSM), the pMSSM, as described in Section 1.2.3.1. In this search, light stau model is focused on the case in which the charginos and neutralinos decay with 100% BR to final states containing tau leptons.

The electro-weakino decay properties highly depend on the electro-weakino masses, as well as the MSSM parameters M_1, M_2, $tan\beta$ and μ in the neutralino and chargino mixing-matrices. The results of this search are using 2012 data of $20.3 fb^{-1}$ and interpreted in two pMSSM-based grids with low M_1 and large $tan\beta = 50$. In these grids, the stau production is enhanced. The processes yielding two or more taus in the final state are mainly production in the context of direct electro-weakino production [85].

5.2 Signal Monte Carlo Samples

The main processes of interest in this grid are: chargino-chargino(C1C1), neutralino-chargino(C1N2) and stau pair production.

5.2.1 The Simplified Models

The search firstly considers simplified model with the direct electro-weakino production leading to at least two leptons in the final state:

- Model A, $\tilde{\chi}_1^{\pm}\tilde{\chi}_2^0$ production;

- Model C, $\tilde{\chi}_1^{\pm}\tilde{\chi}_1^{\pm}$ production.

In these productions, the only free parameters are the masses of: $\tilde{\chi}_1^0$, $\tilde{\chi}_1^{\pm}$, $\tilde{\chi}_2^0$, $\tilde{\nu}$ and $\tilde{l}$. We consider simplified models with intermediate sleptons/sneutrinos. All sparticles other than $\tilde{\chi}_1^0$, $\tilde{\chi}_1^{\pm}$, $\tilde{\chi}_2^0$, left-handed stau and tau sneutrino assumed to be "heavy" O(100 TeV). In this analysis, only stau ($\tilde{\tau}$) correlated scenarios are studied. As a result in these models charginos/neutralinos decay to tau leptons only. The $\tilde{\chi}_1^0$ and $\tilde{\chi}_1^{\pm}$ are assumed to be pure wino. Stau and tau sneutrino are degenerate in assumption, resulting large mass splitting between $\tilde{\chi}_1^0$ and $\tilde{\chi}_1^{\pm}$. Therefore $\tilde{\chi}_1^0$ and $\tilde{\chi}_1^{\pm}$ are also assumed to be mass-degenerate without too much loss of generality. The $\tilde{\chi}_1^{\pm}$ mass is varied between 100 GeV and 500 GeV, whereas the $\tilde{\chi}_1^{\pm}$ mass is varied between 0 and 350 GeV [86].

5.2.2 The pMSSM model for direct electro-weakino production

The interpretation of the results of this analysis also uses two signal grids based on the pMSSM framework. For both grids, squarks and gluinos are heavy (input masses are set to 3 TeV) and $tan\beta = 50$. The criteria enhance stau production. The first grid implemented is produced with fixed stau mass and the following parameters:

- $M_1 = 50GeV$;
- $m_A = 1TeV$;
- $m_h = 123.1GeV$ (maximal stop mixing);
- M_2 and μ are varied between 100 to 500 GeV;
- The mass of the lighter stau, the right-handed, is fixed to 95GeV, while the other sleptons are heavy;
- The LSP is mostly bino.

The second grid, implemented in SUSPECT, is produced with varies stau mass and defined with the following parameters:

- $M_1 = 72GeV$;
- $m_A = 2TeV$;
- $m_h = 125.5GeV$ (stop mixing fixed to higgs mass);
- M_2 and μ are varied between 100 to 600 GeV;
- The lightest stau, fully right-handed, is placed midway between $\tilde{\chi}_1^0$ and $\tilde{\chi}_2^0$ mass, while the other sleptons are heavy;
- The LSP is mostly bino.

In this grid, direct electro-weakino production always dominates over direct stau production.

5.2.3 Direct Stau Production

The direct stau grid is derived from a pMSSM model with very high squark and gluino masses so that they are decoupled from the phenomenology under study. The masses of all electro-weakinos apart from the $\tilde{\chi}_1^0$, are set to 2.5 TeV, thus leaving a single kinematically allowed decay: $\tilde{\tau}^{\pm} \rightarrow \tilde{\chi}_1^0\tau^{\pm}$. The left-handed and right-handed staus have the same mass

varying between 80 and 300 GeV. The mass of the bino-like $\tilde{\chi}_1^0$ is in the range 0-200 GeV [87, 88, 89, 90, 91]. All the feynman diagrams of the interested models are shown on Fig. 5.1.

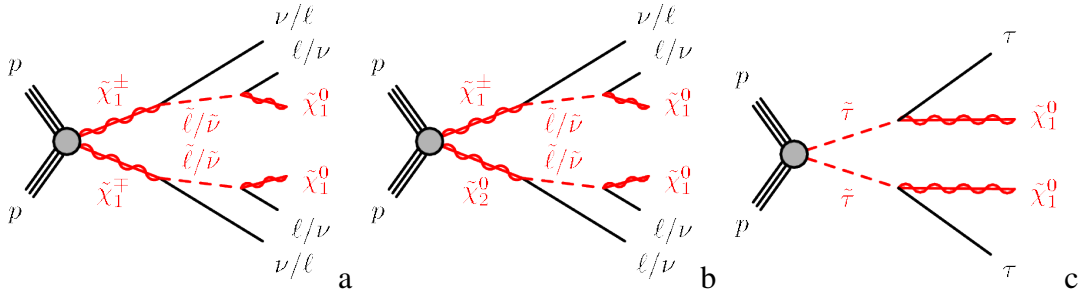

Figure 5.1: Feynman diagrams for $\tilde{\chi}_1^+\tilde{\chi}_1^-$(left) and $\tilde{\chi}_1^\pm\tilde{\chi}_2^0$(middle) decays with intermediate light left-handed charged tau sleptons and sneutrinos, direct-stau(right) decay are also shown.

5.3 Object selection

This section presents the definitions of the objects used in the analysis including jets, electrons, muons, taus and $E_{\mathrm{T}}^{\mathrm{miss}}$. Events are selected with at least two hadronic decaying taus in the final state, with at least one opposite-sign pair. Events are rejected if satisfying either of the following criteria:

- containing additional electrons or muons (e-μ veto);
- containing a jet failing the jet quality criteria;
- containing a primary vertex of less than 5 associated tracks;
- containing either cosmic or "bad" muon.

Two set of object selection criteria are used in this analysis, which is "baseline" and "signal" respectively. Baseline objects are input to the overlap removal procedure. Signal objects are those baseline ones passing the overlap removal with more stringent requirements. For jets, electrons, muons and taus, the object selection has been standardized between this analysis and the SUSY electro-weak production analyses with two light leptons, three and four leptons. All applied object definitions are consistent with SUSYTools-00-03-04 and recommendations from the combined performance groups for Release 17.2 data.

5.3.1 Jets

The jet selection is summarized in Table 5.1. Jets are reconstructed using the anti-k_t jet algorithm with the distance parameter δR set to 0.4 and topological clusters as input. Baseline jets are required to have $p_T > 20GeV$. Any jet overlapping with either electrons or taus within $\delta R < 0.2$ is rejected. Additionally, baseline jets need to pass a loose quality selection (JetID::VeryLooseBad) aiming at rejecting jets which are not associated with real

Table 5.1: The summary of baseline and signal jet selections.

Jets				
	Baseline	Signal		
		L30	B20	F30
Cut	Value/Description	Value/Description		
algorithm	anti-kt(R=0.4)	anti-kt(R=0.4)		
p_T	$p_T > 20GeV$	$> 30GeV$	$> 20GeV$	$> 30GeV$
η	-	$\lvert\eta_{det}\rvert < 2.4$	$\lvert\eta_{det}\rvert < 2.4$	$\lvert\eta_{det}\rvert > 2.4$ $\lvert\eta_{det}\rvert < 4.5$
JVF	-	$\lvert JVF\rvert > 0$ if $p_T < 50GeV$	-	-
b-tag	-	$MV1 < 0.3511$	$MV1 > 0.3511$	-

energy deposits in the calorimeter, such as non-collision background events, cosmic-ray showers and calorimeter noise. No cut is applied on $|\eta|$ for baseline jets.

Additional requirements are placed on the jets, depending on the signal or control region considered. For light central jets a $|JVF| > 0$ is required if $p_T < 50GeV$. B-Jets are required to satisfy the 80% working point of the MV1 algorithm, $MV1 > 0.3511$. Since JVF and b-tagging can only be computed for $|\eta| < 2.4$ due to tracking coverage of the detector, a separate category of jets is defined for the forward region. The definition relies only on the p_T threshold to suppress the contribution from pileup jets.

5.3.2 Taus

The tau reconstruction algorithm is seeded by jets reconstructed with the anti-kt algorithm with a distance parameter $R = 0.4$, considering only jets with $p_t > 10GeV$ and $|\eta| < 2.5$. In the reconstruction procedure, taus are associated to a primary vertex via a dedicated algorithm - Tau Jet Vertex Association (TJVA). The reconstructed energy of the hadronic taus is corrected to the tau energy scale which is calibrated independently of the jet energy scale by a Monte Carlo based procedure . Baseline taus are required to have $p_T > 20GeV$, $|\eta| < 2.47$, and leading track $\eta_{|leadTrack|} < 2.47$, as well as 1 or 3 tracks with the sum of charge equal to $+1$ or -1. Multivariate identification algorithms are available for an improved discrimination between hadronic decaying taus and jets and electrons. The tau identification used in this analysis is based on the Boosted Decision Tree (BDT) method. Baseline taus are required to pass the "medium" selection criteria for the jet discrimination and the "loose" selection criteria for the electron discrimination. Fake tau candidates from jets are thus rejected, while keeping a signal efficiency of 60% (55%) for 1-prong (3-prong) tau candidates for the jet BDT discrimination. Also, the rejection factor of electron fakes is around $10-50$ in different η range, keeping a signal efficiency of 95% for the electron BDT discrimination. Here, the electron BDT discrimination is applied only to 1-prong taus[92].

In addition, a cut-based muon veto is applied to remove tau candidates which comes from anomalous energy deposits in the calorimeter. Over 96% signal efficiency is obtained

by the muon veto, with a 40% reduction of muon fakes. Taus are selected as loose ones after overlap removal procedure and passing only the "loose" jet and electron BDTs. Signal taus are required to pass the "tight" BDT identification additionally. The selection criteria for baseline and signal taus are summarized in the first sub-table of Table 5.2.

5.3.3 Electrons

Electrons are reconstructed starting from electromagnetic clusters and matching to tracks from the inner detector. Information (η and ϕ) from both electromagnetic cluster and the track are used. Baseline electrons are required to pass the "medium++" identification criteria with $p_T > 10GeV$ and $|\eta| < 2.47$. Those electrons surviving after overlap removal with other electrons, jets, muons and taus are used to veto events with any light lepton. Signal electrons are a subset of baseline electrons, passing some additional requirements which is also listed in the second sub-table of Table 5.2.

5.3.4 Muons

Muons are reconstructed using the STACO algorithm. Two types of muons are considered in the analysis as discussed in the muon reconstruction section:

- **"Combine"** muons - reconstructed from tracks that have been independently reconstructed both in the muon system and in the inner detector;
- **"segment-tagged"**muons - using the muon system to tag inner tracks as muons, without requiring a fully reconstructed track in the muon system.

For baseline muons, requirements on the number of hits in pixel, SCT and TRT detectors are applied, as well as kinematic cuts of $p_T > 10GeV$ and $|\eta| < 2.5$. The same as electrons, baseline muons which pass the overlap removal are used to do the light lepton veto. The selection criteria of both baseline and signal muons are also listed in the third sub-table of table 5.2.

5.3.5 MET

The missing transverse energy (E_T^{miss}) is reconstructed using the calibrated electron, muon and jet objects, as well as baseline photons according to SUSYTools $E_{\mathrm{T}}^{\mathrm{miss}}$ definitions. To be more specific, the E_T^{miss} reconstruction algorithm uses the energy deposition in calorimeter cells calibrated according to associated electrons, photons, jets and muons. Cells not associated with any object are also taken into account, and weighted to take into account pile-up effects.

5.4 Cut-based Analysis

5.4.1 Signal regions optimization and definition

After object pre-selection and overlap removal, events with at least two baseline taus are selected. At least one of the taus should satisfy tight BDT identification requirement, and

Table 5.2: The summary of all baseline and signal object selections including taus, electrons, muons.

Taus		
	Baseline	Signal
Cut	Value/Description	Value/Description
algorithm	cluster seeded	cluster seeded
p_T	$p_T > 20GeV$	$p_T > 20GeV$
η	$\|\eta\| < 2.47$ and $\|\eta_{leadTrack}\| < 2.47$	$\|\eta\| < 2.47$ and $\|\eta_{leadTrack}\| < 2.47$
charge	$\|q\| = 1$	$\|q\| = 1$
quality	medium	medium, at least 1 tau being tight
Electrons		
	Baseline	Signal
Cut	Value/Description	Value/Description
algorithm	Egamma	
p_T	$p_T > 10GeV$	-
η	$\|\eta\| < 2.47$	
quality	medium++	tight++
isolation	-	$p_{Tcone30}/p_T < 0.16$ $E^{corr}_{Tcone30}/p_T < 0.18$
tracking cuts	-	various
Muons		
	Baseline	Signal
Cut	Value/Description	Value/Description
algorithm	Staco (combined and segment-tagged)	
p_T	$p_T > 10GeV$	-
η	$\|\eta\| < 2.5$	
quality	medium++	tight++
isolation	-	$p^{trkelstyle}_{Tcone30}/p_T < 0.12$
tracking cuts	-	various

the remaining one(s) must pass the medium identification requirement. Both taus are required to be matched to the corresponding trigger objects at Event Filter (EF). An event is tagged as opposite sign (OS) if at least one tau pair has opposite charge. Events where at least 1 OS tau pair has invariant mass less than 12 GeV are rejected to match the phase space of the Z + *jets* MC samples. This requirement has negligible effects on the signal acceptance.

Some additional requirements are adopted to further reject background events:

- **Jet veto** - $L30 + B20 + F30 = 0$. Here L30 (B20) stands for number of light-flavor (B) jets with $p_T > 30$ (20) GeV, while F30 stands for number of forward jets with $p_T > 30$ GeV. This requirement is very powerful to suppress backgrounds with top quark.
- **Loose jet veto** - $L50 + B20 + F30 = 0$. Here L50 stands for number of light-flavor jets with $p_T > 50$ GeV. The looser jet veto is only used as a replacement to gain sensitivity in direct stau production.
- **B-jet veto** - events containing b-jets are vetoed, $B20 = 0$. This requirement can also

suppress $t\bar{t}$ and single top backgrounds, while keeping signal events which may have a jet due to initial state radiation (ISR) [93].

- **Z-veto** - events with invariant mass of the reconstructed tau pair within 10 GeV from the Z mass are rejected. Due to the invisible part (neutrinos) of the tau decay, the reconstructed invariant mass does not peak at the true Z mass. Previous studies shows that a value of 81 GeV used for the Z-veto is reasonable: $|m(\tau,\tau) - 81| > 10GeV$.
- The **"stransverse mass"** m_T^2, which can be shown to have a kinematic endpoint for events where two massive pair produced particles each decay to two objects, in which one is detected (the lepton) and the other not (the neutralino). In events with more than two taus, m_T^2 is calculated using all possible tau pairs and the largest value is chosen. The definition of m_T^2 is:

$$m_T^2 = \min_{\vec{p}_T^{X(1)} + \vec{p}_T^{X(2)} = \vec{p}_T^{miss}} [max(m_T(1) + m_T(2)],$$

where

$$m_T(i)^2 = m_{vis(i)}^2 + mx^2 + 2[E_{T,vis(i)}E_{T,X(i)} - \vec{p}_T^{vis(i)} \cdot p_T^{X(1)}].$$

- $m_{T\tau 1} + m_{T\tau 2}$: the sum of the transverse mass values of the leading and next-to-leading taus.
- **Meff**: the scalar sum of the missing transverse energy and p_T of the leading and next-to-leading taus.
- $\Delta R(\tau 1, \tau 2)$: the distance between the leading and next-to-leading tau. This requirement is powerful to discriminate signals against back-to-back events such as di-jet or Z decays.

The summary of the SR definitions are shown in Table. 5.3. Four SRs are defined, one for C1C1 and C1N2 respectively and two for direct stau process.

Table 5.3: Signal region definition for the cut-based analysis.

SR-C1N2	SR-C1C1	SR-DS-highMass	SR-DS-lowMass
≥ 2 OS taus	2 OS taus	≥ 2 OS taus	≥ 2 OS taus
b-jet veto	jet veto	looser jet-veto	looser jet-veto
Z-veto	Z-veto	Z-veto	Z-veto
		$\Delta R(\tau,\tau) < 3$	$\Delta R(\tau,\tau) < 3$
$E_T^{miss} > 40$ GeV	$m_T^2 > 30$ GeV	$m_T^2 > 40$ GeV	$m_T^2 > 30$ GeV
$m_T^2 > 100$ GeV	$m_{T\tau 1} + m_{T\tau 2} > 250$ GeV	$m_{eff} > 230$ GeV	$m_{eff} > 260$ GeV

5.4.2 Background Estimation

Generally, the backgrounds in the cut-based analysis are including 3 sources:

- Events with at least 2 fake taus. This background is mainly from multi-jet events. A data-driven method called "ABCD" method is used to estimate the 2-fake-taus contribution. The estimation is validated in tau-tau channel.

- Events with 1 fake taus. This background is mainly from W+jets events. A semi-data-driven method is used to estimate the contribution of these events. $\mu - \tau$ events are selected as the control region (CR) for W+jets background, while $e - \tau$ events are used as validation.
- Irreducible backgrounds: diboson, Z+jets, $t\bar{t}$, $t\bar{t}V$, single top. These backgrounds are estimated using MC simulation and validated in some dedicated CRs.

5.4.2.1 Multi-Jet Background

Multi-jet background is estimated from data using the ABCD method[94]. In the ABCD method, four regions labelled as A (the pre-CR), B, C (the control regions) and D (the pre-SR) are defined in a two-dimensional plane. The axises of the plane are two uncorrelated discriminating variables, as shown in Fig. 5.2.

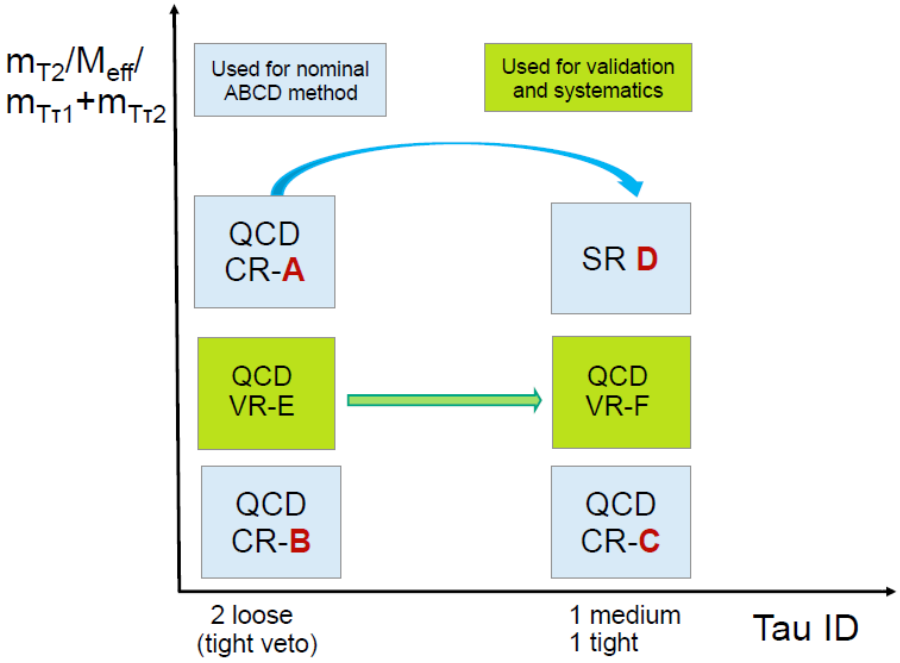

Figure 5.2: Illustration of the ABCD method for the QCD background estimation. The control regions QCD CR-A, CR-B, CR-C and SR-D are shown in light blue. The QCD VR-E and VR-F are validation regions in green, aiming at validating the estimation and calculating the systematics.

In this case the two variables are uncorrelated, the ratio of the event numbers in CR-A and CR-B should equals that of SR-D to CR-C. The transverse factor of event yields from CR-A (N_A) to SR-D (N_D) can be obtained from the event yields in CR-B(N_B) and CR-C (N_C):

$$tf = \frac{N_C}{N_B}, \frac{N_C}{N_B} = \frac{N_D}{N_A}.$$

The tau identification (tau-ID) based on the jet BDT quality requirement and m_T^2 [95] [96] are used as the two uncorrelated variables. The control regions are defined in Table 5.4.

Table 5.4: The QCD control region definition. Only those requirements different from that in the SRs are listed.

Regions	A	B	C
SR-C1N2	$m_{T2} > 100GeV$ at least 2 loose taus tight tau veto	$m_{T2} < 40GeV$ at least 2 loose taus tight tau veto	$m_{T2} < 40GeV$ at least 1 medium tau at least 1 tight tau
SR-C1C1	$E_T^{miss} > 100GeV$ at least 2 loose taus tight tau veto	$20GeV < E_T^{miss} < 60GeV$ at least 2 loose taus tight tau veto	$20GeV < E_T^{miss} < 60GeV$ at least 1 medium tau at least 1 tight tau
SR-DS-highMT2	$M_{eff} > 230GeV$ at least 2 loose taus tight tau veto	$130GeV < M_{eff} < 150GeV$ at least 2 loose taus tight tau veto	$130GeV < M_{eff} < 150GeV$ at least 1 medium tau at least 1 tight tau
SR-DS-lowMT2	$M_{eff} > 260GeV$ at least 2 loose taus tight tau veto	$100GeV < M_{eff} < 150GeV$ at least 2 loose taus tight tau veto	$100GeV < M_{eff} < 150GeV$ at least 1 medium tau at least 1 tight tau

In regions A and B, all candidate taus should pass the loose but fail the tight jet BDT requirement (tight tau event veto) to make sure these regions are orthogonal to the SR. While in regions C and D, all candidate taus must pass the medium jet BDT requirement, and at least one of the 2 taus should pass the tight jet BDT requirement. The regions B and C are selected requiring $m_{T2} < 20$ GeV, whereas in regions A and D $m_{T2} > 30$ GeV is required.

Two validation regions E and F are also defined. The region E (F) has the same definition as the CR-A (CR-D) except for intermediate requirements on the kinematic variable. The validation regions are used to verify the extrapolation of the ABCD estimation, and to estimate the systematic uncertainty from the possible correlation between the tau-id and the kinematic variable. The number of multi-jet events in the control and validation regions (Region A, B, C and E) is estimated from data after subtraction of other SM contributions estimated from MC simulation. Over 92-99% of the events contributing to the control regions A, B and C come from multi-jet production. The number of multi-jet events in the SR-D (validation region F) is estimated with ABCD method by extrapolating from the CR-A (validation region E) multiply the transfer factor TT.

The observed data are in agreement with SM background within uncertainty. The signal contamination in the multi-jet CRs is very small, which can be seen from the reference point contribution.

5.4.2.2 W+jets background

W+jets process with at least one misidentified tau is an important background in the SRs of this analysis. The yields of W+jets in data in the SRs can be estimated by multiply a normalization factor to that in MC. A dedicated control region (WCR) is used to fit the normalization factor. The definition of the WCR is required to be kinematically close to the SR, and to be enriched with $W \rightarrow \mu\nu$ events to suppress multi-jet contamination. Events containing exactly one muon and one opposite electrical charge tau (passing tight jet BDT requirement) are selected. To reduce the contribution from Z+jets production,

Table 5.5: The expected backgrounds in each multi-jet control regions and the estimate of the multi-jet background contribution in the signal regions.

		region A	region B	region C	T = C/B	multi-jet in SR
	Data	6	36907	24601		
SR-C1N2	Z+jets	0.3 ± 0.15	726 ± 28	3981 ± 56	0.554±0.028	2.3±1.4
	W+jets	1.0 ± 0.4	252 ± 82	587 ± 182		
	diboson	0.5 ± 0.26	14.6 ± 4.8	72 ± 20		
	top	0.1 ± 0.06	17.3 ± 2.1	68.0 ± 4.1		
	multi-jet	4.1 ± 2.5	35897 ± 211	19893 ± 168		
	Ref. Point 1	1.9 ± 0.9	1.4 ± 0.5	17.8 ± 2.0		
	Data	19	1274	716		
SR-C1C1	Z+jets	0.1 ±0.1	4.3 ±1.5	15.7 ±2.7	0.543±0.064	6.4±2.7
	W+jets	5.4 ±1.1	11.4 ±6.1	16.1 ±8.5		
	diboson	1.1 ±0.4	0.6 ±0.4	1.6 ±0.8		
	top	0.7 ±0.3	0.6 ±0.3	-0.6 ±2.3		
	multi-jet	11.7 ±4.5	1257 ±36	683 ±28		
	Ref. Point 2	3.8 ±1.4	0.2 ±0.1	1.1 ±0.3		

Table 5.6: Expected numbers of events from SM processes in the multi-jet validation regions, normalized to 20.1 fb^{-1}, as well as the numbers of events observed in data in the validation region. Both statistical and systematics uncertainty are shown.

SM process	multi-jet VR1	multi-jet VR2
W+jets	566 ± 24 ± 188	211 ± 15 ± 71
Z+jets	593 ± 24 ± 100	85.6 ± 9.3 ± 18.7
top	29.9 ± 5.5 ± 7.2	19.3 ± 4.4 ± 4.0
diboson	29.0 ± 5.4 ± 6.5	16.3 ± 4.0 ± 3.6
multi-jet	19440 ± 98 ± 1166	3840 ± 43 ± 230
SM total	20657 ± 103 ± 1185	4172 ± 47 ± 241
Observed	21107	4002
SUSY Ref. point	17 ± 4.1 ± 5.4	12.9 ± 3.6 ± 3.4

$m_{T\tau 1} + m_{T\tau 2} > 80GeV$ is required, and the reconstructed invariant mass of the two leptons, $m_{\tau,\mu}$, must be outside the Z mass window ($12GeV < m_{\tau,\mu} < 40GeV or m_{\tau,\mu} > 100GeV$). To suppress multi-jet and Z+jets events, $E_T^{miss} > 40GeV$ is required, and the leptons are required not to be back-to-back($\delta\phi(\mu,\tau) < 2.7$ and $\delta\eta(\mu,\tau) < 2.0$). The contribution from events with top quarks is highly suppressed by rejecting events containing b-tagged jets $N(B20) = 0$.

Although enriched with W+jets events, the WCR is still contaminated by multi-jet process. This contamination ($N_{qcd}(WCR, OS)$) can be estimated by counting the number of events in data satisfying the same selection but with same-sign (SS) cut on the two leptons like the WCR: $N_{qcd}(WCR, OS) = N_{qcd}(WCR, SS) = N_{data}(WCR, SS) - N_{other}(WCR, SS)$. Here, $N_{other}(WCR, SS)$ stands for the contribution from other SM processes and is estimated using their MC prediction. The method relies on the fact that jets in the multi-jet events have equal possibility to be mis-identified as a τ^+ or a τ^-, while not equal in the W+jets production The estimation of W+jets is validated in a region with $W \to e\nu$ events

(WVR). The WVR is defined in the same way as the WCR except a replacement from an isolated muon to an electro.

The definition of the WCR and WVR are summarized in Table. 5.7. The multi-jet contribution in the WVR is estimated using the same technique as the WCR. The contribution of all SM process in WCR and WVR are shown in Table. 5.8. Generally, the purity of the selection in W+jets events is around 80% (75%) in the WCR(VR). Good agreement is observed between data and SM predictions.

Table 5.7: Definition of the W +jets control region and validation region.

WCR	WVR
1 tight tau	
1 isolated muon	1 isolated electron
opposite charge	
b-jet veto	
$\delta\phi(\mu,\tau) < 2.7$	
$\delta\eta(\mu,\tau) < 2.0$	
$E_T^{miss} > 40GeV$	
$m_{T\tau 1} + m_{T\tau 2} > 80GeV$	
$12GeV < m_{\tau,\mu} < 40GeV or m_{\tau,\mu} > 100GeV$	

Table 5.8: Contributions of all SM process in the W +jets control region and validation region. All numbers are normalized to 20.3 fb^{-1}. The sum in quadrature of statistical and systematic uncertainties are also shown.

process	WCR	WVR
Data	4120	3420
SM total	4100 ± 900	3500 ± 600
W +jets	3300 ± 800	2600 ± 500
Top	250 ± 80	240 ± 70
Diboson	180 ± 50	170 ± 40
Z+jets	140 ± 40	99 ± 31
Multi-jet	250 ± 250	400 ± 200

5.4.2.3 Background with top quark

ABCD MC-driven method is used to estimate the $t\bar{t}$ background due to low statistics in the SRs, compared to direct prediction by Monte Carlo. The same as the multi-jet background, correlation between tauID and the kinematic variables used in the ABCD estimation is tested to be weak, proving it be safely used in the ABCD method. The transfer factor is then calculated as the ratio between the loose tauID region and the medium+tight tauID region.

Since the statistics is still quite limited even with the 2 loose taus requirement, the contribution from single top, $t\bar{t}V$, and t+V events are merged and estimated together with $t\bar{t}$. Another ABCD-like method is used to evaluate all variations due to the experimental uncertainties. The systematic uncertainties are around 30-40% in different SRs, with both theoretical (10-20%) and experimental (10-20%) uncertainties contributed. The largest experimental uncertainties are given by the uncertainties on the tau and jet energy scales, and on the fake tau scale factors (SF).

The other backgrounds like diboson is estimated using the same method.

5.4.3 Results for cut-based analysis

The multi-jet and W+jets contributions are estimated from data, the other processes are taken from MC. m_T^2, E_T^{miss} ,$m_{T\tau 1} + m_{T\tau 2}$, and M_{eff} distributions for data and SM backgrounds in each signal region are shown in Fig. 5.3 . The Z-veto efficiency for data (MC) is 54.8% after jet veto and 60.0% after b-jet veto. Data and SM predictions are showing good agreement in all distributions, with negligible difference (less than 1%).

Results of the background-only likelihood-fit are also presented in Table. 5.9, which shows the fitted numbers of events in the CRs, and the predicted and observed numbers of events in the SRs. Note that in this fit setup, no signal contamination is taken into account in the CRs. Also, Both statistical and systematic uncertainties on SM background and signal samples are taken into account.

See from both the kinematic distributions and the fitted yields, we don't observe any excess in the SRs. The combination of different signal regions is then done by taking for each point in the parameter space the SR with the best expected p-value, with no combined fit among different signal regions.

Breakdown of the dominant systematic uncertainties on background estimation in the direct-stau signal regions are shown in table. 5.10 and table. 5.11. The systematic items with largest contribution are multi-jet estimation (mu_qcd in the table), trigger scale factor (alpha_ANYR_all_TTRIGSF in the table), background statistics (the items with suffix "STA")...

Table.5.12 shows the fitted MC normalization factors in the control regions of multi-jets, W+jets, Z+jets and top processes.

With no excess observed, model-independent upper-limits on the visible cross-section are derived. The upper-limits are defined as efficiency × acceptance × cross-section, as a function of a given signal region. The input of the interpretation includes the number of events observed in a certain region. While, the output of the interpretation is additional parameters representing the non-SM signal strength. In th setup, potential signal contamination in the control regions is ignored. Visible cross-section is obtained by dividing the limits on the number of non-SM events in the SR with the integrated luminosity and efficiency. The limits at 95% confidence level (CL) are shown in Fig. 5.4.

As a result of the C1C1 and C1N2 SRs, chargino masses from 140 up to 300 GeV are excluded for a massless lightest neutralino in the scenario of direct production of chargino pairs. In the case of pair associated production of degenerate charginos and next-to-lightest neutralinos, chargino masses up to 370 GeV are excluded for lightest neutralino masses below 100 GeV.

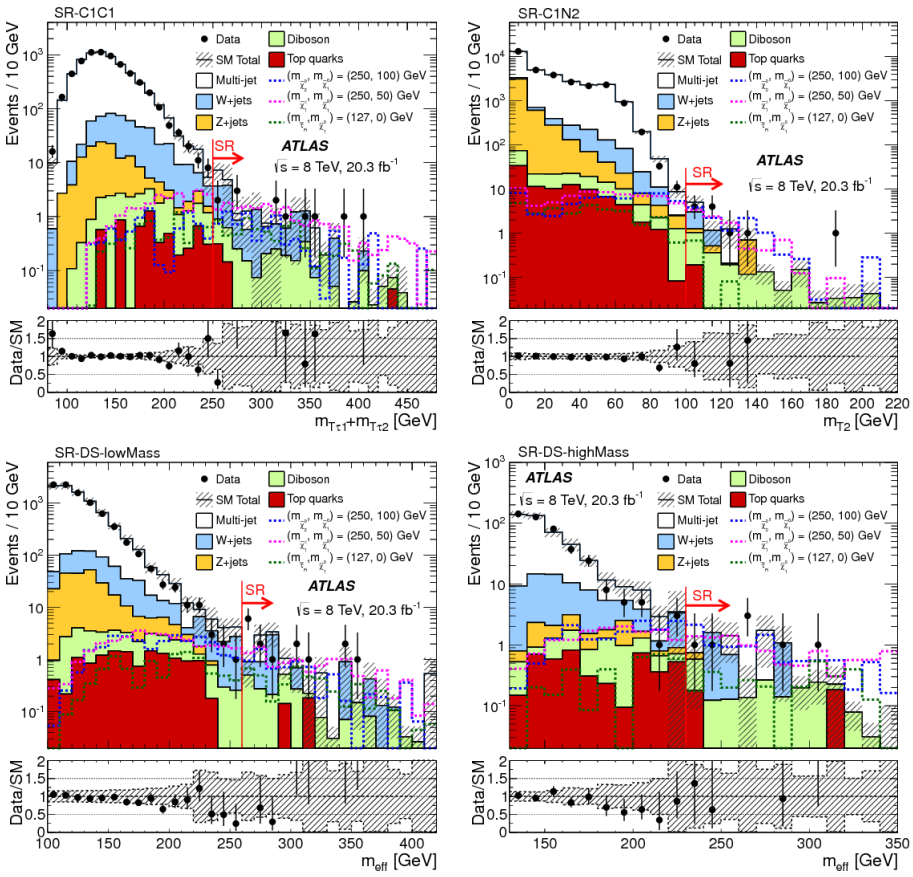

Figure 5.3: Kinematic distribution for data and SM backgrounds in SRs without the last cut: $m_{T\tau 1} + m_{T\tau 2}$ distribution in and out of SR-C1C1 (upper-left); m_{T2} distribution in and out of SR-C1N2 (upper-right); m_{eff} distribution in and out of SR-DSlowMass (lower-left); m_{eff} distribution in and out of SR-DShighMass (lower-right). Both statistical and systematic uncertainty are shown. Distribution for 3 reference points from each model are also shown.

Due to low cross-sections, this analysis is not sensitive enough to direct stau production. Generally, the upper limits for left-handed stau pairs are slightly stronger than the right-handed pairs, due to larger cross-section for left-handed stau pairs. The combined upper limits on the direct stau signal strength are shown in Fig. 5.4 (bottom). The theoretical cross section at NLO is 0.07 (0.17) pb for right (left)-handed stau pair production, while the excluded cross section is 0.26 (0.34) pb. The upper limit on the signal strength for the combined production of right-handed and left-handed stau pairs is 1.17. Note that SR-DS-highMass provides better exclusion in high mass region, while SR-C1C1-lowMT2 works better in low mass region.

5.4.4 Summary for cut-based analysis

In summary, a search for electroweak production of supersymmetric particles with at least two hadronically decaying taus in the final state has been presented. Good agreement be-

Table 5.9: Observed and expected numbers of events in the signal regions for 20.3 fb^{-1}. The contributions of multi-jet and W+jets events were scaled with the normalisation factors obtained from the fit. The shown uncertainties are including both statistical and systematic uncertainties. The one-sided p_0-values and the observed and expected 95% CL upper limits on the visible non-SM cross-section are also given.

SM process	SR-C1N2	SR-C1C1	SR-DS-highMass	SR-DS-lowMass
Top	0.30 ± 0.19	0.7 ± 0.4	0.9 ± 0.4	1.3 ± 0.6
Z+jets	0.9 ± 0.5	0.20 ± 0.17	0.6 ± 0.4	0.40 ± 0.27
W+jets	2.2 ± 0.8	11.2 ± 2.8	2.7 ± 0.9	4.1 ± 1.2
Diboson	2.2 ± 0.9	3.8 ± 1.4	2.5 ± 1.0	2.9 ± 1.0
Multi-jet	2.3 ± 2.0	5.8 ± 3.3	0.9 ± 1.2	2.8 ± 2.3
SM total	7.9 ± 2.4	22 ± 5	7.5 ± 1.9	11.5 ± 2.9
Observed	11	12	7	15
Ref. point 1	11.3 ± 2.8	8.5 ± 2.2	10.2 ± 2.6	7.5 ± 2.0
Ref. point 2	9.2 ± 2.1	20 ± 4	12.4 ± 2.8	12.8 ± 2.7
Ref. point 3	0.8 ± 0.5	7.6 ± 1.9	3.8 ± 1.0	5.2 ± 1.3
p_0	0.20	0.50	0.50	0.21
Expected σ^{95}_{vis} (fb)	$< 0.42^{+0.19}_{-0.11}$	$< 0.56^{+0.25}_{-0.14}$	$< 0.37^{+0.17}_{-0.10}$	$< 0.51^{+0.18}_{-0.15}$
Observed σ^{95}_{vis} (fb)	< 0.59	< 0.37	< 0.37	< 0.66

tween data and SM expectations is observed in all signal regions. These results are used to set limits on the visible cross-section for signal-like events in each signal region. Exclusion limits are set on the parameters of all the signals involved. For simplified models, chargino masses from 140 up to 300 GeV are excluded for a massless lightest neutralino. In the case of chargino pair and chargino with next-to-lightest neutralinos production, chargino masses up to 370 GeV are excluded when the lightest neutralino masses are below 100 GeV. For direct stau production, the best upper limit on the production cross-section is at a stau mass of 80 GeV and a massless LSP.

5.5 MVA for the Direct Stau Production

5.5.1 MVA

In principle, by using a set of suitable discriminating variables, multivariate analysis techniques allow to separate the signal from background as much as possible, thus providing a better method to enhance the signal-to-background ratio compared to the cut-based analysis method. The Toolkit for Multivariate Analysis (TMVA) provides a ROOT-integrated environment for the application of multivariate classification [97]. All multivariate techniques in TMVA belong to the family of supervised learning algorithms. The algorithm examines events with already known output (background or signal) in the training procedure. A mapping function is determined as a result of the training. Then in the application

Table 5.10: Breakdown of the dominant systematic uncertainties on background estimations in the SR-DS-lowMass.

SR-DShighMass	
Total background expectation	11.5
Total statistical	± 3.39
Total background systematic	± 2.88 [25.07%]
mu_qcd	± 1.20 [15.8%]
alpha_ANYR_all_TTRIGSF	± 0.85 [11.2%]
alpha_SR1_BkgW_STA	± 0.80 [10.6%]
alpha_SR1_BkgDibosons_STA	± 0.68 [9.0%]
alpha_ANYR_BkgDibosons_GENERATOR	± 0.44 [5.7%]
alpha_SR1_BkgZ_STA	± 0.40 [5.3%]
alpha_ANYR_all_TIDSF	± 0.37 [4.8%]
alpha_ANYR_all_TES	± 0.34 [4.5%]
mu_w	± 0.28 [3.7%]
alpha_SR1_all_JER	± 0.22 [2.9%]
alpha_SR1_BkgFake_FBGSyst	± 0.21 [2.8%]
alpha_SR1_BkgTop_STA	± 0.21 [2.8%]
alpha_ANYR_all_TFAKESF	± 0.17 [2.2%]
alpha_ANYR_BkgTop_GEN	± 0.16 [2.1%]
alpha_ANYR_BkgZ_GEN	± 0.14 [1.9%]
alpha_ANYR_all_RESOST	± 0.13 [1.7%]
alpha_SR1_all_JES	± 0.12 [1.6%]
alpha_ANYR_all_SCALEST	± 0.11 [1.5%]
alpha_ANYR_all_PILEUP	± 0.11 [1.4%]
alpha_ANYR_BkgTop_XS	± 0.07 [0.91%]
alpha_ANYR_BkgW_GEN	± 0.07 [0.88%]
alpha_ANYR_all_BJET	± 0.05 [0.72%]
alpha_ANYR_BkgTop_PDFERR	± 0.05 [0.69%]
alpha_ANYR_BkgDibosons_PDFERR	± 0.05 [0.67%]
alpha_ANYR_BkgZ_XS	± 0.03 [0.39%]
alpha_ANYR_all_TEVSF	± 0.02 [0.32%]
alpha_ANYR_all_BMISTAG	± 0.02 [0.22%]
alpha_ANYR_BkgZ_PDFERR	± 0.01 [0.16%]
alpha_ANYR_BkgW_PDFERR	± 0.01 [0.07%]

phase, the mapping function will make decision about the event classification (background or signal) of a sample with unknown output.

In this analysis, both signal and background Monte Carlo samples were split in two halves, after a few pre-selection cuts which is shown in Table. 5.13. The pre-selection cuts

Table 5.11: Breakdown of the dominant systematic uncertainties on background estimations in the SR-DS-highMass.

SR-DSlowMass	
Total background expectation	7.57
Total statistical	± 2.75
Total background systematic	± 1.94 [25.59%]
mu_qcd	± 2.25 [19.5%]
alpha_ANYR_all_TTRIGSF	± 1.11 [9.6%]
alpha_SR1_BkgW_STA	± 1.00 [8.7%]
alpha_SR1_BkgDibosons_STA	± 0.56 [4.9%]
alpha_SR1_BkgFake_FBGSyst	± 0.52 [4.5%]
alpha_ANYR_all_TES	± 0.50 [4.3%]
alpha_ANYR_BkgDibosons_GENERATOR	± 0.49 [4.2%]
alpha_SR1_BkgZ_STA	± 0.46 [4.0%]
mu_w	± 0.43 [3.7%]
alpha_ANYR_all_TIDSF	± 0.42 [3.7%]
alpha_SR1_BkgZ_STA	± 0.24 [2.1%]
alpha_ANYR_all_TFAKESF	± 0.17 [1.4%]
alpha_ANYR_BkgTop_GEN	± 0.13 [1.1%]
alpha_ANYR_BkgW_GEN	± 0.12 [1.1%]
alpha_ANYR_BkgTop_XS	± 0.10 [0.87%]
alpha_ANYR_BkgZ_GEN	± 0.09 [0.74%]
alpha_ANYR_BkgTop_PDFERR	± 0.08 [0.70%]
alpha_SR1_all_JES	± 0.08 [0.69%]
alpha_ANYR_BkgDibosons_PDFERR	± 0.06 [0.53%]
alpha_ANYR_all_SCALEST	± 0.06 [0.53%]
alpha_ANYR_all_BJET	± 0.04 [0.36%]
alpha_ANYR_BkgW_PDFERR	± 0.03 [0.28%]
alpha_SR1_all_JER	± 0.03 [0.24%]
alpha_ANYR_all_TEVSF	± 0.02 [0.20%]
alpha_ANYR_all_BMISTAG	± 0.02 [0.19%]
alpha_ANYR_BkgZ_XS	± 0.02 [0.17%]
alpha_ANYR_all_CJET	± 0.02 [0.15%]
alpha_ANYR_all_RESOST	± 0.01 [0.11%]
alpha_ANYR_BkgZ_PDFERR	± 0.01 [0.05%]

will help reduce the background and the training time. The first half of the samples is then used for training and the second half for testing. In particular, odd-numbered events were used for the training while even-numbered events were used for testing and performance evaluation. Different discrimination methods were applied in TMVA with several signal

Table 5.12: Background normalization factors from the background-only fits.

SR	Background type	Normalization factor
SR-C1N2	W+jets	1.002 ± 0.104
SR-C1C1	W+jets	1.002 ± 0.105
SR-DS-highMT2	W+jets	1.002 ± 0.104
SR-DS-lowMT2	W+jets	1.002 ± 0.104
SR-C1N2	multi-jets	0.995 ± 0.857
SR-C1C1	multi-jets	0.999 ± 0.548
SR-DS-highMT2	multi-jets	1.014 ± 1.650
SR-DS-lowMT2	multi-jets	0.997 ± 0.803

Table 5.13: Summary of pre-selections used in MVA training.

pre-selections ("pre-SR")
== 2 medium OS taus
≥ 1 tight tau
b-jet veto
Z-veto
$m_{T2} > 30GeV$

samples, corresponding to different regions of the direct stau phase space. The parameters of each method were optimized in order to maximize the discriminating power.

5.5.2 Discriminating variable and training

In general, discriminating variables for the multivariate analysis are selected with the following requirements:

- **Good MC prediction**. Their distributions in data are expected to be accurately reproduced by MC simulation.
- **Signal and background discrimination power**. Their distributions in signal and background are expected to be different as much as possible.
- **Proper correlation**. They are not highly correlated to each other, thus, the number of variables used in the training are limited.

A large number of variables (up to 20) was initially considered as input for the training procedure, while it is reduced to 12 according to their discrimination power between signal and background and to their agreement in data and MC comparison. The selected input variables for the training procedure are p_T of the leptons, effective mass (m_{eff}), m_{T2}, $m_{\tau,\tau}$, the angle and pseudo-rapidity between the two leading taus and the angles between E_T^{miss} two leading taus. In some sense, the BDT can take use of the correlations between the variables if they are different between the signal and the background. Variables which are highly correlated with others are dropped before the training to avoid duplicating information.

Fig. 5.6 shows the distributions of variables used in the training procedure, after applying the pre-selection cuts. The background used here includes W+jets, Z+jets, top, diboson

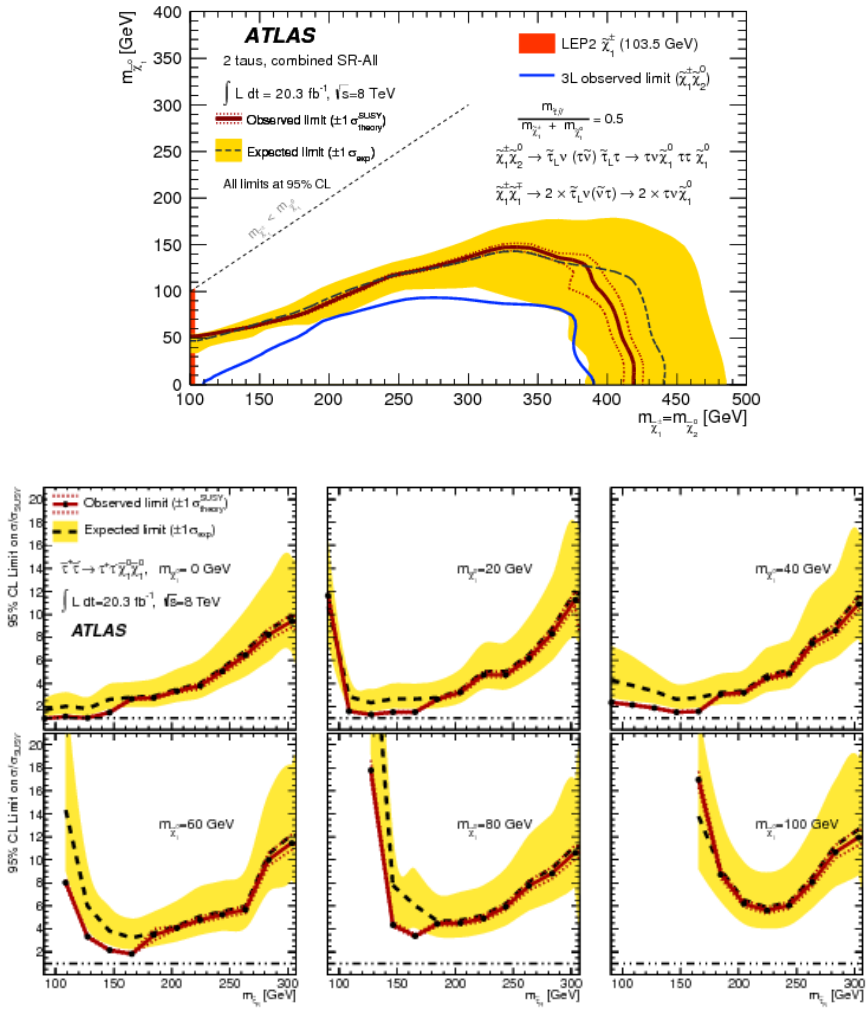

Figure 5.4: 95% CL exclusion limits for simplified models with: a combination of chargino-neutralino and chargino-chargino production (upper) and direct stau production (lower).

Table 5.14: The instruction of BDT parameters and optimized value of them.

BDT parameters	Description	Optimized value
nTrees	Number of trees in the forest	700
nCuts	Number of grid points in variable range used in finding optimal cut in node splitting	20
MaxDepth	Max depth of the decision tree allowed	4
Shrinkage	Learning rate for GradBoost algorithm	0.1

and multi-jet background, with only statistical uncertainty shown. Note that the multi-jet contribution is from ABCD estimation. A reasonable agreement is observed for all the

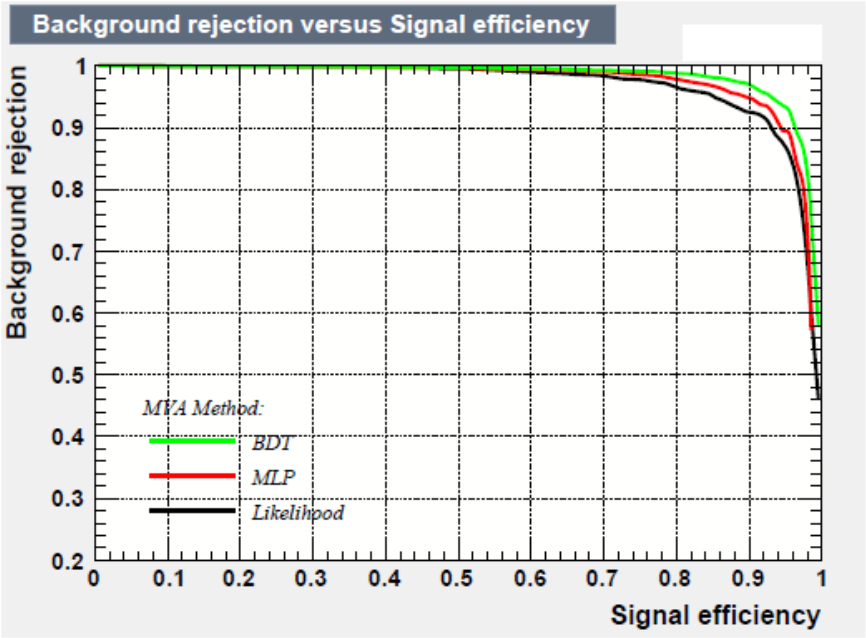

Figure 5.5: The background rejection versus signal efficiency after pre-selection cuts for different TMVA methods.

chosen variables between data and SM, which indicates a well modelling of MC prediction for non-multi-jet backgrounds, as well as a perfect estimation on multi-jet background.

The linear correlation coefficients among the different input variables after pre-selection cuts are shown in Fig 5.7 for the signal (on the left) and background (on the right). The signal stands for the reference point with stau mass of 100 GeV and a massless LSP. It can be observed that most of the variables are generally poorly correlated except in some expected cases, as meff , $E_{\mathrm{T}}^{\mathrm{miss}}$, m_T^2 and $m_{T\tau 1}$, $m_{T\tau 2}$. To further check the modeling of correlation between variables, the two dimensional correlation between m_T^2 and other 11 input variables before gaussian decorrelation after pre-selection cuts for both data and SM backgrounds is shown in Fig. 5.8 . We can see that there is no significant correlation difference between data and SM background. We also checked the correlation after gaussian decorrelation and find there is no hidden disagreements from the decorrelation process.

5.5.3 BDT response and SR definition

Several discrimination methods were tested and compared in TMVA: Boosted Decision Trees (BDT), Likelihood, Neural Network... The best discriminating power was achieved with the BDT technique, as shown in Fig. 5.5. BDT is a well known algorithm which can be straightforward interpreted as a simple two-dimensional tree structure. In the algorithm, a forest of decision trees is created. A certain event will be classified as signal or background with the majority vote done by each tree of the forest. Since BDT needs large training samples compared to other classifiers, an overtraining test is essential in case of limited statistics. Overtraining should be kept under control by properly tuning the parameters of

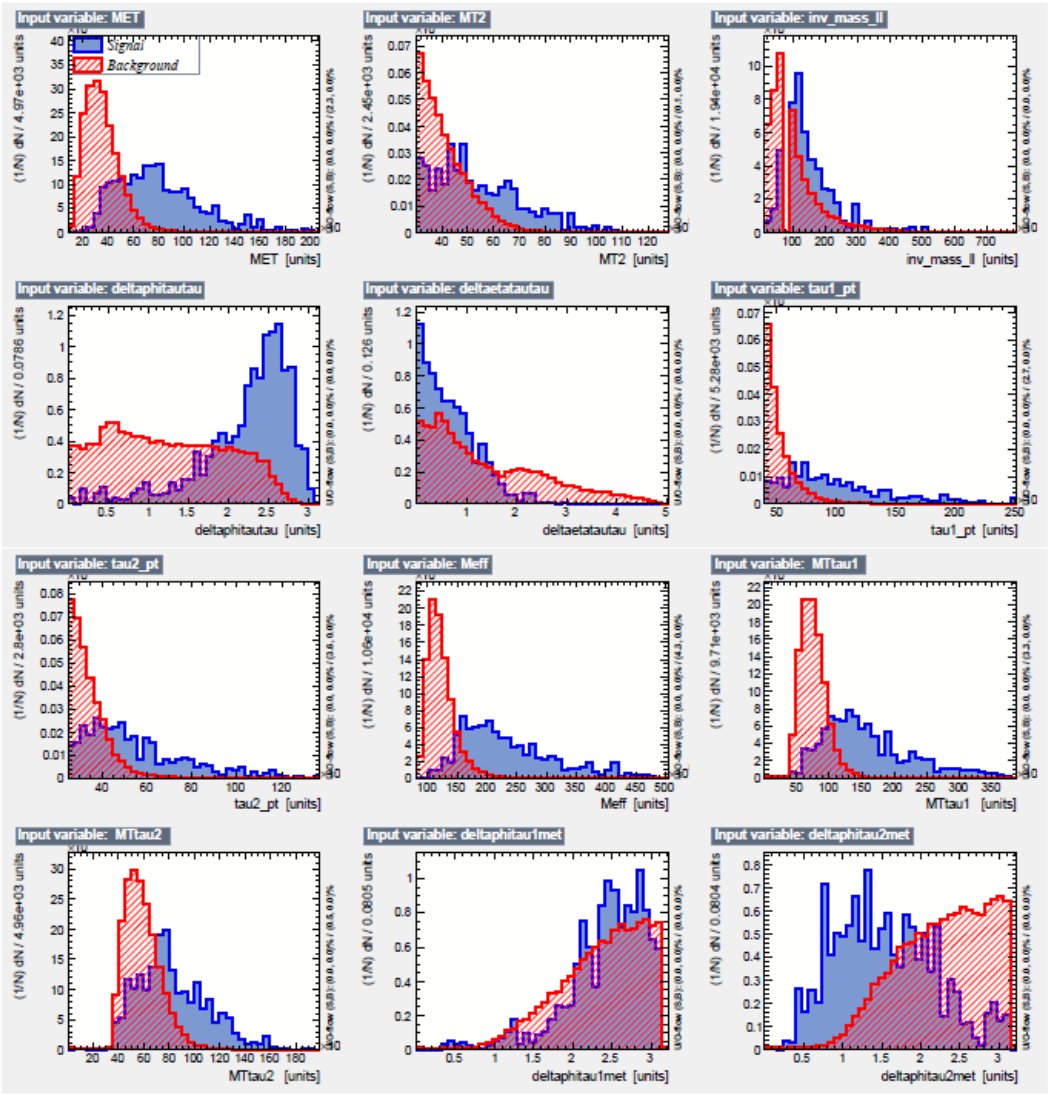

Figure 5.6: The distribution of the input variables for signal and background in TMVA. The signal used is from the reference point with stau mass of 100 GeV and massless LSP, normalized to the background.

the BDT, and checked by looking at the Kolmogorov-Smirnov test results.

In this analysis, the optimized BDT parameter is summarized in Table. 5.14. The **nTrees** stands for the number of trees in a forest. The forest is a set of trees which has Ntree members and each of the members is made up of several events by a repeated sampling from all the original sample. Generally, large nTree value helps increase sensitivity. However, if nTree is too large, the number of events in each tree should be limited to avoid being recounted too many times, which will cause a decrease in sensitivity. A scanning on nTree in the range between 200 and 1000 is applied (according to the available Monte Carlo statistics) and $nTrees = 700$ is the most optimized value. **nCuts** is a parameter which decides the granularity of the input variables in order to set a cut value which optimize the separation for each tree. The default value of nCuts=20 proved to be a good compromise

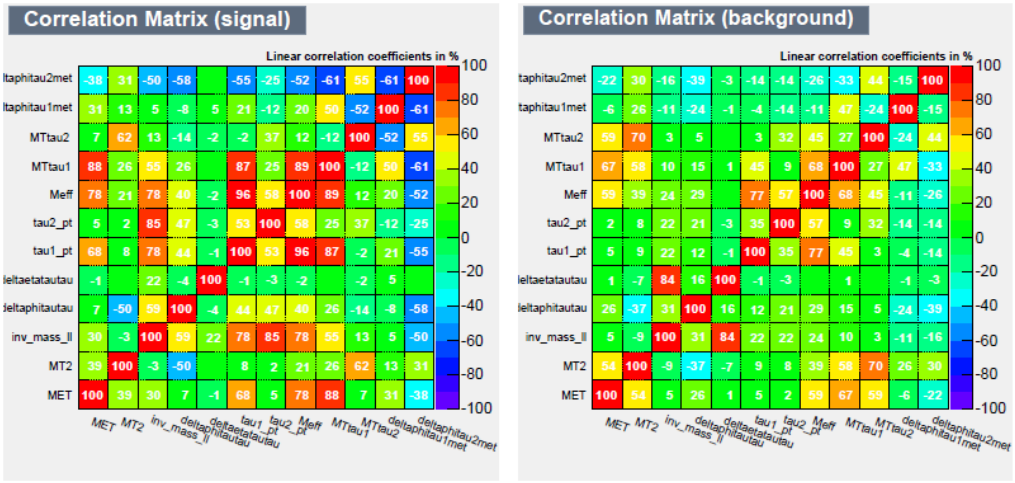

Figure 5.7: Linear correlation coefficients among the different input variables after preselection cuts for the signal (on the left) and background (on the right).

Table 5.15: The three reference points used for BDT parameter optimization.

benchmark	stau mass(GeV)	LSP mass(GeV)	raw events
benchmark point 1	100	0	125k
benchmark point 2	160	0	125k
benchmark point 3	80	40	125k

between computing time and step size. The **MaxDepth** is an positive integer which limits the level of the cell tree. $MaxDepth = 4$ works best for this analysis after dedicated optimization. Its robustness can be enhanced by reducing the learning rate of the algorithm through the **Shrinkage** parameter, which controls the weight of the individual trees. A small shrinkage (0.1-0.3) demands more trees to be grown but can significantly improve the accuracy of the prediction in discriminate cut settings. All the other parameters are set as default value.

The three reference points used in the optimization is listed in the table 5.15, which are choosed from the signal points with larger sensitivity compared with others and can cover different mass parameter regions. Here, benchmark point 1 (2) is chosen from massless LSP and low (high) stau mass region and benchmark point 3 is chosen from higher LSP and medium stau mass region. See from the overtraining test plot shown in Fig. 5.9, no problem is observed with the training.

After the training phase, BDT learns the features of both signal and background, and determines accordingly a set of probabilistic weights. In the application procedure, BDT provides a response value (marked as t_{cut}) for each event. Fig. 5.13 shows the t_{cut} distributions for all the background sources and the 3 signal benchmark points. The multi-jet background contribution is dominant when $tcut < 0$, while when $tcut > 0$, the multi-jet and W+jets background dominants, followed by top, diboson and Z+jets background.

The signal region is defined with a cut-off on BDT response which provides the best

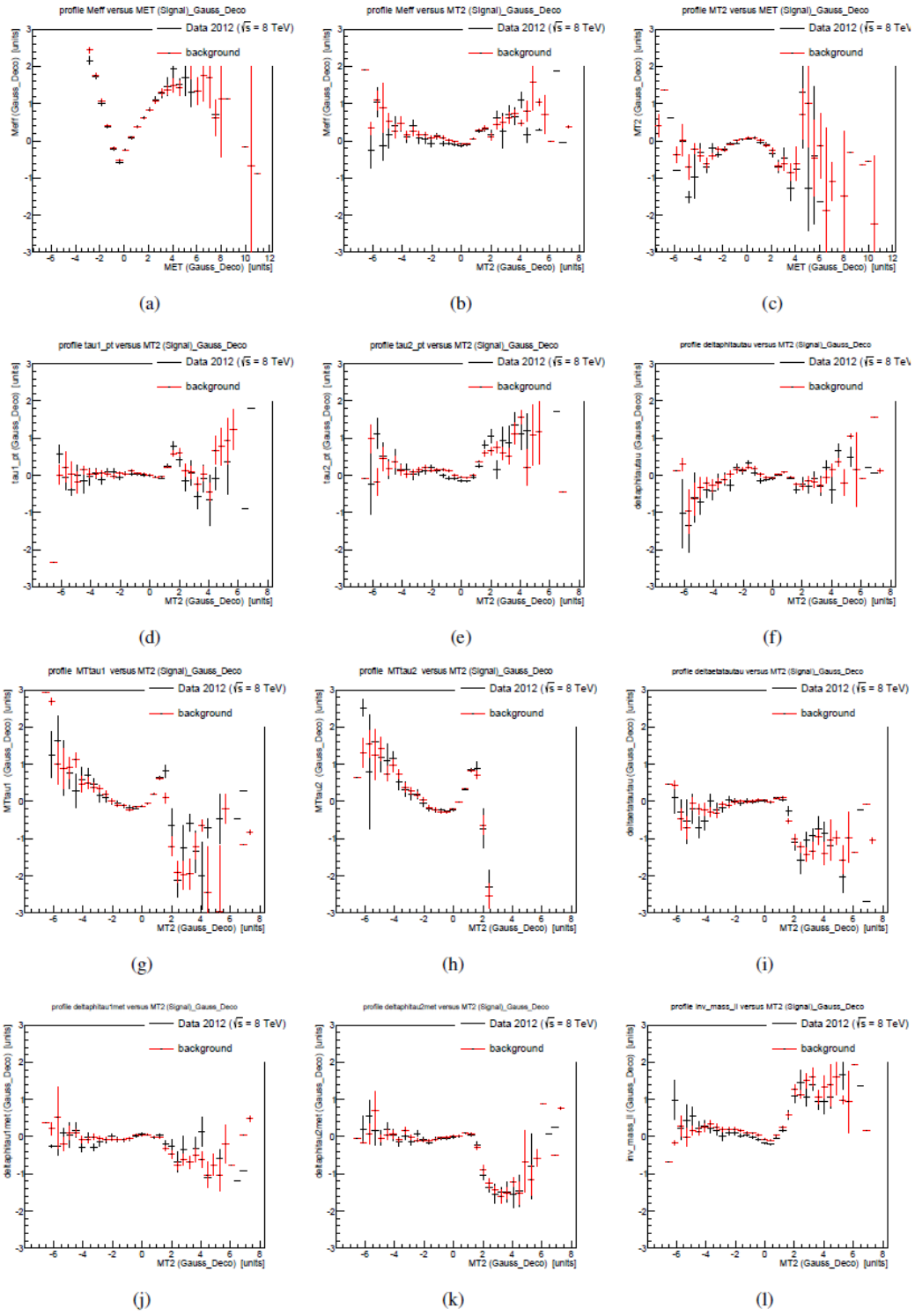

Figure 5.8: Two dimensional correlations between m_{T2} and other input variables after pre-selection cuts for both data and SM backgrounds.

discovery significance Zn:

$$Zn = \sqrt{2}erf^{-1}(1-2p),$$

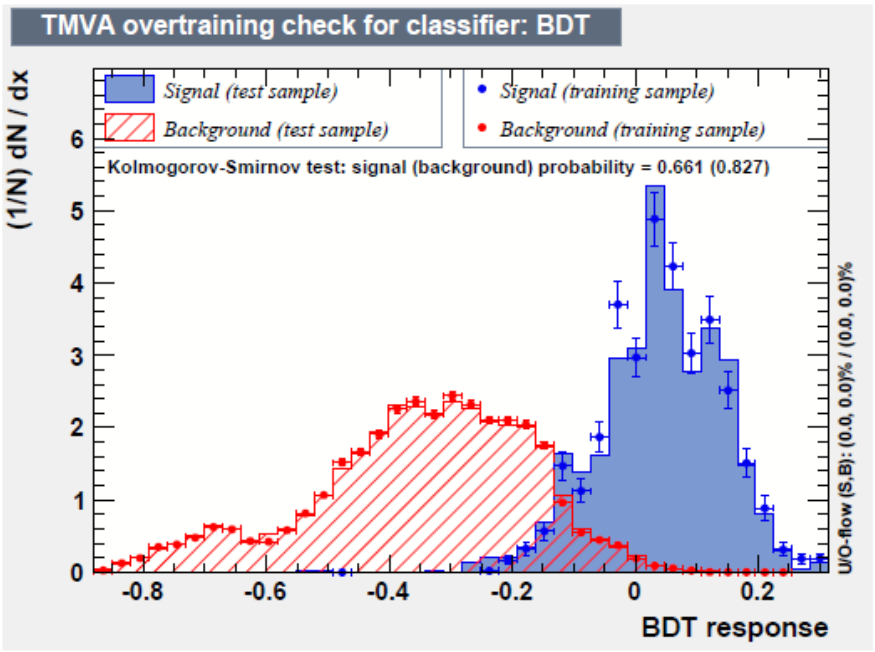

Figure 5.9: BDT response distributions for trained (dots) and tested (histogram) events after pre-selection cuts. Signals are in blue, while backgrounds are in red.

Table 5.16: Signal region (SR) definition, which is similar as the preSR except with additional $t_{cut} > 0.07$.

pre-selections ("pre-SR")
== 2 medium OS taus
$\geq$ 1 tight tau
b-jet veto
Z-veto
$m_{T2} > 30GeV$
$t_{cut} > 0.07$

Table 5.17: Multi-jet and W validation region definition.

multi-jet VR1	multi-jet VR2	W-VR1	W-VR2
exactly two OS taus	exactly two OS taus	exactly two OS taus	exactly two OS taus
b-jet veto	b-jet veto	b-jet veto	b-jet veto
Z-veto	Z-veto	Z-veto	Z-veto
$30 < m_{T2} < 50GeV$	$50 < m_{T2} < 80GeV$	$m_{T2} > 30GeV$	$m_{T2} > 30GeV$
-	-	$E_{\mathrm{T}}^{\mathrm{miss}} > 100GeV$	$E_{\mathrm{T}}^{\mathrm{miss}} > 90GeV$
$t_{cut} < 0.07$	$t_{cut} < 0.07$	$-0.2 < t_{cut} < 0.07$	$-0.2 < t_{cut} < 0.07$

where

$$p \propto \int_0^\infty dbG(b; N_b, \delta b) \sum_{i=N_{data}}^{\infty} \frac{e^{-b} b^i}{i!}.$$

Table 5.18: Expected numbers of events from SM processes in the W validation regions, normalized to 20.1 fb^{-1}, and the numbers of events observed in data in the validation region. Both statistical and systematics uncertainty are shown. The "top" contribution includes the single top, $t\bar{t}$,and $t\bar{t}V$ processes.

SM process	W VR1	W VR2
W+jets	19.9 ± 4.4 ± 6.9	33.4 ± 5.5 ± 12.1
Z+jets	2.3 ± 1.5 ± 0.7	4.4 ± 2.1 ± 1.4
top	5.4 ± 2.3 ± 1.3	8.1 ± 2.9 ± 1.8
diboson	4.7 ± 2.2 ± 1.0	7.1 ± 2.7 ± 1.5
multi-jet	5.9 ± 2.4 ± 1.2	17.0 ± 8.7 ± 8.8
SM total	38.2 ± 6.1 ± 7.2	70.0 ± 11.2 ± 15.2
Observed	33	65
SUSY Ref. point	3.4 ± 1.9 ± 1.2	5.6 ± 2.4 ± 1.6

30% systematics are in assumption during the scanning of the t_{cut}, which is also compared with 50%, shown in Fig. 5.10 The final t_{cut} is set to 0.07 since it provides the best Zn value.

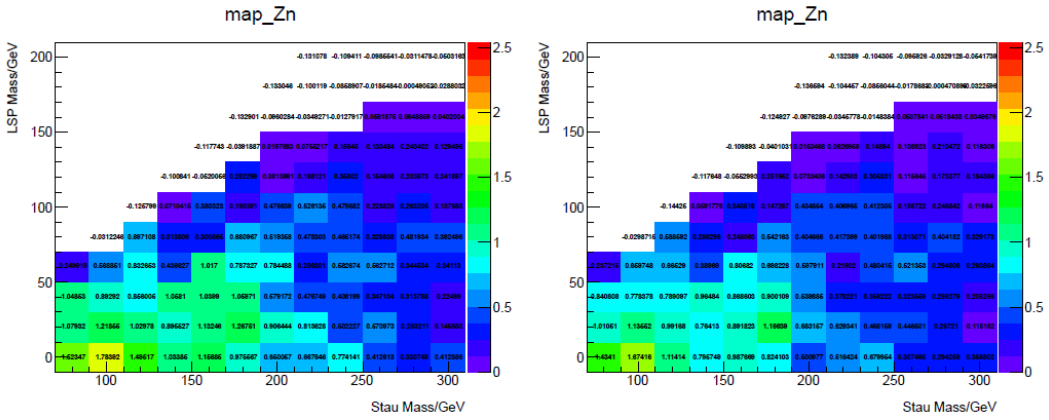

Figure 5.10: Comparison for Zn map with different systematic assumption, (a) with the 30% systematic assumption, (b) with the 50% systematic assumption

And, the SR definition is the same as the pre-SR but with $t_{cut} > 0.07$.

5.5.4 Results and uncertainty

Expected numbers of events from SM processes in the signal region normalized to 20.1 fb^{-1} are shown in table 5.19. The expected event yields for the SUSY Ref. point are also shown in the same table. Fig. 5.11 shows the BDT response distribution in the signal region before last cut (N-1 cut). A reasonable agreement between data and SM is observed both in and out of the SR. Fig. 5.12 shows the reasonable agreement between data and SM in BDT response and other kinematic distributions in the validation regions. Since no significant excess observed in the signal region (shown in Fig. 5.13), we set the exclusion limit.

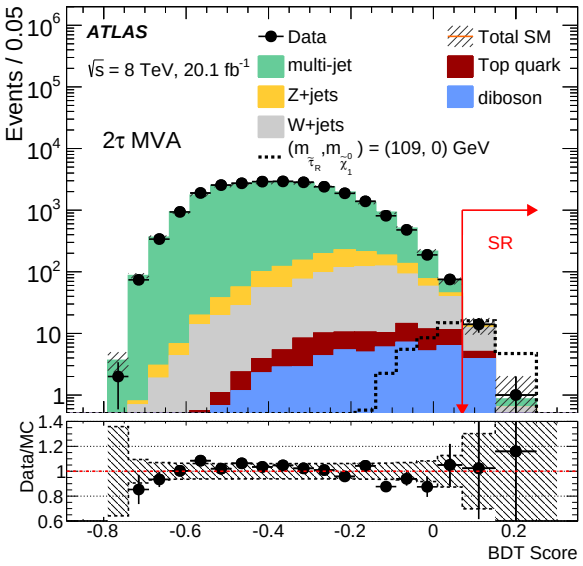

Figure 5.11: Distribution of BDT response for both data and MC.

Table 5.19: Observed and expected numbers of events in the signal regions for 20.1 fb^{-1}. The contributions of multi-jet and W+jets events were scaled with the normalisation factors obtained after fit. The shown uncertainties are the sum in quadrature of statistical and systematic uncertainties, with correlation of systematic uncertainties among control regions and background processes is fully taken into account. The "top" contribution includes the single top, $t\bar{t}$,and $t\bar{t}V$ processes.

SM process	SR
top	1.24 ± 0.85
Z+jets	0.89 ± 1.22
W+jets	7.27 ± 3.37
diboson	4.36 ± 1.59
multi-jet	0.93 ± 2.63
SM total	14.7 ± 5.10
Observed	15
SUSY Ref. point	20.9 ± 5.0
p_0	0.46
Expected $\sigma_{vis}^{95}(fb)$	0.67
Observed $\sigma_{vis}^{95}(fb)$	0.67

Tables 5.21 show the fitted numbers of events in the control regions, as well as the predicted and observed numbers of events in the signal regions. Table 5.22 shows the breakdown of the dominant systematic uncertainties on background estimates in the signal region. Due to the fact that two different multi-jet background estimations (ABCD method and OS-SS method) have been used to multi-jet CR and W CR separately, there are two types of multi-jet samples shown in the background fit table: FAKE defines the multi-jet estimation in multi-jet CR and SR; FAKEw defines the multi-jet estimation in W CR.

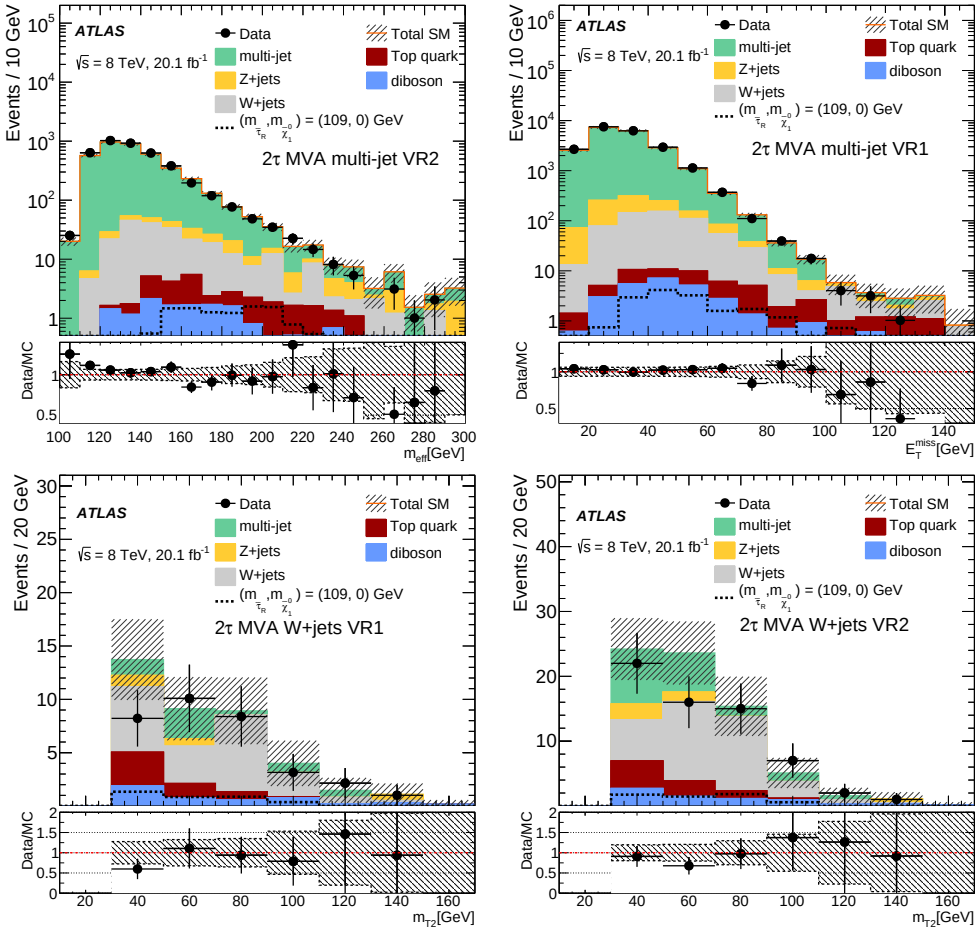

Figure 5.12: E_T^{miss}, m_{eff} and MT2 distribution for direct stau VRs.

Table 5.20: W CR and multi-jet CR definition used in the combined fit. Signal region (SR) definition is also shown here as comparison.

W CR	multi-jet CR	Signal region
1 tight tau and 1 isolated muon with opposite charge	== 2 loose OS taus	== 2 medium OS taus
-	== 0 tight tau	≥ 1 tight tau
b-jet veto	b-jet veto	b-jet veto
$12GeV < m_{\tau,\mu} < 40GeV$ or $m_{\tau,\mu} > 100GeV$	Z-veto	Z-veto
$\delta\phi(\tau,\mu) < 2.7$, $\delta\eta(\tau,\mu) < 2.0$	-	-
$E_{\mathrm{T}}^{\mathrm{miss}} > 40GeV$	$m_{T2} > 30GeV$	$m_{T2} > 30GeV$
$m_{T,\tau} + m_{T,\mu} > 80GeV$	$t_{cut} > 0.07$	$t_{cut} > 0.07$

Model-independent upper limits on the visible cross-section are also derived for the BDT SR, with the HistFitter framework [98]. The upper limits on the cross section for direct stau production are shown in Fig.5.14 for a combination of right-handed and left-handed staus pairs. The best observed upper limit on the signal strength is found for a stau mass of 100 GeV and a massless $\tilde{\chi}_1^0$, which can be excluded. The theoretical cross section

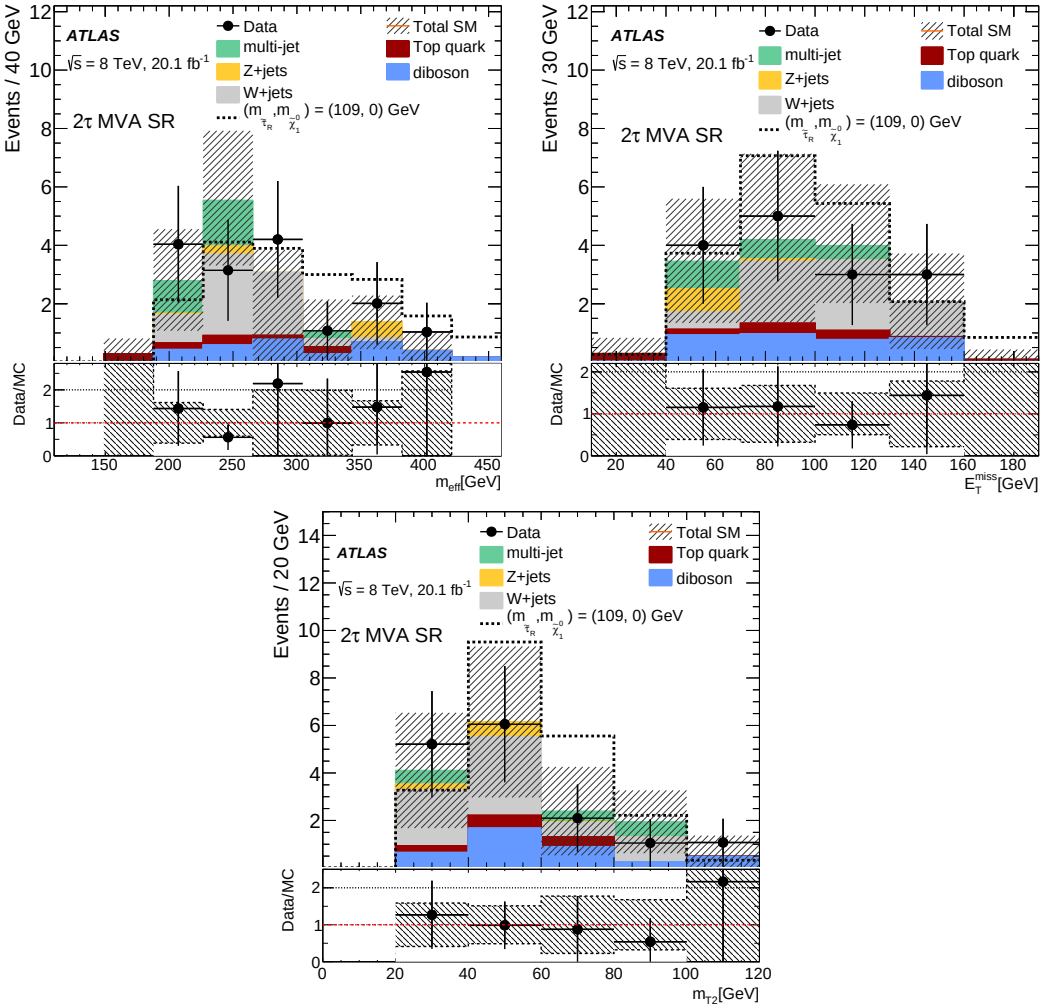

Figure 5.13: E_T^{miss}, m_{eff} and distribution for direct stau SR.

at NLO is 0.04 (0.09) pb for right(left)-handed stau pair production; the excluded cross section is 0.06 (0.21) pb. All those results are now part of an ATLAS publication [99]. The comparison of MVA and cut-based analysis are shown in Fig. 5.15.

Generally, the best expected p-value of the signal points are mainly obtained by MVA analysis, especially in low LSP and $\tilde{\tau}$ mass region. Note that the training procedure takes only the low LSP and $\tilde{\tau}$ mass point as input. So in the future with more statistics from data, it would be possible for this analysis to explore higher along the LSP and $\tilde{\tau}$ mass axis. It is also prospecting to have several SRs defined, each with a different signal point involved in the training procedure. This would help a lot in the high LSP and $\tilde{\tau}$ mass region.

Table 5.21: Fit results for an integrated luminosity of 20.1fb^{-1}. Nominal MC expectations (normalised to MC cross-sections) are given for comparison. Systematic uncertainty shown only for background estimation in the SR. For the other items, both statistical and systematic uncertainty are shown.

	W CR	multi-jet CR	Signal region
Observed events	3991	10	15
Fitted bkg events	3990.40 ± 63.64	10.01 ± 3.98	14.69 ± 5.13
Fitted diboson events	184.23 ± 46.44	1.64 ± 1.50	4.36 ± 1.59
Fitted top events	242.96 ± 67.83	$0.71^{+1.08}_{-0.71}$	1.24 ± 0.85
Fitted wjets events	3179.47 ± 151.00	5.73 ± 5.05	7.27 ± 3.37
Fitted FAKE events	0.00 ± 0.00	$1.93^{+5.11}_{-1.93}$	$0.93^{+2.63}_{-0.93}$
Fitted FAKEw events	240.63 ± 83.06	0.00 ± 0.00	0.00 ± 0:00
Fitted zjets events	143.10 ± 28.46	0.00 ± 0.00	$0.89^{+1.22}_{-0.89}$
MC exp. SM events	4069.34 ± 1028.76	10.00 ± 5.98	14.60 ± 5.98
MC exp. diboson events	184.29 ± 46.84	1.71 ± 1.51	4.36 ± 1.60
MC exp. top events	242.99 ± 68.30	$0.74^{+1.12}_{-0.74}$	1.25 ± 0.85
MC exp. wjets events	3258.50 ± 1010.44	6.13 ± 5.76	7.45 ± 4.48
MC exp. FAKE events	0.00 ± 0.00	$1.41^{+3.77}_{-1.41}$	$0.65^{+1.70}_{-0.65}$
MC exp. FAKEw events	240.42 ± 83.89	0.00 ± 0.00	0.00 ± 0.00
MC exp. zjets events	143.13 ± 28.73	0.00 ± 0.00	$0.89^{+1.23}_{-0.89}$

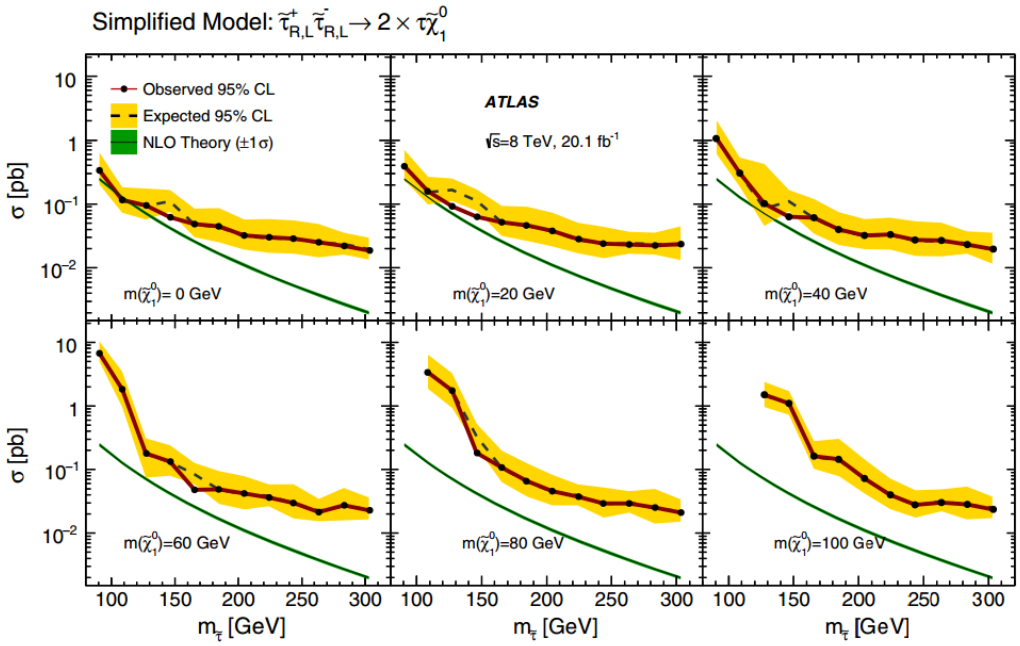

Figure 5.14: The expected upper limits on the cross-sections of direct stau production with the MVA SR.

Table 5.22: Breakdown of the dominant systematic uncertainties on background estimates in the signal region. Note that the individual uncertainties can be correlated, and do not necessarily add up quadratically to the total background uncertainty. The percentages show the size of the uncertainty relative to the total expected background.

Uncertainty of channel	SR
Total background expectation	14.69
Total statistical($\sqrt{N_{exp}}$	±3.83
Total background systematic	±5.13 [34.95%]
stat SR	±2.97 [20.2%]
RESOST	±2.90 [19.7%]
uncertainty on the norm factor of W	±2.22 [15.1%]
tauTFAKESF	±2.05 [13.9%]
generator uncertainty of W+jets	±1.90 [12.9%]
JES	±1.54 [10.5%]
SCALEST	±1.52 [10.3%]
meff weight	±1.45 [9.9%]
uncertainty on the norm factor of QCD	±1.29 [8.8%]
generator uncertainty of diboson	±0.90 [6.1%]
tauTTRIGSF	±0.57 [3.9%]
tauTIDSF	±0.42 [2.8%]
pileup	±0.32 [2.2%]
tauTES	±0.23 [1.6%]
generator uncertainty of top	±0.17 [1.1%]
bjet	±0.14 [0.98%]
JER	±0.12 [0.83%]
generator uncertainty of Z+jets	±0.11 [0.74%]
mistagjet	±0.06 [0.43%]
cjet	±0.05 [0.32%]
systematics from multi-jet estimation in SR	±0.05 [0:32%]

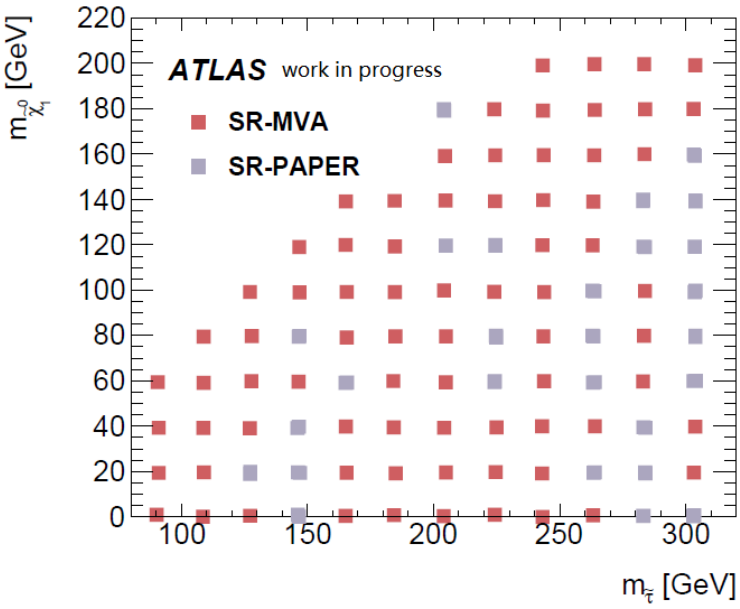

Figure 5.15: SR with best expected p-value for each point in direct stau production, brown for MVA and grey for cut-based analysis.

Chapter 6

Search for supersymmetry in final states with jets and two same-sign leptons or three leptons

6.1 Introduction

This chapter presents the search for SUSY particles in final states with two light-leptons (electrons or muons) of the same electric charge (same-sign leptons, SS) or three leptons (3L), jets and missing transverse momentum (MET, $E_{\mathrm{T}}^{\mathrm{miss}}$) [100, 101, 102]. Searches with SS light-leptons in final state is sensitive to a wide variety of models based on very different assumptions. With low SM backgrounds, such analyses have been conducted by ATLAS since the beginning of data-taking. The results presented here are using data collected in 2015 and up to July 2016 by the ATLAS experiment at a center-of-mass energy of $\sqrt{s} = 13TeV$, with a total integrated luminosity of $13.2fb^{-1}$.

Several signal benchmarks for a few SUSY scenarios are used in the analysis. Observed data and predicted SM yields are compared in a set of signal regions. The estimation of the backgrounds are sorted into 3 categories:

- **Prompt SS leptons process** - background events with prompt same-sign leptons. These backgrounds are estimated using Monte Carlo simulation, with theoretical computations of their cross-sections.
- **Charge-flipped electrons process** - background events with one of the leptons being charge-misidentified. These background are estimated using data-driven estimation with charge-flip rate measured in some dedicated regions.
- **Fake-lepton process** - events with at least one of the other objects (jet/photon...) reconstructed as a lepton. These backgrounds are also estimated using data-driven method called “Matrix Method”.

These background yields are compared to observed data in a few validation regions (VR) enriched in the corresponding processes. Statistical interpretation of the observations in the signal regions (SR) is performed through the HistFitter framework [98].

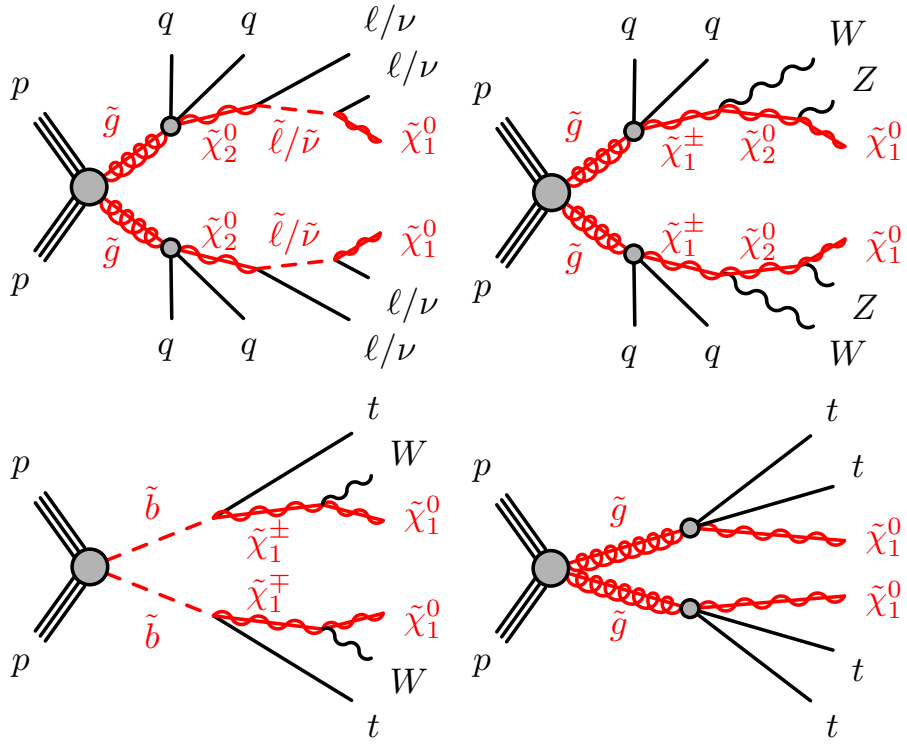

Figure 6.1: Decay modes in the four benchmark SUSY scenarios, featuring $\tilde{g}\tilde{g}(upper)$, $\tilde{b_1}\tilde{b_1^*}(lower-left)$, and $\tilde{g}\tilde{g} \rightarrow tt\tilde{\chi}_1^0 tt\tilde{\chi}_1^0(lower-right)$ pair production.

6.2 SS2l/3l SUSY scenarios

All the Frynmen diagrams of the 4 relevant benchmark SUSY scenarios are shown in Fig. 6.1 [103].

6.2.1 Gluino pair production with stop-mediated decay

In this scenario, gluinos are coupling preferentially to stops which are lighter than the other squarks. However, gluinos are assumed to be lighter than stops, and decay via a virtual stop into a top-quark triplet:

$$\tilde{g} \rightarrow t\bar{t}\tilde{\chi}_1^0.$$

The pair production of gluinos leads to a final state containing four top-quarks and two neutralinos. This model is commonly used as a benchmark to compare analyses sensitivities since its characteristic final state is accessible in many experimental signatures. In the competition against other analyses, earlier searches of SS-leptons final state showed only competitive power in the diagonal region [104, 105, 106]. Particular attention has been payed in the choice of SRs for this region in the phase space.

To be more specific, in the signal samples used in this analysis, the mass of the lightest stop is fixed to 10 TeV and is mostly Right-handed, with only gluino pair production considered. B-tagged jets are typically contained in the signal events. That's why this scenario is used as benchmark to define the signal regions with more than 3 b-jets. The region

of phase-space are constrained by $\delta m(\tilde{g},\chi_1^0) < 2m_t$, where gluinos decay via one or two offshell top quarks. We also call it "Gtt" as the abbreviated form of this scenario.

6.2.2 GG2step

This scenario features gluino pair-production with two-step decays via neutralinos χ_2^0 and sleptons:

$$\tilde{g} \to q\bar{q}\tilde{\chi}_2^0 \to q\bar{q}(\tilde{l}l/\tilde{\nu}\nu) \to q\bar{q}'(\ell\ell/\nu\nu)\tilde{\chi}_1^0,$$

therefore the b-jet multiplicity in this scenario is low. The final state consists of charged leptons, four jets and invisible part (neutrinos and neutralinos). The average jet multiplicity is the smallest among all the 4 interested scenarios. Another characteristic is the large fraction of events with several leptons. The same-sign leptons + jets search is very competitive for this model, unlike the other scenarios that have a rather low acceptance due to the measured branching ratios [107]. This scenario is used as as benchmark to define the signal regions with 3 leptons and no b-jet.

The signal grids is built with varies gluino and $\tilde{\chi}_1^0$ masses. The $\tilde{\chi}_2^0$ mass is chosen half-way between the gluino and LSP masses, and the sleptons masses are also set equal and half-way between the $\tilde{\chi}_2^0$ and LSP. The right handed sleptons are assumed heavy and do not participate to the decay. The generated MC samples assume equal probability of the decay of the decay through all squarks except top squarks, which can lead to final states with several b-jets.

Also, we consider another scenario which features gluino pair-production with two-step decays via gauginos and W and Z bosons,

$$\tilde{g} \to q\bar{q}'\tilde{\chi}_1^\pm \to q\bar{q}'W\tilde{\chi}_2^0 \to q\bar{q}'WZ\tilde{\chi}_1^0,$$

mediated by generic heavy squarks of the first and second generations. The final state consists of two W and two Z bosons (possibly offshell), four jets and invisible parts. Experimentally, this scenario leads to events with large jet multiplicities and a fair branching ratio for dileptonic final states. Signal regions with many jets but none tagged as a b-jet is defined aiming at this scenario. The signal grid is built with variable gluino and $\tilde{\chi}_1^0$ masses, and the $\tilde{\chi}_1^\pm$ and $\tilde{\chi}_2^0$ masses are set such that masses, and the latter half-way between the gluino and $\tilde{\chi}_1^0$, and the former lies half-way between $\tilde{\chi}_1^\pm$ and $\tilde{\chi}_1^0$ masses.

6.2.3 Direct sbottom

In this scenario, bottom squarks are rather light and assumed to decay in a top quark and a chargino $\tilde{\chi}_1^\pm$, with a subsequent decay $\tilde{\chi}_1^\pm \to W^\pm\tilde{\chi}_1^0$. It provides complementarity to the mainstream $\tilde{b}_1 \to b\tilde{\chi}_1^0$. This final state may lead to various experimental signatures, and the model has been considered so far only by the same-sign leptons and jets search [108] [109]. Typically, signal events in this scenario contain one or two b-tagged jets, making it a benchmark to define the signal regions with ≥ 1 b-jet. The model focuses on the case that chargino-neutralino mass difference is fixed to 100 GeV, therefore always allowing on-shell W bosons in the $\tilde{\chi}_1^\pm \to W^\pm\tilde{\chi}_1^0$ decay. Note that only pair production of the lightest sbottom is considered in this analysis.

6.3 Object selection

This section will present all the objects that are used in the analysis, including electrons, muons, jets and missing transverse energy. The definitions of these objects uses the recommendations by corresponding performance group[110], and is coherent with SUSYTools-00-07-89, analysis release Base2.4.15, the METUtilities-00-02-30 and ElectronEfficiencyCorrection-00-01-66 packages.

Compared to the previous studies in RUN1, this analysis encounters increased level of pile up and collision energy. Therefore, MV2 B-tagging algorithm are used instead of MV1 in RUN1. Meanwhile, the cuts of the variable m_{eff} increase due to the abandon of m_T (too much correlated with other variables).

6.3.1 Jets

The jets used in this analysis are reconstructed using the anti-k_t jet algorithm (see chapter 3) with the distance parameter ΔR set to 0.4, calibrated with the EMTopo scheme applying the jet area pile-up corrections. The jet selections are mainly including:

- Transverse momenta and pseudorapidity, $p_T > 20$ and $|\eta| < 2.8$.
- Jet Vertex Tagger (JVT) requirements. jets with $p_{\mathrm{T}} < 50$ GeV, $|\eta| < 2.4$ and $JVT < 0.64$ after the overlap removal procedure are rejected. This is aiming at reducing the effects of pileup[111].
- Bad jet veto. Any event with a jet ($|\eta| < 4.9$) tagged as "bad" according to the Very-Loose criterion is rejected. This helps remove events with fake $E_{\mathrm{T}}^{\mathrm{miss}}$.
- The MV2c20 algorithm is used for tagging of b-jets, at the 70% efficiency working point. This neural network based algorithm uses output from JetFitter+IP3D, IP3D and SV1 algorithms. The 70% efficiency working point was optimized in a study using MC15 simulated signal and background samples.

All the jet selection is summarized in Table 6.1.

Table 6.1: Summary of the jet selection criteria.

Pre-selected jet	
Collection	AntiKt4EMTopo
Acceptance	$p_T > 20GeV$, $\|\eta\| < 2.8$
Jet vertex tagger	reject jets with $p_T < 60GeV$, $\|\eta\| < 2.4$ $JVT < 0.59$ after overlap removal
b-jets	
Acceptance	$p_T > 20GeV$, $\|\eta\| < 2.5$
b-tagging	MV2c10 algorithm 70% OP MV2c10 algorithm 85% OP for overlap removal

6.3.2 Electrons

Two sets of electron selections are used in the analysis:

- the baseline electrons. A few relatively loose cuts are applied to select this set of electrons. The baseline electrons are used in overlap removal procedure and the background estimation.
- the signal electrons. The signal electrons are selected from the baseline ones, by adding a few more tight cuts. They are used for the signal region definition.

As recommended by the Egamma-CP group, the likelihood-based electron identification are used for RUN-2 since it provides more than twice background rejection than the cut-based one. The likelihood-based electron identifier provides 4 working points (`VeryLooseLH`, `LooseLH`, `MediumLH`, `TightLH`) as output. An electron with $E_T > 10$ GeV and $|\eta| < 2.47$ can be selected as a baseline one if it satisfy the LooseLH requirements. Note that electrons in the LAr crack region ($1.37 < |\eta| < 1.52$) are rejected since they are highly contaminated by non-prompt electrons. Also, the transverse impact parameter significance ($|d_0/\sigma(d_0)|$) is required to be less than 5 for the baseline electrons, which is recommended by the Tracking-CP group. This helps reduce the rate of charge mis-identification (also called "charge-flip" electron).

Additional requirements are needed for a baseline electrons to be a signal one. MediumLH identification is required and the longitudinal impact parameter ($|z_0 \cdot sin(\theta)| <$) should be within 0.5 mm, which is also recommended by the Tracking-CP group.

For all the events in MC, a multiplicative event weight is applied for each baseline/signal electron. These weights are aiming at corrections for differences in efficiency between data and MC. The summary of the electron selections are shown in Table. 6.2 (left).

Table 6.2: Summary of the lepton selection criteria.

	Pre-selected Electron	Pre-selected Muon
Acceptance	$p_T > 10GeV$, $\eta^{clust} < 2.47$ except $1.37 < \eta^{clust} < 1.52$	$p_T > 10GeV$, $\|\eta\| < 2.5$
Quality	LooseAndBLayerLLH	$xAOD :: Muon :: Medium$
Impact parameter	$\|d_0/\sigma(d_0)\| < 5.0$	
	Signal Electron	Signal Muon
Quality	MediumLLH $\|\eta\| < 2.0$	– –
Isolation	"FixedCutTight"	"FixedCutTightTrackOnly"
Impact parameter	$z_0 sin\theta < 0.5mm$	$z_0 sin\theta < 0.5mm$ $\|d_0/\sigma(d_0)\| < 3.0$

6.3.3 Muons

The same as the electrons, the muons are also selected into baseline and signal muons. As a recommendation by the Muon-CP group, RUN-2 muon reconstruction combines the

STACO and MUID chains in RUN-1 to achieve best performance, which has also 4 working points as output: `Tight`, `Medium`, `Loose` and `VeryLoose`.

The baseline muon are also used in the overlap removal procedure as well as the background estimation. They are selected with a few cuts, including muon-ID (Medium), $p_T > 10$ GeV, $|\eta| < 2.4$. While the signal muons is required to be more tight with some cuts on the transverse impact parameter significance and the longitudinal impact parameter, as summarized in Table. 6.2 (right). The same as the electron, a multiplicative event weight is applied for all muons in a MC event.

6.3.4 Missing transverse energy

The missing transverse energy (E_T^{miss}) uses the xAOD container MET_Ref_Final as input. Calibrated electron, muon, jet and photons objects are used in the reconstruction.

6.4 Event selection

The following trigger strategy is used in the analysis:

- **2015 data**: For events with $E_T^{miss} < 250$ GeV, we use the logical "or" of the 3 dilepton triggers: HLT_2e12_lhloose_L12EM10VH, HLT_e17_lhloose_mu14, HLT_mu18_mu8noL1. For events with $E_T^{miss} > 250$ GeV, we use the logical "or" of the dilepton triggers above and HLT_xe70.
- **2016 data**: For events with $E_T^{miss} < 250$ GeV, we use the logical "or" of the 3 dilepton triggers: HLT_2e17_lhvloose_nod0, HLT_e17_lhloose_nod0_mu14, HLT_mu20_mu8noL1. For events with $E_T^{miss} > 250$ GeV, we use the logical "or" of the dilepton triggers above and HLT_xe100_mht_L1XE50.

The following criteria are applied after the trigger selection to select a sample of two same-sign or three leptons:

- **Jet cleaning**: as the Jet-Etmiss group recommends, events are required to pass the VeryLooseBad set of cleaning requirements. If any pre-selected jets fails the jet quality criteria, the event would be rejected. These requirements can help remove events with significant energy deposit, such as cosmic rays, beam-induced particles, as well as noise.
- **Primary Vertex**: events are selected only if they have a primary vertex.
- **Bad Muon Veto**: events are rejected if they contain at least one "bad" muon before the overlap removal. The "bad" definition is: $\sigma(q/p)/(q/p) > 0.2$.
- **Cosmic Muon Veto**: in order to reduce the effect of cosmic rays, events are rejected if any of the muons are a cosmic muon candidate. If a pre-selected muon satisfies $|z_0| < 1.0$ mm and $|d_0| < 0.2$ mm, it is taken as a cosmic muon candidate.
- **At least two leptons**: at least two signal leptons are required for each selected event, of which the two leading leptons must have transverse momentum larger than 20 GeV. Moreover, if the event contains a third signal lepton with $p_T > 10$GeV, the event is regarded as a three-lepton event, otherwise as a two-lepton event.

- **Same-sign**: if the event is a two-lepton event, the two leading leptons have to with the same charge.

The data sample is then divided into three channels depending on the flavor of the two leptons forming the same-sign pair ($ee, \mu\mu, e\mu$). If more than one same-sign pairs can be built, the one involving the leading lepton (otherwise the pair involving the sub-leading lepton) will be used in the channel classification.

6.5 Signal regions optimization and definition

The optimization of the signal regions was performed in assumption that the final data sample reach an integrated luminosity of 10 fb^{-1} The value is an estimation of the dataset available by end of July 2016 combined with 2015 data, While finally, the integrated luminosity reaches 13.2 fb^{-1}, which is close to the estimated one.

The optimization consists of two steps. The first step would be a loose classification of events in terms of number of b-jets or leptons in the final state:

- 3 leptons, b-jet veto, low jet multiplicity. This category is associated to $\tilde{g}\tilde{g}$ production with $\tilde{g} \rightarrow q\tilde{q}$.
- 2 SS leptons, b-jet veto, high jet multiplicity. This category is associated to $\tilde{g}\tilde{g}$ production with $\tilde{g} \rightarrow q\tilde{q}WZ$
- 2 SS leptons, >= 1 b-jet. This category is associated to sbottom production
- 2 SS leptons, >= 3 b-jets. This category is associated to gluino pair production with $tt\tilde{\chi}_1^0$.

The second step is the optimization of the cut-off point for other main discriminant variables, like number of jets above a certain p_T threshold, m_{eff} and E_T^{miss}). The discovery significance Zn is also used in this analysis to determine the best configuration of the variables, which is implemented in the TROOT as the function RooStats::NumberCountingUtils::BinomialExpZ() [112]. 30% systematic uncertainty is assumed as the input of Zn calculation, which is realistic based on 2015 results. Note that only configurations with at least two signal events are kept. As an example, the distribution of discovery significance as a function of $m\tilde{b}$ and $m\tilde{\chi}_1^0$ are shown in figure. 6.2 and figure. 6.3.

The final proposal for the SRs to be used for a luminosity scenario of 10 fb^{-1} is summarized in Table 6.3. In the case of $3l$ and $\geq 2l$+b-jet veto, two signal regions are defined targeting either compressed spectra or large mass splittings. In the case of $\geq 2l+b-jetveto$, one single SR was found to have a good performance across the whole signal grids.

6.6 Background Estimation

With the SRs defined, the main backgrounds should include the following three categories:

- Prompt SS leptons process. This category consists of events that have two prompt leptons. Since these events are difficult to be distinguished from the signal, Monte Carlo simulation is used to estimate the contribution.

Table 6.3: Definitions of the RPC signal regions for $10 fb^{-1}$

SR	N_ℓ	$N^{20}_{b\text{-jets}}$	N_{jets}	$p_{\text{T}}^{\text{jets}}$	$E_{\text{T}}^{\text{miss}}$ [GeV]	m_{eff} [GeV]
SR3L1	≥3	=0	≥4	40	>150	-
SR3L2	≥3	=0	≥4	40	>200	1500
SR0b1	≥2	=0	≥6	25	>150	>500
SR0b2	≥2	=0	≥6	40	>150	>900
SR1b	≥2	≥1	≥6	25	>200	>650
SR3b	≥2	≥3	≥6	25	>150	>600

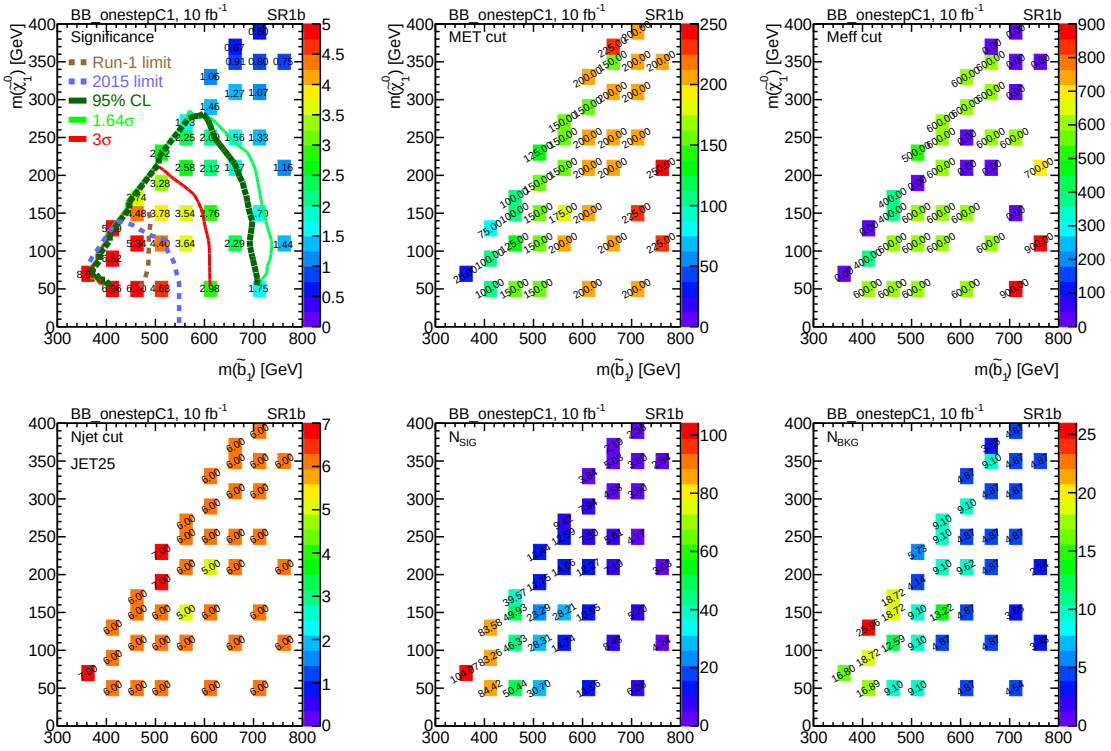

Figure 6.2: Discovery significance for the SRs without b-jets defined, with assumed luminosity of $10 fb^{-1}$.

- Charge-flipped electrons process. This kind of event contains one charge-misidentified electron. The possibility of a electron being charge-misidentified is measured in some dedicated CRs, which will be used in the data-driven estimation of the charge-flip contribution.

- Fake-lepton process. The fake-lepton process stands for events with at least one of the leptons being fake. Matrix-Method are used to estimate its contribution.

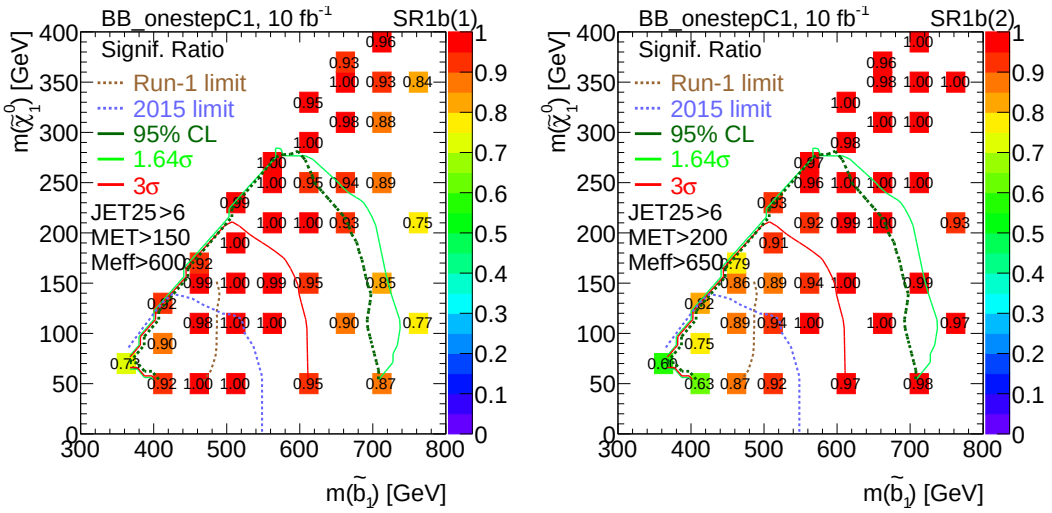

Figure 6.3: Discovery significance for the SRs with b-jets defined, with assumed luminosity of $10 fb^{-1}$.

6.6.1 Background Estimation - fake leptons

Some processes produce objects that will be misidentified as leptons, such as heavy flavor meson decays, converted photons origins, light hadrons faking the electron shower, in-flight decays of kaons or pions to muons... Generally, these objects have bad response to the electron/muon identification, as well as non-zero impact parameters and bad isolation. These properties can be used in distinguishing the fake leptons from the prompt ones. Matrix method is used as an accurate estimation on the fake lepton contribution, making use of the properties. Meanwhile, ABCD method and MC template fit are used as cross-check.

6.6.1.1 Matrix Method

Being a purely data-driven approach, the matrix method is commonly used in many analyses to estimate the fake object contribution in the regions of interest. Generally, a fake lepton will have low probability to satisfy some tight requirements like lepton identification, isolation and impact parameters cuts. Suppose that:

- we have x fake leptons and y real leptons in the signal lepton set, while the signal set has n leptons totally;
- we have m leptons selected as baseline leptons with tight selection;
- the fake leptons have a possibility ζ to pass the tight selection to be a signal lepton;
- the prompt leptons have a possibility ϵ to pass the tight selection to be a signal lepton;

then in the signal lepton set, we will have averagely x/ζ fake leptons and y/ϵ prompt leptons. So we have the following equations:

$$m = x/\zeta + y/\epsilon;$$

$$n = x + y.$$

On the contrary, it can be obtained that:

$$\begin{pmatrix} x \\ y \end{pmatrix} = \begin{pmatrix} \frac{\zeta}{\zeta-\epsilon} & \frac{-\zeta\epsilon}{\zeta-\epsilon} \\ \frac{-\epsilon}{\zeta-\epsilon} & \frac{\zeta\epsilon}{\zeta-\epsilon} \end{pmatrix} \begin{pmatrix} m \\ n \end{pmatrix} \tag{6.1}$$

This equation joint the number of fake signal leptons (x), real signal leptons (y) with number of total signal leptons (n) and baseline leptons (m), by a matrix with two important parameters ζ and ϵ. The parameters ζ is called fake lepton efficiency (fake rate) while ϵ is known as real lepton efficiency (real efficiency). The m and n values can be simply obtained by counting the SR and CR lepton numbers. With the knowledge of ζ and ϵ, it will be possible for us to calculate the x and y value. To be more specific, ζ and ϵ need to be measured in dedicated samples enriched in prompt or fake leptons respectively.

The uncertainties on ζ and ϵ will have large influence on the matrix method predictions. Moreover, if the signal lepton set has low statistics, and the estimated value of ζ is relatively higher than ϵ, negative yields would be obtained through the matrix method output.

Experimentally, the two same-sign lepton selection require a 4-dimensional matrix to do the estimation. We have assumed that the leading lepton would have the same possibility with the sub-leading one to make the calculation more simplified and accurate in such low statistic regions.

6.6.1.2 Fake rate measurement

Baseline-to-signal efficiency for fake leptons is measured in a sample enriched in fake leptons from $t\bar{t}$ processes, mostly semileptonic decays of bottom-flavoured hadrons. For that we select events with exactly two same-sign leptons and at least one b-jet in the eμ and $\mu\mu$ channels, which we use to measure respectively the efficiencies for electrons and muons. One of the muons, labelled tag, is required to satisfy a tight signal muon criteria to further increase the likelihood for it to be a prompt muon. For the electron (muon) fake rate extraction, the tag should verify $p_T > 30GeV$ (51 GeV) and must have triggered the event recording (via the mu26_imedium, mu18_mu8noL1 (mu26_imedium, mu20_2mu4noL1) triggers for 2015 (2016) data). We then require both $p_{Tcone30}$ and $E_{Tcone30}$ to be below $0.06 \times 30GeV(51GeV)$. MC simulations indicate that such an event selection is indeed dominated by $t\bar{t}$ processes in both channels, similarly to the signal regions (even those with b-jet veto). The origin and nature of the fake leptons composing this sample are therefore not very different than that in the signal regions. The efficiency can then be measured with the other baseline lepton in the event (probe).

Electron fake rate

As the ee channel is dominated by charge flip electrons, the measurement in data is performed using $e\mu$ pairs in which the muon is considered to be the tag lepton; the tag muon is trigger-matched, and must have a p_T greater than the probe electron. After the subtraction of estimated contributions from processes with prompt same-sign leptons or charged-flipped electrons, the rate is simply taken as the ratio between the number of signal and baseline probe electrons:

$$\zeta = \frac{N^{data}_{tight} - N^{cf}_{tight} - N^{prompt}_{tight}}{N^{data}_{loose} - N^{cf}_{loose} - N^{prompt}_{loose}}.$$

The background subtraction in the control regions are shown in the top of Fig. 6.4. The numbers of events with tight (signal) and loose (baseline, but not signal) probe electrons used for the measurement are shown in Table 6.4 for data and for Monte Carlo. The measured electron fake rates and their uncertainties are shown in Table 6.5. As a cross check, the fake rate using pure MC-driven estimation are shown in Fig. 6.5.

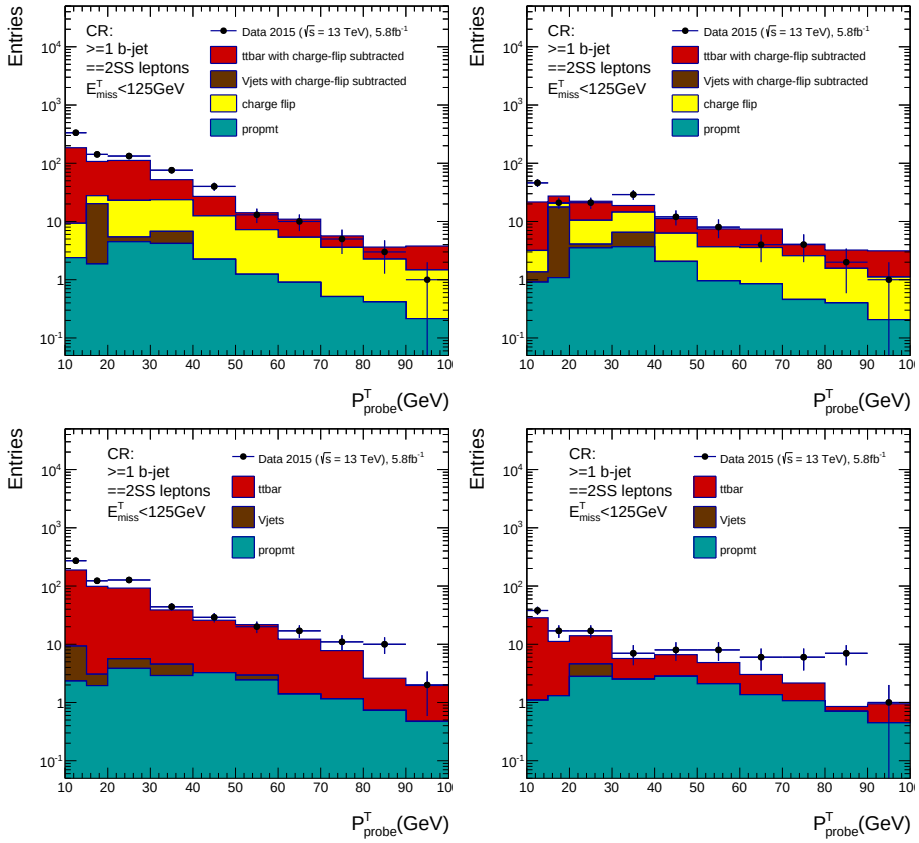

Figure 6.4: Backgound subtraction in the control regions for fake rate measurement: tag μ + baseline electron (top-left); tag μ + signal electron (top-right); tag μ + baseline muon (bottom-left); tag μ + signal muon(bottom-right).

Muon fake rate

The measurement of muon fake rate is performed in data with di-muon events using similar method as the electron except that the muons will not have charge-flip background contamination:

$$\zeta = \frac{N^{data}_{tight} - N^{prompt}_{tight}}{N^{data}_{loose} - N^{prompt}_{loose}}.$$

The background subtraction in the muon control regions are shown in the bottom of Fig. 6.4.

Another difference lies in the case when the probe muon is over 51 GeV in p_T. The 51 GeV threshold is the turning point of a tag muon to fire the single muon trigger. In the case the p_T of both mouns larger than 51 GeV, the tag and the probe muons would have reduced differentiation, causing an increasing probability for the tag muon to be fake. Thus, special treatment has been done to estimate the fake rate for muons above 51 GeV. The numbers

Table 6.4: Number of selected events with a tag muon and a probe electron in data and MC, as used for the electron fake rate computation in the presence of at least one b-jet.(first two tables) Only statistical uncertainties are shown, including the uncertainties on the charge flip rates. The third table shows for reference the number of events in which the "tag" muon fails and the probe electron passes the signal requirements, which is not used in the measurement but gives a rough idea of how often the tag muon might be a fake muon (and therefore the probe electron a real electron), which biases the measurement.

Samples	$10 < p_T < 15GeV$	$15 < p_T < 20GeV$	$20 < p_T < 30GeV$	$30 < p_T < 40GeV$	$40 < p_T < 60GeV$	$60 < p_T < 80GeV$
Events with a tight probe electron						
Data	110.00	39.00	43.00	55.00	39.00	22.00
Multi-boson	1.21 ± 0.27	1.01 ± 0.23	1.70 ± 0.37	1.60 ± 0.89	1.07 ± 0.24	0.59 ± 0.20
$t\bar{t}$ + W/Z	0.92 ± 0.05	1.14 ± 0.05	3.07 ± 0.09	2.78 ± 0.08	3.60 ± 0.09	1.81 ± 0.07
Other	0.44 ± 0.07	0.52 ± 0.08	1.26 ± 0.12	1.33 ± 0.12	1.36 ± 0.18	0.51 ± 0.07
Charge flip	2.24 ± 0.07 ± 1.69	3.32 ± 0.08 ± 2.59	10.70 ± 0.18 ± 1.79	13.67 ± 0.27 ± 0.75	13.75 ± 0.28 ± 0.63	8.87 ± 0.32 ± 0.79
Events with a loose probe electron						
Data	884.00	369.00	287.00	111.00	65.00	14.00
Multi-boson	1.41 ± 0.41	0.75 ± 0.24	0.67 ± 0.17	0.58 ± 0.23	0.26 ± 0.15	0.01 ± 0.00
$t\bar{t}$ + W/Z	1.32 ± 0.06	0.93 ± 0.05	1.34 ± 0.06	0.72 ± 0.04	0.48 ± 0.03	0.16 ± 0.02
Other	2.00 ± 0.71	0.99 ± 0.21	0.86 ± 0.10	0.49 ± 0.10	0.26 ± 0.05	0.09 ± 0.03
Charge flip	19.15 ± 0.49 ± 21.59	12.82 ± 0.39 ± 15.44	24.02 ± 0.62 ± 6.24	20.29 ± 0.77 ± 1.03	18.28 ± 0.85 ± 0.85	5.69 ± 0.57 ± 0.68
When tag muon fails signal cuts, probe electron passes signal cuts						
Data	43.00	24.00	37.00	12.00	9.00	4.00
Multi-boson	0.41 ± 0.18	0.07 ± 0.04	0.40 ± 0.15	0.20 ± 0.08	0.27 ± 0.09	0.22 ± 0.10
$t\bar{t}$ + W/Z	0.19 ± 0.02	0.24 ± 0.02	0.66 ± 0.04	0.70 ± 0.04	0.95 ± 0.05	0.41 ± 0.03
Other	0.24 ± 0.10	0.20 ± 0.04	0.27 ± 0.05	0.39 ± 0.16	0.41 ± 0.06	0.18 ± 0.04

Table 6.5: Electron fake rate measured in data together with its statistical uncertainty. The systematic uncertainty originating from the subtraction of "background" and charge-flip processes is also displayed.

p_T bin	$10 < p_T < 15GeV$	$15 < p_T < 20GeV$	$20 < p_T < 30GeV$	$30 < p_T < 40GeV$	$p_T > 40GeV$
ξ_e	0.109 ± 0.010 ± 0.001	0.085 ± 0.015 ± 0.003	0.092 ± 0.022 ± 0.014	0.286 ± 0.049 ± 0.020	0.296 ± 0.077 ± 0.046

of events with tight and loose probe muons used for the measurement are shown in Table 6.6. The measured muon fake rates and their uncertainties are shown in Table 6.7. As a cross check, the fake rate using pure MC-driven estimation are shown in Fig. 6.6.

Systematics for fake rate estimation

The following systematics sources are considered for the fake rate estimation:

- Contamination of fake muons in the tag leptons; The tag-and-probe method used for the fake rate estimation is based on the assumption that the tag lepton is a real muon. With the new (much tighter) tag definition, the tag muon is most of the time real. Thus, this source of systematic uncertainty is generally low.
- Background subtraction when estimating the fake rate. The contribution of prompt and charge-misID events are subtracted in the $t\bar{t}$-dominant control region where we measure the fake lepton rates. The effect of the prompt process is assigned by varying the MC normalizations by 30%, to cover the uncertainty on the production cross-section and statistics uncertainty [113]. Also, the effect of the statistics and systematics uncertainty of the charge-misID subtraction are considered for the electron fake rate estimation.
- Different environment between the CR and SR.

The assignment of the background subtraction systematics are shown on Table 6.8 and Table 6.9(second uncertainty column).

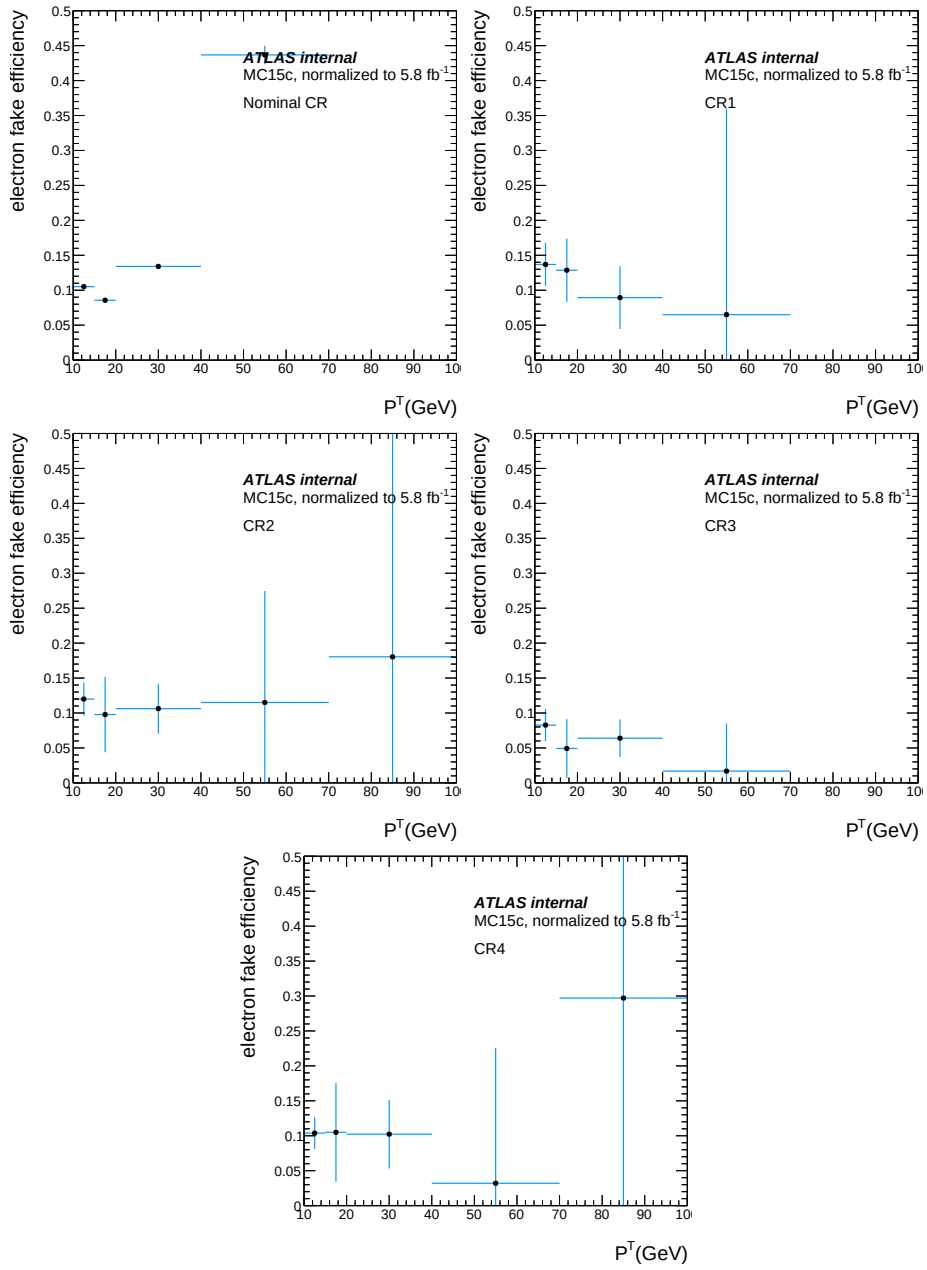

Figure 6.5: Electron fake rate in the CRs.

The fake leptons efficiencies are also affected by the nature of the fake leptons, and the events that produce them being different between the measurement and signal regions. This source of systematics are estimated by defining dedicated CRs respectively for the 6 RPC SRs and comparing the difference of fake rate estimated in the CRs to the nominal value. The definition of the CRs are shown on Table 6.10. $t\bar{t}$ Monte Carlo and truth match leptons are used for the study to avoid the cases with a fake tag muon, as well as gaining more statistics. The assigned systematics on the fake rate estimation are summarized in Table 6.8 and Table 6.9. Given all these results, we choose to assign an overall systematic

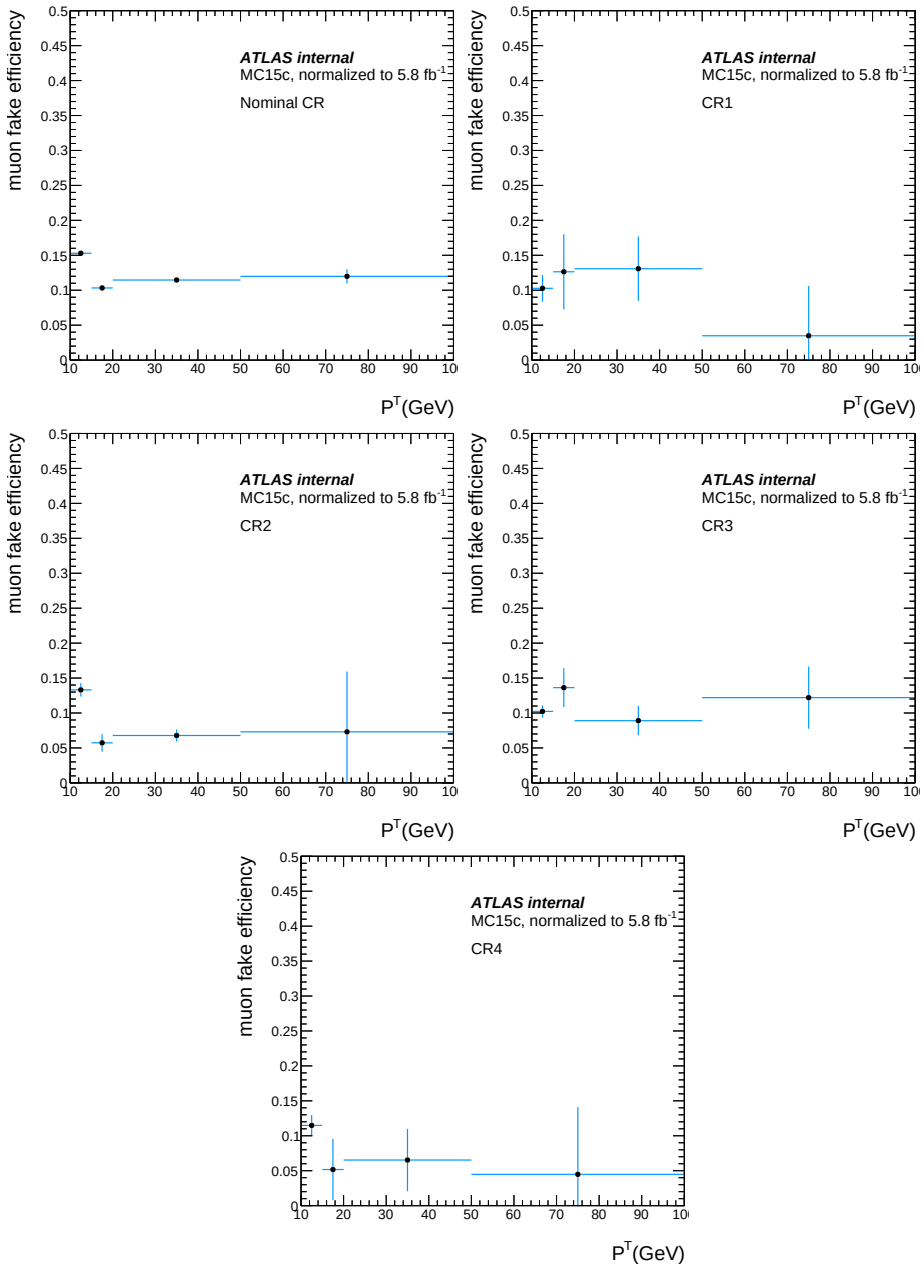

Figure 6.6: Muon fake rate in the CRs.

uncertainty of 50%.

6.6.1.3 Real efficiency measurement

Baseline-to-signal efficiency for real leptons is measured in a high purity data sample using $Z \to ee$ and $Z \to \mu\mu$ tag-and-probe. Firstly, events are selected by a single lepton trigger: e24_lhmedium_L1EM20VH or e24_lhtight_nod0_ivarloose for electrons, mu20_iloose_L1MU15 or mu24_ivarloose for muons. Secondly, the tag lepton should be signal muon and have triggered the event recording, with $p_T > 25GeV$. Thirdly, the probe lepton satisfies baseline

Table 6.6: Number of selected events with a tag muon and a probe muon in data and MC, as used for the muon fake rate computation (first two tables), in the presence of at least one b-jet. The numbers in the last columns correspond to the n2 and n1. Only statistical uncertainties are shown. The third table shows for reference the number of events in which the "tag" muon fails and the probe muon passes the signal requirements, which is not used in the measurement but gives a rough idea of how often the tag muon might be a fake muon (and therefore the probe muon a real muon), which biases the measurement.

Samples	$10 < p_T < 15GeV$	$15 < p_T < 20GeV$	$20 < p_T < 30GeV$	$30 < p_T < 40GeV$	$40 < p_T < 51GeV$	$p_T > 51GeV$
Events with a tight probe muon						
Data	101.00	37.00	32.00	17.00	14.00	19.00
Multi-boson	0.41 ± 0.20	0.87 ± 0.39	1.06 ± 0.32	0.97 ± 0.25	1.44 ± 0.76	0.75 ± 0.20
$t\bar{t}$ + W/Z	1.29 ± 0.06	1.43 ± 0.06	3.14 ± 0.09	3.21 ± 0.09	3.16 ± 0.09	3.93 ± 0.10
Other	0.63 ± 0.10	0.76 ± 0.13	1.18 ± 0.15	1.04 ± 0.11	0.89 ± 0.09	1.32 ± 0.21
Events with a loose probe muon						
Data	518.00	263.00	217.00	74.00	39.00	81.00
Multi-boson	0.89 ± 0.32	0.44 ± 0.17	0.82 ± 0.27	0.24 ± 0.10	0.31 ± 0.26	0.23 ± 0.16
$t\bar{t}$ + W/Z	0.71 ± 0.04	0.52 ± 0.03	0.68 ± 0.04	0.47 ± 0.04	0.24 ± 0.02	0.41 ± 0.03
Other	0.79 ± 0.09	0.52 ± 0.13	0.61 ± 0.17	0.17 ± 0.04	0.17 ± 0.05	0.38 ± 0.16
When tag muon fails signal cuts, probe muon passes signal cuts						
Data	17.00	2.00	10.00	3.00	4.00	45.00
Multi-boson	0.17 ± 0.13	0.01 ± 0.00	0.11 ± 0.06	0.26 ± 0.12	0.06 ± 0.04	0.12 ± 0.05
$t\bar{t}$ + W/Z	0.15 ± 0.02	0.17 ± 0.02	0.34 ± 0.03	0.33 ± 0.02	0.39 ± 0.03	0.26 ± 0.02
Other	0.06 ± 0.02	0.10 ± 0.03	0.22 ± 0.05	0.19 ± 0.05	0.17 ± 0.05	0.10 ± 0.04

Table 6.7: Muon fake rate measured in data and the associated statistical uncertainty. The systematic uncertainty originating from the subtraction of "background" is also displayed.

p_T bin	$10 < p_T < 15GeV$	$15 < p_T < 20GeV$	$20 < p_T < 30GeV$	$30 < p_T < 40GeV$	$40 < p_T < 51GeV$	$p_T > 51GeV$
ε_μ	0.161 ± 0.015 ± 0.001	0.115 ± 0.019 ± 0.003	0.110 ± 0.022 ± 0.006	0.139 ± 0.044 ± 0.016	0.182 ± 0.071 ± 0.029	0.140 ± 0.043 ± 0.017

requirements and the invariant mass of the tag and probe leptons should be within the Z mass window (between 80 and 100 GeV). Then the efficiency is measured as a function of p_T and η, shown in Fig. 6.7.

The following systematic uncertainties are assigned to the measured efficiencies:

- Background contamination: the background subtraction procedure in the measurement will bring systematics, although the overall effect should be quite limited.
- Trigger: a systematic uncertainty accounting for a potential bias at trigger level is considered in the previous analysis. It varies between 0 and 4%, depending on the p_T range.
- Extrapolation to busy environments: efficiencies are typically lower in such environments due to the proximity of jets and leptons; an uncertainty is assigned by comparing efficiencies in simulated $Z \rightarrow ll$ and Gtt events.

Evaluation of the background contamination in electron real efficiency measurement

The background contamination has been evaluated on data using a background template method. A sample enriched in background is obtained by reverted the calorimeter and track isolation cuts and requesting the electron object to fail the mediumLH identification. Two variation of the background template definition has been also defined to asses a systematic

Table 6.8: Electron fake rate systematics uncertainty as a function of p_{T} and SR.

p_{T}(GeV)	fake contanimation for tag	background subtraction	SR	variation for SRs	total
[10, 15]	1%	5%	SR3l	30%	30%
[10, 15]	1%	5%	SR0b	14%	15%
[10, 15]	1%	5%	SR1b	21%	22%
[10, 15]	1%	5%	SR3b	1%	5%
[15, 20]	1%	6%	SR3l	49%	49%
[15, 20]	1%	6%	SR0b	14%	15%
[15, 20]	1%	6%	SR1b	42%	42%
[15, 20]	1%	6%	SR3b	25%	26%
[20, 40]	2%	20%	SR3l	35%	40%
[20, 40]	2%	20%	SR0b	23%	31%
[20, 40]	2%	20%	SR1b	53%	57%
[20, 40]	2%	20%	SR3b	25%	32%
[40, 70]	2%	33%	SR3l	49%	59%
[40, 70]	2%	33%	SR0b	23%	40%
[40, 70]	2%	33%	SR1b	53%	62%
[40, 70]	2%	33%	SR3b	25%	42%

Table 6.9: Muon fake rate systematics uncertainty as a function of p_{T} and SR.

p_{T} (GeV)	fake contamination for tag	background subtraction	SR	variation for SRs	total
[10, 15]	1%	1%	SR3l	32%	32%
[10, 15]	1%	1%	SR0b	14%	14%
[10, 15]	1%	1%	SR1b	32%	32%
[10, 15]	1%	1%	SR3b	24%	24%
[15, 20]	1%	2%	SR3l	25%	25%
[15, 20]	1%	2%	SR0b	45%	45%
[15, 20]	1%	2%	SR1b	35%	35%
[15, 20]	1%	2%	SR3b	49%	49%
[20, 30]	1%	4%	SR3l	13%	14%
[20, 30]	1%	4%	SR0b	48%	48%
[20, 30]	1%	4%	SR1b	22%	23%
[20, 30]	1%	4%	SR3b	43%	43%
[30, 50]	1%	20%	SR3l	32%	38%
[30, 50]	1%	20%	SR0b	48%	52%
[30, 50]	1%	20%	SR1b	35%	40%
[30, 50]	1%	20%	SR3b	49%	53%

Table 6.10: Definition of CRs used for fake rate systematics assignment.

SR	N_ℓ	$N^{20}_{b\text{-jets}}$	N_{jets}	$p_{\text{T}}^{\text{jets}}$	Comments
CR1	≥3	=0	≥4	40	defined for 3l-SRs
CR2	≥2	=0	≥5	25	defined for 0b-SRs
CR3	≥2	≥1	≥6	25	defined for SR1b
CR4	≥2	≥2	≥5	25	defined for SR3b

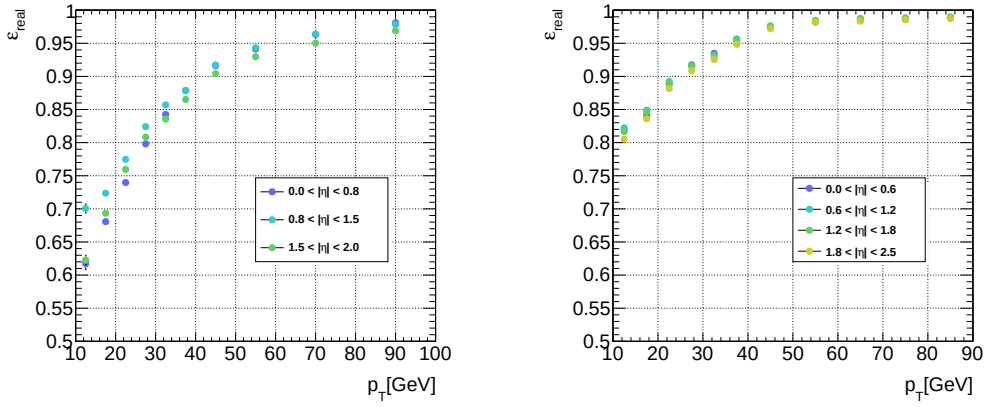

Figure 6.7: Real efficiency for electrons and muons.

on the template definition. Table. 6.11 summarizes the background template definitions.

Table 6.11: The definition of the background templates used to estimate the background contamination. The variation 1 and 2 templates are used to assess the systematic caused by the background contamination.

cut	variation 1 template	baseline template	variation 2 template
Identification	-	fail medium LH	fail medium LH
Calorimeter isolation	$E_T^{topocone20}/p_T > 6\%$	$E_T^{topocone20}/p_T > 15\%$	$E_T^{topocone20}/p_T > 20\%$
Track isolation	$p_T^{varcone20}/p_T > 6\%$	$p_T^{varcone20}/p_T > 8\%$	$p_T^{varcone20}/p_T > 15\%$

As a result shown in Fig. 6.8, the estimated background contribution in all the p_T and η bins are rather small (less than 1% of the baseline statistics).

6.6.1.4 Closure test

The charge-flip background should be subtracted in the fake-rate estimation. A closure test for the subtraction is indispensable as a validation of the charge-flip rate in $t\bar{t}$ and V + *jets* sample. Two regions in different $b-$ *jet* multiplicity was considered for the charge-flip closure test, definition shown on Table 6.12.

SS events and OS events are selected separately in the charge-flip closure test. The OS events are applied with charge-flip weight using rate estimated based on data or MC15 respectively. The contribution of charge-flip lepton background can also be estimated directly

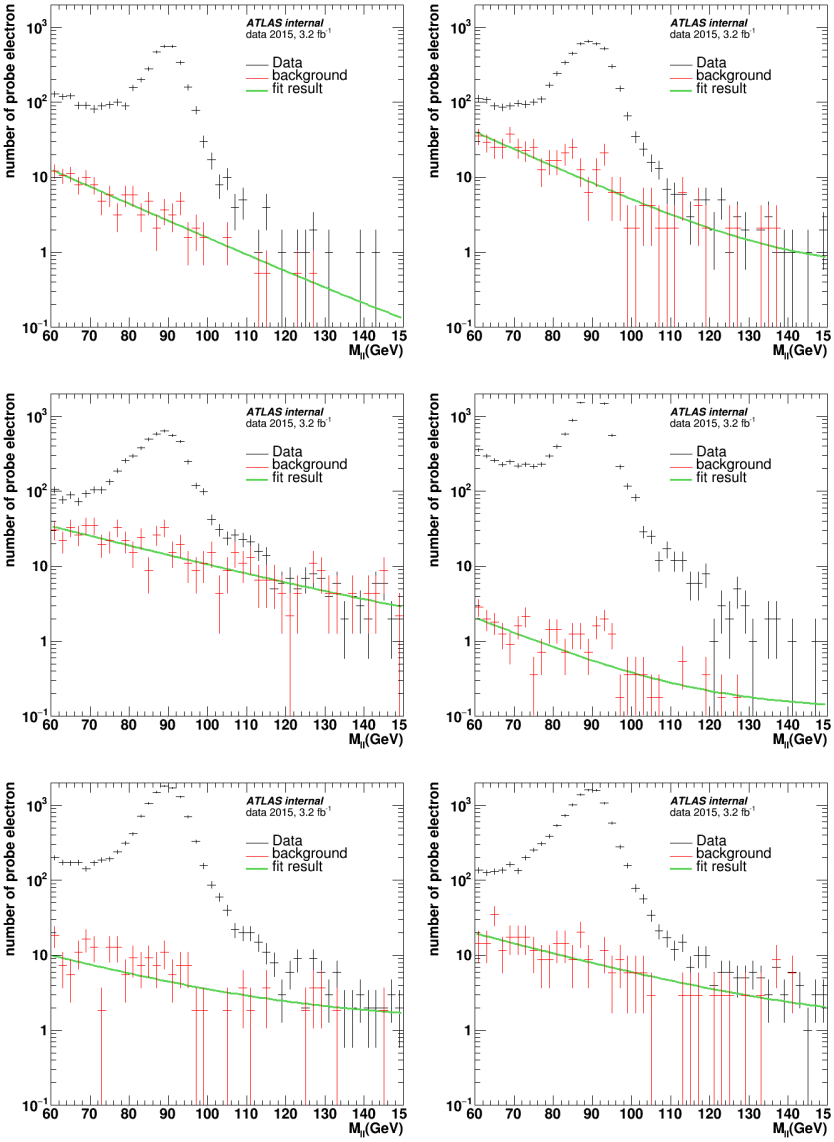

Figure 6.8: Background subtraction for electron real efficiency measurement. The top 3 plots represents the $10 < p_T < 15GeV$ region, with $0 < |\eta| < 0.8$, $0.8 < |\eta| < 1.37$ and $1.52 < |\eta| < 2.0$ respectively. The lower 3 plots represents the $15 < p_T < 20GeV$ region, with $0 < |\eta| < 0.8$, $0.8 < |\eta| < 1.37$ and $1.52 < |\eta| < 2.0$ respectively.

	Leptons	Jets
0-$b$jet region	$\geq$2 signal lepton p^T>10GeV	exactly 0 $b-jet$ p^T>20GeV
1-$b$jet region	$\geq$2 signal lepton p^T> 10GeV	$\geq$1 $b-jet$ p^T> 20GeV

Table 6.12: Lepton and $b-jet$s selection cuts of the region for charge-flip closure test.

using the truth information from the SS events. Number of jets distributions are used to perform the comparison between the two estimations of charge-flip, shown on Figure 6.9. The SS distribution should be consistent with the OS distribution using MC charge-flip rate. This is observed from the distribution, showing a good charge-flip subtraction in the fake-rate CR.

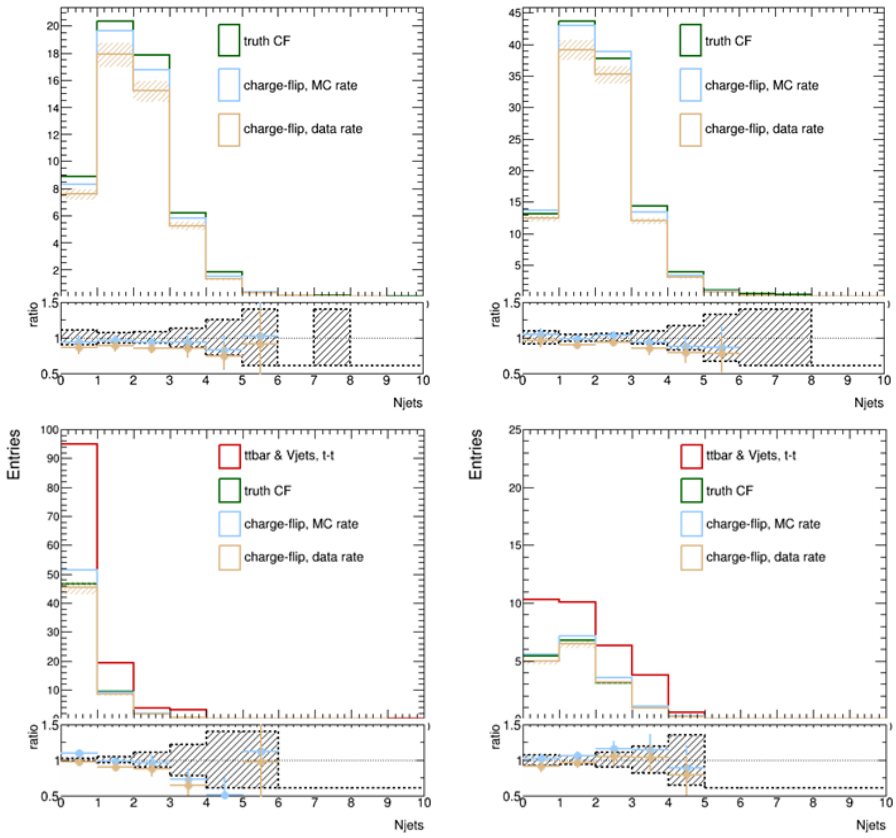

Figure 6.9: Distributions of number of jets for $t\bar{t}$ and V + *jets* sample: e-e channel, region 0-*b*jet (a), e-μ channel, region 0-*b*jet (b), e-e channel, region 1-*b*jet (c), e-μ channel, region 1-*b*jet (d). Comparisons are shown among: SS charge-flip events with truth selection (green histogram); OS events with charge-flip weight using rate from MC (blue); OS events with charge-flip weight using rate from data (golden).

6.6.1.5 Expected yields in signal regions

The expected yield for processes with fake leptons in the SRs are shown in Table 6.13. They are compared for cross-check with other methods, which shows consistency with each other.

6.6.2 Background with prompt leptons

The prompt same-sign lepton events can only be estimated using Monte Carlo simulation, due to the difficulty in discriminating them from the signal.

Table 6.13: Expected yields for background processes with fake leptons in the signal regions, shown for $13.2 fb^{-1}$. Both statistical and systematic uncertainties are included.

	SR3L1	SR3L2	SR0b1	SR0b2	SR1b
Raw matrix method	0.10 ± 0.29 ± 0.39	0.04 ± 0.15 ± 0.14	2.92 ± 1.09 ± 1.64	0.37 ± 0.43 ± 0.31	3.25 ± 1.08 ± 1.78
($t\bar{t}$ MC)	1.08 ± 0.21 ± 0.00	0.16 ± 0.11 ± 0.00	1.95 ± 0.40 ± 0.00	0.22 ± 0.06 ± 0.00	1.83 ± 0.21 ± 0.00
MC template	2.00 ± 0.47 ± 0.38	0.41 ± 0.33 ± 0.11	3.79 ± 0.93 ± 0.71	0.31 ± 0.09 ± 0.03	2.86 ± 0.33 ± 0.29
Final estimate	0.29 ± 0.29	0.15 ± 0.15	2.92 ± 1.09 ± 1.64	0.37 ± 0.43 ± 0.31	3.25 ± 1.08 ± 1.78

	SR3b	SR1b-GG	SR1b-DD	SR3b-DD
Raw matrix method	0.20 ± 0.44 ± 0.22	0.21 ± 0.24 ± 0.25	2.48 ± 1.00 ± 1.33	0.48 ± 0.48 ± 0.34
($t\bar{t}$ MC)	0.08 ± 0.03 ± 0.00	0.31 ± 0.08 ± 0.00	2.63 ± 0.51 ± 0.00	0.10 ± 0.03 ± 0.00
MC template	0.13 ± 0.05 ± 0.02	0.42 ± 0.10 ± 0.05	3.79 ± 0.68 ± 0.34	0.14 ± 0.05 ± 0.02
Final estimate	0.20 ± 0.44 ± 0.22	0.21 ± 0.24 ± 0.25	2.48 ± 1.00 ± 1.33	0.48 ± 0.48 ± 0.34

Prompt same-sign process and theoretical uncertainty

$t\bar{t}$ pair production with a leptonically-decaying W or Z boson constitutes the main source of background with prompt same-sign leptons. Results from the nominal MadGraph+Pythia8 sample are compared to alternative samples with varied normalization and factorization scales. The difference between the samples are recorded as the theoretical uncertainty.

Diboson processes decaying into $lll\nu$, $ll\nu\nu$ or $l\nu\nu\nu$ were estimated using simulation at NLO by the Sherpa 2.1.1 generator. The theoretical uncertainty of these processes is evaluated by comparing at truth level the results from the nominal samples with the following ones:

- Alternative samples with the factorization scale varied up and down by a factor of two from the nominal value.
- Alternative samples with the renormalization scale varied up and down by a factor of two from the nominal value.
- Alternative samples with the resummation scale varied up and down by a factor of two from the nominal value.
- Alternative samples with the CKKW merging scale scale varied up and down to a value of 15 and 30 GeV (with a value of 20 GeV used in the nominal samples).

Other rare processes are including:

Higgs boson production in association with a $t\bar{t}$ pair;

Higgs boson production in association with a W or Z;

$t\bar{t}WW$, tZ, $t\bar{t}t\bar{t}$ and $t\bar{t}t$ processes;

Triboson processes (WWW , WWZ, WZZ and ZZZ).

The generator cross-sections (at NLO) are used when normalising these backgrounds[114], and a 50% uncertainty is assigned on the summed contributions of all these processes.

All the experimental systematics considered for those processes are including:

- **Jet energy scale**
  Strongly reduced uncertainty sets provided by the JetEtMiss group, aiming at analyses which are not sensitive to jet-by-jet correlations arising from changes to the jet energy scale.

- **Jet energy resolution**
  An extra p_T smearing is applied to the jets in MC to account for a possible underestimate of the jet energy resolution.
- **Flavor tagging**
  Uncertainty caused in the flavour tagging of jets, provided by the Flavour Tagging CP group.
- **Egamma resolution**
  Uncertainty caused by the energy scale of electrons and photons.
- **Electron efficiency**
  Uncertainty sources associated with the electron efficiency scale factors provided by the Egamma-CP group.
- **Muon efficiency**
  Uncertainty sources associated with the muon efficiency scale factors provided by the Muon-CP group.
- **Muon resolution uncertainty**
  Uncertainty sources associated with the smearing of the inner detector and muon spectrometer tracks.
- **Muon momentum scale**
  Associated with the scale of the momentum of the muon objects.
- E_T^{miss} **soft term uncertainties**
  Associated with the MET reconstruction. Note that the JES and JER are also propagated to the E_T^{miss} uncertainties.
- **Pileup reweighting**
  Associated with the Pileup weight of the MC events.

All the experimental uncertainties are applied also on the signal samples when computing exclusion limits on SUSY scenarios. The yields of all the prompt lepton backgrounds are shown in Fig. 6.14.

Table 6.14: Expected yields for background processes with prompt leptons, in the SRs for $13.2 fb^{-1}$. Both statistical and theory uncertainties are included.

	$t\bar{t}V$	VV	Rare
SR3L1	0.77 ± 0.04 ± 0.23	4.18 ± 0.56 ± 1.67	0.80 ± 0.12 ± 0.40
SR3L2	0.12 ± 0.01 ± 0.04	0.70 ± 0.23 ± 0.32	0.21 ± 0.04 ± 0.10
SR0b1	0.90 ± 0.05 ± 0.27	3.72 ± 0.46 ± 1.49	0.77 ± 0.08 ± 0.38
SR0b2	0.23 ± 0.02 ± 0.07	0.71 ± 0.20 ± 0.43	0.18 ± 0.04 ± 0.09
SR1b	3.55 ± 0.10 ± 1.07	0.47 ± 0.17 ± 0.24	2.68 ± 0.14 ± 1.34
SR3b	0.36 ± 0.03 ± 0.11	0.00 ± 0.00 ± 0.00	0.89 ± 0.05 ± 0.44
SR1b-GG	0.59 ± 0.04 ± 0.18	0.08 ± 0.05 ± 0.04	0.63 ± 0.06 ± 0.32
SR1b-DD	4.62 ± 0.10 ± 1.38	0.61 ± 0.24 ± 0.31	2.55 ± 0.13 ± 1.27
SR3b-DD	0.48 ± 0.03 ± 0.14	0.00 ± 0.00 ± 0.00	0.76 ± 0.04 ± 0.38

6.6.3 Background with charge-flipped electrons

In a charge-flipped event, one of the electric charge of the electrons is mis-identified. The charge mis-identification is mostly created by additional close-by tracks formed by the original electron when interacting with the material of the inner tracker. If one of the secondary electron tracks is preferred in the reconstruction of the electron candidate, the charge assigned to the electron might be incorrect. Such events are strongly associated to analyses relying on same-sign leptons final states. As shown in Fig. 6.10, in many cases, the ratio between number of OS pair events and SS pair events is 10^2. This causes the fact that even with very low probability ($< 1\%$) for a electron to be charge mis-identified, the OS events flipped into the SS category would be not negligible. Charge-flip is negligible for muons due to much fewer interaction with matter.

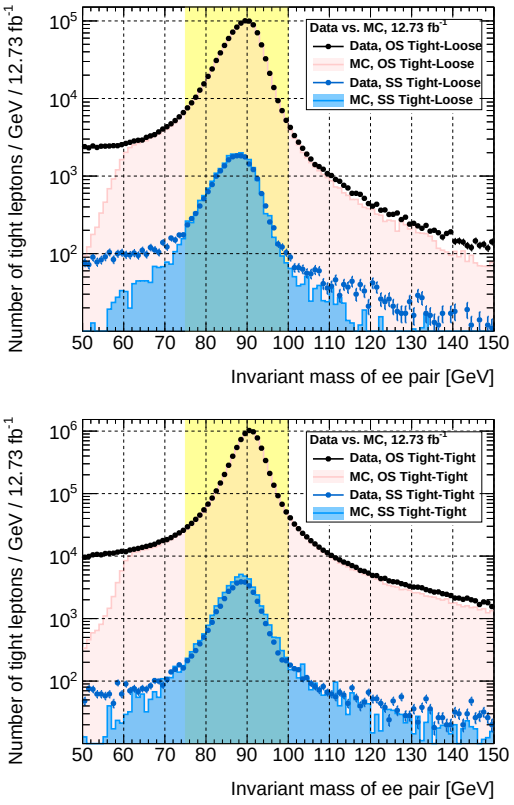

Figure 6.10: Invariant mass of opposite- and same-sign electron pairs, when both electrons satisfy signal requirements (upper) or one of them fails them (lower).

A pure data-driven method is used to estimate the contribution of charge-flip background, starting with the measurement of charge-flip rate ξ, which is the probability for an electron to be charge mis-identified. The basic idea to estimate ξ is to calculate the rate between number of SS pair electrons and OS pairs in a pure $Z \to ee$ sample. Theoretically, all the electron pairs should be OS as the decay product of Z^0. However, due to charge-flip, we can observe some SS electron pair in the $Z \to ee$ sample. Conversely, the SS electron pairs in $Z \to ee$ events must contain one charge-flipped electron. Here, the case with both

electrons charge-flipped are ignored since the probability is too small. A global charge-flip rate can be obtained with:

$$\xi = \frac{N_{Zee}^{SS}}{N_{Zee}^{SS} + N_{Zee}^{OS}}.$$

To be more accurate, the ξ value has to be assigned as a function of p_T and η. However, it is hard to distinguish which of the 2 SS electrons is the charge-flipped one; and if the 2 electrons are in different p_T or η bin, this method does not work anymore. Moreover, the limited statistics of SS events bring bias to the binned measurement. The most efficient and less biased use of the available statistics is obtained by simultaneously extracting the rates in all bins, with the maximization of the likelihood function describing the Poisson-expected yields of SS pairs:

$$L(\{N_{\varpi}^{\mathrm{SS,obs}}\}|\{\xi(\eta,p_{\mathrm{T}})\}) = \prod_{\varpi} \mathcal{P}\left(N_{\varpi}^{\mathrm{SS,obs}}|w_{\mathrm{flip}}(\xi(\eta_1,p_{\mathrm{T},1}),\bar{\xi}(\eta_2,p_{\mathrm{T},2}))\times N_{\varpi}^{\mathrm{OS+SS,obs}}\right) \qquad (6.2)$$

with $\varpi = (\eta_1, p_{T1}, 1, \eta_2, p_{T2}, 2)$ indexing bins, where (arbitrarily) $p_{T,\tau 1} > p_{T,\tau 2}$; the expression of w_{flip} is given by (1).

Background subtraction is done through a simple linear extrapolation of the invariant mass distribution sidebands. The charge-flip rates measured in data and MC are shown on Figure.6.11. In data, the nominal rates (signal electrons) go up to 0.7% in the barrel

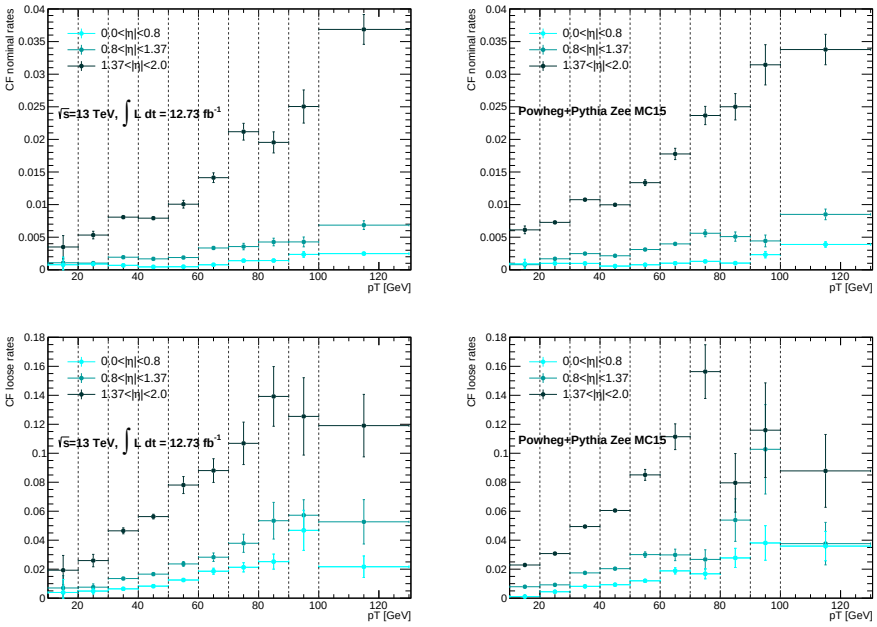

Figure 6.11: Charge-flip rate measured in data and MC.

region ($|\eta| < 1.37$), and increase up to 3.6% in the end-cap region ($|\eta| > 1.37$). For baseline electrons failing signal requirements, the rates are relatively higher, with 4-6% in the barrel region and up to 9-12% in the end-cap region.

The main uncertainties on the charge-flip rate measurement come from the background subtraction. The background is re-estimated using the following variations of the selection to assess the uncertainty:

(1) $75 < M_{ee} < 100GeV$, no background subtraction;

(2) $75 < M_{ee} < 100GeV$, sidebands of 20 GeV;

(3) $75 < M_{ee} < 100GeV$, sidebands of 25 GeV (nominal measurement);

(4) $75 < M_{ee} < 100GeV$, sidebands of 30 GeV;

(5) $80 < M_{ee} < 100GeV$, sidebands of 20 GeV.

The comparison of configurations 1 and 3 will display the effect of applying the background subtraction or not. By comparing configurations 3 and 5, we can reveal the impact of the width of the Z mass window. Also, the sideband width effects can be evaluated with comparison among configuration 3, 2 and 4. As a result, the systematic uncertainty of signal electrons charge-flip rates is usually between 2% and 15%, while for baseline ones failing the tight selection, the value is around 3-25%.

With the knowledge of the electron charge flip rates ξ in term of η and p_T, we can predict the charge flip yields by applying a weight to all the opposite-sign leptons pairs:

$$w_{flip} = \xi_1(1 - \xi_2) + (1 - \xi_1)\xi_2,$$

where $\xi(i) = 0$ for muons. The estimated charge-flip background in the SRs are shown in Table. 6.15.

Table 6.15: Expected yields for background processes with charge-flipped electrons, in the signal regions proposed in Section 6.5, shown for $13.2fb^{-1}$. Uncertainties include all statistical and systematic sources. Charge-flip processes do not contribute to regions SR3L1 and SR3L2, which require ≥ 3 leptons.

	SR0b1	SR0b2	SR1b	SR3b
Charge-flip DD	0.50 ± 0.09 ± 0.02	0.08 ± 0.03 ± 0.01	1.43 ± 0.18 ± 0.07	0.14 ± 0.03 ± 0.01
($t\bar{t}$ MC)	0.38 ± 0.08 ± 0.00	0.07 ± 0.02 ± 0.00	1.94 ± 0.33 ± 0.00	0.15 ± 0.06 ± 0.00
MC template	0.37 ± 0.08 ± 0.04	0.07 ± 0.02 ± 0.01	1.91 ± 0.32 ± 0.22	0.15 ± 0.06 ± 0.02

	SR1b-GG	SR1b-DD	SR3b-DD
Charge-flip DD	0.18 ± 0.07 ± 0.01	1.74 ± 0.20 ± 0.08	0.14 ± 0.03 ± 0.01
($t\bar{t}$ MC)	0.26 ± 0.07 ± 0.00	1.50 ± 0.16 ± 0.00	0.17 ± 0.06 ± 0.00
MC template	0.26 ± 0.06 ± 0.03	1.48 ± 0.15 ± 0.17	0.17 ± 0.06 ± 0.02

6.7 Validation regions

A few validation regions are defined with $E_T^{miss} > 50$ GeV and 2 jets with $p_T > 25$ GeV as pre-selection to compared the distributions between data and the predicted backgrounds. Fig. 6.12 shows the distributions for an inclusive same-sign leptons selection; while Fig. 6.13 shows the distributions in splitted lepton-flavour channels. Also, dedicated

regions enriched with prompt same-sign leptons are used to verify the simulation of these processes, like $t\bar{t}V$, VV... The expected and observed event yields have good agreement with each other.

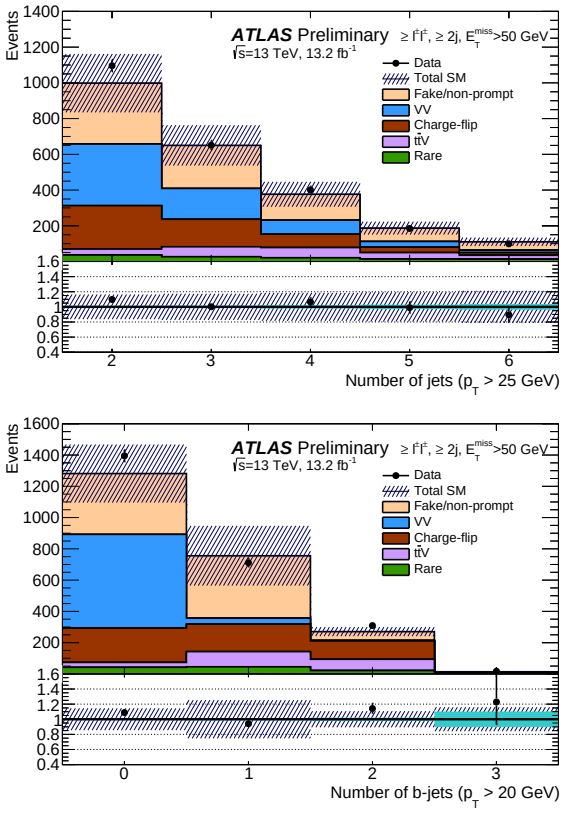

Figure 6.12: Comparisons between observed data (2015+2016, 13.2 fb^{-1}) and expected SM+detector backgrounds for 2 same-sign leptons ($p_T > 20GeV$), $E_{\mathrm{T}}^{\mathrm{miss}}$ and 2 jets ($p_T > 25GeV$). Uncertainties include statistical sources, as well as systematic uncertainties for the data-driven backgrounds.

6.8 Results and Interpretation

The statistical interpretations of the observations are performed with the HistFitter tool, which is commonly used within the SUSY working group. Hypothesis testing is performed with the corresponding one-sided profile likelihood ratio, and upper limits are provided as one-sided 95% confidence level intervals in the CLs formalism. With this setup and low event counts in the regions of interest, there is no noticeable profiling of any of the nuisance parameters.

Comparisons between observed data (2015+2016, 13.2 fb^{-1}) and expected SM backgrounds for events with $\geq$ 2 same-sign leptons are shown in Fig. 6.14. Both statistical and systematic uncertainties are considered. The event yields of the SRs are shown in Table. 6.18.

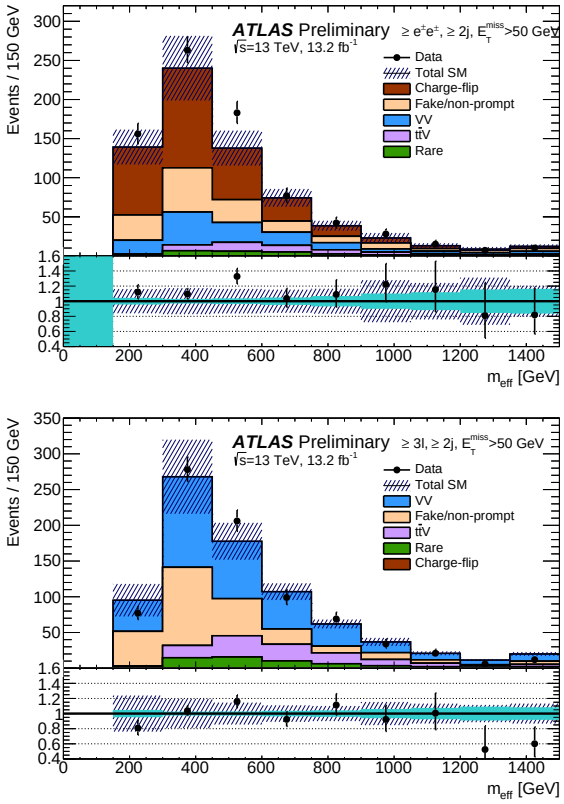

Figure 6.13: Comparisons between observed data (2015+2016, 13.2 fb^{-1}) and expected SM+detector backgrounds for 2 same-sign electrons ($p_T > 20GeV$), $E_{\mathrm{T}}^{\mathrm{miss}}$ and 2 jets ($p_T > 25GeV$). Uncertainties include statistical sources, as well as systematic uncertainties for the data-driven backgrounds.

Among all the processes that we studied, no significant excess is observed from the results. Exclusion limits for this analysis are presented in Figure 6.15. Compared to the 2015 results, we have expanded the exclusion limit quite a bit:

- for the gluino-pair production via neutralino and W/Z, the excluded region is extended up to 1.55 TeV along the gluino mass axis and 850 GeV along the neutralino mass axis.
- for the gluino-pair production via sleptons, the excluded region is extended up to 1.7 GeV along the gluino mass axis and 1.1 GeV along the neutralino mass axis.
- for the sbottom pair production, the excluded region is extended up to 700 GeV along the sbottom mass axis and 250 GeV along the neutralino mass axis.
- for the Gtt process, the excluded region is extended up to 1.5 TeV along the gluino mass axis and 900 GeV along the neutralino mass axis.

The same-sign two lepton or three lepton channel are more competitive in the diagonal region than the other channels, as expected. All of these results are now part of an ATLAS conference note [100].

As an extension of the study, the full 2015 and 2016 data ($36fb^{-1}$) was then used to

Table 6.16: Systematic uncertainties on the measured real lepton efficiency, separating sources affecting the measurement itself (background subtraction), the extrapolation to busy environments, and the bias caused by trigger-matching for electrons.

electrons (measurement ⊕ busy ⊕ trigger)		
	$0.4 < \Delta R(e, \text{jet}) < 0.6$	$\Delta R(e, \text{jet}) > 0.6$
$p_{\text{T}} < 15GeV$	$5 - 7\% \oplus 8\% \oplus$ n.a.	$5 - 7\% \oplus 4\% \oplus$ n.a.
$15 < p_{\text{T}} < 20GeV$	$3 - 5\% \oplus 8\% \oplus$ n.a.	$3 - 5\% \oplus 4\% \oplus$ n.a.
$20 < p_{\text{T}} < 35GeV$	$1 - 3\% \oplus 8\% \oplus 4\%$	$1 - 3\% \oplus 4\% \oplus 4\%$
$35 < p_{\text{T}} < 50GeV$	$0.2 - 1\% \oplus 8\% \oplus 2\%$	$0.2 - 1\% \oplus 4\% \oplus 2\%$
$50 < p_{\text{T}} < 60GeV$	$0.2 - 0.5\% \oplus 8\% \oplus 1\%$	$0.2 - 0.5\% \oplus 4\% \oplus 1\%$
$p_{\text{T}} > 60GeV$	$0 - 0.5\% \oplus 5\% \oplus 0.5\%$	$0 - 0.5\% \oplus 5\% \oplus 0.5\%$

muons (measurement ⊕ busy)		
	$0.4 < \Delta R(\mu, \text{jet}) < 0.6$	$\Delta R(\mu, \text{jet}) > 0.6$
$p_{\text{T}} < 15GeV$	$1\% \oplus 30\%$	$1\% \oplus 10\%$
$15 < p_{\text{T}} < 20GeV$	$0.5\% \oplus 20\%$	$0.5\% \oplus 7\%$
$20 < p_{\text{T}} < 35GeV$	$0.1\% \oplus 20\%$	$0.1\% \oplus 7\%$
$35 < p_{\text{T}} < 50GeV$	$0.1\% \oplus 10\%$	$0.1\% \oplus 5\%$
$50 < p_{\text{T}} < 80GeV$	$0.1\% \oplus 5\%$	$0.1\% \oplus 3\%$
$p_{\text{T}} > 80GeV$	$0.1\% \oplus 1\%$	$0.1\% \oplus 1\%$

Table 6.17: Fake lepton background yields $13.2 fb^{-1}$ estimated with the ABCD method in the different signal regions, for the three $\ell + X$ templates, and for the two alternative normalization regions CRa and CRb. They are compared to the nominal estimates from the matrix method in the first column. Only statistical uncertainties are displayed.

SR	**matrix method**	**ABCD**					
		$\ell + j$ CRa	$\ell + j$ CRb	$\ell + b$ CRa	$\ell + b$ CRb	$\ell + \gamma$ CRa	$\ell + \gamma$ CRb
SR3L1	0.1 ± 0.3	0.1 ± 0.6	1.1 ± 1.0	0.2 ± 1.2	2.3 ± 2.2	0.2 ± 1.5	3.1 ± 4.7
SR3L2	0.0 ± 0.1	0.2 ± 0.4	0.0 ± 0.5	0.5 ± 1.2	0.1 ± 1.4	–	–
SR0b1	2.9 ± 1.1	1.1 ± 0.9	10.7 ± 2.4	1.2 ± 1.0	11.4 ± 2.6	1.0 ± 0.9	10.0 ± 4.4
SR0b2	0.4 ± 0.4	1.8 ± 1.0	0.9 ± 0.7	1.8 ± 1.0	1.0 ± 0.8	< 0.6	< 0.5
SR1b	3.3 ± 1.1	2.6 ± 0.8	5.0 ± 0.9	2.7 ± 0.8	4.8 ± 0.9	4.0 ± 1.7	5.6 ± 1.9
SR3b	0.2 ± 0.4	1.1 ± 0.6	0.6 ± 0.5	1.4 ± 0.8	0.7 ± 0.6	1.4 ± 1.2	0.7 ± 0.7
SR1b-GG	0.2 ± 0.2	0.2 ± 0.2	0.2 ± 0.1	0.1 ± 0.1	0.1 ± 0.0	0.2 ± 0.3	0.2 ± 0.2
SR1b-DD	2.5 ± 1.0	1.8 ± 0.7	2.9 ± 0.9	1.7 ± 0.7	2.7 ± 0.8	1.9 ± 0.9	3.1 ± 1.2
SR3b-DD	0.5 ± 0.5	0.1 ± 0.3	0.4 ± 0.4	0.1 ± 0.4	0.6 ± 0.5	0.1 ± 0.4	0.6 ± 0.6

further search for interesting signals and I partly contributed to this search at the end of my thesis. The newly updated results has recently been published [101]. In the latest study, we still get no significant excess. However, more area in the phase space is excluded as shown in Fig. 6.16:

- for the gluino-pair production via neutralino and W/Z, the excluded region is expanded for 50 GeV along the gluino mass axis and 50 GeV along the neutralino mass axis.

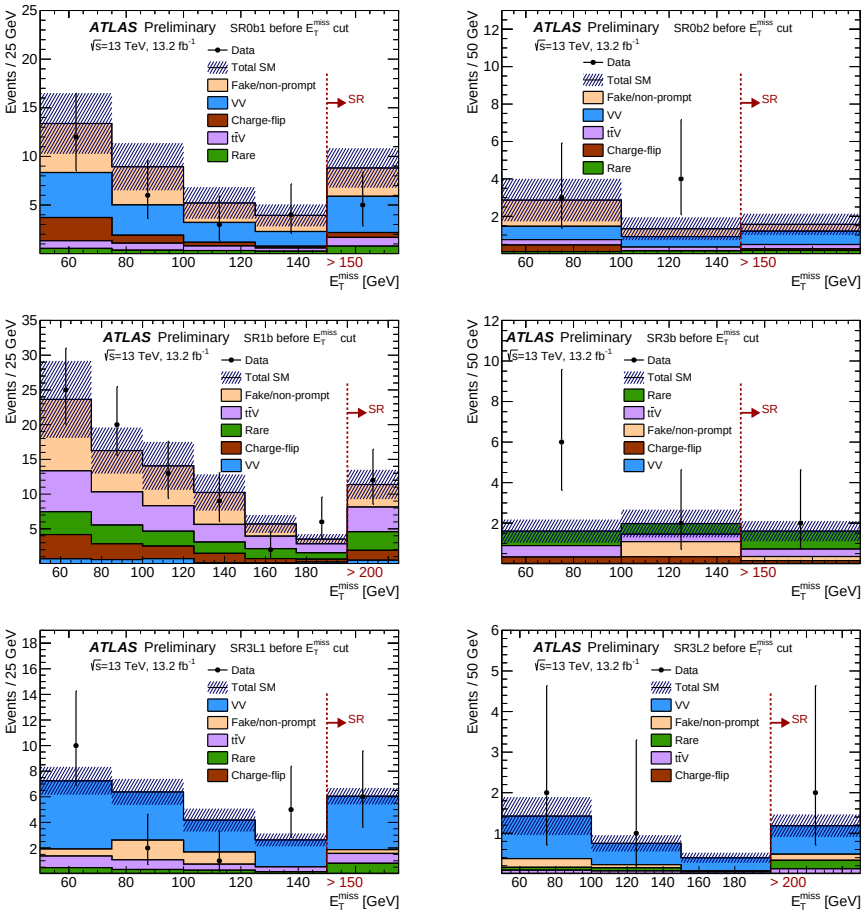

Figure 6.14: Comparisons between observed data (2015+2016, 13.2 fb^{-1}) and expected SM+detector backgrounds for 6 signal regions. Uncertainties include statistical sources, as well as systematic uncertainties for the data-driven backgrounds.

Table 6.18: Expected background yields in the signal regions SR3L1, SR3L2, SR0b1, SR0b2 and SR1b. The event yields are given for 13.2fb^{-1}. The uncertainties displayed include both systematic and statistical sources.

	SR3L1	SR3L2	SR0b1	SR0b2	SR1b	SR3b
Observed	6	2	5	0	12	2
SM total	6.05 ± 2.15	1.18 ± 0.49	8.81 ± 2.87	1.57 ± 0.77	11.40 ± 2.76	1.60 ± 0.61
ttZ	0.69 ± 0.25	0.10 ± 0.04	0.45 ± 0.18	0.10 ± 0.04	1.58 ± 0.55	0.19 ± 0.07
ttW	0.09 ± 0.04	0.02 ± 0.01	0.45 ± 0.17	0.13 ± 0.06	1.97 ± 0.68	0.17 ± 0.06
Diboson	4.18 ± 1.96	0.70 ± 0.43	3.72 ± 1.86	0.71 ± 0.52	0.47 ± 0.41	0.00 ± 0.00
Rare	0.80 ± 0.44	0.21 ± 0.13	0.76 ± 0.44	0.18 ± 0.12	2.69 ± 0.90	0.89 ± 0.31
Fakes	0.29 ± 0.29	0.15 ± 0.15	2.92 ± 1.97	0.37 ± 0.53	3.25 ± 2.08	0.20 ± 0.49
MisCharge	0.00 ± 0.00	0.00 ± 0.00	0.50 ± 0.09	0.08 ± 0.03	1.43 ± 0.19	0.14 ± 0.03

- for the gluino-pair production via sleptons, the excluded region is expanded for 200 GeV along the gluino mass axis and 100 GeV along the neutralino mass axis.
- for the sbottom pair production, the excluded region is expanded for 50 GeV along the

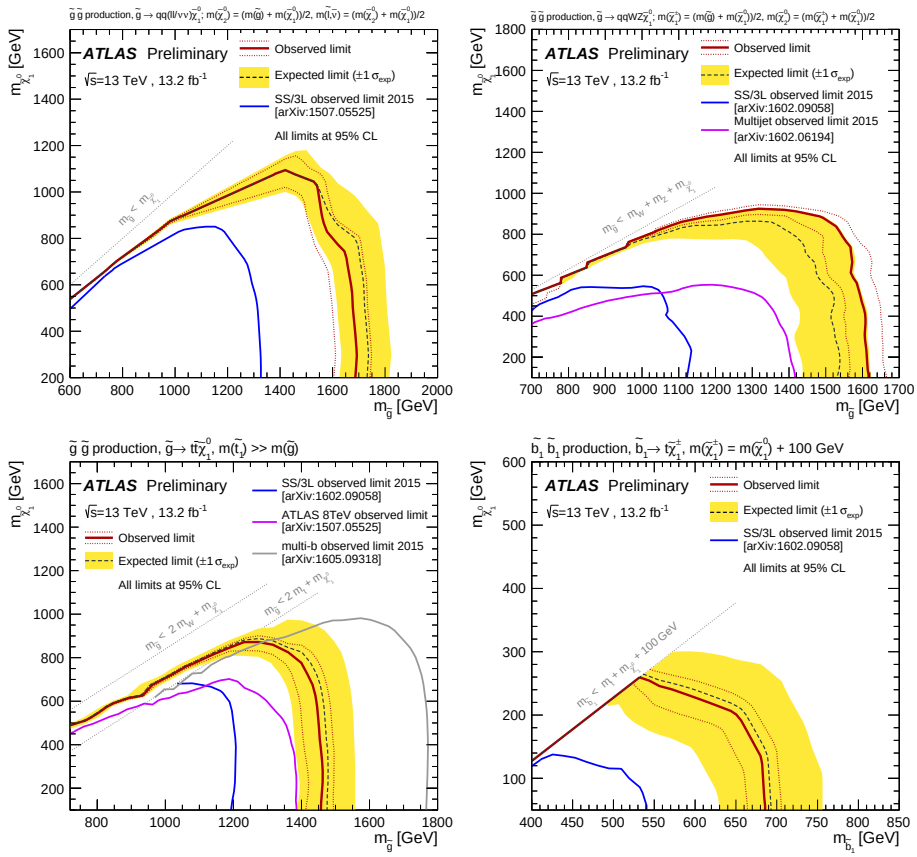

Figure 6.15: Exclusion limits on superpartner masses in different SUSY scenarios, for 13.2 fb^{-1} . The signal regions used to contain each scenario are specified in the captions.

sbottom mass axis and 50 GeV along the neutralino mass axis.

- for the Gtt process, the excluded region is expanded for 200 GeV along the gluino mass axis.

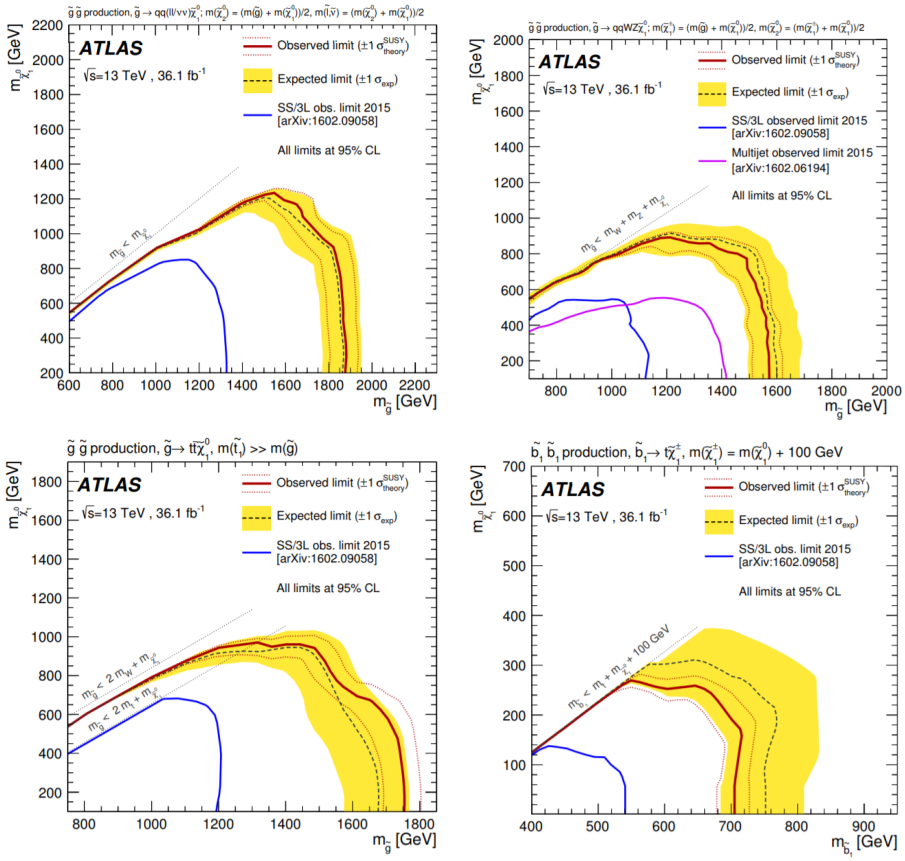

Figure 6.16: Exclusion limits on superpartner masses in different SUSY scenarios, for 36 fb^{-1} .

Chapter 7

Conclusion

The Standard Model describes the elementary particles and their interactions. The theory has been quite successful in predicting the W/Z bosons and the Higgs boson. SUSY, one of the most popular theories describing the physics beyond the Standard Model, gives predictions to a list of new particles - supersymmetry particles. The predicted particles are named sparticles, which are superpartners of each SM particle in the chiral multiplets. The MSSM is one of the realization of SUSY, it helps with the completion of the SM for the following unsolved issues: hierachy problem, dark matter, origin of gravity and no gauge unification at higher scale, etc.

As the world's largest hadron accelerator and collider, the Large Hadron Collider (LHC) was built aiming for accurate measurement of SM and dedicated search for physics beyond the SM. ATLAS, one of the two general purpose detectors, has started data-taking since 2010. The two main periods of the ATLAS data-taking are known as RUN1 (2010-2013, with an center-of-mass energy of 7-8 TeV) and RUN2 (2015-now, with an initial center-of-mass energy of 13 TeV). The total integrated luminosity of the taken data in RUN1 (RUN2) is 20.1 (36.5) fb^{-1}.

Many searches have been done using the collected data by ATLAS. During my PhD, I mainly contributed to two of the SUSY searches, after my qualification work about the τ-track-counting uncertainty estimation. The first study presented in this thesis is about the search for direct stau production with final states of at least two opposite-sign taus and missing-transverse energy in proton-proton collision at an 8 TeV center of mass energy and a $20.1 fb^{-1}$ integrated luminosity. The second one is about a search for squarks and gluinos strong production in final states with jets and two same-sign leptons or three leptons at 13 TeV proton-proton collision and a $13.2 fb^{-1}$ integrated luminosity (data collected till June, 2016).

For the τ-track-counting uncertainty estimation, $Z \rightarrow \mu\mu$ events are selected from both data and Monte Carlo simulation to be further applied into a tag-and-probe method. The behaviours of the probe muon from both data and MC are studied. The track-counting strategy is used as a sub-algorithms inside the "anti-KT" algorithms. It counts and decides the number of tracks that are located in the region around a certain object (pion, muon, etc.). This is quite important for the jet/tau reconstruction in the ATLAS experiment. Thus, the accuracy of the track-counting is essential in many analyses that include tau-leptons and multi-jets in the final state. For any analysis that uses the track-counting, the uncertainty

of the algorithms should be taken into account. The difference between the response from data and MC is assigned as the systematics of track counting, as shown in Chapter. 4.

The direct production of third generation slepton ($\tilde{\tau}$) are studied as it provides a clear structure of decay mode, strong correlation to the tau-lepton in final state, as well as quite low background. A traditional cut-and-count analysis is published targeting this scenario. However, due to very low cross-section, the sensitivity of the cut-and-count analysis is quite limited [85].

An Multi-Variate Analysis is then introduced to improve the sensitivity for the direct-stau production. This is done by using a set of suitable discriminating variables to reach the maximum separation power. The Toolkit for Multivariate Analysis (TMVA) makes use of a training phase, by examing events with the given variables from both signal and background respectively. The training procedure results in an evaluation function with an output value showing the degree of how a certain event is like a signal (or background). The signal and background mixture is then applied with the obtained function to give more sensitivity of the study. The Boosted Decision Tree (BDT) is adopted after comparison with other methods that provided by TMVA, as it provides the highest sensitivity and more intuitionistic algorithms in training. The BDT response is then used in the definition of Signal Region (SR).

With the determination of SR, the main background would be events from the following process: W+jets, Z+jets, multi-jets and processes with top quark. The backgrounds are estimated (and validated) using different methods (and Validation Regions). "ABCD" method is used for the multi-jet background estimation. The result of this study shows no significant excess for the "direct-stau" process. However, the region in the phase-space where $m(LSP) = 0GeV$ and $m(\tilde{\tau})$ $100GeV$ is excluded [99].

Generally, the MVA analysis shows better performance than the cut-based one, especially in low LSP and $\tilde{\tau}$ mass region. In the future with more statistics from data, it would be possible for this analysis to explore higher along the LSP and $\tilde{\tau}$ mass axis. It is also prospecting to have several SRs defined, each with a different signal point involved in the training procedure. This would help a lot in the high LSP and $\tilde{\tau}$ mass region.

The search for squarks and gluinos strong production with two same-sign or three light-leptons is studied using 2015-2016 data. The corresponding channels of this search is popular due to very low SM backgrounds. The interested scenarios include gluino pair production with stop-mediated decay, gluino pair-production with two-step decays via neutralinos and sleptons (or gauginos and W and Z bosons), direct decay of sbottom. Dedicated SRs are then defined aiming at all the processes.

The background of SS-2l analysis can be mainly classified into three categories: Prompt SS leptons process, Charge-flipped electrons process and Fake-lepton process. The "Prompt lepton" background is predicted relying on Monte Carlo simulation of the relevant processes. The "Charge-flip" background is estimated using charge-flip rate calculated by data-driven estimation. The "fake-lepton" background is estimated using another data-driven methods, known as the "Matrix-Method". The Matrix-Method uses fake-lepton-efficiency (also named "fake-rate") and real-lepton-efficiency as input. The fake-rate and real-efficiency are assigned in dedicated control regions.

The result of this study shows no significant excess for all the correlated process [100]. However, the limit in phase-space are largely extended:

- for the gluino-pair production via neutralino and W/Z, the excluded region is extended up to 1.55 TeV along the gluino mass axis and 850 GeV along the neutralino mass axis.
- for the gluino-pair production via sleptons, the excluded region is extended up to 1.7 GeV along the gluino mass axis and 1.1 GeV along the neutralino mass axis.
- for the sbottom pair production, the excluded region is extended up to 700 GeV along the sbottom mass axis and 250 GeV along the neutralino mass axis.
- for the Gtt process, the excluded region is extended up to 1.5 TeV along the gluino mass axis and 900 GeV along the neutralino mass axis.

The newly updated results of this analysis is published using full 2015 and 2016 data. More area in the phase space is excluded [101]:

- for the gluino-pair production via neutralino and W/Z, the excluded region is expanded for 50 GeV along the gluino mass axis and 50 GeV along the neutralino mass axis.
- for the gluino-pair production via sleptons, the excluded region is expanded for 200 GeV along the gluino mass axis and 100 GeV along the neutralino mass axis.
- for the sbottom pair production, the excluded region is expanded for 50 GeV along the sbottom mass axis and 50 GeV along the neutralino mass axis.
- for the Gtt process, the excluded region is expanded for 200 GeV along the gluino mass axis.

With more statistics in the future data taking, this channel would be more competitive in the diagonal region of the phase space. The background estimation can also be improved with more data. The measurement of fake rate, real efficiency and charge-flip rate would be much more accurate, leading to large reduction of systematics. Other background estimation methods would also be possible, like fake-factor method. Also, more statistics make it possible for multivariate analysis, which would probably increase the signal sensitivity quite a bit.

Bibliography

[1] G. Aad *et al.* [ATLAS Collaboration], "Observation of a new particle in the search for the Standard Model Higgs boson with the ATLAS detector at the LHC," Phys. Lett. B **716** (2012) 1 doi:10.1016/j.physletb.2012.08.020 [arXiv:1207.7214 [hep-ex]].

[2] S. Chatrchyan *et al.* [CMS Collaboration], "Observation of a new boson at a mass of 125 GeV with the CMS experiment at the LHC," Phys. Lett. B **716** (2012) 30 doi:10.1016/j.physletb.2012.08.021 [arXiv:1207.7235 [hep-ex]].

[3] G. Aad *et al.* [ATLAS and CMS Collaborations], "Combined Measurement of the Higgs Boson Mass in pp Collisions at $\sqrt{s} = 7$ and 8 TeV with the ATLAS and CMS Experiments," Phys. Rev. Lett. **114** (2015) 191803 doi:10.1103/PhysRevLett.114.191803 [arXiv:1503.07589 [hep-ex]].

[4] G. Aad *et al.* [ATLAS Collaboration], "Measurement of the Higgs boson mass from the $H \to \gamma\gamma$ and $H \to ZZ^* \to 4\ell$ channels with the ATLAS detector using 25 fb^{-1} of pp collision data," Phys. Rev. D **90** (2014) no.5, 052004 doi:10.1103/PhysRevD.90.052004 [arXiv:1406.3827 [hep-ex]].

[5] G. Aad *et al.* [ATLAS Collaboration], "Observation and measurement of Higgs boson decays to WW* with the ATLAS detector," Phys. Rev. D **92** (2015) no.1, 012006 doi:10.1103/PhysRevD.92.012006 [arXiv:1412.2641 [hep-ex]].

[6] G. Aad *et al.* [ATLAS Collaboration], "Measurements of Higgs boson production and couplings in the four-lepton channel in pp collisions at center-of-mass energies of 7 and 8 TeV with the ATLAS detector," Phys. Rev. D **91** (2015) no.1, 012006 doi:10.1103/PhysRevD.91.012006 [arXiv:1408.5191 [hep-ex]].

[7] K. A. Olive *et al.* [Particle Data Group], "Review of Particle Physics," Chin. Phys. C **38** (2014) 090001. doi:10.1088/1674-1137/38/9/090001

[8] Michael E. Peskin (Author), Daniel V. Schroeder, "An Introduction To Quantum Field Theory," ISBN-13: 978-0201503975 ISBN-10: 0201503972

[9] W.N. Cottingham and D.A. Greenwood, "AN INTRODUCTION TO THE STANDARD MODEL OF PARTICLE PHYSICS," Cambridge University Press

[10] O. A. Ducu, "Search for new physics in events with same sign leptons and missing energy with ATLAS at LHC," CPPM-T-2015-06, CERN-THESIS-2015-163.

[11] X. RUAN, "Search for Higgs boson in the $WW^{(*)}$ channel in ATLAS and drift time measurement in the liquid argon calorimeter in ATLAS," CERN-THESIS-2012-188.

[12] L. Yao, "Contribution to the Higgs boson discovery in the diphoton channel at LHC," 1 vol.(176 p.). p.159-164. Index

[13] K. Nakamura *et al.* [Particle Data Group], "Review of particle physics," J. Phys. G **37** (2010) 075021. doi:10.1088/0954-3899/37/7A/075021

[14] S. L. Glashow, "Partial Symmetries of Weak Interactions," Nucl. Phys. **22** (1961) 579. doi:10.1016/0029-5582(61)90469-2

[15] G. Jungman, M. Kamionkowski and K. Griest, "Supersymmetric dark matter," Phys. Rept. **267** (1996) 195 doi:10.1016/0370-1573(95)00058-5 [hep-ph/9506380].

[16] S. Dimopoulos, S. Raby and F. Wilczek, "Supersymmetry and the Scale of Unification," Phys. Rev. D **24** (1981) 1681. doi:10.1103/PhysRevD.24.1681

[17] T. Li, "Lecture: introduction to the Natural Supersymmetry Standard Model."

[18] R. Barbier *et al.*, "R-parity violating supersymmetry," Phys. Rept. **420** (2005) 1 doi:10.1016/j.physrep.2005.08.006 [hep-ph/0406039].

[19] M. F. Sohnius, "Introducing Supersymmetry," Phys. Rept. **128** (1985) 39.

[20] N. Sakai, "Naturalness in Supersymmetric Guts," Z. Phys. C **11** (1981) 153. doi:10.1007/BF01573998

[21] P. Bechtle, T. Plehn and C. Sander, "Supersymmetry," arXiv:1506.03091 [hep-ex].

[22] P. de Jong [ATLAS and CMS Collaborations], "Supersymmetry searches at the LHC," arXiv:1211.3887 [hep-ex].

[23] B. Dumont, "Higgs, supersymmetry and dark matter after Run I of the LHC," arXiv:1411.3465 [hep-ph].

[24] J. Wess and B. Zumino, "Supergauge Transformations in Four-Dimensions," Nucl. Phys. B **70** (1974) 39. doi:10.1016/0550-3213(74)90355-1

[25] S. Ferrara and B. Zumino, "Supergauge Invariant Yang-Mills Theories," Nucl. Phys. B **79** (1974) 413. doi:10.1016/0550-3213(74)90559-8

[26] D. V. Volkov and V. P. Akulov, "Is the Neutrino a Goldstone Particle?," Phys. Lett. **46B** (1973) 109. doi:10.1016/0370-2693(73)90490-5

[27] P. Fayet, "Supersymmetry and Weak, Electromagnetic and Strong Interactions," Phys. Lett. **64B** (1976) 159. doi:10.1016/0370-2693(76)90319-1

[28] J. Ellis, "Prospects for Supersymmetry at the LHC and Beyond," PoS PLANCK **2015** (2015) 041 [arXiv:1510.06204 [hep-ph]].

[29] G. R. Farrar and P. Fayet, "Phenomenology of the Production, Decay, and Detection of New Hadronic States Associated with Supersymmetry," Phys. Lett. **76B** (1978) 575. doi:10.1016/0370-2693(78)90858-4

[30] I. Melzer-Pellmann and P. Pralavorio, "Lessons for SUSY from the LHC after the first run," Eur. Phys. J. C **74** (2014) 2801 [arXiv:1404.7191 [hep-ex]].

[31] R. Barbieri and G. F. Giudice, "Upper Bounds on Supersymmetric Particle Masses," Nucl. Phys. B **306** (1988) 63. doi:10.1016/0550-3213(88)90171-X

[32] L. Evans and P. Bryant, "LHC Machine," JINST **3** (2008) S08001. doi:10.1088/1748-0221/3/08/S08001

[33] W. W. Armstrong *et al.* [ATLAS Collaboration], "ATLAS: Technical proposal for a general-purpose p p experiment at the Large Hadron Collider at CERN," CERN-LHCC-94-43.

[34] S. Chatrchyan *et al.* [CMS Collaboration], "The CMS Experiment at the CERN LHC," JINST **3** (2008) S08004. doi:10.1088/1748-0221/3/08/S08004

[35] "LHC luminosity (RUN-1)." https://twiki.cern.ch/twiki/bin/view/AtlasPublic/LuminosityPublicResults

[36] "LHC luminosity (RUN-2)." https://twiki.cern.ch/twiki/bin/view/AtlasPublic/LuminosityPublicResultsR

[37] G. Aad *et al.* [ATLAS Collaboration], "The ATLAS Experiment at the CERN Large Hadron Collider," JINST **3** (2008) S08003. doi:10.1088/1748-0221/3/08/S08003

[38] G. Aad *et al.*, "ATLAS pixel detector electronics and sensors," JINST **3** (2008) P07007. doi:10.1088/1748-0221/3/07/P07007

[39] A. Ahmad *et al.*, "The Silicon microstrip sensors of the ATLAS semiconductor tracker," Nucl. Instrum. Meth. A **578** (2007) 98. doi:10.1016/j.nima.2007.04.157

[40] M. Capeans *et al.* [ATLAS Collaboration], "ATLAS Insertable B-Layer Technical Design Report," CERN-LHCC-2010-013, ATLAS-TDR-19.

[41] [ATLAS Collaboration], "ATLAS IBL: a challenging first step for ATLAS Upgrade at the sLHC," arXiv:1109.3372.

[42] W. Lampl *et al.*, "Calorimeter clustering algorithms: Description and performance," ATL-LARG-PUB-2008-002, ATL-COM-LARG-2008-003.

[43] [ATLAS Collaboration], "ATLAS liquid argon calorimeter: Technical design report," CERN-LHCC-96-41.

[44] [ATLAS Collaboration], "ATLAS muon spectrometer: Technical design report," CERN-LHCC-97-22, ATLAS-TDR-10.

[45] H. H. J. ten Kate, "The ATLAS Superconducting Magnet System: Status of Construction and Installation," IEEE Trans. Appl. Supercond. **16** (2006) no.2, 499. doi:10.1109/TASC.2006.871348

[46] [ATLAS Collaboration], "Review of the ATLAS Technical design report on the forward detectors for the measurement of elastic scattering and luminosity," CERN-LHCC-2008-013, LHCC-G-140.

[47] Sjostrand, T., "Monte Carlo generators for the LHC."

[48] T. Sjostrand, S. Mrenna and P. Z. Skands, "A Brief Introduction to PYTHIA 8.1," Comput. Phys. Commun. **178** (2008) 852 doi:10.1016/j.cpc.2008.01.036 [arXiv:0710.3820 [hep-ph]].

[49] G. Aad *et al.* [ATLAS Collaboration], "Expected Performance of the ATLAS Experiment - Detector, Trigger and Physics," arXiv:0901.0512 [hep-ex].

[50] M. Aharrouche *et al.* [ATLAS Collaboration], "Reconstruction of low-mass electron pairs," ATL-PHYS-PUB-2009-007, ATL-COM-PHYS-2009-173.

[51] M. Aharrouche *et al.* [ATLAS Collaboration], "Calibration and performance of the electromagnetic calorimeter," ATL-PHYS-PUB-2009-003, ATL-COM-PHYS-2009-169.

[52] [ATLAS Collaboration], "Photon Conversions at $\sqrt{s} = 900$ GeV measured with the ATLAS Detector," ATLAS-CONF-2010-007.

[53] G. Aad *et al.* [ATLAS Collaboration], "Electron and photon energy calibration with the ATLAS detector using LHC Run 1 data," Eur. Phys. J. C **74** (2014) no.10, 3071 doi:10.1140/epjc/s10052-014-3071-4 [arXiv:1407.5063 [hep-ex]].

[54] [ATLAS Collaboration], "Expected photon performance in the ATLAS experiment," ATL-PHYS-PUB-2011-007, ATL-COM-PHYS-2010-1051.

[55] F. Dudziak, "Electron reconstruction and identification in ATLAS. Implication for the Higgs into four electron final state.," ATL-PHYS-PROC-2010-039, ATL-COM-PHYS-2010-319.

[56] G. Aad *et al.* [ATLAS Collaboration], "Electron reconstruction and identification efficiency measurements with the ATLAS detector using the 2011 LHC proton-proton collision data," Eur. Phys. J. C **74** (2014) no.7, 2941 doi:10.1140/epjc/s10052-014-2941-0 [arXiv:1404.2240 [hep-ex]].

[57] The ATLAS collaboration [ATLAS Collaboration], "Electron efficiency measurements with the ATLAS detector using the 2012 LHC proton-proton collision data," ATLAS-CONF-2014-032.

[58] D. Adams *et al.*, "Muon reconstruction and identification: Studies with simulated Monte Carlo samples," ATL-PHYS-PUB-2009-008, ATL-COM-PHYS-2009-151.

[59] S. Hassani, L. Chevalier, E. Lancon, J. F. Laporte, R. Nicolaidou and A. Ouraou, "A muon identification and combined reconstruction procedure for the ATLAS detector at the LHC using the (MUONBOY, STACO, MuTag) reconstruction packages," Nucl. Instrum. Meth. A **572** (2007) 77. doi:10.1016/j.nima.2006.10.340

[60] T. Lagouri *et al.*, "A Muon Identification and Combined Reconstruction Procedure for the ATLAS Detector at the LHC at CERN," IEEE Trans. Nucl. Sci. **51** (2004) 3030. doi:10.1109/TNS.2004.839102

[61] K. A. Assamagan *et al.* [ATLAS Collaboration], "Muons in the calorimeters: Energy loss corrections and muon tagging," ATL-PHYS-PUB-2009-009, ATL-COM-PHYS-2009-153.

[62] K. A. Assamagan and Y. Coadou, "The hadronic tau decay of a heavy charged Higgs in ATLAS," ATL-PHYS-2000-031, ATL-COM-PHYS-2000-017, CERN-ATL-PHYS-2000-031.

[63] A. Deandrea, "Charged Higgs in models with singlet neutrino in large extra dimensions," hep-ph/0206283.

[64] V. Khachatryan *et al.* [CMS Collaboration], "Reconstruction and identification of tau lepton decays to hadrons and tau neutrino at CMS," JINST **11** (2016) no.01, P01019 doi:10.1088/1748-0221/11/01/P01019 [arXiv:1510.07488 [physics.ins-det]].

[65] S. Frixione and B. R. Webber, "Matching NLO QCD computations and parton shower simulations," JHEP **0206** (2002) 029 doi:10.1088/1126-6708/2002/06/029 [hep-ph/0204244].

[66] M. Heldmann and D. Cavalli, "An improved tau-Identification for the ATLAS experiment," ATL-PHYS-PUB-2006-008, ATL-COM-PHYS-2006-010.

[67] E. Richter-Was and T. Szymocha, "Hadronic tau identification with track based approach : the $Z \to \tau\tau, W \to \tau\nu$ and dijet events from DC1 data samples," ATL-PHYS-PUB-2005-005, ATL-COM-PHYS-2004-080.

[68] [ATLAS Collaboration] "Detector Level Jet Corrections" https://twiki.cern.ch/twiki/bin/view/AtlasPublic/JetCalCSCNote#Figures

[69] [ATLAS Collaboration], "Jet energy scale and its systematic uncertainty for jets produced in proton-proton collisions at sqrt(s) = 7 TeV and measured with the ATLAS detector," ATLAS-CONF-2010-056.

[70] G. Aad *et al.* [ATLAS Collaboration], "Jet energy measurement with the ATLAS detector in proton-proton collisions at $\sqrt{s}$ = 7 TeV," Eur. Phys. J. C **73** (2013) no.3, 2304 doi:10.1140/epjc/s10052-013-2304-2 [arXiv:1112.6426 [hep-ex]].

[71] M. Cacciari, G. P. Salam and G. Soyez, "The Anti-k(t) jet clustering algorithm," JHEP **0804** (2008) 063 doi:10.1088/1126-6708/2008/04/063 [arXiv:0802.1189 [hep-ph]].

[72] C. Pizio, "Missing transverse energy measurement in ATLAS detector: first LHC data results and importance for physics study," CERN-THESIS-2010-180.

[73] [ATLAS Collaboration], "Performance of the Missing Transverse Energy Reconstruction and Calibration in Proton-Proton Collisions at a Center-of-Mass Energy of 7 TeV with the ATLAS Detector," ATLAS-CONF-2010-057.

[74] [ATLAS Collaboration], "Observation of $W \to \tau\nu$ Decays with the ATLAS Experiment," ATLAS-CONF-2010-097.

[75] [ATLAS Collaboration], "Observation of $Z \to \tau_h\tau_l$ Decays with the ATLAS detector," ATLAS-CONF-2010-010.

[76] [ATLAS Collaboration], "Reconstruction, Energy Calibration, and Identification of Hadronically Decaying Tau Leptons," ATLAS-CONF-2011-077.

[77] [ATLAS Collaboration], "Determination of the tau energy scale and the associated systematic uncertainty in proton-proton collisions at sqrts= = 7 TeV with the ATLAS detector at the LHC in 2011," ATLAS-CONF-2012-054.

[78] [ATLAS Collaboration], "Performance of the ATLAS Inner Detector Track and Vertex Reconstruction in the High Pile-Up LHC Environment," ATLAS-CONF-2012-042.

[79] [ATLAS Collaboration], "Performance of the Reconstruction and Identification of Hadronic Tau Decays in ATLAS with 2011 Data," ATLAS-CONF-2012-142.

[80] [ATLAS Collaboration], "Performance of the Reconstruction and Identification of Hadronic Tau Decays with ATLAS," ATLAS-CONF-2011-152.

[81] [ATLAS Collaboration], "Measurement of hadronic tau decay identification efficiency using W-¿taunu events," ATLAS-CONF-2011-093.

[82] [ATLAS Collaboration], "Muon reconstruction efficiency in reprocessed 2010 LHC proton-proton collision data recorded with the ATLAS detector," ATLAS-CONF-2011-063.

[83] G. Aad *et al.* [ATLAS Collaboration], "Measurement of the Z to tau tau Cross Section with the ATLAS Detector," Phys. Rev. D **84** (2011) 112006 doi:10.1103/PhysRevD.84.112006 [arXiv:1108.2016 [hep-ex]].

[84] M. L. Mangano, M. Moretti, F. Piccinini, R. Pittau and A. D. Polosa, "ALPGEN, a generator for hard multiparton processes in hadronic collisions," JHEP **0307** (2003) 001 doi:10.1088/1126-6708/2003/07/001 [hep-ph/0206293].

[85] G. Aad *et al.* [ATLAS Collaboration], "Search for the direct production of charginos, neutralinos and staus in final states with at least two hadronically decaying taus and missing transverse momentum in pp collisions at $\sqrt{s}$ = 8 TeV with the ATLAS detector," JHEP **1410** (2014) 096 doi:10.1007/JHEP10(2014)096 [arXiv:1407.0350 [hep-ex]].

[86] D. R. Tovey, "On measuring the masses of pair-produced semi-invisibly decaying particles at hadron colliders," JHEP **0804** (2008) 034 doi:10.1088/1126-6708/2008/04/034 [arXiv:0802.2879 [hep-ph]].

[87] W. Beenakker, M. Klasen, M. Kramer, T. Plehn, M. Spira and P. M. Zerwas, "The Production of charginos / neutralinos and sleptons at hadron colliders," Phys. Rev. Lett. **83** (1999) 3780 Erratum: [Phys. Rev. Lett. **100** (2008) 029901] doi:10.1103/PhysRevLett.100.029901, 10.1103/PhysRevLett.83.3780 [hep-ph/9906298].

[88] M. Drees, R. Godbole and P. Roy, "Theory and phenomenology of sparticles: An account of four-dimensional N=1 supersymmetry in high energy physics," Hackensack, USA: World Scientific (2004) 555 p

[89] G. Aad *et al.* [ATLAS Collaboration], "Search for supersymmetry in events with four or more leptons in $\sqrt{s}$ = 8 TeV pp collisions with the ATLAS detector," Phys. Rev. D **90** (2014) no.5, 052001 doi:10.1103/PhysRevD.90.052001 [arXiv:1405.5086 [hep-ex]].

[90] D. Zanzi, "Search for the Standard Model Higgs Boson in Hadronic $\tau^+\tau^-$ Decays with the ATLAS Detector," CERN-THESIS-2014-085, MPP-2014-224.

[91] [ATLAS Collaboration], "A search for high-mass ditau resonances decaying in the fully hadronic final state in pp collisions at $\sqrt{s}$ = 8 TeV with the ATLAS detector," ATLAS-CONF-2013-066.

[92] [ATLAS Collaboration], "Commissioning of the ATLAS high-performance b-tagging algorithms in the 7 TeV collision data," ATLAS-CONF-2011-102.

[93] [ATLAS Collaboration], "Using boosted decision trees for tau identification in the ATLAS experiment," http://cds.cern.ch/record/2244641/

[94] Z. Marshall, "Re-defining the Standard QCD Di-Jet Samples," Tech. Rep. REFERENCES 203 CERN, Geneva, Jul,. Internal note. ATL-COM-PHYS-2011-992

[95] G. Polesello and D. R. Tovey, "Supersymmetric particle mass measurement with the boost-corrected contransverse mass," JHEP **1003** (2010) 030 doi:10.1007/JHEP03(2010)030 [arXiv:0910.0174 [hep-ph]].

[96] V. Khachatryan *et al.* [CMS Collaboration], "Searches for Supersymmetry using the M_{T2} Variable in Hadronic Events Produced in pp Collisions at 8 TeV," JHEP **1505** (2015) 078 doi:10.1007/JHEP05(2015)078 [arXiv:1502.04358 [hep-ex]].

[97] A. Hocker *et al.*, "TMVA - Toolkit for Multivariate Data Analysis," PoS ACAT (2007) 040 [physics/0703039 [PHYSICS]].

[98] M. Baak, G. J. Besjes, D. Côte, A. Koutsman, J. Lorenz and D. Short, "HistFitter software framework for statistical data analysis," Eur. Phys. J. C **75** (2015) 153 doi:10.1140/epjc/s10052-015-3327-7 [arXiv:1410.1280 [hep-ex]].

[99] G. Aad *et al.* [ATLAS Collaboration], "Search for the electroweak production of supersymmetric particles in $\sqrt{s}$=8 TeV pp collisions with the ATLAS detector," Phys. Rev. D **93** (2016) no.5, 052002 doi:10.1103/PhysRevD.93.052002 [arXiv:1509.07152 [hep-ex]].

[100] The ATLAS collaboration [ATLAS Collaboration], "Search for supersymmetry with two same-sign leptons or three leptons using 13.2 fb^{-1} of $\sqrt{s}$ = 13 TeV pp collision data collected by the ATLAS detector," ATLAS-CONF-2016-037.

[101] M. Aaboud *et al.* [ATLAS Collaboration], "Search for supersymmetry in final states with two same-sign or three leptons and jets using 36 fb^{-1} of $\sqrt{s}$ = 13 TeV pp collision data with the ATLAS detector," arXiv:1706.03731 [hep-ex].

[102] G. Aad *et al.* [ATLAS Collaboration], "Search for supersymmetry at $\sqrt{s}$ = 13 TeV in final states with jets and two same-sign leptons or three leptons with the ATLAS detector," Eur. Phys. J. C **76** (2016) no.5, 259 doi:10.1140/epjc/s10052-016-4095-8 [arXiv:1602.09058 [hep-ex]].

[103] C. Borschensky, M. Krämer, A. Kulesza, M. Mangano, S. Padhi, T. Plehn and X. Portell, "Squark and gluino production cross sections in pp collisions at $\sqrt{s}$ = 13, 14, 33 and 100 TeV," Eur. Phys. J. C **74** (2014) no.12, 3174 doi:10.1140/epjc/s10052-014-3174-y [arXiv:1407.5066 [hep-ph]].

[104] G. Aad *et al.* [ATLAS Collaboration], "Search for supersymmetry in final states with jets, missing transverse momentum and one isolated lepton in $\sqrt{s}$ = 7 TeV pp collisions using 1 fb^{-1} of ATLAS data," Phys. Rev. D **85** (2012) no.1, 012006 Erratum: [Phys. Rev. D **87** (2013) 099903] doi:10.1103/PhysRevD.85.012006, 10.1103/PhysRevD.87.099903 [arXiv:1109.6606 [hep-ex]].

[105] G. Aad *et al.* [ATLAS Collaboration], "Search for gluinos in events with two same-sign leptons, jets and missing transverse momentum with the ATLAS detector in pp collisions at $\sqrt{s}$ = 7 TeV," Phys. Rev. Lett. **108** (2012) 241802 doi:10.1103/PhysRevLett.108.241802 [arXiv:1203.5763 [hep-ex]].

[106] G. Aad *et al.* [ATLAS Collaboration], "Search for supersymmetry at $\sqrt{s}$=8 TeV in final states with jets and two same-sign leptons or three leptons with the ATLAS detector," JHEP **1406** (2014) 035 doi:10.1007/JHEP06(2014)035 [arXiv:1404.2500 [hep-ex]].

[107] G. Aad *et al.* [ATLAS Collaboration], "Summary of the searches for squarks and gluinos using $\sqrt{s}$ = 8 TeV pp collisions with the ATLAS experiment at the LHC," JHEP **1510** (2015) 054 doi:10.1007/JHEP10(2015)054 [arXiv:1507.05525 [hep-ex]].

[108] The ATLAS collaboration, "Search for Bottom Squark Pair Production with the ATLAS Detector in proton-proton Collisions at $\sqrt{s}$ = 13 TeV," ATLAS-CONF-2015-066.

[109] G. Aad *et al.* [ATLAS Collaboration], "ATLAS Run 1 searches for direct pair production of third-generation squarks at the Large Hadron Collider," Eur. Phys. J. C **75** (2015) no.10, 510 Erratum: [Eur. Phys. J. C **76** (2016) no.3, 153] doi:10.1140/epjc/s10052-015-3726-9, 10.1140/epjc/s10052-016-3935-x [arXiv:1506.08616 [hep-ex]].

[110] ATLAS Internal, "Tracking CP Recommendations for ICHEP 2016/20.7," url: https://twiki.cern.ch/twiki/bin/view/AtlasProtected/TrackingCPICHEP2016.

[111] The ATLAS collaboration [ATLAS Collaboration], "Tagging and suppression of pileup jets," ATLAS-CONF-2014-018.

[112] "CERN TROOT." http://root.cern.ch/

[113] LHC SUSY Cross Section Working Group, "SUSY Cross Sections using 13, 14, 33 and 100 TeV pp collisions, 2015" url: https://twiki.cern.ch/twiki/bin/view/LHCPhysics/SUSYCrossSections.

[114] A. Sherstnev and R. S. Thorne, "Parton Distributions for LO Generators," Eur. Phys. J. C **55** (2008) 553 doi:10.1140/epjc/s10052-008-0610-x [arXiv:0711.2473 [hep-ph]].

Abstract

Since a long time, humans have been eager to explore and understand the foundations and basic elements of the universe. The Standard Model (SM) was built up, since the second half of the 20th century, to give answers on elementary physics by introducing all the elementary particles including quarks, leptons, gauge bosons and the Higgs boson.

The Large Hadron Collider (LHC) is the largest collider located at CERN (European Organization for Nuclear Research), Geneva. Massive collision dataset was produced and collected since 2009 at a collision center of mass energy of up to 8 TeV before 2012 (Run1) and 13 TeV in 2015 and 2016 (Run2). The ATLAS detector, located at one of the LHC interaction points revealed in 2012 the last member of the SM elementary particles, the Higgs boson. Meanwhile, more thoughts and questions were raised-up, such as the hierarchy problem, the dark matter, the origin of gravity and gauge unification at higher scale. Supersymmetry(SUSY) models are an appealing extension of the SM to answer some of these questions.

SUSY theory models link each boson (of integer spin) to a certain fermion (of half-integer spin) as super-partner. New elementary particles like squarks, sleptons, gauginos and higgsinos are introduced. The simplest form of spontaneously-broken supersymmetry is called Minimal Supersymmetric Standard Model (MSSM), a very good candidate for beyond Standard Model physics.

In this thesis, a brief presentation of the Standard Model and of the main supersymmetry models is given first. Then the LHC complex and the ATLAS detector are described followed by a performance study on tau isolation. The main part of the document finally describes in details two searches for SUSY particles with the ATLAS detector and the obtained results.

The first one is a search for direct stau production with final state of two opposite-sign taus and multi-jets in proton-proton collision at an 8 TeV center of mass energy and a 20.1 fb^{-1} integrated luminosity. The low cross-section for signals in the Electro-Weak sector has pushed to use multivariable analysis techniques to improve the sensitivity. No significant excess over the Standard Model expectation was observed. Upper-limit was set on the cross-section of the signal models. For "direct stau" search, we excluded the signal point with $m(LSP) = 0$ GeV and $m(\tilde{\tau}) = 100$ GeV.

The second one is a search for squarks and gluinos strong production in final states with jets and two same-sign leptons or three leptons at 13 TeV proton-proton collision and a 13.2 fb^{-1} integrated luminosity. No significant excess over the Standard Model expectation was observed. Upper-limit was set on the cross-section of all the models involved. Generally, region with $\tilde{g}$ mass up to 1.7 TeV have been excluded.

Résumé

Depuis longtemps, l'homme est profondément intéressé à explorer et tenter de comprendre les fondements de notre univers. Le Modèle Standard (SM) des particules a été construit au cours de la deuxième moitié du 20ème siècle pour répondre aux questionnements en physique corpusculaire en introduisant toutes les particules élémentaires que sont les quarks, les leptons, les bosons de jauge et le boson de Higgs.

Le grand collisionneur de Hadron (LHC) est le plus grand et plus puissant accélérateur au monde, situer au CERN (Organisation Européenne pour la recherche Nucléaire) à Genève. Une énorme quantité de données de collision a été produite et collectée depuis 2009 à une énergie de collision atteignant 8 TEV dans le centre de masse en 2012 (Run1) et 13 TeV en 2015 et 2016 (Run2). Le détecteur ATLAS, situé sur une de point de collision du LHC, a permis de découvrir en 2012 le boson de Higgs, dernier des constituants du SM non encore découvert. Mais d'autre questions et réflexions ont surgi, comme le problème de la hiérarchie, la matière noire, l'origine de la gravité ou encore l'unification de jauge à grande échelle. Les modèles supersymétriques ou SUSY sont une élégante extension du modèle standard apportant une réponse à certaines de ces questions.

Les modèles théoriques SUSY relient chaque boson (de spin entier) à un fermion spécifique (de spin demi entier) comme super partenaire. De nouvelles particules élémentaires telles que les squarks, sleptons, sgauginos ou higgsinos sont ainsi introduites. La forme la plus simple de brisure spontanée de supersymétrie est appelée le Modèle Standard Super-symétrique Minimal (MSSM), un très bon candidat de physique au-delà du modèle standard.

Dans cette thèse, une brève description du Modèle Standard et des principaux modèles super-symétriques est d'abord donnée. Le LHC et le détecteur ATLAS sont ensuite présentés suivi d'une étude de performance sur l'isolation des taus. La partie principale du mémoire décrit enfin en détails deux recherches de particule SUSY avec le détecteur ATLAS et les résultats obtenus.

La première recherche décrite est celle de production directe de stau avec un état final à deux tau de signes opposés et plusieurs jets dans des collisions proton proton a 8 TeV d'énergie dans le centre de masse et une luminosité totale intégrée de 20.1 fb^{-1}. La faible section efficace pour des signaux dans le secteur électrofaible a nécessité l'utilisation de techniques d'analyse multi variables (MVA) pour améliorer la sensibilité de la recherche. Aucun excés significatif par rapport au Modèle Standard n'a été observé. Des limites supérieures ont été extraite sur la section efficace des modèles de signal. Pour la recherche direct de "stau", le signal est exclu pour $m(LSP) = 0GeV, m(stau) = 100$ GeV.

La deuxième recherche présentée est celle de la production forte de squarks et de gluions avec des états finaux, à deux leptons de mêmes signes ou à trois leptons, associées à des jets dans des collisions proton-proton à $\sqrt{s} = 13$ TeV et une luminosité intégrée de 13.2 fb^{-1}. Aucun excès significatif par rapport au Modèle Standard n'a été observé. Une limite supérieure a été extraite sur la section efficace de tous les modèles impliqués. La région avec une masse de gluino inférieure à 1.7 TeV a été exclue.